Washington University in St. Louis
Washington University Open Scholarship

McKelvey School of Engineering Theses & Dissertations | McKelvey School of Engineering

5-28-2024

Investigation of Volatility, Composition, and Gas-Particle Phase Partitioning of Atmospheric Organic Compounds through Novel Instrumentation and Techniques

Karolina Cysneiros de Carvalho
Washington University – McKelvey School of Engineering

Follow this and additional works at: https://openscholarship.wustl.edu/eng_etds

 Part of the Atmospheric Sciences Commons

Recommended Citation

Cysneiros de Carvalho, Karolina, "Investigation of Volatility, Composition, and Gas-Particle Phase Partitioning of Atmospheric Organic Compounds through Novel Instrumentation and Techniques" (2024). *McKelvey School of Engineering Theses & Dissertations*. 1057.
https://openscholarship.wustl.edu/eng_etds/1057

This Dissertation is brought to you for free and open access by the McKelvey School of Engineering at Washington University Open Scholarship. It has been accepted for inclusion in McKelvey School of Engineering Theses & Dissertations by an authorized administrator of Washington University Open Scholarship. For more information, please contact digital@wumail.wustl.edu.

WASHINGTON UNIVERSITY IN ST. LOUIS

McKelvey School of Engineering
Department of Energy, Environmental & Chemical Engineering

Dissertation Examination Committee:
Brent Williams, Chair
Rajan Chakrabarty
Peter DeCarlo
Randall Martin
Jay Turner

Investigation of Volatility, Composition, and Gas-Particle Phase Partitioning of Atmospheric Organic Compounds through Novel Instrumentation and Techniques

by
Karolina Cysneiros de Carvalho

A dissertation presented to
the McKelvey School of Engineering
of Washington University in
partial fulfillment of the
requirements for the degree
of Doctor of Philosophy

August 2024
St. Louis, Missouri

© 2024, Karolina Cysneiros de Carvalho

Table of Contents

List of Figures

List of Tables

Acknowledgments

"C'mon, we are already late for school!" I would try to make my brother get up as he hit the snooze button for the fifth time. As a twelve-year-old kid, missing the 7 am class was a disaster.

Undoubtedly, that passion for knowledge is, in part, the reason why this dissertation exists; the other part, and more important part, belongs to all the people that I crossed paths with throughout my life. I acknowledge here those who stuck with me over the last six years, but I am grateful for all the interactions that led me to this day. I carry those fond memories deeply within my heart.

To my advisor, Dr. Brent Williams, thank you for believing in me from day one. Thank you for giving me the opportunity and space to grow. This experience changed my family and I's life and I hope I can be a source of positive change to someone else as you were to me.

I also would like to thank my committee for their time and valuable input: Dr. Rajan Chakrabarty, Dr. Peter DeCarlo, Dr. Randall Martin, and Dr. Jay Turner. I owe special thanks to Jay, for all the support when Brent was away, and to Pete, for the help during the ALPACA campaign.

I need to acknowledge all the staff in the EECE department for aiding with purchases, reimbursements, room reservations, and so much more, facilitating my work over the years.

I say without any hesitation that I had the most incredible co-workers during my shared time in the ACT laboratory. Chris, Mike, Claire, and Audrey, your selflessness and kindness, especially during my first years in the Ph.D. program, shaped me as a researcher, and they will always be a source of inspiration in my professional and personal life. Sohyeon, we shared the ups and downs of this six-year journey. Your presence and support made a difference until the end. Jhao-Hong and Tyler, thanks for the friendship over the last few years.

To the ALPACA researchers, thank you all for making it a great campaign amid a global pandemic and for all the collaboration during the years that followed. My mentees, Martha Bransky and Ashutosh Nehete, thank you for helping with the VAPS and the SV-TAG.

I am only able to call St. Louis home because of the wonderful friends I made in this program. Jake and Anna Meyer, Matt and Leila Amrofell, Pradeep Prathibha, Payton Beeler, Katherine,

Rhiannon Carr, Garrett Roell, Matt Lima, and Puneet Dhatt. Thanks for the fun times! I will miss you all! Andressa, Gustavo, and now Ben, you guys are my chosen family. Thanks for the love and Brazilian warmth.

Tori, Neil, Matt, Ethan, Renny, and Ennis, we go way back! Thanks for the constant support and understanding of my absence, especially over the last few months.

I am forever indebted to my parents, Ruy and Heloisa, for the gift of life and for going above and beyond to ensure that me and my siblings had the resources necessary to grow up with integrity.

Nandinha and Leo, my older sister's heart fills with pride watching you grow and become an example of dignity, perseverance, and strength. I have been away for a while now and I am sad to have missed some important milestones in your lives, but our loving bond gives me the courage to continue to follow my dreams. Voinha, Grandma Vera, you are my reference for love in this world, and I miss you every day.

Cindy, my mother-in-law, thank you for taking me as your daughter and not measuring any efforts to ensure my well-being.

Finally, to my life partner, Alex, only you know the true depth of the work written on these pages. You saw my struggles, and while you could not take the weight off my shoulders, you helped with lifting it when I was too tired to keep going. I appreciate you and cherish you, always!

Thank you all!

“Happiness is only real when shared” – C.M.

Karolina Cysneiros de Carvalho

Washington University in St. Louis

August 2024

ABSTRACT OF THE DISSERTATION

Investigation of Volatility, Composition, and Gas-Particle Phase Partitioning of Atmospheric Organic Compounds through Novel Instrumentation and Techniques

by

Karolina Cysneiros de Carvalho

Doctor of Philosophy in Energy, Environmental & Chemical Engineering

Washington University in St. Louis, 2024

Professor Brent Williams, Chair

Atmospheric aerosols are ubiquitous indoors and outdoors and their impact on human life on Earth is extensive. Aerosol particles scatter and absorb solar radiation, are key in the formation of clouds and precipitation, and can affect the abundance and distribution of greenhouse and atmospheric trace gases by physicochemical multiphase processes, thus they play an important role in regulating regional and global climate. On the other hand, poor indoor and outdoor air quality associated with high particulate matter (PM) levels is among the leading health risks worldwide, affecting life quality and expectancy by increasing the risk of cancer, cardiovascular and respiratory diseases. Organic aerosols (OA) have been recognized to account for a significant portion of atmospheric PM covering a wide range of volatilities that encompass thousands of individual compounds. Therefore, the extent of aerosols impact on human life strongly depends on the volatility and chemical composition of the species that comprise the OA population. The work presented in this dissertation focuses on the improvement of OA characterization through the development of novel instrumentation and methods, and the application of these techniques to investigate the process influencing aerosols' volatility and chemical composition variability.

Chapter 2 discusses the challenges in recovering volatility information through thermal evaporation measurements alone and presents improvements in OA volatility characterization when combining thermal evaporation with thermal desorption gas chromatography-mass spectrometry. Chapter 3 focuses on the full development of a modified Semi-Volatile Thermal Desorption Aerosol Gas Chromatograph (SV-TAG) with an automatic calibration system. This version of the SV-TAG features a newly developed cell designed to improve the collection of intermediate volatility and semi-volatile gases and particles, extending the analytical capability of the instrument in the quantification of higher-volatility chemical species. This new instrument was deployed during the Alaskan Layered Pollution and Chemical Analysis (ALPACA) field campaign to help understand the dynamics of speciated gas-particle partitioning under extreme cold and dark conditions with results discussed in Chapter 4. The time-dependent chemical information provided by the SV-TAG also aided in the investigation of the major sources contributing to poor air quality during wintertime in this Arctic region, which is detailed in Chapter 5.

CHAPTER 1

Introduction

1.1. Background and Motivation

By definition, an aerosol is a suspension of liquid, solid, or mixed particles in a gas with diameters varying from 10^{-9} to 10^{-4} m.[1] Atmospheric aerosols are ubiquitous indoors and outdoors and their impact on human life on Earth is extensive. Aerosol particles scatter and absorb solar radiation, are key in the formation of clouds and precipitation, and can affect the abundance and distribution of greenhouse and atmospheric trace gases by physicochemical multiphase processes. Thus, they play an important role in regulating regional and global climate.[2-4] Moreover, particles of biological origin are essential for the natural reproduction of plants and fungi but they can also spread airborne viruses and bacterial material causing or worsening infectious and allergic diseases.[5,6] Lastly, poor indoor and outdoor air quality associated with high particulate matter (PM) levels is among the leading health risks worldwide,[7,8] affecting life quality and expectancy by enhancing the risk of cancer, and cardiovascular and respiratory diseases.[9,10]

Atmospheric aerosols originate from a wide variety of natural and anthropogenic sources. Undergoing physical and chemical transformations throughout its lifetime, each particle carries a chemical signature reflecting its direct source and the extent of its aging processes.[11,12] Consequently, atmospheric aerosols are remarkably diverse in their composition, comprising both inorganic and organic species of varying concentrations. Organic aerosols (OA) have been recognized to account for a significant portion of atmospheric particulate matter[13,14] covering a wide range of volatilities that encompass thousands of individual compounds.[15] While OA components classified as extremely low- and low-volatility organic compounds (E/LVOCs)

predominantly or entirely reside in the particle phase, intermediate volatility and semi-volatile organic compounds (I/SVOCs) can exist in both the particle and gas phases and partition among these phases depending on system conditions. Both OA composition and volatility distribution ultimately influence its fate and determine the extent of its environmental and health effects.

The components that comprise the aerosol particle influence both aerosol-radiation interactions and aerosol-cloud interactions, playing an important role in the radiative energy budget of the Earth. Sulfate, nitrate, and sea-salt aerosols can be considered purely scattering at visible wavelengths, having an overall net cooling effect, and on the other hand, aerosols containing black and organic carbon strongly absorb energy in the UV range, contributing to atmospheric warming.[16] Water-soluble aerosols, including inorganic and organic species, are more efficient cloud condensation nuclei (CCN) than insoluble species.[2] These more hygroscopic aerosols contribute to a larger cloud droplet number, compared to less hygroscopic particles of the same size, resulting in enhanced cloud reflectivity and cooling of the climate.[17]

The potential toxic effects of air pollution also depend on the chemical species that constitute the aerosol population.[18] For instance, polycyclic aromatic hydrocarbons (PAHs) are widespread in the atmosphere substantially due to the fossil-fuel-intensive economy of the Anthropocene.[19] Their genotoxic, mutagenic, and carcinogenic properties pose a great risk to human health.[20] Also abundant in air, oxygenated and nitrated PAHs, either co-emitted or formed through photochemical reactions of PAHs, have been observed to have even more detrimental biological effects compared to their parent PAHs due to the formation of stronger DNA adducts and reactive oxygen species, which elevate their carcinogenicity and oxidative potential.[21]

The OA volatility distribution dictates, in part, the size of the aerosol particles, as an aerosol containing higher volatility species is more likely to shrink as a result of small ambient

perturbations than an OA containing less volatile compounds. The initial concentration of a chemical species in the aerosol particle also influences its subsequent condensation and thus particle growth.[22] The particle size is a crucial parameter in CCN activation (i.e. the potential for an atmospheric particle to become a cloud droplet),[17] and intrinsically related to the aerosols' optical properties that ultimately determine the amount of absorbed and scattered radiation.[1-3,16]

Concerning health effects, the OA volatility influences the size of the aerosol particle before exposure and the physical state of its components after inhalation, two important parameters associated with exposure bioaccessibility (i.e. the amount of a substance available for absorption in the human system).[23] For instance, while compounds associated with larger particles are usually less bioaccessible because absorption by the human cells depends on the desorption rate of a compound from the particle bulk, chemical compounds carried by ultrafine particles can be readily bioavailable given the potential to travel deeper in the lungs and infiltrate cellular membranes completely.[21,23] However, SVOCs deposited in the upper respiratory tract can rapidly become bioaccessible due to breathing cycle dilution-induced particle-to-gas phase partitioning.[24]

Therefore, to fully address the impact of atmospheric OA on human life, it is imperative to characterize both OA composition and volatility distribution. Given that the atmosphere is a dynamic environment, spatial and temporal variations in emissions sources affect these properties. Moreover, the evaporation and condensation of chemical species from and into the aerosol particles, whether resulting from meteorological changes (i.e. temperature, humidity) and/or homogenous, heterogenous, and multiphase chemical reactions, also promote changes in the overall composition and volatility distribution of the OA population. Thus, in addition to determining the OA chemical profile and its volatility, it is crucial to investigate the dynamics of the process influencing the variability of these properties throughout the OA lifetime.

Thermodenuders have been widely used in efforts to quantify OA volatility by providing thermograms (mass fraction remaining curves) obtained from the continuous exposure of an aerosol population to different temperatures.[25-27] Dynamic aerosol evaporation models are needed in most cases for the interpretation of thermograms, but recovering OA volatility distribution from temperature-changing evaporation measurements is very challenging since thermograms are affected not only by thermodynamic parameters but also depend on the aerosol population volatility distribution itself.[28] Coupling thermodenuders and isothermal dilution measurements have been demonstrated to be a promising way of constraining OA volatility, resulting in lower measurement uncertainties.[28,29] This methodology is advantageous because it provides knowledge about the OA full volatility distribution, but on the other hand, lacks relevant chemical information.

The Thermal Desorption Aerosol Gas Chromatogram (TAG) was the first field-deployable instrument to provide hourly, *in situ* quantified speciation of atmospheric organic compounds.[30] Although designed to measure low-volatility species by aerosol inertial impaction onto a custom collection and thermal desorption cell (I-CTD), the system also allows a qualitative evaluation of gas-phase I/SVOCs that are collected via diffusion onto the internal walls of the cell.[31] The first Semi-Volatile TAG (SV-TAG) was idealized to address the I-CTD-TAG's limited gas-phase quantification capabilities by substituting the impactor-based cell with a high-surface metal-fiber filter cell (F-CTD), allowing gas and particle quantification of I/SVOCs.[32] The addition of a second parallel cell to the SV-TAG allowed for particle-phase fraction estimations, while online derivatization improved the throughput of highly oxidized organic molecules.[33] In this work, a combination of thermal evaporation and thermal desorption instrumentation and analysis techniques are developed and applied to provide improved OA chemical and physical characterization and investigate the factors altering these properties over the OA lifetime.

1.2. Objectives

With the importance of atmospheric aerosols' volatility and chemical composition elucidated, the work presented in this dissertation focuses on the development of novel instrumentation and techniques, their application to improve the characterization of OA volatility distribution and speciation, and to investigate the factors that contribute to the variability of these properties, such as multiphase transport and emission sources.

Within the OA volatility and composition characterization, the objectives of this work are:

1. Estimate the volatility distribution and evaporation rates of secondary OA coupling thermodenuder and thermal desorption gas chromatography measurements;
2. Develop and characterize an improved version of the SV-TAG system by extending its analytical capability in the quantification of speciated gases and particles;

Within the factors promoting changes in OA composition and volatility, this work investigates:

3. The dynamics of gas-particle partitioning under extreme cold and dark conditions;
4. The sources and processes contributing to air pollution during wintertime in the Arctic.

A diagram illustrating the interconnection between each objective is provided in **Figure 1.1.**

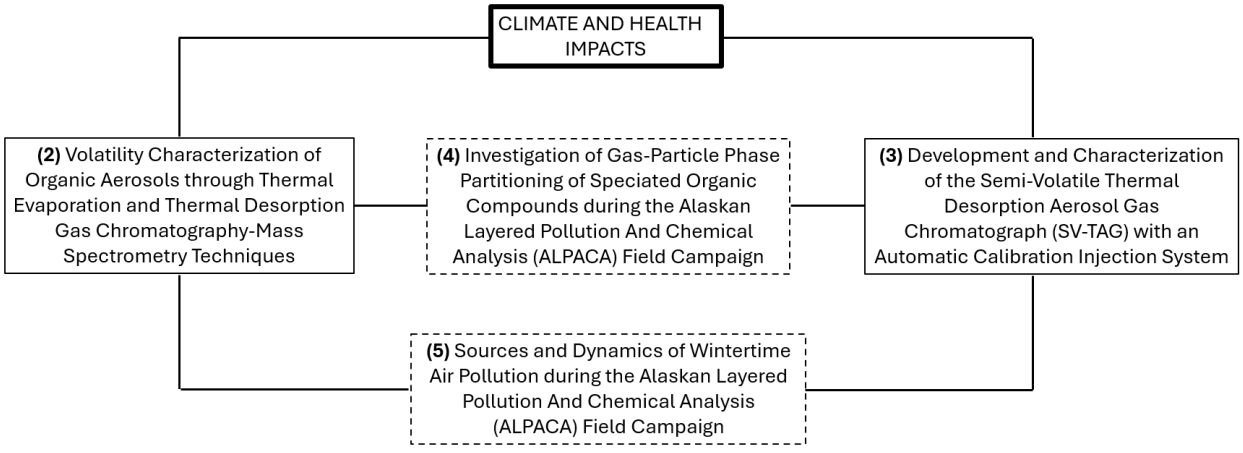

Figure 1.1. Flow diagram of the dissertation. Bold box highlights the relevance of studying organic aerosols (OA). Solid boxes represent the chapters on OA characterization. Dashed boxes are the chapters on the investigation of processes that impact OA volatility and chemical composition. Numbers in parathesis are the dissertation chapters.

1.3. Summary of Chapters

1.3.1. Chapter 2: Volatility Characterization of Organic Aerosols through Thermal Evaporation and Thermal Desorption Gas Chromatography-Mass Spectrometry Techniques

The importance of the multicharged aerosol size distribution in recovering volatility information from size-selected aerosol evaporation measurements is demonstrated by studying the mass transfer dynamics of a single compound aerosol system. Mass fraction remaining curves were generated using a Volatility Tandem Differential Mobility Analyzer (V-TDMA) and an Aerosol Mass Spectrometer (AMS). By using a new aerosol charge-dependent evaporation kinetic model, the singly charged aerosol population was found to contribute to less than 30% of the total 200 nm azelaic acid particle mass. When accounting for the remainder charge distribution, the expected thermogram-sigmoid shape was recovered, increasing the complexity of using dynamic transfer models to estimate aerosol volatility distribution. The relevance of coupling different techniques to improve OA volatility characterization was evidenced by combining thermal evaporation and thermal desorption gas chromatography-mass spectrometry (TD-GC/MS). GC-volatility-constrained evaporation rates and chemical composition of secondary OA (SOA) produced by the oxidation of different precursors were investigated. It was observed that thermally labile compounds dominate monoterpene ozonolysis SOA. For each VOC precursor, the fragments from the least volatile SOA components eluted in earlier GC retention times and were less oxidized than the most volatile components, suggesting oligomerization during SOA formation. The volatility-oxidation correlation observed within each SOA held true when comparing these two properties across different SOA, corroborating the broader conclusion of this study that the least volatile SOA material can also be less oxidized.

1.3.2. Chapter 3: Development and Characterization of the Semi-Volatile Thermal Desorption Aerosol Gas Chromatograph (SV-TAG) with an Automatic Calibration Injection System

A modified dual-cell SV-TAG instrument was fully developed to improve the collection of gas and particle I/SVOCs, extending the analytical capability of the instrument in the quantification of higher-volatility chemical species. For this version of the SV-TAG, a new dual-stage collection cell (FT-CTD cell) was constructed combining the previous metal fiber filter design with a custom backup collection cell composed of Tenax® TA sorbent. The efficacy of incorporating a VOC sorbent was demonstrated by comparing the new collector design with the previous single-stage cell (featuring solely the high-surface-area metal fiber filter), and with a dual-stage design comprising the metal filter on the first stage and a quartz filter on the second stage. While all three collectors showed comparable efficiencies in the recovery of low-volatility analytes, the dual-stage Tenax® cell was responsible for 60%, on average, of the total signal observed by three different collectors at the retention time window corresponding to high-volatility IVOCs. Calculated limits of detection of selected compounds injected in the FT-CTD cell and eluting in the IVOC retention time window were on the order of magnitude of 0.01 ng. When considering a 10-minute collection at 8.3 $L.min^{-1}$, this detection limit corresponds to 0.12 $ng.m^{-3}$, which is below measured concentrations for most compounds of interest. This dual-cell arrangement provides more accurate gas-particle partitioning quantification compared to the single-cell systems. However, a prerequisite to reliable measurements is the characterization of the differences in analyte retention and transfer between collectors. Thus, this SV-TAG also incorporates a custom-developed, highly reproducible, automatic calibration injection system that allows the continuous injection of tracking liquid standards providing a means to correct for inter-cell variability.

1.3.3. Chapter 4: Investigation of Gas-Particle Phase Partitioning of Speciated Organic Compounds during the Alaskan Layered Pollution And Chemical Analysis (ALPACA) Field Campaign

The Alaskan Layered Pollution And Chemical Analysis (ALPACA) field campaign was deployed in Fairbanks, Alaska, during the winter of 2022 to investigate air pollution sources and transformations under sustained cold and dark conditions. The SV-TAG provided hourly measurements of outdoor and indoor OA gas and particle concentrations to help understand the dynamics of phase partitioning and the extent of this process upon infiltration in this extreme environment. Measurements were compared against the absorptive partitioning theory, commonly used to describe gas-particle phase dynamics in atmospheric models. The wintertime temperatures induced shifts in compounds' vapor pressures to lower values, enhancing gas-to-particle phase partitioning. However, the observed particle-bound measurements did not agree with the modeled calculations. Phase state estimations demonstrated that the aerosol particles adopted a semi-solid viscous state throughout the campaign and the extent of evaporation and condensation was affected by this increase in particle viscosity. These results demonstrated that the assumption of instantaneous reversible equilibrium used to predict phase partitioning dynamics is not suitable to describe this process under cold and dark conditions. The dependence of equilibration timescales on both volatility and bulk diffusivity needs to be accounted for when predicting gas-particle phase partitioning of atmospheric OA during wintertime in Arctic regions to accurately address their impacts on both climate and health.

1.3.4. Chapter 5: Sources and Dynamics of Wintertime Air Pollution during the Alaskan Layered Pollution And Chemical Analysis (ALPACA) Field Campaign

The time-dependent chemical information provided by the SV-TAG during the ALPACA campaign also benefitted the investigation of the sources and dynamics of atmospheric OA that contribute to wintertime air pollution in the Fairbanks region. Using Positive Matrix Factorization (PMF) to track co-varying individual chemical species, five factors were identified as major components impacting air quality in a residential neighborhood. One factor represented higher volatility species that demonstrated significant changes in gas- and particle-phase emissions due to the temperature-induced shift in their vapor pressures. A traffic commute source was also identified, showing higher contributions in the late afternoon/early evening possibly associated with emissions from cold engines. The overall heating factor indicated that both fuel oil and wood combustion are a source of ground-level pollution in the neighborhood. Interestingly, a softwood-dominant factor was found to co-vary with the strength of surface-based temperature inversions, suggesting gas-to-particle phase partitioning enhancement under stable atmospheric conditions. Finally, meteorological conditions and diagnostic ratio analysis proposed that PAHs measured at the house site could be associated with both residential heating and power generation emissions.

1.3.5. Chapter 6: Conclusions

In the final chapter, key findings are summarized along with future directions that expand upon the work presented in this dissertation.

References

1. Seinfeld JH, Pandis SN. *Atmospheric Chemistry and Physics: From Air Pollution to Climate Change*. Wiley; 2016.

2. Penner J, Andreae M, Annegarn H, et al. Aerosols, their direct and indirect effects. In: *Climate Change 2001: The Scientific Basis: Contribution of Working Group I to the Third Assessment Report of the Intergovernmental Panel on Climate Change*. Cambridge University Press; 2001:289-348.

3. Myhre G, Shindell D, Bréon F, et al. Anthropogenic and natural radiative forcing. In: *Climate Change 2013 - The Physical Science Basis: Working Group I Contribution to the Fifth Assessment Report of the Intergovernmental Panel on Climate Change*. Cambridge University Press; 2013:659-740.

4. Pöschl U, Shiraiwa M. Multiphase Chemistry at the Atmosphere–Biosphere Interface Influencing Climate and Public Health in the Anthropocene. *Chemical Reviews*. 2015;115(10):4440-4475.

5. Fröhlich-Nowoisky J, Kampf CJ, Weber B, et al. Bioaerosols in the Earth system: Climate, health, and ecosystem interactions. *Atmospheric Research*. 2016;182:346-376.

6. Prather KA, Marr LC, Schooley RT, McDiarmid MA, Wilson ME, Milton DK. Airborne transmission of SARS-CoV-2. *Science*. 2020;370(6514).

7. World Health Organization (WHO). Ambient (outdoor) air quality and health. Published December 19, 2022. Accessed March 2024. https://www.who.int/news-room/fact-sheets/detail/ambient-(outdoor)-air-quality-and-health

8. World Health Organization (WHO). Household Air Pollution and Health. Published November 28, 2022. Accessed March 2024. https://www.who.int/news-room/fact-sheets/detail/household-air-pollution-and-health

9. Lelieveld J, Pozzer A, Pöschl U, Fnais M, Haines A, Münzel T. Loss of life expectancy from air pollution compared to other risk factors: a worldwide perspective. *Cardiovascular Research*. 2020;116(11).

10. Hill W, Lim EL, Weeden CE, et al. Lung adenocarcinoma promotion by air pollutants. *Nature*. 2023;616(7955):159-167.

11. Pöschl U. Atmospheric Aerosols: Composition, Transformation, Climate and Health Effects. *Angewandte Chemie International Edition*. 2005;44(46):7520-7540.

12. Seinfeld JH. Tropospheric Chemistry And Composition | Aerosols/Particles. *Elsevier eBooks*. Published online January 1, 2015:182-187.

13. Jacobson MC, Hansson HC ., Noone KJ, Charlson RJ. Organic atmospheric aerosols: Review and state of the science. *Reviews of Geophysics*. 2000;38(2):267-294.

14. Jimenez JL, Canagaratna MR, Donahue NM, et al. Evolution of organic aerosols in the atmosphere. *Science (New York, NY)*. 2009;326(5959):1525-1529.

15. Donahue NM, Kroll JH, Pandis SN, Robinson AL. A two-dimensional volatility basis set – Part 2: Diagnostics of organic-aerosol evolution. *Atmospheric Chemistry and Physics*. 2012;12(2):615-634.

16. Li J, Carlson BE, Yung YL, et al. Scattering and absorbing aerosols in the climate system. *Nature Reviews Earth & Environment*. 2022;3(6):363-379.

17. McFiggans G, Artaxo P, Baltensperger U, et al. The effect of physical and chemical aerosol properties on warm cloud droplet activation. *Atmospheric Chemistry and Physics*. 2006;6(9)

18. Liu F, Nga Lee Ng. *Toxicity of Atmospheric Aerosols: Methodologies & Assays*. American Chemical Society; 2023.

19. Patel AB, Shaikh S, Jain KR, Desai C, Madamwar D. Polycyclic Aromatic Hydrocarbons: Sources, Toxicity, and Remediation Approaches. *Frontiers in Microbiology*. 2020;11.

20. John Kilpatrick D. *Investigating the Relationship of COPD, Lung Cancer, and Polycyclic Aromatic Hydrocarbons from Ambient Air Pollution*. Dissertation. 2019.

21. Lammel G, Kitanovski Z, Kukučka P, et al. Oxygenated and Nitrated Polycyclic Aromatic Hydrocarbons in Ambient Air—Levels, Phase Partitioning, Mass Size Distributions, and Inhalation Bioaccessibility. *Environmental Science & Technology*. 2020;54(5):2615-2625.

22. Pankow JF. An absorption model of gas/particle partitioning of organic compounds in the atmosphere. *Atmospheric Environment*. 1994;28(2):185-188.

23. Wei W, Ramalho O, Mandin C. Modeling the bioaccessibility of inhaled semivolatile organic compounds in the human respiratory tract. *International Journal of Hygiene and Environmental Health*. 2020;224:113436-113436.

24. Liu C, Zhang Y, Weschler CJ. Exposure to SVOCs from Inhaled Particles: Impact of Desorption. *Environmental Science & Technology*. 2017;51(11):6220-6228.

25. Cappa CD. A model of aerosol evaporation kinetics in a thermodenuder. *Atmospheric Measurement Techniques*. 2010;3(3):579-592.

26. Sung Hoon Park, Rogak SN, Grieshop AP. A Two-Dimensional Laminar Flow Model for Thermodenuders Applied to Vapor Pressure Measurements. *Aerosol Science and Technology*. 2012;47(3):283-293.

27. Cain KP, Pandis SN. A technique for the measurement of organic aerosol hygroscopicity, oxidation level, and volatility distributions. *Atmos. Meas. Tec*. 2017;10(12):4865-4876.

28. Cain KP, Karnezi E, Pandis SN. Challenges in determining atmospheric organic aerosol volatility distributions using thermal evaporation techniques. *Aerosol Science and Technology*. 2020;54(8):941-957.

29. Louvaris EE, Karnezi E, Kostenidou E, Kaltsonoudis C, Pandis SN. Estimation of the volatility distribution of organic aerosol combining thermodenuder and isothermal dilution measurements. *Atmospheric Measurement Techniques*. 2017;10(10):3909-3918.

30. Williams BJ, Goldstein AH, Kreisberg NM, Hering SV. An In-Situ Instrument for Speciated Organic Composition of Atmospheric Aerosols: Thermal Desorption Aerosol GC/MS-FID (TAG). *Aerosol Science and Technology*. 2006;40(8):627-638.

31. Williams BJ, Goldstein AH, Kreisberg NM, Hering SV. In situ measurements of gas/particle-phase transitions for atmospheric semivolatile organic compounds. *Proceedings of the National Academy of Sciences of the United States of America*. 2010;107(15):6676-6681.

32. Zhao Y, Kreisberg NM, Worton DR, Teng AP, Hering SV, Goldstein AH. Development of an *In Situ* Thermal Desorption Gas Chromatography Instrument for Quantifying Atmospheric Semi-Volatile Organic Compounds. *Aerosol Science and Technology*. 2012;47(3):258-266.

33. Isaacman-VanWertz G, Kreisberg NM, Yee LD, et al. Online derivatization for hourly measurements of gas- and particle-phase semi-volatile oxygenated organic compounds by thermal desorption aerosol gas chromatography (SV-TAG). *Atmospheric Measurement Techniques*. 2014;7(12):4417-4429.

CHAPTER 2

Volatility Characterization of Organic Aerosols through Thermal Evaporation and Thermal Desorption Gas Chromatography-Mass Spectrometry Techniques

Abstract

Volatility is one of the most important physical properties of organic aerosols (OA), determining the dynamics of particle formation and growth in the atmosphere. Despite its relevance, multicomponent OA volatility distribution estimations are still uncertain. This chapter elucidates the challenges of characterizing OA volatility using thermal evaporation techniques alone and, provides an alternative approach by coupling thermal evaporation and thermal desorption gas chromatography-mass spectrometry (TD-GC/MS). In the first part of this work, it is demonstrated that when modeling the evaporation kinetics of a monodisperse aerosol population pre-selected using a differential mobility analyzer (DMA), the multicharged size distribution must be considered since the singly charged particles only account for a fraction of the total evaporated mass. This consideration increases the complexity of recovering volatility information from thermal evaporation measurements, which are already influenced by several other parameters. In the second part of this work, the volatility characterization of secondary OA (SOA) produced from the ozonolysis of α-pinene, limonene, and β-pinene was studied by constraining the volatility basis set on chemical speciation using a faster, higher mass output TD-GC/MS-based instrument and monitoring their evaporation at different temperatures. It was observed that SOA chromatograms were dominated by thermal decomposition products. In addition, fragments from the least volatile SOA components eluted in earlier GC retention times and were less oxidized than the most volatile components. These observations suggest that monoterpene ozonolysis SOA produced in these experiments were composed of highly labile oligomeric material. Overall, limonene-originating SOA were more oxidized than α-pinene and β-pinene ozonolysis products due to the higher reactivity of the former precursor. Its faster evaporation rates corroborate the broader conclusion of this study that the least volatile SOA material can also be less oxidized.

2.1. Introduction

Atmospheric secondary organic aerosols (SOA) are formed in the atmosphere through the oxidation of gaseous precursors and subsequent condensation of the low-volatility reaction products.[1] Secondary aerosol formation is the main driver of $PM_{2.5}$ pollution events,[2] and is a dominant component of atmospheric organic aerosols (OA) even in urban locations.[3] The volatility distribution of SOA is a key quantity that has to be well understood to accurately describe SOA formation, growth, and ultimate fate in the atmosphere.[4] Thermal evaporation techniques have been widely applied to study OA volatility, including temperature-changing evaporation in thermodenuders (TD)[5-9] as well as isothermal dilution-induced evaporation.[10-12]

A TD comprises a heated tube where volatile particle components evaporate, followed by a cooling section with activated carbon to prevent vapor re-condensation. The most common way of reporting thermodenuder measurements is by thermograms, which represent the aerosol mass fraction remaining (MFR) as a function of the TD temperature. Since equilibrium is rarely reached inside the thermodenuder,[13] a dynamic aerosol evaporation model is needed for the interpretation of thermal evaporation measurements and the estimation of OA volatility.[13-15] A full description of the aerosol size distribution and the radial dependence of its concentration in the TD is needed to solve the time-evolving mass transfer equation (Equation 2.1) and compute the shrinkage of the particles due to evaporation.

$$\frac{dD_p}{dt} = -\frac{4D_{i,air}M_i}{\rho_i D_p RT} {p_i}^o \exp\left(\frac{4\sigma_i M_i}{\rho_i D_p RT}\right) f(Kn_i \alpha_i) \rightarrow$$

$$\int_{D_{pi}}^{D_{pf}} \frac{D_p}{f(Kn_i \alpha_i)} \exp\left(\frac{-4\sigma_i M_i}{\rho_i D_p RT}\right) dD_p = -\frac{4D_{i,air}M_i}{\rho_i D_p RT} \Delta t \qquad \textbf{(2.1)}$$

where $D_{i,air}$ is the diffusion coefficient of the evaporating specie in air at the TD temperature T; M_i is the evaporating specie's molecular weight; ρ_i is its density; D_p is the particle's diameter; R

is the gas ideal law constant; $p_i{}^o$ is the vapor pressure of the evaporating species over a flat surface; σ_i is its surface tension; $F(Kn_i, \alpha_i)$ is the correction factor due to non-continuous effects (Kn_i) and imperfect surface accommodation (α_i).

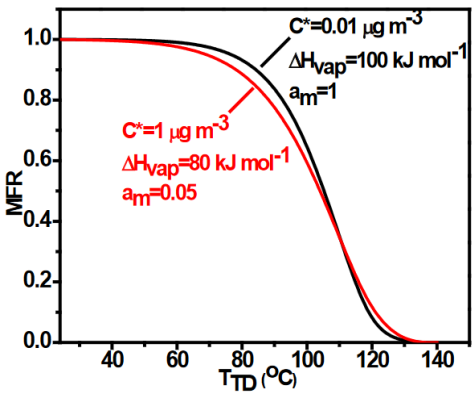

Figure 2.1. Modeled thermograms of organic aerosols of different properties. Source: Karnezi et al.[17]

However, recovering multicomponent volatility distribution from TD measurements has been demonstrated to be very challenging[16] because thermograms are affected not only by thermodynamic parameters but also depend on the aerosol population volatility distribution itself.[17] **Figure 2.1** illustrates the statement above. Modeled thermograms considering OA of different volatilities (orders of magnitude) demonstrate that it is possible to obtain very similar curves by adjusting parameters that affect their evaporation kinetics. In this example, the reduction in saturation concentration (vapor pressure) is balanced by changes in the accommodation coefficient and the vaporization enthalpy.

In efforts to simplify model calculations, the time-dependent evaporation equation is often solved for a monodisperse aerosol population.[13-17] Experimentally, this is achieved using a differential mobility analyzer (DMA) to pre-select an electrical mobility diameter, sharpening the initial size distribution that is then evaporated in the TD.[5,6] Experimental thermograms are generated by measuring the remaining mass after aerosol evaporation at different temperatures while modeling the evaporation kinetics provides a means to estimate the aerosol volatility distribution. However, previously developed models tend to yield steeper thermograms compared to experimental mass-based data[14,15] and the mass accommodation coefficient has been suggested to play a role in the observed discrepancies.

In the first part of this work, the evaporation of a single-component aerosol is studied by generating thermograms using a Volatility Tandem Differential Mobility Analyzer (V-TDMA) and an Aerosol Mass Spectrometer (AMS). A new kinetic model, which takes into consideration the multicharged nature of the monodisperse aerosol population is used to interpret its evaporation dynamics. Comparing the resulting curves from both instruments, the role of the unity mass accommodation coefficient assumption in the calculations of OA volatility is discussed.

Isothermal dilution-induced evaporation measurements do not require the knowledge of the enthalpy of vaporization or mass accommodation coefficient for OA volatility distribution estimations, but this approach only provides collective information of low-volatility compounds (LVOCs) and extremely low-volatility compounds (ELVOCs) without any distribution details.[16] Furthermore, studies have shown that the use of isothermal dilution on its own usually results in worse estimates of volatility distributions compared to TD alone.[17] Coupling TD and isothermal dilution measurements have been demonstrated to be a promising way of constraining OA volatility, resulting in lower measurement uncertainties.[16-20] This approach is advantageous because it provides knowledge about the OA full volatility distribution, but on the other hand, lacks the detailed chemical characterization required to fully understand evaporation-driven changes in composition-dependent properties, such as oxidation levels and hygroscopicity.[8]

In a recent study, Cain et al[16] restated the necessity to combine different techniques in order to entirely understand OA properties such as volatility. Therefore, in the second part of this work, fast thermal desorption gas chromatography-mass spectrometry (TD-GC/MS) and thermodenuder measurements are combined to investigate the volatility distribution of SOA formed from the ozonolysis of α-pinene, limonene, and β-pinene. The fast GC/MS system uses a short non-polar column, providing measurements of volatility distribution independent of the thermodenuder. It

also complements the evaporation of bulk aerosol mass with the knowledge of chemical classes and even some individual compounds. This chemical composition measurement along with the evaporation information can give practical insights in understanding the volatility of OA and help with elucidating their atmospheric evolution and fate.

2.2. Materials and Methods

2.2.1. Single-Component Aerosol Thermograms

Experimental Setup

To elucidate the challenges in recovering aerosol volatility information from thermodenuder measurements, azelaic acid was evaporated and thermograms were generated using measurements from both a V-TDMA (custom-built)[21] and a High-Resolution Time-of-Flight AMS (HR-ToF-AMS, Aerodyne, Inc., Billerica, MA). The experimental setup is shown in **Figure 2.2.** Azelaic acid (Catalog #246379, Sigma Aldrich, St. Louis, MO) aerosol particles were produced by atomizing, at 3 atm, an acid solution of 1 $mg.mL^{-1}$ concentration prepared using 18 MΩ deionized water. The polydisperse aerosol passed through a series of diffusion dries packed with silica and it was subsequently diluted with clean dry air before entering an equilibration tank. After 15-30 minutes, the equilibrated aerosol was neutralized using Po-210 strips to generate a steady-state charge distribution. This inlet size distribution was then computed by a Scanning Mobility Particle Sizer (SMPS, Model 3081 DMA, Model 3022A CPC, TSI, Inc., Shoreview, MN) sampling at 0.3 $L.min^{-1}$ while an initial mobility diameter of 200 nm was selected by the first DMA (sample flow rate of 1.6 $L.min^{-1}$ and sheath flow rate of 15 $L.min^{-1}$). Evaporation was achieved by exposing the aerosol to different temperatures (23°C, 30°C, 38°C, 46°C, 52°C, 58°C and 63°C) in an oven that comprises 15.25 m of 0.95 cm thin walled copper tubing suspended inside an insulated

container. The long tubing results in an extended residence time (26.5 seconds), featuring constant temperatures throughout its entire length providing well-characterized temperature measurements for vapor pressure estimation. A bypass line of residence time less than 1.25 seconds was used to sample the aerosol when evaporation was not desired. The second DMA (sample flow rate of 1.5 $L.min^{-1}$ and sheath flow rate of 15 $L.min^{-1}$) coupled with the CPC (Model 3776, TSI, Inc., Shoreview, MN) granted the measurements to estimate the change in particle mobility diameter after evaporation, while the AMS, operated in V-mode and sampling at 0.1 $L.min^{-1}$, provided aerosol total mass evaluations.

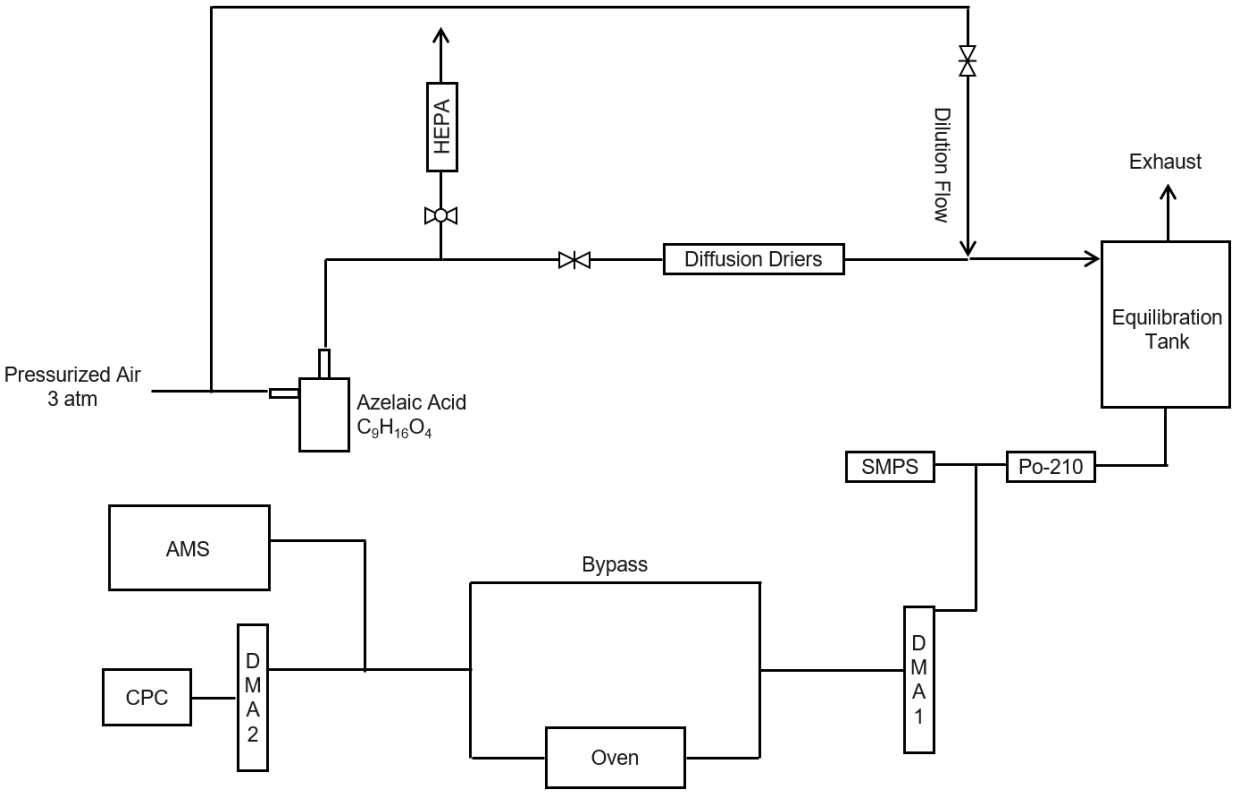

Figure 2.2. Experimental setup used to study single-component aerosol volatility.

V-TDMA Thermograms

To interpret volatility measurements a new V-TDMA model was applied.[22] One of the advantages of this new model is that it does not assume the peak of the inverted CPC response

before and after evaporation is equal only to the peak of the singly charged particles in experimental size distribution. Instead, the model keeps track of the experimental size distributions as a function of particle charge. Briefly described, the model uses the provided initial size distribution entering the first DMA and its transfer function to generate the selected size distribution prior to evaporation as a function of the particle charge. Next, using the evaporation parameters given by the user (mass accommodation, surface tension, and vapor pressure) and the second DMA transfer function, it solves the mass transfer equation (Equation 2.1) at each temperature studied and tries to predict the CPC response after evaporation.

Assuming constant values for the mass accommodation coefficient and surface tension, the value for vapor pressure is adjusted to match the measured CPC response and the one predicted by the model. Once this is achieved, the third-moment integration on the recorded charge-dependent size distributions after the oven is used to estimate the aerosol mass concentration after evaporation. At each evaporating temperature, an updated inlet size distribution was used in the model. Particle loss affects the model's total estimated mass directly by decreasing the number of particles in the system, and indirectly, by influencing the aerosols' evaporation rates. Since particle loss is a function of particle size, and thus, a function of temperature, for each evaporation experiment, particle loss was accounted for by adjusting the measured exit DMA2 population by comparing it with the exit DMA1 population before solving the mass transfer equation.

For this study, azelaic acid molecular weight and density values were obtained from Design Institute for Physical Property Research/AIChE (DIPPR®) project 801 database.[23] Respectively, these values are equal to 188.22 $g.mol^{-1}$ and 1.251 $g.m^{-3}$. The value for the mass accommodation, a parameter in the correction factor $f(Kn, \alpha)$ was assumed to be equal to one. The surface tension value was calculated as 0.129 $J.m^{-2}$. Diffusion coefficients were estimated at each evaporating

temperature from the Chapman–Enskog kinetic theory. Details about these model inputs can be found in Appendix A2 (**Section A2.1**).

To generate a thermogram with the V-TDMA, the calculated remaining mass after evaporation is divided by the total system mass at ambient temperature before evaporation (i.e. reference mass). The aerosol reference mass was estimated by sampling 200 nm azelaic acid aerosol particles through the bypass line and measuring it with the V-TDMA and the AMS before starting the evaporation experiments. The V-TDMA charge-dependent total system mass was calculated using a custom MATLAB routine. Briefly, the routine inverts the second DMA transfer function to determine the total number of particles detected by DMA2. Next, using the SMPS size distribution and the first DMA transfer function, it calculates the size distribution exiting DMA1. This information (size distribution) coupled with the total population exiting DMA2 (accounts for particle loss) is then used to estimate the first, second, third, fourth, and fifth charge masses and the total mass concentration of the system.

The calculated initial mass concentration was 19.52 $\mu g.m^{-3}$, which is low enough to assume negligible re-condensation after evaporation[14,15,24] and opt out of a denuder after the long residence time oven since this device could be disadvantageous in promoting further particle evaporation after gas-phase removal.[24] Ideally, a reference mass is calculated before each evaporation experiment to avoid overestimation or underestimation of MFR due to fluctuations in the atomization process. However, investigation of the initial size distributions obtained with the SMPS throughout the study demonstrated that the total generated mass remained constant for the time period considered as seen in **Figure A2.2** (Appendix A2 – Section A2.1). Thus, justifying the use of one constant reference mass concentration for all mass fraction remaining calculations.

AMS Thermograms

AMS data was processed in Igor Pro using the SQUIRREL version 1.62A toolkit for unit mass resolution analysis, and the PIKA version 1.22A toolkit for high-resolution analysis to obtain the total organic ion signal measured by the instrument during the study. The AMS signal was then calibrated to the V-TDMA charge-dependent aerosol mass by sampling different concentrations of 200 nm azelaic acid aerosol particles through the bypass line and measuring it with both instruments. The same MATLAB routine used to calculate the initial reference mass concentration for the V-TDMA thermogram was used to estimate the bypass masses at varying azelaic concentrations. The resulting calibration curve is shown in **Figure A2.3** (Appendix A2 – Section A2.2). At each evaporation experiment, the AMS signal was then related to the V-TDMA mass using the calibration curve, and an AMS thermogram was generated by dividing the AMS mass after each evaporation by the AMS reference bypass mass.

2.2.2. Volatility Characterization of Laboratory-Generated SOA

Experimental Setup

The experimental apparatus to study SOA volatility distribution is shown in **Figure 2.3**. Ozone (O_3) was produced by irradiating 0.4 L.min^{-1} of pure oxygen (O_2) with mercury lamps (λ = 185 nm; BHK, Inc., Ontario, CA) and introduced into the 13-L Potential Aerosol Mass (PAM) Oxidation Flow Reactor (OFR),[25,26] used here as a mixing volume to promote the ozonolysis of α-pinene, limonene, and β-pinene. An O_3 analyzer, (Model 49i, Thermo Scientific, Franklin, MA) that utilizes UV photometric detection, provided ozone concentration measurements to ensure stable SOA formation throughout the study. For each experiment, a different precursor was injected into the PAM by sampling the volatile organic compound (VOC) through a bubbler using

pure nitrogen gas (N_2) as a carrier. The VOC mass flow controller was calibrated to a constant bubble flow rate of one bubble per second. Ammonium sulfate aerosol particles were produced by atomizing, at 3 atm, a solution of 10 $mg.mL^{-1}$ concentration prepared using 18 MΩ deionized water. The polydisperse particles were added into the PAM to act as a condensation nuclei for the VOC oxidation products. Water vapor was introduced into the system with a 1.6 L min^{-1} of humidified N_2, maintaining a relative humidity inside the mixing reactor of 38.8% ± 0.4 (one standard deviation) measured with a relative humidity and temperature probe with manufacturer-specified accuracy of 1.5% (Vaisala, Inc., Woburn, MA). The total initial flow into the PAM was equal to 3 $L.min^{-1}$, giving an average residence time of 260 s (~ 4.33 minutes) for SOA production. All chemicals used in these experiments were purchased from Sigma Aldrich (St. Louis, MO).

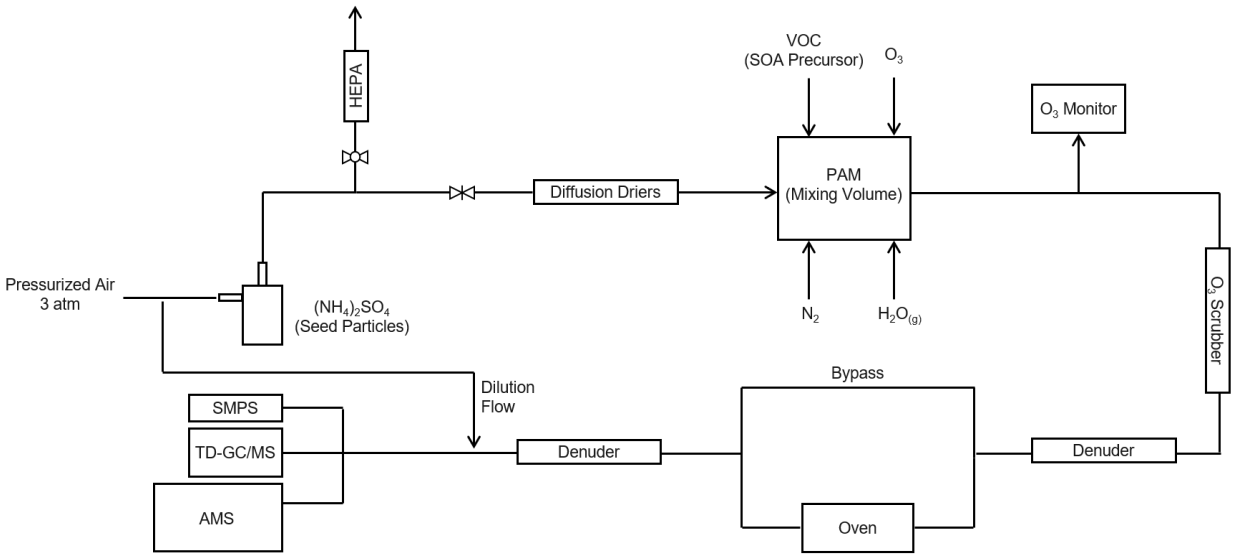

Figure 2.3. Experimental setup used to study the volatility of SOA produced from the ozonolysis of α-pinene, limonene, and β-pinene.

After exiting the PAM, the ozonolysis products passed through an annular denuder containing Carulite 200 (manganese dioxide/copper oxide catalyst; Carus Corporation, Peru, IL), followed by a parallel plate activated carbon denuder (Sunset Laboratory, Inc., Tigard, OR) to

remove the remainder gaseous components. The SOA was then exposed to different evaporating temperatures (22ºC, 59ºC, and 88ºC) in a long-residence time (26.5 s) oven. A second parallel plate denuder was installed after the oven to prevent re-condensation of the evaporated material given the high SOA yields. The aerosol was further diluted to allow sampling by the HR-ToF-AMS at 0.1 $L.min^{-1}$ (Aerodyne, Inc., Billerica, MA), the SMPS at 0.3 $L.min^{-1}$ (Model 3081 DMA, Model 3022A CPC, TSI, Inc., Shoreview, MN) and the custom TD-GC/MS instrument at 3.4 $L.min^{-1}$, described in detail below. Each precursor was evaluated separately. The PAM reactor was cleaned overnight before each different VOC experiment by continuously flowing clean dry air while the internal UV lamps were on. The initial experimental conditions of each precursor are outlined in **Table A2.2** (Appendix A2 – Section A2.3).

Instrumentation

The AMS operated in V-mode measuring non-refractory PM bulk composition for particles with aerodynamic diameter values between 50-1000 nm. Detailed operational description of the AMS system can be found elsewhere.[27] For the GC/MS analysis, the generated SOA was collected for 20 minutes at 3.4 $L.min^{-1}$ onto an impactor-based collection and thermal desorption (I-CTD) cell developed for the original Thermal desorption Aerosol Gas chromatograph (TAG) system.[28] Following sample collection, the I-CTD cell was purged for 2.5 min. at 100 sccm to eliminate water and oxygen from the system, and then heated to 250°C at a temperature rate of approximately 0.5°C per second. This temperature setpoint was held for 5 minutes. During this thermal desorption step, the volatilized sample was carried out by a helium stream onto the head of the 1-meter low-polarity fused silica column, (Rxi-5Sil MS, 0.15 mmID, 0.15 μm df, (Restek Corporation, Bellefonte, PA) placed inside a 0.53 mmID Restek Hydroguard-Treated MXT metal column,

initially maintained at room temperature, resulting in the re-condensation of the sample prior to chromatograph separation. To transfer the thermally desorbed material from the head of the column to the HR-ToF-MS, the column was heated by applying an electrical current using an external power supply. Current was increased to a maximum amperage of 1.9A by applying a square root ramp rate and held at that setpoint for 5 minutes. An important feature observed in this TD-GC/MS measurements is that some thermally labile compounds break down during thermal desorption, resulting in fragments that are too volatile to recondense on the GC column head and therefore, travel straight to the detector.[29] For this study, the thermal decomposition window is defined from 0 to 12 min. as seen in **Figure 2.4**, which also highlights the temperature and electrical current profiles for the I-CTD cell and GC column, respectively. The HR-ToF-MS used by both the AMS and the GC/MS instrument was programmed to scan a *m/z* range of 29-450. The lower *m/z* limit was determined to eliminate large signals associated with H_2O (*m/z* 18) and N_2 (*m/z* 28), but it still includes O_2 (*m/z* 32) and Ar (*m/z* 40) to allow investigation of leaks.

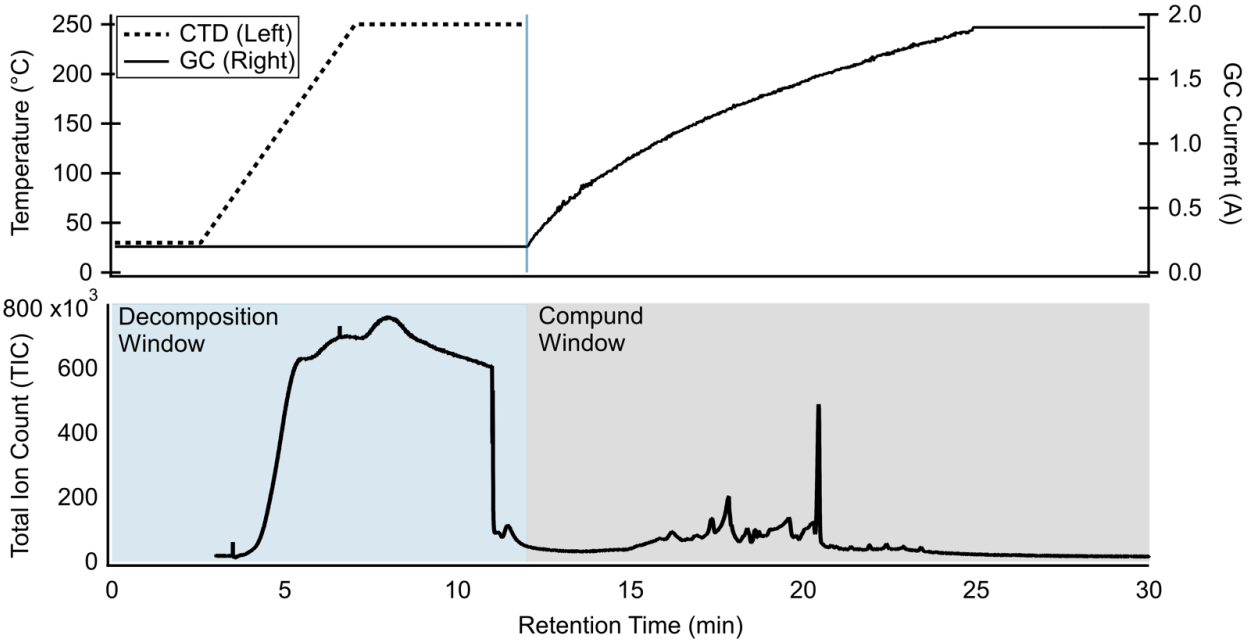

Figure 2.4. TD-GC/MS method run and example chromatogram. Top plot shows the temperature and electrical current profiles for the I-CTD cell and GC column, respectively. The example chromatogram on the bottom highlights the different analytical windows.

Volatility Basis Set

To relate the GC volatility dimension to a known volatility basis set, 1 µL of a 50 ng.µL^{-1} pre-mixed even-numbered alkane (C12-C40) standard mixture (Catalog # 68281, Sigma Aldrich, St. Louis, MO) was injected into the system described above. By considering the region where each individual alkane eluted, the SOA evaporation chromatograms from each precursor were divided, providing a measurement of volatility distribution independent of the oven. For each precursor, the chromatogram at ambient temperature (22^{o}C) was used as the reference chromatogram for retention time (RT) shifts. **Figure 2.5** shows, as an example, the compound window chromatograms from the evaporation of α-pinene ozonolysis products after RT shift and the definition of the volatility basis set i.e., Region 1 (R1), Region 2 (R2), and Region 3 (R3).

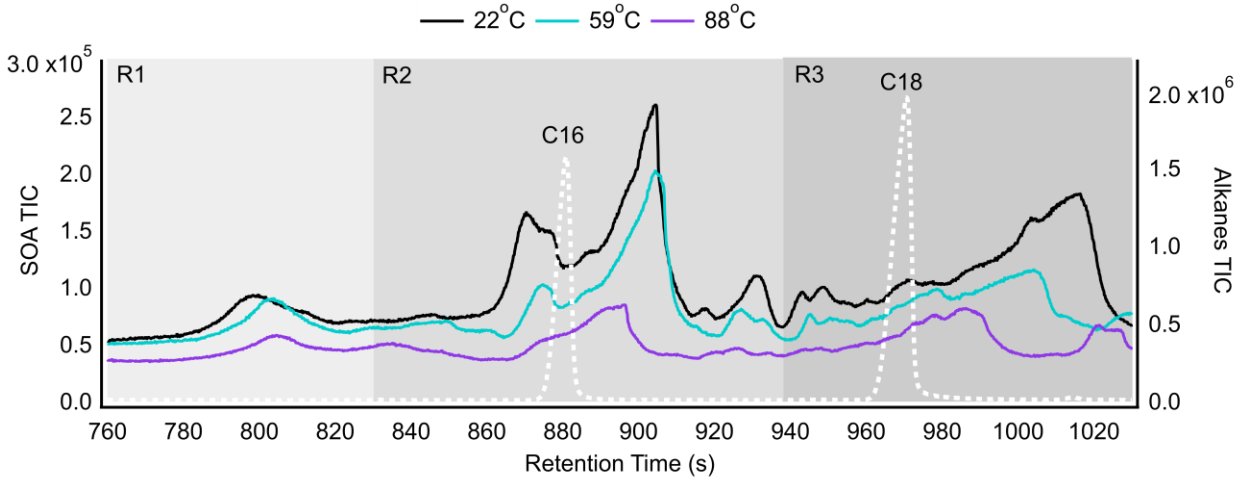

Figure 2.5. Compound window chromatograms from the evaporation of α-pinene ozonolysis products after retention time shift and definition of the volatility regions from the alkane standards injections. Solid lines represent SOA total ion count (TIC) chromatograms. Dotted line is the alkane series TIC. Shaded grays define the three volatility dimensions.

Thus, considering the individual alkanes, R1 corresponds to a volatility range that encompass an effective saturation mass concentration[30] of $10^5 < C^* < 10^4\ \mu g.m^{-3}$; R2 corresponds to a lower range between $10^4 < C^* < 10^3\ \mu g.m^{-3}$ and R3 represents

$10^3 < C^* < 10^2\ \mu g.m^{-3}$. Note that, traditionally, these ranges embody compounds classified as intermediate volatility organic compounds (IVOCs), therefore the analysis here presented characterizes secondary IVOCs associate with SOA formed from the ozonolysis of different monoterpenes. **Figures A2.4 and A2.5** (Appendix A2 – Section A2.4) illustrate the same respective volatility regions for limonene-, and β-pinene-originating SOA.

Data Analysis

AMS data was processed in Igor Pro using the SQUIRREL version 1.62A toolkit for unit mass resolution analysis, and the PIKA version 1.22A toolkit for high-resolution analysis. Mass concentrations were obtained by the standard ammonium nitrate ionization efficiency calibration. Change in the total condensed SOA mass due to fluctuations in the seed number concentration during each precursor experiment was evaluated and it was concluded that it is reasonable to neglect increases in total SOA mass due to increases in ammonium sulfate concentrations. The details about the analysis and calculations can be found in Appendix A2 (**Section A2.4**).

Chromatogram binning Positive Matrix Factorization (PMF) for mass spectral deconvolution analysis was used to provide chemically resolved volatility information.[31] This PMF technique identifies repeating fragmentation patterns within chromatograms, providing a simplified and rapid approach to identifying individual species and classes of compounds and analyzing their abundances. PMF was performed separately in each volatility dimension of the chromatograms. Since compound separation is partially sacrificed in the short-column TD-GC/MS system, PMF compound identification using a mass spectral database is challenging. Thus, for each factor, an approximate CHO formula was derived using high-resolution ion mass analysis. First, the molecular formula of the five most abundant unique ions in the respective PMF mass

spectrum was determined, and then considering the highest value of each element, a CHO formula could be estimated. Even when an acceptable mass spectrum-factor match was achieved using the National Institute for Standards and Technology (NIST) Mass Spectral Search Program (Demo Version 2.0f) database, the high-resolution ion mass analysis results were used for comparison consistency across factors. A summary of the PMF analysis can be found in Appendix A2 (**Section A2.4**) alongside details about the high-resolution ion mass analysis.

As the SOA evaporates, a decrease in total measured mass can also result from an increase in particle loss to the walls of the oven due to a decrease in particle diameter. It was observed that evaporating α-pinene SOA from 40ºC to 100ºC, shifts the lognormal size distribution arithmetic mean diameter from 133 nm to 108 nm (**Figure A2.10** – Appendix A2 – Section A2.4). Oxford[32] discusses in detail particle losses as a function of particle diameter in the extended residence time oven. The difference in particle penetration for this difference in diameter is less than 5%, thus, here, the effect of particle losses on the presented SOA evaporation results is neglectable.

2.3. Results and Discussion

2.3.1. Single-Component Aerosol Thermograms

Comparing the AMS and the V-TDMA (1st charge only) thermograms in **Figure 2.6A** it is clear that the model underestimates the MFR at higher temperatures, meaning that it would predict higher vapor pressures at higher temperatures. This was observed in previous models, in which calculated MFR generated steeper thermograms compared to size-selected aerosol measurements.[14,15] The accommodation coefficient is defined as a deviation from the theoretical maximum evaporation rate. Park et al[15] modified this parameter to fit their developed model to the mass-based measurement, suggesting that there are factors contributing to evaporation kinetic

limitations in the studied single-component aerosol. However, it is generally accepted that for individual organic compounds the surface mass accommodation coefficient is unity (or very close).[33,34] When investigating the presented model results still assuming the mass accommodation coefficient equal to one but taking into account the multicharged nature of the inlet size distribution, it is observed that the sigmoid shape of the curves agrees, verifying that particle charge distribution plays an important role in recovering volatility information from thermograms. **Figure 2.6B** shows the charge deconvoluted MFR obtained with the V-TDMA. One can notice that after 50°C the contribution of the singly charged particles to the remaining evaporating mass negligible. Indeed, it was calculated that the singly charged distribution is at most 28% of the total mass measured by the AMS. This elucidates that the multicharged response is not insignificant and indeed has a larger influence on thermograms than the singly charged particles.

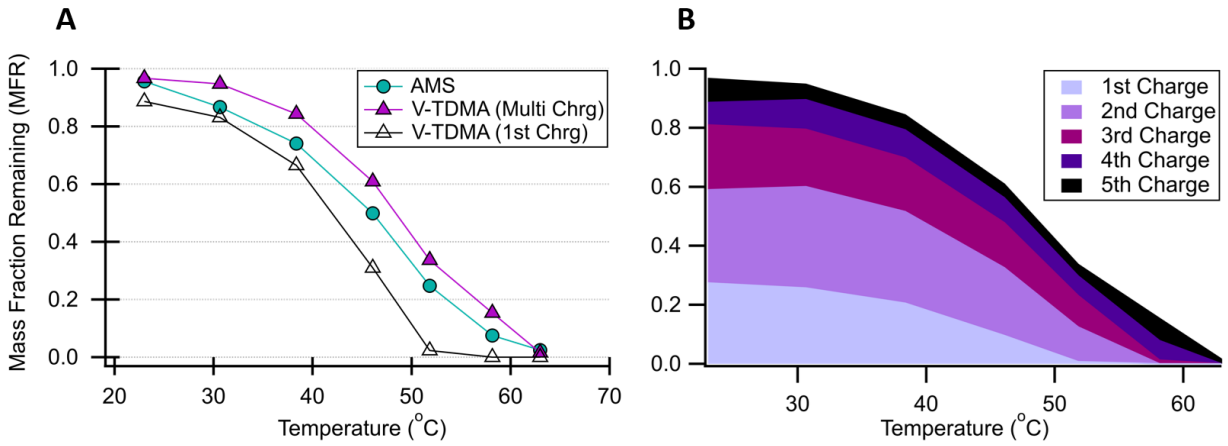

Figure 2.6. Azelaic acid thermograms. **(A)** MFR curves obtained with the AMS and the V-TDMA (multicharged and singly charged). **(B)** Charge-deconvoluted V-TDMA thermogram.

A closer investigation shows that both the AMS and V-TDMA thermograms start together at a mass fraction slightly less than one since the reference mass was sampled through the bypass line which has a lower residence time compared to the oven. However, from the first to the second temperature measurement, the AMS response decays faster than the V-TDMA. The difference

between the two curves throughout the entire experiment (except for the last temperature point) is equal to 0.079 ± 0.032. This observation suggests that either the V-TDMA model overestimates the total mass of the system, or there is a decrease in the AMS collection efficiency when particles are sampled through the bypass line (calibration) compared to when they evaporate in the oven.

If the V-TDMA model calculations yielded a greater mass concentration compared to the AMS, this would have been observed from the first MFR point, therefore, it is speculated that the discrepancy between the curves arises from a change in the AMS collection efficiency. Given that at 31°C the particles have not yet evaporated significantly, it is unlikely that the change in the AMS response emerges from the decrease in transmission efficiency through the aerodynamic lenses and inlet system due to a decrease in particle diameter.[35]

However, the AMS total particle collection efficiency (CE) after the inlet system is dominated by the magnitude of particles bouncing from the vaporizer.[36] As previously stated, AMS mass calibration was performed at ambient temperature by sampling azelaic acid particles through the short residence time bypass line. Although a set of diffusion driers was used after atomization, the aerosol particles likely contained residual water during this procedure. The presence of liquid water, decreases particle bounce, increasing the AMS collection efficiency. After exposing the aerosol through the long residence time oven at a slightly higher temperature than ambient conditions, the residual water evaporated, and the solid particles after the oven, now have a decreased CE compared to the liquid-aerosol sampled during calibration, a possible justification for the observed offset between the AMS and V-TDMA MFR estimations.

Indeed, Huffman et al[37] indicated that if the AMS collection efficiency due to bounce decreased after the evaporation of some of the particle material in the TD, leaving more of the solid, less-volatile material behind, the apparent volatility reported by the TD-AMS measurements

would be higher than the real volatility. This is exactly what the results here presented suggest, given the faster evaporation rates observed with the AMS compared to the V-TDMA estimations. The discrepancy between the instruments at the last evaporating temperature could be a result of the combined particle bounce and losses in the inlet system due to the smaller particle diameters.

Available literature values for the thermodynamic properties of azelaic acid (i.e. vapor pressure, enthalpy of vaporization, and surface tension) at standard conditions (298K, 1 atm) were compared with the V-TDMA results to increase the validity of this work. The natural log of the estimated vapor pressures linearly correlates to the inverse of the thermodenuder temperature, as predicted by the Clausius-Clapeyron relationship (Equation 2.2) and plotted in **Figure 2.7**. Vapor pressures at any temperature within the range studied can be estimated using the linear fit equation. The slope can be used to calculate the enthalpy of vaporization of the pure aerosol. **Table 2.1** summarizes the comparison results.

$$ln\frac{p_1^o}{p_2^o} = -\frac{\Delta H_{vap}}{R}\left(\frac{1}{T_1} - \frac{1}{T_2}\right) \quad \textbf{(2.2)}$$

Where p_1^o and p_2^o are the vapor pressures at T_1 and T_2, respectively; R is the ideal gas constant; and ΔH_{vap} is the enthalpy of vaporization.

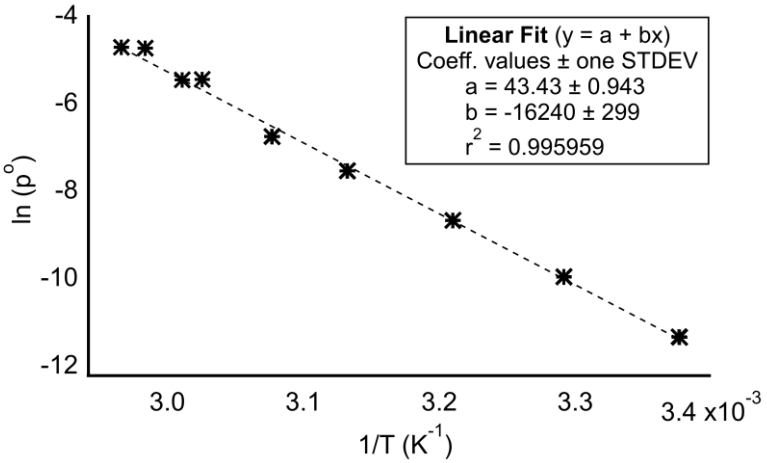

Figure 2.7. V-TDMA estimated vapor pressures from the evaporation of azelaic acid.

TABLE 2.1. Comparison between azelaic acid thermodynamic properties.

	T_{ref} (K)	P^o (Pa) at T_{ref}	ΔH_{vap} (J.mol^{-1}) at T_{ref}	σ (J.m^{-2})
This study	298.0	1.56E-05	135.0	0.129
Saleh (2010)[a]	298.0	1.40E-05	145.0	N/A
Database[b]	298.0	1.65E-05	137.6	0.0315

Abbreviations and symbols: T_{ref}, reference temperature; P^o, vapor pressure; ΔH_{vap}, enthalpy of vaporization, σ, surface tension.
[a]Saleh et al[38] evaluated the aerosol at equilibrium using the integrated volume method approach.
[b]Values calculated using parametrization equations from the Design Institute for Physical Property Research/AIChE (DIPPR®) project 801 database.[23]

In Saleh et al[38], azelaic thermodynamic properties were determined using the Integrated Volume Method (IVM) which does not require knowledge of diffusion coefficient, surface tension, and mass accommodation coefficient because the aerosol is investigated at equilibrium. The fact that there is good agreement between both the equilibrium and the kinetic approach here presented, increases the significance of this study. Vapor pressure and enthalpy of vaporization estimation from the DIPPR® project 801 database[23] are also in accordance with the V-TDMA calculations. Surface tension values differ by an order of magnitude, probably from extrapolation of the parametrization equation. Regardless, since the particles examined in this study are too large, the Kelvin effect is not relevant, and the value of the surface tension has practically no effect on the observed vapor pressure results.[17]

It is concluded here that; indeed, the mass accommodation coefficient is an important parameter that must be studied to accurately predict the evaporation rates of multicomponent aerosols. However, the results from this work suggest that, by pre-selecting a particle mobility diameter to simplify dynamic mass transport model calculations for the estimation of aerosol volatility distribution using thermal evaporation techniques, one must account for the multicharged nature of the aerosol reduced size distribution before investigation of potential kinetic limitations represented by less-than-unity mass accommodation coefficients.

2.3.2. Volatility Characterization of Laboratory-Generated SOA

SOA Yields and Thermal Stability

Figure 2.8A shows the SOA yields obtained from the ozonolysis of α-pinene, limonene, and β-pinene measured by the AMS at 22°C. While limonene and α-pinene secondary products show high organic mass concentrations, ~ 90-120 $\mu g.m^{-3}$; β-pinene yields are much lower, at a total measured concentration around 20 $\mu g.m^{-3}$ under similar experimental conditions. This reduced yield can be explained by the low reactivity of β-pinene molecules. Indeed, β-pinene-O_3 reaction constant is approximately 6 times smaller than α-pinene ozonolysis because the latter species has an endocyclic double bond, whereas β-pinene has an exocyclic double bond.[39]

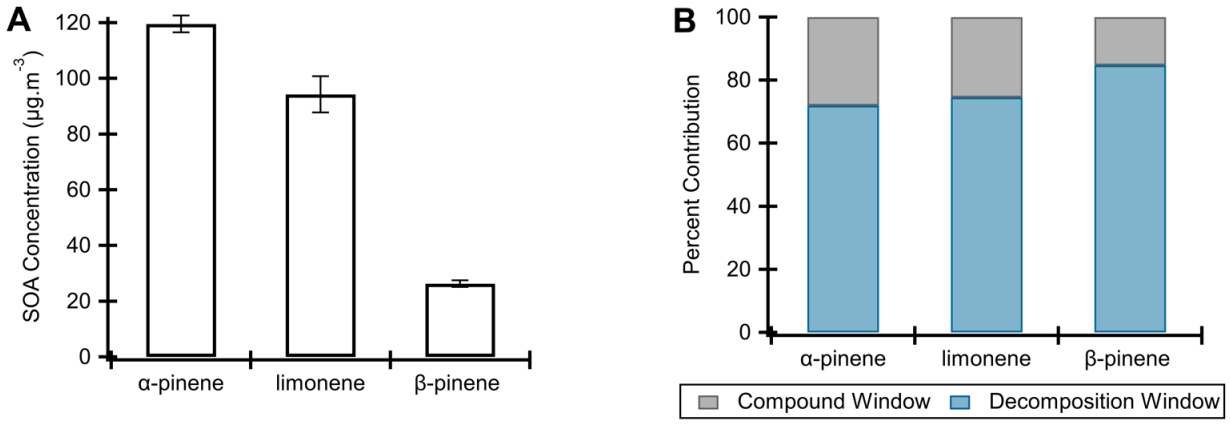

Figure 2.8. Resulting secondary organic aerosol from α-pinene, limonene, and β-pinene ozonolysis. **(A)** Total organic mass yields measured by the AMS. Error bars denote one standard deviation of the mean. **(B)** TD-GG/MS decomposition and compound window percent contribution to the total ion signal measured by the system.

On the other hand, limonene has two double bonds (one endocyclic and one exocyclic), making it more reactive than α-pinene and therefore expected to produce SOA with higher yields.[40] However, here, limonene yields were statistically lower than α-pinene. Previous studies have shown that the magnitude of the limonene ozonolysis reaction varies, depending on whether one or both of its unsaturated bonds are ozonated, which in turn depends on whether ozone is in excess

compared to limonene as well as the available time for the reaction to take place.[41] The endocyclic bond may react 10-50 faster than the exocyclic bond.[42] Since ozone was in excess for all the experiments here presented, the lower limonene yields compared to α-pinene might be due to insufficient time in the mixing volume for the completion of the exo bond ozonolysis reaction.

The contribution of the thermal decomposition window and the compound window products to the overall measured SOA mass at the reference ambient temperature was evaluated by integrating the reference total ion signal chromatograms after air signal removal for both analytical windows. **Figure 2.8B** shows that for all three precursors, the decomposition window dominates the SOA chromatograms (>70%), suggesting that the majority of the ozonolysis products formed during these experiments are thermally labile. This observation is corroborated by numerous previous studies.

Stark et al[43] observed that 65% of citric acid (commonly used as a proxy for highly oxidized SOA species) decomposes substantially in their thermal desorption chemical ionization MS system, with approximately 20% of its mass detected as gas-phase CO_2, CO, and H_2O. Zhao et al[44] produced SOA from heterogeneous oxidation of glutaric acid, and from α-pinene ozonolysis in a flow tube reactor (FTR) of 1-minute residence time. They observed distinct monomer and dimer/oligomer components in both SOA systems yet, both α-pinene- and glutaric acid-originating SOA reacted in the particle phase during rapid heating under moderate desorption temperatures (less than 100 °C). In addition to new oligomer formation reactions, the authors observed monomers formed by irreversible oligomer thermal decomposition.

Hall and Johnston[45] studied the effect of heating α-pinene ozonolysis SOA formed in a 23-second residence time FTR using a thermodenuder coupled with soft ionization high resolution mass spectrometry. They reported that both higher-volatility monomers and lower-volatility

oligomers were transferred to the gas phase upon heating the SOA to 100^{o}C. When the evaporated gaseous species were allowed to re-condense onto the particles, they found that most of the material was monomeric. The chemical analysis of these compounds corresponded to oligomer decomposition products, confirming the high thermal instability of oligomeric SOA.

These thermal evaporation- and thermal desorption-induced compositional changes of SOA increase the significance of coupling both techniques for improved volatility characterization. For instance, estimated volatilities from detected elemental formulas will predict much higher SOA volatility since many of the species result from thermal decomposition products rather than actual SOA molecules. On the other hand, as previously discussed, recovering volatility from thermal evaporation alone is challenging, relying on the knowledge of many thermodynamic parameters, also influenced by the charge-dependent aerosol size distribution, and the SOA volatility distribution itself. Now, the additional irreversible decomposition of SOA oligomers upon heating in a thermodenuder, would also result in higher volatility estimations even if the time-evolving mass-transfer model accurately predicted the dynamics of evaporation.

When combining both techniques, it is possible to compare evaporation rates between pre-determined volatility dimensions giving insights on the extent of the thermal decomposition experienced by the aerosol. This information integrated with chemical knowledge is key for more accurate SOA volatility characterization, as detailed in the following section.

Volatility-Constrained Evaporation Rates

PMF was applied separately in each volatility region (i.e. R1, R2, R3, and thermal decomposition) for all three precursors. All factors that were considered unique in the PMF solution were summed at each temperature and an equivalent mass fraction remaining curve was

generated by dividing each factor by the total factor abundance as a function of the evaporating temperature. **Figure 2.9** shows the obtained results, referred to as factor fraction remaining (FFR) curves. To ensure that the selected factors represent the overall evaporation behavior of each SOA, their mean factor thermograms (obtained by averaging the calculated FFR at each temperature across all regions) were compared to their AMS thermograms (**Figure A2.11** – Appendix A2 – Section 2A.5). For all three precursors the absolute percent difference between the AMS and PMF SOA curves are less than 12%, supporting the following FFR-based volatility analysis.

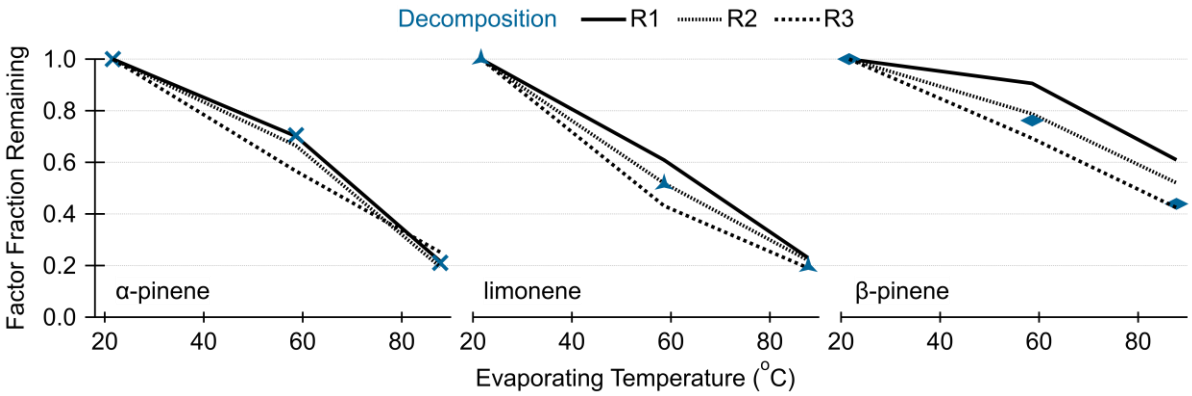

Figure 2.9. Volatility-constrained evaporation rates of secondary aerosol produced from the ozonolysis of α-pinene, limonene, and β-pinene, respectively. Lines represent each volatility dimension in the compound window, while markers display decomposition window trends.

An interesting behavior is observed when investigating the trends illustrated in **Figure 2.9**. For all three precursors, SOA molecules eluting in R1 demonstrated higher resistance to evaporation, followed by molecules eluting in R2 and R3, respectively; suggesting that species eluting in higher C^* windows are actually less volatile than those eluting in lower C^* windows. This contradicting behavior can be explained by the thermal lability of the compounds the comprise the aerosol particle. Since most of the SOA products decompose during thermal desorption[43,44] (see Figure 2.8B), and possibly upon heating in the oven[45], the molecules eluting in the GC compound window are predominantly fragments of lower volatility SOA compounds

rather than actual SOA molecules. This affirmation is corroborated by the good agreement between the decomposition window and compound window thermograms.

Empowered by this knowledge, one can infer from the observed volatility-constrained evaporation rates that, the least volatile SOA molecules produced in these experiments decompose to a greater extent, forming smaller fragments, thus eluting in earlier RT; while the more volatile SOA material show lesser degradation, decomposing into larger fragments, which in turn elutes in later RT. This behavior suggests that the least volatile SOA molecules are highly thermally labile.

Many factors influence the intrinsic thermal stability of an organic compound, including molecular weight, functional groups, branch degree, etc. A rule of thumb is that thermal stability increases with molecular weight and functionalization,[46] while volatility tends to mirrors this behavior, i.e., larger, and more functionalized molecules usually have lower vapor pressures.[47] The fact that the least volatile SOA material seems to be more thermally labile, suggests that they possibly comprise of lower molecular weight (less stable) highly functionalized molecules (less volatile); or by equal rationalization, they can be formed by higher molecular weight (less volatile) but less functionalized chemical species (less stable). In the next section, the volatility-constrained composition of these SOA fragments is investigated.

Volatility-Constrained Composition

For each volatility region, each factor mass spectrum was assigned a corresponding elemental formula using the high-resolution ion mass analysis detailed in Appendix A2 (**Section A2.4)**. Volatility-constrained oxidation levels were estimated by averaging the molecular oxygen to carbon (O:C) ratios across all factors in the specific region. The results, highlighted in **Figure 2.10,** show a mutual characteristic between all three different monoterpene SOA, that is: species

eluting in earlier RT are overall less oxidized than species eluting in later RT. Combining this information with the previous results leads to the conclusion that the least volatile SOA material is also less oxidized. Although counter-intuitive, this relationship between SOA oxidation levels and volatility is not an unusual observation. Ye et al[48] reported the same correlation when investigating the composition of the aerosol particulate-phase from the ozonolysis of α-pinene. Moreover, studying the hygroscopicity, volatility, and oxidation levels of SOA coupling different techniques, Cain et al have[8,20] also reported the simultaneous decrease in the O:C ratios and volatility of α-pinene and limonene ozonolysis SOA.

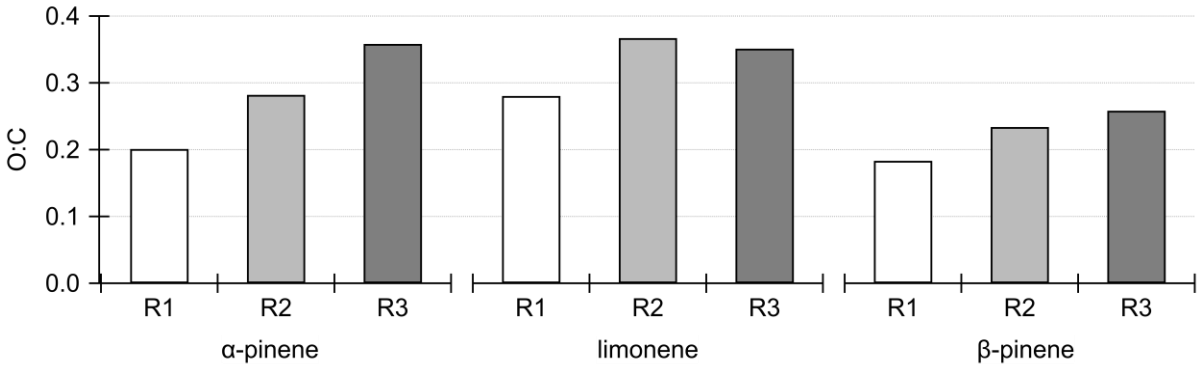

Figure 2.10. Volatility-constrained oxygen to carbon ratios of secondary aerosol produced from the ozonolysis of α-pinene, limonene, and β-pinene, respectively.

One explanation for this finding could be the production of oligomers that form high molecular weight low-volatility material without adding additional oxygenated functionality.[47] Several studies characterizing laboratory SOA using soft-ionization mass spectrometry have found that the initial oxidation products often react, most likely in the particle phase, to form oligomers, even in short time scales (≤ 1 minute) and low aerosol loadings.[44,45,49-51] Meaning that there is no intrinsic kinetic barrier to oligomerization in SOA formation. Furthermore, studies have shown that 50% or more of the particle mass of these laboratory generated SOA are indeed composed of oligomeric species,[49-52] while Hall and Johnston[45] demonstrated the thermal instability of

oligomeric SOA. Therefore, the results here presented suggest the presence of highly thermally labile oligomers in all three different monoterpene ozonolysis SOA that decompose upon heating into smaller molecules with lower O:C ratios eluting in early GC retention times.

Monoterpene SOA Differences

It is also of interest to understand the differences in properties of SOA formed by the three monoterpenes considered in this study. **Figure 2.11** summarizes the averaged evaporation rates (not including the decomposition window) and oxidation levels of each produced SOA. It is observed that limonene ozonolysis SOA are more volatile, in addition of being more oxidized than α-pinene and β-pinene ozonolysis products. This result is corroborated by a previous study[20] in which the authors observed that limonene ozonolysis SOA were comprised of, approximately 42% of semi-volatile organic compounds (SVOCs), while α-pinene-O_3 SOA contained 26% SVOCs. The O:C ratios reported for limonene-LVOC-SOA was equal to 0.57, being 24% higher than what they observed for the LVOC contents of α-pinene SOA.

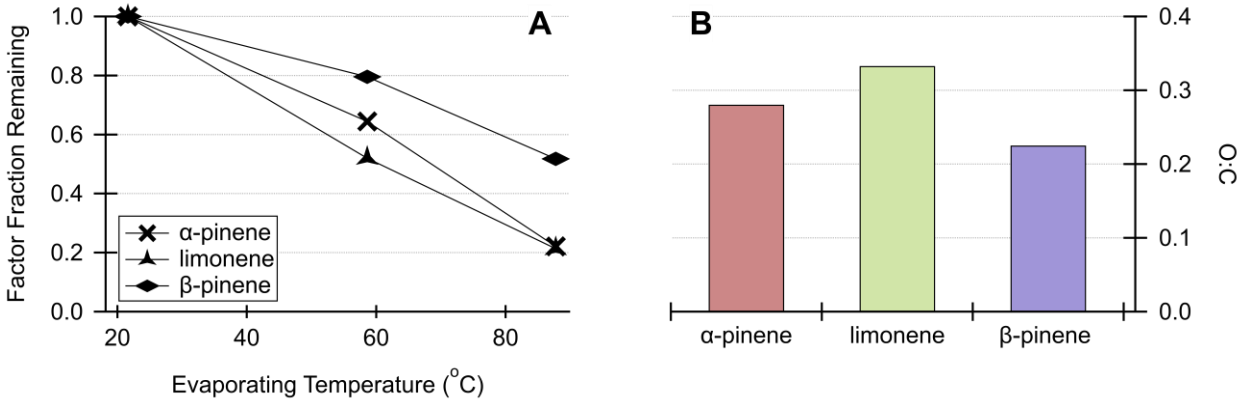

Figure 2.11. Comparison between secondary aerosol produced from the ozonolysis of α-pinene, limonene, and β-pinene. **(A)** Compound window average evaporation rates. **(B)** Compound window average oxygen to carbon levels.

The fact that SOA formed from limonene ozonolysis in this study are composed of more volatile, more oxidized molecules suggest they comprise of less oligomeric material compared to α-pinene- and β-pinene-originating SOA. Although, the instrumentation here applied make it not possible to investigate the latter affirmation, Liu et al[53] using Electrospray Ionization Fourier Transform Ion Cyclotron Resonance Mass Spectrometry (ESI-FT-ICR MS) reported a higher dimer-to-monomer content in β-pinene ozonolysis SOA compared to limonene-O_3 SOA. The latter precursor SOA having a balanced dimer-to-monomer distribution, as well as higher O:C ratios. A possible explanation is that, while there is no kinetic barrier to oligomerization in SOA production, monomer formation from β-pinene ozonolysis is controlled by the extent of the slow precursor-O_3 reaction. On the other hand, the significant reactivity of limonene molecules promotes efficient oxidation, yielding high monomer content of higher O:C levels. This VOC specific analysis strengthens the broader volatility-constrained results of this study that showed lower oxidation levels in the least volatile SOA components.

Volatility-Oxidation Correlation from the Thermal Decomposition Window Analysis

An alternative approach to investigate the level of oxidation of the different SOA is through the MS signal *m/z* 44 (CO_2^+), often used as an indicator of oxygenated aerosol.[54,55] In the decomposition window, a *m/z* 44 signal occurs with the decarboxylation of thermally labile species and generally increases as the oxidation level of the OA increases.[29,56] However, a *m/z* 44 signal could also arise from remaining CO_2 gas in the desorption cell due to incomplete purging prior to cell desorption. The discussion in Appendix A2, **Section A2.5** demonstrates that the *m/z* 44 signal in the decomposition window indeed corresponds to the degradation of thermally labile organic species rather than resulting from instrument artifact, validating the following analysis.

For each monoterpene SOA produced in this study, the ratio of the thermal decomposition *m/z* 44 signal to the total ion signal (after air signal removal) observed in the same analytical window was calculated at each evaporating temperature to understand the relationship between oxidation level and volatility across the different SOA. **Figure 2.12** summarizes the observed trends. Note that, as the oven temperature increases, the relative *m/z* 44 signal decreases, indicating that the more volatile, less oxidized material evaporates leaving behind the least volatile SOA components of lower oxygen content. It is worth mentioning that the degree of oxidation of limonene-originating SOA derived from this analysis is also higher than α-pinene and β-pinene ozonolysis SOA. Both observations are in good agreement with the conclusions inferred from the compound window analysis.

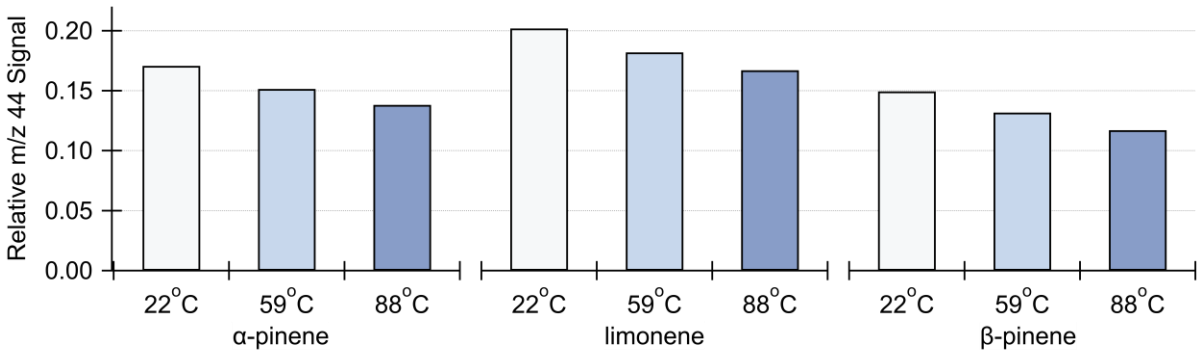

Figure 2.12. Temperature-dependent relative *m/z* 44 signal (to the total ion count signal in the thermal desorption analytical window) of secondary organic aerosol produced from the ozonolysis of α-pinene, limonene, and β-pinene.

2.4. Conclusions

This chapter discussed the challenges in studying aerosol volatility using thermal evaporation measurements alone and evidenced the importance of coupling different techniques to improve OA characterization. In the first part of this work, it is demonstrated that when modeling the evaporation kinetics of a monodisperse aerosol population pre-selected using a

DMA, the multicharged size distribution must be considered since the singly charged particles only account for a fraction of the total evaporated mass. In the considered azelaic acid evaporation experiments, it was calculated that the singly charged distribution was at most 28% of the total particle mass. Modeled and measured thermograms were in better agreement using a new V-TDMA mass-transfer model, demonstrating that prior to addressing uncertainty in volatility estimation due to potential kinetic limitations represented by the less-than-unity mass accommodation coefficient, it is necessary to account for the multicharged size distribution of a size-selected evaporating aerosol.

In the second part of this work, it was observed that thermally labile compounds dominate monoterpene ozonolysis SOA, with the least volatile species decomposing into small fragments, eluting in GC retention time windows that do not correspond to their actual volatility. Therefore, reiterating the need to combine different techniques in order to fully understand SOA volatility. Investigation of volatility-constrained O:C ratios showed that these fragments originating from the low volatility SOA components were also less oxidized leading to the hypothesis of oligomerization during SOA formation. This last statement could not be fully examined given the extensive molecular fragmentation that arises from the considered instrumentation. However, high oligomer content in monoterpene SOA is supported by numerous previous studies.

Finally, by comparing the overall evaporation rates and oxidation levels across SOA from different precursors, it was noted that limonene ozonolysis products were more volatile and had higher O:C ratios than α-pinene- and β-pinene-originating SOA, which suggested a more equally monomer-oligomer distribution in the former. The volatility-oxidation correlation conveyed from the limonene SOA analysis validates the broader observation of this study, i.e., SOA produced in

these experiments had components of lower volatility that were less oxidized than the more volatile compounds, most likely arising from oligomerization reactions during SOA formation.

Although the presented analysis was performed on very high aerosol mass loadings, in future climate scenarios where, increased temperatures cause higher biogenic VOC emissions, which in turn leads to higher SOA mass formation, the investigation of volatility and composition of laboratory-generated SOA provide valuable insights into the extent SOA formation and composition change under these unprecedented atmospheric conditions.

References

1. Srivastava D, Vu TV, Tong S, Shi Z, Harrison RM. Formation of secondary organic aerosols from anthropogenic precursors in laboratory studies. *Climate and Atmospheric Science*. 2022;5(1).

2. Volkamer R, Jimenez JL, San Martini F, et al. Secondary organic aerosol formation from anthropogenic air pollution: Rapid and higher than expected. *Geophy. Res. Letters*. 2006;33(17).

3. Jimenez JL, Canagaratna MR, Donahue NM, et al. Evolution of organic aerosols in the atmosphere. *Science (New York, NY)*. 2009;326(5959):1525-1529.

4. Shrivastava M, Cappa CD, Fan J, et al. Recent advances in understanding secondary organic aerosol: Implications for global climate forcing. *Reviews of Geophysics*. 2017;55(2).

5. Woo Jin An, Pathak RK, Lee BH, Pandis SN. Aerosol volatility measurement using an improved thermodenuder: Application to secondary organic aerosol. *Journal of Aerosol Science*. 2007;38(3):305-314.

6. Faulhaber AE, Thomas B, José Jiménez, Jayne JT, Worsnop DR, Ziemann PJ. Characterization of a thermodenuder-particle beam mass spectrometer system for the study of organic aerosol volatility and composition. *Atmos. Measurement Techniques*. 2009;2(1):15-31.

7. Cappa CD, Wilson KS. Evolution of organic aerosol mass spectra upon heating: implications for OA phase and partitioning behavior. *Atmospheric Chemistry and Physics*. 2011;11(5):1895-1911.

8. Cain KP, Pandis SN. A technique for the measurement of organic aerosol hygroscopicity, oxidation level, and volatility distributions. *Atmos. Meas. Tech*. 2017;10(12):4865-4876.

9. Pothier MA, Boedicker E, Pierce JR, Vance M, Farmer DK. From the HOMEChem frying pan to the outdoor atmosphere: chemical composition, volatility distributions and fate of cooking aerosol. *Environmental Science: Processes & Impacts*. 2023;25(2):314-325.

10. Vaden TD, Imre D, Beranek J, Shrivastava M, Zelenyuk A. Evaporation kinetics and phase of laboratory and ambient secondary organic aerosol. *Proceedings of the National Academy of Sciences of the United States of America*. 2011;108(6):2190-2195.

11. Wilson JM, Imre D, Beranek J, Shrivastava MB, Zelenyuk A. Evaporation Kinetics of Laboratory-Generated Secondary Organic Aerosols at Elevated Relative Humidity. *Environmental Science & Technology*. 2014;49(1):243-249.

12. Tikkanen OP, Buchholz A, Arttu Ylisirniö, Siegfried Schobesberger, Annele Virtanen, Yli-Juuti T. Comparing secondary organic aerosol (SOA) volatility distributions derived from isothermal SOA particle evaporation data and FIGAERO–CIMS measurements. *Atmospheric Chemistry and Physics*. 2020;20(17):10441-10458.

13. Riipinen I, Pierce JR, Donahue NM, Pandis SN. Equilibration time scales of organic aerosol inside thermodenuders: Evaporation kinetics versus thermodynamics. *Atmospheric Environment*. 2010;44(5):597-607.

14. Cappa CD. A model of aerosol evaporation kinetics in a thermodenuder. *Atmospheric Measurement Techniques*. 2010;3(3):579-592.

15. Sung Hoon Park, Rogak SN, Grieshop AP. A Two-Dimensional Laminar Flow Model for Thermodenuders Applied to Vapor Pressure Measurements. *Aerosol Sci. Tech.* 2012;47(3):283.

16. Cain KP, Karnezi E, Pandis SN. Challenges in determining atmospheric organic aerosol volatility distributions using thermal evaporation techniques. *Aerosol Science and Technology*. 2020;54(8):941-957.

17. Karnezi E, Riipinen I, Pandis SN. Measuring the atmospheric organic aerosol volatility distribution: a theoretical analysis. *Atmospheric Measurement Techniques*. 2014;7(9):2953-2965.

18. Grieshop AP, Miracolo MA, Donahue NM, Robinson AL. Constraining the Volatility Distribution and Gas-Particle Partitioning of Combustion Aerosols Using Isothermal Dilution and Thermodenuder Measurements. *Environmental Science & Technology*. 2009;43(13):4750-4756.

19. Louvaris EE, Karnezi E, Kostenidou E, Kaltsonoudis C, Pandis SN. Estimation of the volatility distribution of organic aerosol combining thermodenuder and isothermal dilution measurements. *Atmospheric Measurement Techniques*. 2017;10(10):3909-3918.

20. Cain KP, Liangou A, Davidson ML, Pandis SN. α-Pinene, Limonene, and Cyclohexene Secondary Organic Aerosol Hygroscopicity and Oxidation Level as a Function of Volatility. *Aerosol and Air Quality Research*. 2021;21(5):200511.

21. Oxford CR, Rapp CM, Wang Y, et al. Development and qualification of a VH-TDMA for the study of pure aerosols. *Aerosol Science and Technology*. 2019;53(2):120-132.

22. Oxford CR, Dang AJ, Rapp CM, Williams BJ. Interpretation of Volatility Tandem Differential Mobility Analyzer (V-TDMA) data for accurate vapor pressure and enthalpy measurement: Operational considerations, multiple charging, and introduction to a new analysis program (TAO). *Aerosol Science and Technology*. 2020;54(4):410-425.

23. American Institute of Chemical Engineers (AIChE). *DIPPR Project 801 - Full Version*. Design Institute for Physical Property Research

24. Saleh R, Shihadeh A, Khlystov A. On transport phenomena and equilibration time scales in thermodenuders. *Atmospheric Measurement Techniques*. 2011;4(3):571-581.

25. Kang EG, Root MJ, Toohey DW, Brune WH. Introducing the concept of Potential Aerosol Mass (PAM). *Atmospheric Chemistry and Physics*. 2007;7(22):5727-5744.

26. Lambe AT, Ahern A, Williams LR, et al. Characterization of aerosol photooxidation flow reactors: heterogeneous oxidation, secondary organic aerosol formation and cloud condensation nuclei activity measurements. *Atmospheric Measurement Techniques*. 2011;4(3):445-461.

27. DeCarlo PF, Kimmel JR, Trimborn A, et al. Field-Deployable, High-Resolution, Time-of-Flight Aerosol Mass Spectrometer. *Analytical Chemistry*. 2006;78(24):8281-8289.

28. Williams BJ, Goldstein AH, Kreisberg NM, Hering SV. An In-Situ Instrument for Speciated Organic Composition of Atmospheric Aerosols:Thermal DesorptionAerosol GC/MS-FID (TAG). *Aerosol Science and Technology*. 2006;40(8):627-638.

29. Williams BJ, Zhang Y, Zuo X, et al. Organic and inorganic decomposition products from the thermal desorption of atmospheric particles. *Atmospheric Measurement Techniques*. 2016;9(4):1569-1586.

30. Donahue NM, Robinson AL, Stanier CO, Pandis SN. Coupled Partitioning, Dilution, and Chemical Aging of Semivolatile Organics. *Environmental Science & Technology*. 2006;40(8):2635-2643.

31. Zhang Y, Williams BJ, Goldstein AH, Docherty K, Ulbrich IM, Jimenez JL. A Technique for Rapid Gas Chromatography Analysis Applied to Ambient Organic Aerosol Measurements from the Thermal Desorption Aerosol Gas Chromatograph (TAG). *Aerosol Science and Technology*. 2014;48(11):1166-1182.

32. Oxford CR. *The Role of Multi-Charged Responses: Construction and Application of a Tandem Differential Mobility Analyzer (TDMA)*. Dissertation. 2019.

33. Kulmala M, Wagner PE. Mass accommodation and uptake coefficients — a quantitative comparison. *Journal of Aerosol Science*. 2001;32(7):833-841.

34. Julin J, Winkler PM, Donahue NM, Wagner PE, Riipinen I. Near-Unity Mass Accommodation Coefficient of Organic Molecules of Varying Structure. *Environmental Science & Technology*. 2014;48(20):12083-12089.

35. Liu P, Deng R, Smith KJ, et al. Transmission Efficiency of an Aerodynamic Focusing Lens System: Comparison of Model Calculations and Laboratory Measurements for the Aerodyne Aerosol Mass Spectrometer. *Aerosol Science and Technology*. 2007;41(8):721-733.

36. Huffman JA, Jayne JT, Drewnick F, et al. Design, Modeling, Optimization, and Experimental Tests of a Particle Beam Width Probe for the Aerodyne Aerosol Mass Spectrometer. *Aerosol Science and Technology*. 2005;39(12):1143-1163.

37. Huffman JC, Ziemann PJ, Jayne JT, Worsnop DR, Jimenez JL. Development and Characterization of a Fast-Stepping/Scanning Thermodenuder for Chemically-Resolved Aerosol Volatility Measurements. *Aerosol Science and Technology*. 2008;42(5):395-407.

38. Saleh R, Khlystov A, Shihadeh A. Effect of Aerosol Generation Method on Measured Saturation Pressure and Enthalpy of Vaporization for Dicarboxylic Acid Aerosols. *Aerosol Science and Technology*. 2010;44(4):302-307.

39. Zhang D, Zhang R. Ozonolysis of α-pinene and β-pinene: Kinetics and mechanism. *The Journal of Chemical Physics*. 2005;122(11):114308.

40. Saathoff H, Naumann KH, Ottmar Möhler, et al. Temperature dependence of yields of secondary organic aerosols from the ozonolysis of a-pinene and limonene. *Atmospheric Chemistry and Physics*. 2009;9(5):1551-1577.

41. Waring MS. Secondary organic aerosol formation by limonene ozonolysis: Parameterizing multi-generational chemistry in ozone- and residence time-limited indoor environments. *Atmospheric Environment*. 2016;144:79-86.

42. Zhang J, Huff KE, Pandis SN, Donahue NM. Secondary Organic Aerosol Formation from Limonene Ozonolysis: Homogeneous and Heterogeneous Influences as a Function of NO_x. *The Journal of Physical Chemistry A*. 2006;110(38):11053-11063.

43. Stark H, Reddy, Thompson SL, et al. Impact of Thermal Decomposition on Thermal Desorption Instruments: Advantage of Thermogram Analysis for Quantifying Volatility Distributions of Organic Species. *Environmental Science & Technology*. 2017;51(15):8491-8500.

44. Zhao Z, Yang X, Lee J, et al. Diverse Reactions in Highly Functionalized Organic Aerosols during Thermal Desorption. *ACS Earth and Space Chemistry*. 2019;4(2):283-296.

45. Hall WA, Johnston MV. The Thermal-Stability of Oligomers in Alpha-Pinene Secondary Organic Aerosol. *Aerosol Science and Technology*. 2012;46(9):983-989.

46. Blake ES, Hammann WC, Edwards JW, Reichard TE, Ort MR. Thermal Stability as a Function of Chemical Structure. *Journal of Chemical & Engineering Data*. 1961;6(1):87-98.

47. Donahue NM, Kroll JH, Pandis SN, Robinson AL. A two-dimensional volatility basis set – Part 2: Diagnostics of organic-aerosol evolution. *Atmospheric Chemistry and Physics*. 2012;12(2):615-634.

48. Ye Q, Wang M, Hofbauer V, et al. Molecular Composition and Volatility of Nucleated Particles from α-Pinene Oxidation between −50 °C and +25 °C. *Environmental Science & Technology*. 2019;53(21):12357-12365.

49. Heaton KJ, Dreyfus MA, Wang S, Johnston MV. Oligomers in the Early Stage of Biogenic Secondary Organic Aerosol Formation and Growth. *Environmental Science & Technology*. 2007;41(17):6129-6136.

50. Heaton KJ, Sleighter RL, Hatcher PG, Hall WA, Johnston MV. Composition Domains in Monoterpene Secondary Organic Aerosol. *Environmental Science & Technology*. 2009;43(20):7797-7802.

51. Gao S, Keywood M, Ng NL, et al. Low-Molecular-Weight and Oligomeric Components in Secondary Organic Aerosol from the Ozonolysis of Cycloalkenes and α-Pinene. *The Journal of Physical Chemistry A*. 2004;108(46):10147-10164.

52. Hall WA, Johnston MV. Oligomer Content of α-Pinene Secondary Organic Aerosol. *Aerosol Science and Technology*. 2011;45(1):37-45.

53. Liu D, Zhang Y, Zhong S, et al. Large differences of highly oxygenated organic molecules (HOMs) and low-volatile species in secondary organic aerosols (SOAs) formed from ozonolysis of *β*-pinene and limonene. *Atmospheric Chemistry and Physics*. 2023;23(14):8383-8402.

54. Zhang Q, Worsnop DR, Canagaratna MR, Jimenez JL. Hydrocarbon-like and oxygenated organic aerosols in Pittsburgh: insights into sources and processes of organic aerosols. *Atmospheric Chemistry and Physics*. 2005;5(12):3289-3311.

55. Canonaco F, Slowik JG, Baltensperger U, Prévôt ASH. Seasonal differences in oxygenated organic aerosol composition: implications for emissions sources and factor analysis. *Atmospheric Chemistry and Physics*. 2015;15(12):6993-7002.

56. Fortenberry C, Walker MJ, Zhang Y, Dhruv Mitroo, Brune WH, Williams BJ. Bulk and molecular-level characterization of laboratory-aged biomass burning organic aerosol from oak leaf and heartwood fuels. *Atmospheric Chemistry and Physics*. 2018;18(3):2199-2224.

CHAPTER 3

Development and Characterization of the Semi-Volatile Thermal Desorption Aerosol Gas Chromatograph (SV-TAG) with an Automatic Calibration Injection System

Abstract

This chapter describes the development and characterization of a modified Semi-Volatile Thermal Desorption Aerosol Gas Chromatograph (SV-TAG), an *in situ* instrument designed for the measurement of gas- and particle-phase of semi- to low-volatility organic compounds in the atmosphere. For this SV-TAG system, a new dual-stage collection cell was developed to improve the collection of intermediate volatility and semi-volatile organic compounds (I/SVOCs), extending the analytical capability of the instrument in the quantification of higher-volatility chemical species. This enhanced collection capability is highlighted by comparing the new dual-stage cell against two different designs. The custom SV-TAG comprises two identical, newly developed, collection cells arranged in parallel for simultaneous sampling, while a denuder in-line provides a direct measure of gas-particle phase partitioning. The instrument also features an automatic calibration injection system (AutoInject) that improves the reliability of the SV-TAG measurements by the higher frequency of tracking standard injections and the decrease in uncertainties associated with manual calibration, such as contamination and human imprecision. Here, the performance of the custom AutoInject and SV-TAG systems are evaluated in both laboratory and field settings. Measurement artifacts that arise from instrument operation and the redesigned collection cells are investigated. Injection of external standards is used to explore the new volatility range of the instrument, examine intercell sensitivity, and determine limits of detection (LOD) for selected compounds.

3.1. Introduction

Intermediate volatility and semi-volatile organic compounds (I/SVOCs) comprise chemical species with an effective saturation concentration (C*), at 298K, between 10^{-1} to 10^{6} μg.m^{-3}, roughly corresponding to the volatility range of C12–C32 *n*-alkanes.[1] I/SVOCs are either emitted directly into the atmosphere or formed through the oxidation of higher volatility compounds,[2-6] contributing significantly to both gas- and particle-phase air pollution.[7] Owing to the volatility dimension they encompass, I/SVOCs are in a dynamic gas-particle phase equilibrium driven by environmental changes, such as temperature and relative humidity, as well as changes in aerosol concentration and composition.[1,8-11] The specific components of I/SVOCs and their volatility distributions will thus determine their impacts on the environment and human health.

Despite recent advances in the development of emission inventories used in chemical transport models to estimate I/SVOC environmental abundances and address their climate impact,[12-14] the lack of source-speciated gas- and particle-phase experimental data is still a limiting factor contributing to large uncertainties. For instance, a study published this year highlighted the need for experimental data on nighttime oxidation of I/SVOCs to better predict secondary organic aerosol (SOA) yields from on-road emissions.[15] Furthermore, a recent investigation on the sources of organic aerosols in eastern China revealed that non-mobile emissions of I/SVOCs are a substantial contributor to SOA formation and urged the need for speciated measurements of the I/SVOC emissions from these non-tail pipe sources.[16]

Indoors, many I/SVOCs are present at even higher concentrations than outdoors given their broad use in common industrialized products, such as cleaning agents and personal care products, building and furnishing materials, and electronic components.[17] Slowly emitted from their primary sources, indoor I/SVOCs can linger for years as a result of partitioning among the gas phase, indoor

and outdoor-originating airborne particles, settled dust, and available surfaces.[18] Exposure to indoor air pollution has been linked to increased risk of respiratory problems, immune suppression, cancers, dementia, and reproductive issues.[19] I/SVOCs can enter the human body through transdermal permeation, ingestion, and inhalation of both gaseous and particle species.[18-21] Therefore, improved time-resolved measurements of I/SVOCs are necessary to accurately assess indoor exposure, as minor environmental perturbations can significantly alter their gas-particle phase partitioning, and thus their exposure pathways.

The Thermal Desorption Aerosol Gas Chromatogram (TAG) was the first field-deployable instrument to provide hourly, *in situ* quantified speciation of atmospheric organic compounds.[22,23] Although designed to measure low-volatility species by aerosol inertial impaction onto a custom collection and thermal desorption cell (I-CTD), the system also allows qualitative evaluation of gas-phase I/SVOCs that are collected via diffusion onto the internal walls of the cell during ambient sampling.[8,9] The first Semi-Volatile TAG (SV-TAG) was idealized to address the I-CTD-TAG's limited gas-phase quantification capabilities by substituting the impactor-based cell with a high-surface metal-fiber filter cell (F-CTD), allowing quantification of I/SVOCs in the particle phase and the gas-phase by sampling alternately with and without an in-line upstream denuder.[24]

Both the I-CTD-TAG and the SV-TAG feature one collection cell, thus estimations of gas-particle phase partitioning assume that the ambient aerosol remains constant over the two hours necessary to obtain one denuded and one non-denuded sample. This need for interpolation introduces a source of error in the measurements of phase partitioning with the TAG,[8,25] later addressed by the development of the first dual-cell SV-TAG system, in which two FT-CTDs simultaneously collect a denuded and non-denuded sample. Online derivatization also improved the throughput of highly oxidized organic molecules in the dual-cell SV-TAG system.[26]

Here, we introduce a modified version of the dual-cell SV-TAG system featuring a modified collection and thermal desorption cell aimed at enhancing I/SVOCs collection and expanding the analytical capability of the system in the quantification of gas-particle phase partitioning. The new collector combines the previous metal fiber filter design with a custom backup collection cell composed of Tenax® TA sorbent. This dual-stage design is capable of effectively trapping I/SVOCs at the high end of the volatility dimension, providing quantitative measurements of species as volatiles as naphthalene. The instrument also incorporates a custom automatic calibration injection system, improving the reliability of the SV-TAG measurements achieved by the higher frequency of tracking standard injections and the decrease in uncertainties associated with manual calibration, such as contamination and human imprecision.

3.2. Materials and Methods

3.2.1. SV-TAG and AutoInject Overview

The instrument described in this chapter is a modified SV-TAG system, an *in situ* instrument designed for the measurement of gas- and particle-phase of semi- to low-volatility organic compounds in the atmosphere.[22,24,26] A schematic of the developed apparatus is shown in **Figure 3.1.** For this version of the SV-TAG, a new collection cell was developed to improve I/SVOCs measurements, extending the instrument's analytical capability by combining the previous metal fiber filter design with a custom backup collection cell composed of Tenax® TA sorbent. The SV-TAG features two identical dual-stage collection cells arranged in parallel for simultaneous ambient sampling. An in-line upstream denuder provides direct measurements of gas-particle phase partitioning without any need for interpolation between points. Samples' thermal desorption and subsequent gas chromatography-mass spectrometry (TD-GC/MS) analysis

is performed in series. Instrument performance evaluation and mass quantification of the collected samples are achieved by continuous injection of internal and external liquid standards through the built-in automatic calibration injection system.

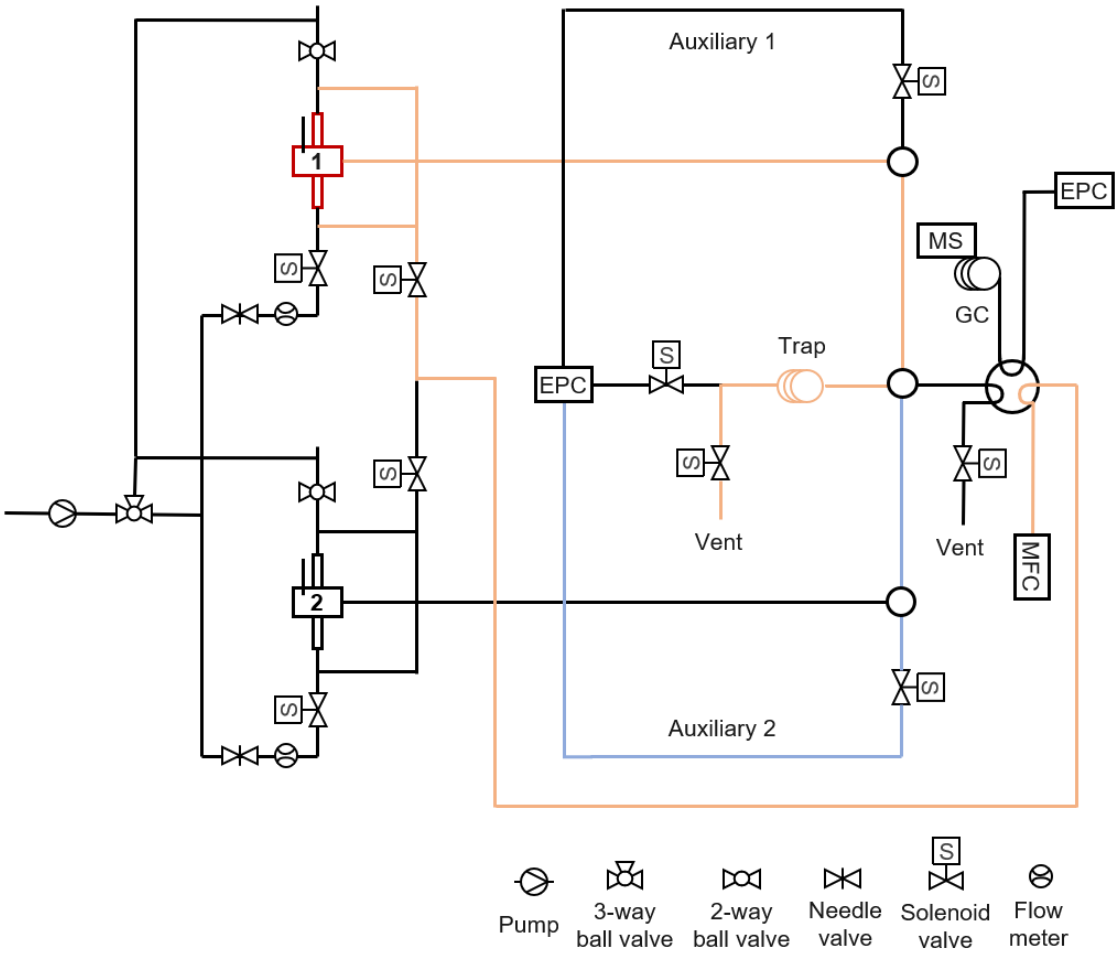

Figure 3.1. Flow diagram of the SV-TAG instrument. Highlighted orange paths demonstrate helium flow from cell 1 to the focusing trap column during the first step of the thermal desorption process. Blue lines represent auxiliary helium flow to avoid cell-to-cell contamination during this process. Flows are reversed during sample transfer from cell 2 to the focusing trap.

The calibration apparatus is a modified version of the AutoInject system described by Isaacman et al.[27] This system consists of four pressurized reservoirs which are selected using a multiport selector, to deliver liquid to fill two sample loops of 5 μL of volume, which are then simultaneously injected via a multiport valve into the SV-TAG dual-stage cells. Each reservoir

holds approximately 2 mL of liquid enough for about 200 injections under the conditions further described in **Section 3.2.3**. This allows for the instrument to run for extended periods without the need to refill a reservoir, thus decreasing the operator's exposure to chemicals. The automatic aspect of this device also improves the reliability of the SV-TAG measurements by increasing the frequency of tracking standard injections as well as by eliminating imprecision and minimizing contamination associated with manual syringe injections. Both the SV-TAG and the AutoInject systems are controlled by a custom LabVIEW (National Instruments, Austin, TX) program run.

3.2.2. The Dual-Stage Collection Cell

Figure 3.2 displays the SV-TAG dual-stage Filter-Tenax® Collection and Thermal Desorption (FT-CTD) cell highlighting each of the collection stages. The filter stage (stage 1 – **Figure 3.2A**) comprises a 37 mm in diameter Bekipor® stainless steel fiber filter (3AL3, Bekaert Fiber Technology, Belgium). This filter has a total fiber surface area of approximately 160 cm^2 per cm^2 and it is passivated with an Inertium® coating (Advanced Materials Components Express, Lemont, PA, USA), allowing quantitatively collection of gas-phase compounds with volatility as high as tetradecane, which is found almost entirely (>99%) in the gas phase under ambient conditions.[24] The filter is housed between two modified VCR® gaskets (Swagelok Company, USA) outfitted with two metal plates that accommodate four 50 W cartridge heaters (0.125" diameter - 1.25" long) and two 1/16" temperature-sensing thermocouples (ARI FCTD, Aerodyne, Inc., Billerica, MA). Cooling fins were installed on the outside of the metal plate to assist the blower-induced convective heat transfer after completion of thermal desorption.

The second stage of the FT-CTD uses Tenax® TA (Buchem B.V, Apeldoorn, Netherlands), a porous polymer resin based on 2,6-diphenylene oxide specifically designed for the trapping of

VOCs and I/SVOCs directly from air, or from the purging of liquid/solid sample matrices in the approximate volatility range of *n*-C6 to *n*-C26.[28] The most common method for the analysis of the trapped compounds is through TD-GC/MS.[28-32] The Tenax® thermal stability, low levels of impurity and low affinity for water make it a suitable sorbent for this type of analysis.[33-35] However, several studies have reported artifact formation when the polymer is exposed to species such as hydroxy radicals (OH), ozone (O3), nitrogen dioxide (NO2), nitrogen oxide (NO), and reactive gaseous mixtures.[36-42] Therefore, Tenax® artifacts that arise from the SV-TAG operation are addressed here and discussed in **Section 3.3.2.**

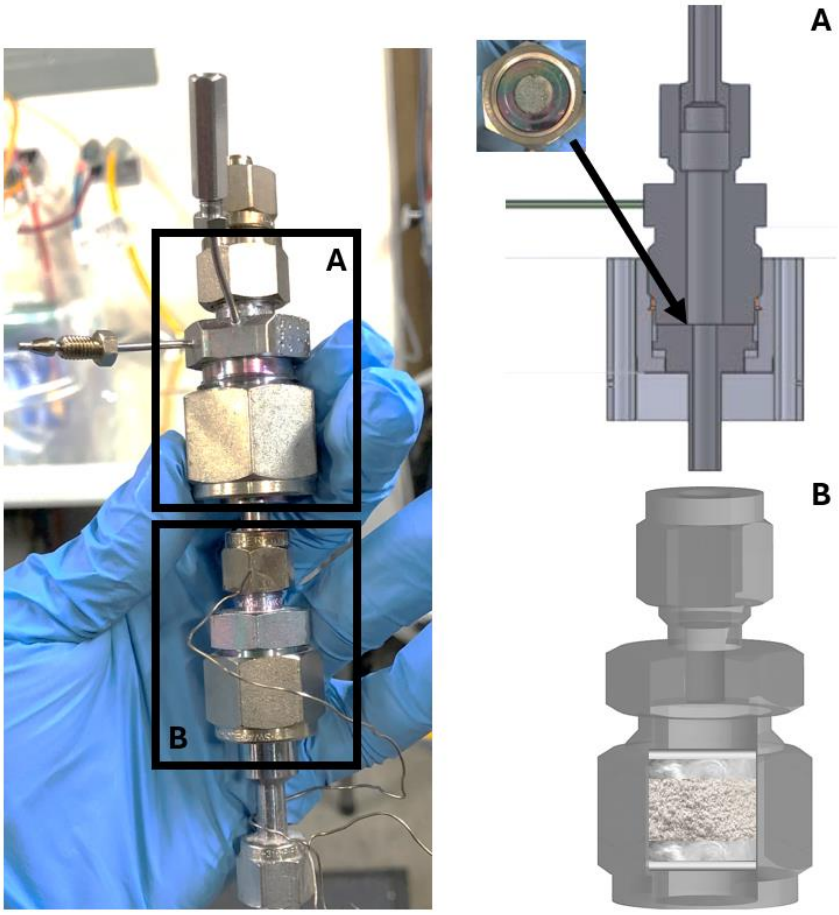

Figure 3.2. The dual-stage Filter-Tenax Collection and Thermal Desorption cell (FT-CTD). **(A)** First stage: composed of a passivated high-surface-area Bekipor® stainless steel fiber filter. **(B)** Second stage: contains 30 mg of Tenax® TA 60-80 mesh between two layers of glass wool outfitted by two thin passivated 200 mesh metal grids.

The collector contains 30 mg of Tenax® TA 60-80 mesh (SIS Instruments) placed in between two layers of glass wool (Sigma Aldrich) outfitted by two thin passivated 200 mesh metal grids. Both the glass wool and the grids are used to prevent Tenax® displacement during high-flow sampling and thermal desorption in the system. The custom cell is constructed with Inertium® passivated stainless steel Swagelok fittings (SS-810-6-2, SS-810-P, 316L-8TB7-6-4) illustrated in a detailed schematic in **Figure 3.2B** and heated by a 36" long rope heater controlled by one 1/16" temperature-sensing thermocouple.

In total, the FT-CTD cell has three heated zones PID-controlled by the custom LabVIEW (National Instruments, Austin, TX) interface. Inspired by the work of Dang et al,[43] the LabVIEW code integrates a heater shut-off feature, triggered whenever a temperature zone's response is outside of the expected calculated values. This irregularity-detection component is crucial to prevent irreversible heat damage to the collection cells as well as to the SV-TAG system in its entirety, providing better control and instrument reliability during field deployments.

3.2.3. Description and Operation of the SV-TAG and AutoInject System

In the SV-TAG system, samples are collected simultaneously at 8.3 $L.min^{-1}$ into the custom FT-CTD cells described in the previous section. **Figure A3.1** (Appendix A3 – Section A3.2) illustrates this process. To ensure identical sample size of each cell as well as to aid in diagnosing loss in collection efficiency due to filter clogging or Tenax® aging, sample flow is measured by two mass flow meters (AWM5000 Series, Honeywell International, USA) that can be manually adjusted through two needle valves (SS-OKS2, Swagelok Company, Maryland Heights, MO) placed downstream of the cells. Precise flow control is achieved by operating the needle valve

between 20-80% of its flow coefficient (C_v). In the SV-TAG, this translates to sampling flow control from 4.2 to 16.1 $L.min^{-1}$ on each cell.

One cell collects a non-denuded sample (gas plus particle), while the other cell collects a denuded sample (particle only). Automatic actuated two 3-way ball valves installed in-line (SS-44XS6-1466, MS142-ACX, Swagelok Company, Maryland Heights, MO) allow for the roles of the cells to be swapped to avoid cell-to-cell bias. A 40 cm long (30 mm OD) 500-channel activated carbon denuder (ADI-DEN2, Aerosol Dynamics Inc., Berkeley, CA) is used to remove gas phase species. This denuder device was designed for the effective removal of SVOCs with minimal particle losses (<5%) at ambient concentration levels.[24]

Comparison between non-denuded and denuded samples provides a direct measurement of phase partitioning. This denuder-difference analysis technique is expected to result in lower error than a filter-difference measurement as discussed in detail by Zhao et al.[24] To minimize negative artifacts from denuder sampling (i.e., removal of particle phase compounds from volatilization in the denuder due to the removal of the gas phase) the total residence time of the sample in the denuder was kept low (~ 2 seconds). The Tenax® efficacy as a VOC sorbent, combined with extended periods of sample collection, is responsible for vapors being efficiently collected and retained in the FT-CTD cells.

To enable correction due to run-to-run variability, internal standards are injected in both cells immediately after collection using the custom AutoInject system. A schematic of the apparatus is shown in **Figure 3.3**. Four reservoirs of liquid are maintained in an insulated Peltier-cooled aluminum block. A digital microprocessor-based thermocontroller (TLZ10, Ascon Technologic, USA) is used to maintain the custom refrigerator at a temperature of 10°C. Reservoirs are constructed with a standard 10 mm x 75 mm Pyrex test tube capped with a 10 mm compression

fitting (SS-602-1, Swagelok Company) using PTFE ferrules. A close-up schematic of the reservoirs is shown in **Figure 3.3.C**, and as described in previous work,[27] they consist of 1/16"OD stainless steel tubing that is inserted and silver brazed through the cap. One tube reaches the bottom of the reservoir for liquid delivery and another tube is kept at the top for pressurization. In this system, reservoirs are pressured to 30 psig with helium distributed by 0.02"ID clear Teflon® tubing (#1500, Upchurch Scientific, Northbrook, IL) through a 6-port manifold (P-152-01, Upchurch Scientific, Northbrook, IL).

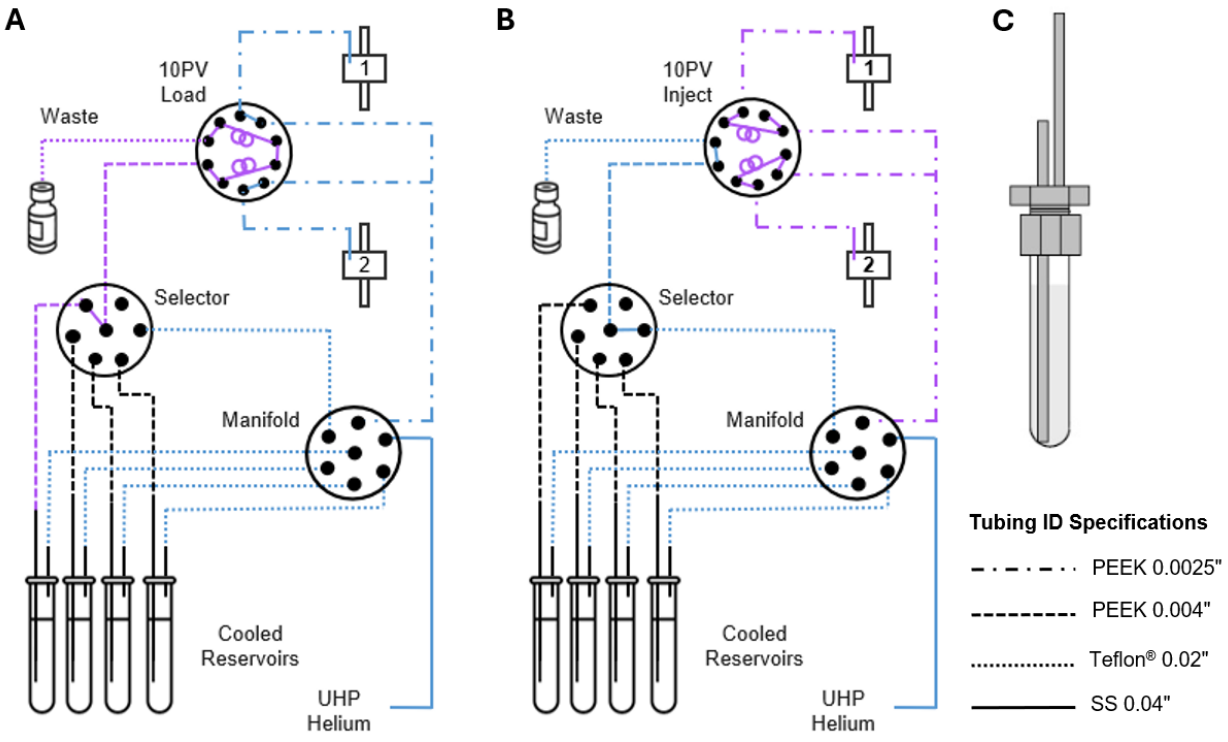

Figure 3.3. Flow diagram of the custom AutoInject apparatus. Helium lines are highlighted in blue while liquid lines are displayed in purple. **(A)** Load position: selector's port 1 fills the two 5 µL sample loops in the 10-port valve (10PV) with the excess liquid collected onto glass wool at the bottom of the waste vial. **(B)** Inject position: the manifold delivers helium to backflush the sample loops into the custom collection cells in the SV-TAG instrument. The selector's port is switched from the reservoirs to the helium manifold to purge excess liquid remaining in the lines. **(C)** Close-up reservoir design.[27]

The liquid delivery tube of each reservoir is connected to a 6-port selector valve (Rheodyne MHP7970-000, IDEX Health & Science LLC, Rohnert Park, CA) by 50 cm of 1/16"OD 0.004"ID polyether ether ketone (PEEK) tubing (#1561, Upchurch Scientific, Northbrook, IL). Twenty centimeters of the same tubing is used to connect the 6-port selector to port #1 of a 10-port valve (Rheodyne MHP7960-000, IDEX Health & Science LLC, Rohnert Park, CA) configured for liquid injection through two 5 μL sample loops (Rheodyne 7755-020, Cole Parmer, Vernon Hills, IL). The clear Teflon® tubing is also used in the waste line since it allows for physical observation of air-to-liquid transitioning when filling the injection loops which aids in the development of an optimized method focused on minimizing standard waste during operation.

The helium lines that bypass the reservoirs and are used for injection are 1/16"OD 0.0025"ID PEEK (#1560, Upchurch Scientific, Northbrook, IL). When the system is idle (i.e., the 10-port valve is in the load position and none of the reservoirs are selected) these lines deliver a bleed flow of about 2 sccm into the collection cells which minimizes the lingering of volatile species in the injection line, thus reducing carry-over from injection to injection. The AutoInject is connected to the FT-CTD cells by a low-pressure 0.05"ID PEEK union (P-703-01, Upchurch Scientific, Northbrook, IL) connected to a 5 cm capillary 1/16"OD 0.01"ID stainless steel tubing (T5C10, Valco Instruments Company Inc., Houston, TX) that is finally connected to the collection cells using a Valco 0.01"ID stainless steel union.

The opaque non-reactive nature of the PEEK polymer prevents exposure of the liquid standard to light. Small ID tubing is crucial in this system for three main reasons: first, to minimize evaporation of the liquid that is temporarily stored outside of the custom refrigerator before injection; second, to regulate the flows in the AutoInject system since no flow control devices are

used. Lastly, to minimize waste, once all liquid downstream of the selector must be injected or discarded during each injection cycle.

A typical injection cycle lasts approximately 50s per reservoir used: approximately 25s to load the liquid into the sample loop, illustrated in **Figure 3.3A**, and 25s to flush the solution with helium into the cells as shown in **Figure 3.3B.** Washing the loop after standard injections with pure solvent is another essential aspect to reduce carry-over of volatile species that can linger in the injection line. Therefore, it takes approximately 2 minutes (including some time for valve transitions in between) to perform a full standard injection with this custom AutoInject system. All valves (6-port selector, 6-port valve) are actuated automatically through a custom LabVIEW (National Instruments, Austin, TX) written code integrated into the SV-TAG program.

Following standard injection, both FT-CTD cells are purged at 25 sccm for 2 minutes to remove water and oxygen from the system as a result of the previous ambient collection. The hydrophobicity of the Tenax® minimizes the collection of water, however, during sampling, the cells' temperatures are maintained between 25-30ºC, higher than the average ambient dew point, further avoiding water-related artifacts in the SV-TAG. After purging, samples are transferred from the cells to the GC/MS in a two-step thermal desorption process illustrated in **Figure A3.2** (Appendix A3 – Section A3.2).

First, compounds collected are thermally desorbed and transferred onto a focusing trap (held at 30ºC) at relatively high helium flow rates (40 to 100 sccm) for 5 minutes, while the dual-stage FT-CTD temperatures are ramped to 300ºC (stage 1 - filter) and 280ºC (stage 2 – Tenax®). Temperatures and helium flow rate are held for 4 minutes at the end of the ramp to ensure complete transfer of the least volatile, higher molecular weight material. Stage 2 is ramped to a slightly lower temperature compared to stage 1 to lengthen the Tenax® lifetime. This temperature difference does

not affect mass quantification since the analytes trapped on the Tenax® have higher vapor pressures and thus, are expected to desorb at lower temperatures.

To ensure that both the filter and the Tenax® are predominantly back flushed, desorption-purging flow is split using restrictive capillaries such that the majority of the helium (~80%) enters at the bottom of the FT-CTDs. In addition, an auxiliary helium flow (0.5 sccm) is introduced downstream of the non-desorbed cell to prevent cell-to-cell contamination. **Figure 3.1** illustrates FT-CTD1 desorption exemplifying the flow paths described during this first step of the thermal desorption process. All surfaces in the sample flow path are held at 310°C and passivated with Inertium® coating to enable quantitative collection by efficient sample transfer.

The focusing trap consists of 100 cm of MXT®-5 metal column (Restek Corporation, Bellefonte, PA), 0.53 mm ID, featuring a thick (1.5 μm) non-polar stationary phase. During the second step of the thermal desorption process, the focusing trap is heated to 300°C for 5 minutes while being backflushed at 2 sccm onto the head of the GC column (held at 50°C), where the sample re-condenses for subsequent MS analysis. To ensure direct sample transfer to the GC/MS system, all lines of the SV-TAG are pressurized preceding the backflush of the focusing trap. Capillaries are used in the helium auxiliary lines to further prevent cell contamination.

Here, an RTX-5Sil MS (20 m long, 0.18 mm ID, 0.18 μm film thickness) non-polar fused silica capillary column (Restek Corporation, Bellefonte, PA) was installed in an Agilent 6890A GC (Agilent Technologies, Santa Clara, CA) for the chromatograph separation while a 70eV quadrupole mass spectrometer (G1098, 5973N MSD, Agilent Technologies, Santa Clara, CA) provides mass spectral detection. Each chromatograph analysis lasts approximately 17 minutes. Helium flow through the column is set to 1 sccm while a temperature ramp of $22.50^{o}C.min^{-1}$ heats the GC from 50°C to 315°C (hold 3 min.).

A typical SV-TAG duty cycle (**Figure A3.2** – Appendix A3 – Section A3.2) consists of a 10-minute collection and injection of standards (2 min.) on both cells; FT-CTD2 14-minute two-step desorption (9 min. FT-CTD→Trap, 5 min. Trap→GC) and chromatographic analysis (17 min.); followed by desorption and analysis of FT-CTD1. Collection of the subsequent sample begins after exactly one hour. Compound identification is achieved by search with the National Institute for Standards and Technology (NIST) Mass Spectral Search Program (Demo Version 2.0f) and peak integration is performed using the TAG ExploreR and iNtegration (TERN) software written in Igor Pro (Wavemetrics, Inc, Lake Oswego, OR).

3.2.4. Liquid Calibration Standards

Liquid calibration standard solutions were used to evaluate the systems' performance. A 5 ng.μL^{-1} deuterated solution prepared from pure components was used for the reproducibility analysis of the AutoInject system, while diluted solutions from a purchased mix (EPA 625 Semivolatile Calibration Mix, Sulpeco 506559, Sigma Aldrich, St. Louis, MO) were used to assess the volatility range of the SV-TAG instrument, examine intercell sensitivity, and determine limits of detection (LOD) for selected compounds. As described in previous work,[9,22,43] LOD is defined as three times the variation of the baseline signal (Equation 3.1).

$$Limit\ of\ detection\ (LOD) = \frac{3\sigma_{baseline}}{S} \quad \textbf{(3.1)}$$

Where $3\sigma_{baseline}$ is the standard deviation of the quantification ion at the compound retention time, and S is the slope of the calibration curve. Baseline signals were taken from cell-specific blank desorption chromatograms considering 21 scans with the compound of interest retention time as the midpoint.

Liquid solutions were prepared in chloroform (HPLC Plus, for HPLC, GC, and residue analysis, ≥99.9%, Sigma Aldrich, St. Louis, MO) which is volatile enough to be almost fully purged from the system prior to sample desorption. A list of the chemical species that comprise the standard solutions along with relevant physical properties is provided in **Tables A3.1** and **A3.2** (Appendix A3 – Section A3.1).

3.2.5. Field Testing Methods

The performance of the dual-stage collection cells was evaluated during the Alaskan Layered Pollution And Chemical Analysis (ALPACA) field campaign, which took place in Fairbanks, AK from January to February 2022 to improve understanding of pollution sources and fate in cold climate regions when atmospheric photochemical activity is weakened.[44] The SV-TAG was deployed along with complementary gas-phase (PTR-ToF-MS - Proton Transfer Reaction Time-of-Flight Mass Spectrometer) and particle-phase mass spectrometers (ATOFMS - Aerosol Time-of-Flight Mass Spectrometer and AMS - Aerosol Mass Spectrometer) to investigate the dynamics of outdoor and indoor gas-particle phase partition under Arctic wintertime conditions.

The SV-TAG sampled with the newly developed FT-CTD cells arranged in parallel for simultaneous collection alternating between indoor and outdoor samples. One cell collected a non-denuded sample (gas-plus-particle), while the other collected a denuded sample (particle-only). The roles of the cells were swapped every other collection to avoid cell-to-cell bias. Study details are provided in **Chapter 4**, including a description of the SV-TAG inlets that enabled the indoor/outdoor sampling strategy. For the field data used in this chapter, the SV-TAG collection method and TD-GC/MS analysis, as well as data processing (i.e., compound identification and peak integration) were achieved as detailed in **Section 3.2.3.**

3.2.6. Positive Matrix Factorization Analysis

Chromatogram binning Positive Matrix Factorization (PMF) is a statistical tool developed to analyze complex chemical data by identifying components that co-vary over time.[45,46] Here, chromatogram binning PMF for mass spectral deconvolution was used to investigate Tenax® artifact formation in the dual-stage cell and to compare the collection capability between different cell designs. This PMF technique identifies repeating fragmentation patterns within chromatograms, providing a simplified and rapid approach to identify individual species and classes of compounds and analyze their timeseries trends.

For each analysis, respective chromatograms were binned by retention time as described in previous work.[45] A bin width of 1 scan per bin was chosen to preserve the instrument's chemical resolution, thus optimizing PMF outputs. PMF calculations were performed within a desired retention time window. The model factorizes the input binned chromatogram matrix into a time series and a profile matrix. The profile matrix consists of mass spectral information corresponding to a compound or class of compounds present in the chromatograms, and the user selects the number of factors that best describe the dataset for the analysis considered.

To examine Tenax® degradation products, PMF was used to obtain qualitative trends over time of previously identified individual compounds. Therefore, PMF calculations for this purpose covered only the retention time window of each compound of interest, and the number of solutions chosen was the minimum value that provided confident compound identification. When investigating unknown potential Tenax® artifacts and comparing the collection capability between different cell designs, the number of factors was determined to maximize identifiable unique factors while minimizing factor splitting, which occurs when too many factors are used to explain

the dataset and information of a compound/compound class is distributed across multiple factors. Pertinent details about each PMF analysis performed are provided in their respective sections.

3.3. Results and Discussion

3.3.1. SV-TAG and AutoInject Method Evaluation

System Blanks

System blanks chromatograms are obtained in the SV-TAG from its default TD-GC/MS method (detailed in **Section 3.2.3**) without prior sample collection or injection of target analytes. Blanks are an essential element in method validation for quantitative analysis in analytical systems.[47,48] In addition to matrix interference determinations,[49] limits of detection, and limits of quantification estimations,[48,50] they are fundamental for instrumental and sampling artifact corrections preceding advanced data processing.[45,46]

Figure 3.4A displays the overlaid FT-CTD1 and FT-CTD2 total ion count (TIC) chromatograms obtained from a default SV-TAG system blank analysis. Although there is reproducibility across cells, their chromatograms appear contaminated by the presence of high-intensity peaks. Single ion extraction, illustrated in **Figure 3.4B**, revealed the dominance of siloxane peaks at *m/z* 73, 207, 253, 281, 327, and 405 which are recognized impurities from silicon grease or GC column bleed.[51] The latter process refers to the slow release of the liquid phase from the inner wall of the capillary column as a result of slow thermal degradation. Therefore, by definition is a continuous process that causes a baseline rise, not resolved peaks. However, other sources of siloxanes in GC/MS systems, such as inlet contamination and the use of polydimethylsiloxane-based septa, can contribute to GC/MS blank peaks.

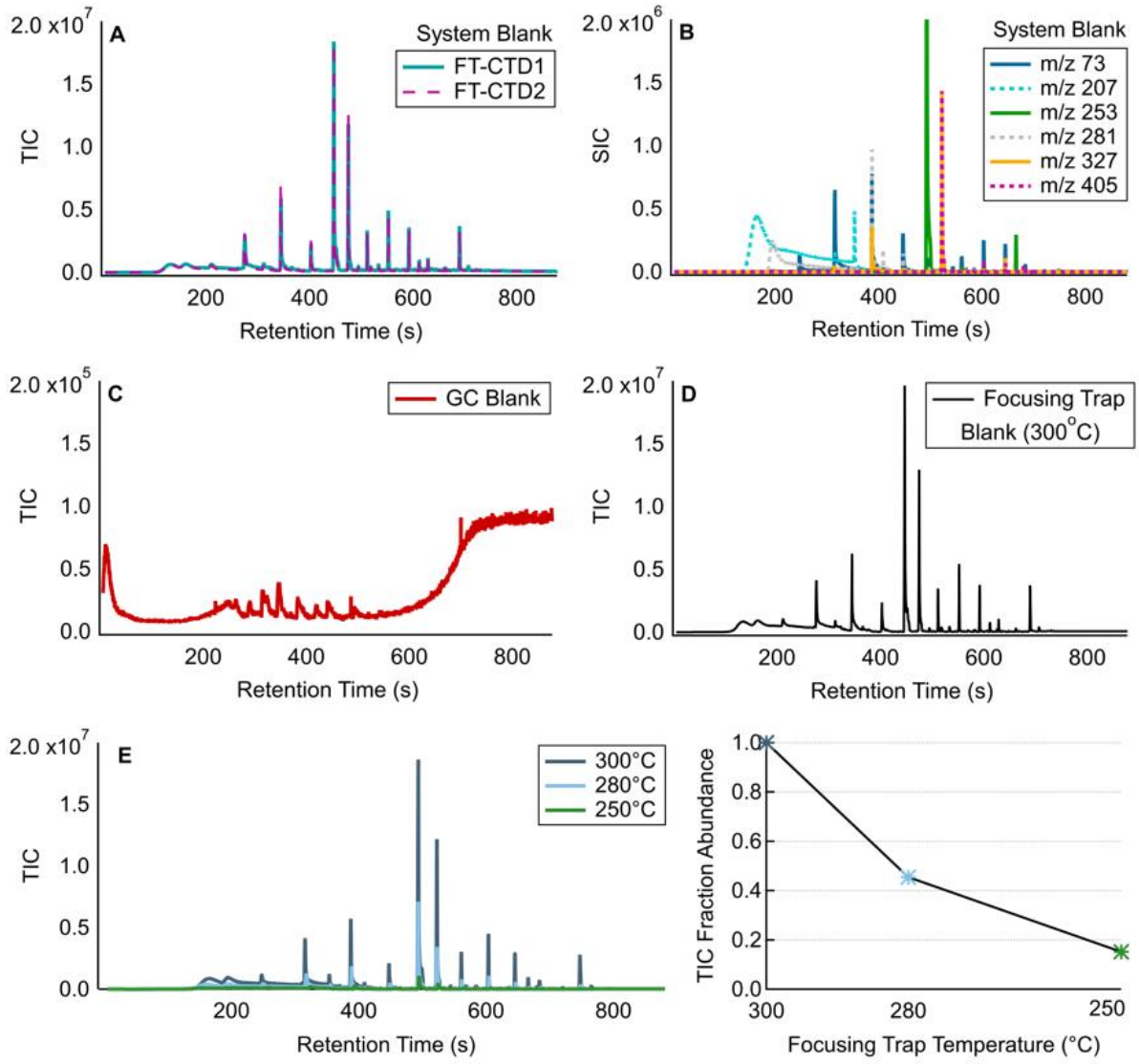

Figure 3.4. SV-TAG system blank analysis. **(A)** Overlaid FT-CTD1 and FT-CTD2 total ion count (TIC) blank chromatograms. **(B)** Single ion count (SIC) chromatograms extracted from FT-CTD1 blank TIC. (C)-(E) summarizes tests performed in the system to investigate the origin of the peaks observed in the system blank. **(C)** GC blank chromatogram generated by ramping the oven without loading any sample into the GC/MS system. **(D)** The resulting chromatogram from a modified method where thermal desorption of the collection cells is bypassed and the focusing trap is heated and directly backflushed onto the GC column. **(E)** Temperature effect on the focusing trap blank chromatograms. The y-axis on the right plot is the fraction of the integrated TIC chromatogram at each temperature relative to the total abundance observed at 300°C.

To investigate if the observed SV-TAG blank peaks originated from the GC/MS system, a GC blank run was performed. This analysis consisted of ramping the GC column by the default

chromatographic method without sample introduction through the thermal desorption process. The resulting chromatogram is shown in **Figure 3.4C** and exhibits an elevated baseline as a function of the GC temperature as predicted from column bleed chromatograms. Thus, this indicates that the SV-TAG blanks are not composed of peaks deriving from the GC/MS system.

The SV-TAG also features a focusing trap silica-based metal column that is heated to 300^{o}C and backflushed onto the head of the GC/MS system. This column is also expected to thermally degrade at elevated temperatures. Therefore, it is conjectured that the observed peaks in the system blank chromatograms are a result of focusing trap column bleed that is re-condensing onto the head of the GC column and eluting the system as discrete peaks once GC analysis begins.

An SV-TAG-modified method was developed to evaluate the hypothesis above. In this method, thermal desorption of the collection cells is bypassed and the focusing trap is heated and directly backflushed onto the GC column. The results, displayed in **Figure 3.4D**, show good agreement with **Figure 3.4A** attesting that the SV-TAG system blanks are dominated by recondensed column bleed. For additional corroboration, sequential runs were performed by heating the focusing trap column to 280^{o}C and 250^{o}C. Results are shown in **Figure 3.4E.** It was noted that the intensity of the peaks decreased with decreasing temperatures, an expected observation since less column thermal degradation is foreseen at lower temperatures.

In the SV-TAG system, these background peaks can serve as internal calibrants and aid in evaluating system performance. For instance, an increase in the intensity of the focusing trap bleed suggests an elevation in the concentration of oxygen in the system. This can indicate inefficient purging caused by misfunction of flow controllers and valves, as well as the development of air leaks in the system. Early issue detection, provides faster troubleshooting, prevents permanent damage, and increases instrument-control reliability.

Intercell and System Contamination

The addition of two auxiliary helium lines (**Figure 3.1**) was designed to provide a means to transfer the thermal desorption flow from one collection cell to the focusing trap while maintaining the other cell free from contamination. To investigate the efficiency of these flows, as well as to examine potential system contamination during sample transfer from the focusing trap to the GC column, single-cell collection experiments were conducted. Non-quantitative incense emissions were collected in only one cell by keeping the sample valve of the other cell closed. The order of the TD-GC/MS analysis of each collection cell was determined in each run to probe the experimental objectives listed in **Table 3.1**.

TABLE 3.1. The experimental approach to investigate SV-TAG intercell and system contamination during sample collection and transfer.

Run Type and Number	Desorption 1	Desorption 2	Objective
System Blank (#1)	FT-CTD2	FT-CTD1	Baseline for FT-CTD2 contamination analysis
Collection FT-CTD1 (#2)	FT-CTD2	FT-CTD1	FT-CTD2 contamination during sample collection
System Blank (#3)	FT-CTD2	FT-CTD1	FT-CTD2 contamination during sample transfer
System Blank (#4)	FT-CTD1	FT-CTD2	Baseline for FT-CTD1 contamination analysis
Collection FT-CTD2 (#5)	FT-CTD1	FT-CTD2	FT-CTD1 contamination during sample collection
System Blank (#6)	FT-CTD1	FT-CTD2	FT-CTD1 contamination during sample transfer

Figure 3.5A highlights the results from investigating potential contamination of FT-CTD2 during FT-CTD1 collection and transfer. **Figure 3.5B** summarizes the analysis of FT-CTD1 contamination during FT-CTD2 collection and transfer. Markers differentiate each cell, arranged in each of four plots by their desorption order. The y-axis in **Figures 3.5A1** and **3.5B1** represents TIC chromatogram abundances, calculated as the total area of the chromatograms obtained from

each run. **Figures 3.5A2** and **3.5B2** display the fraction of the abundance of each run relative to the abundance observed in the respective system blank prior to collection.

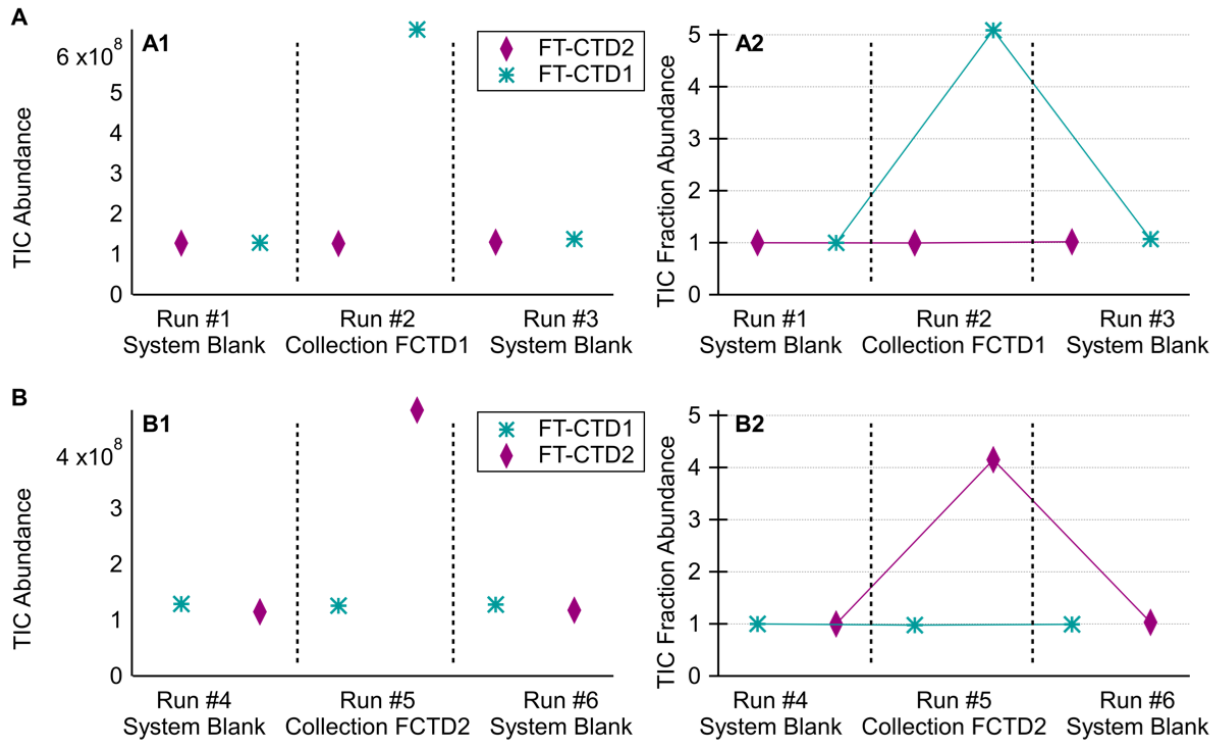

Figure 3.5. Analysis of SV-TAG intercell and system contamination. **(A)** Highlights the results from investigating potential contamination of FT-CTD2 during FT-CTD1 collection and transfer. **(B)** Display the results from investigating potential contamination of FT-CTD1 during FT-CTD2 collection and transfer. Markers differentiate each cell, arranged in each of four plots by their desorption order. **(A1)-(B1)** Represents the total ion count (TIC) chromatogram abundances. **(A2)-(B2)** Displays the fraction of the abundance of each run relative to the abundance observed in the respective system blank prior to collection.

Considering run #1 to run #2 in **Figure 3.5A1**, there is an increase in FT-CTD1 TIC abundance due to the collection of incense-related emissions. The total material sampled represented a five-fold increase in the abundance of FT-CTD1's chromatogram compared to its blank (**Figure 3.5A2)**. Yet, an increase in FT-CTD2 TIC abundance was not observed, implying that the latter was not affected during this single-cell collection test. Comparing run #2 to run #3, FT-CTD2 abundance remained unchanged as seen by the constant-unity TIC fraction abundance

value. This result confirms the efficacy of the auxiliary flows in preventing FT-CTD2 contamination, and the adequacy of the direction of the flows during sample transfer from the focusing trap to the GC/MS system. On the other hand, a 7% increase was observed in FT-CTD1 blank chromatogram obtained after TD-GC/MS sample analysis. This increase is a consequence of sample carryover, i.e. the amount of collected material remaining in FT-CTD1 following the standard thermal desorption run. However, this is considered a small percentage and indicates efficient FT-CTD1 thermal desorption and transfer even for high collection loads.

A similar analysis can be performed for the results presented in **Figure 3.5B**. In summary, FT-CTD1 remained absent from contamination during FT-CTD2 sample collection and transfer, demonstrating the bidirectional efficacy of the auxiliary flows. Only a 3% carryover was observed in FT-CTD2 after analysis of the collected sample. The difference between sample carryover observed in each cell is conjectured to be related to unequal sample loadings (from the comparison between collection abundances in **Figures 3.5A1 and 3.5B1**) rather than differences in collection capabilities and transfer efficiency across cells. In **Section 3.3.2**, the collection reproducibility of the cells is investigated. Further insights into the collector's transfer efficiency are provided in the remainder of this section.

AutoInject Reproducibility

A prerequisite of an efficient automatic calibration system is the capability to carry out highly reproducible injections. Here, this characteristic is evaluated using the custom AutoInject system through nine consecutive injections containing 5 $ng.\mu L^{-1}$ of deuterated alkanes, polycyclic aromatic hydrocarbons (PAHs), and acids. A full compound list is found in **Table A3.1** (Appendix A3 – Section A3.1). Deuterated analytes were chosen due the data availability from the ALPACA

field campaign. However, the following findings should translate to the reproducibility of non-deuterated analytes of the same chemical classes which represent environmental-relevant species.

In **Figure 3.6** the response of each compound relative to its average response over the nine runs is plotted on the y-axis. The left plot represents the reproducibility results from injections in FT-CTD1, while FT-CTD2 results are shown on the right plot. Each marker differentiates each chemical class, demonstrating the significant intercell reproducibility of the AutoInject system across different functional groups. By visual inspection, deviation from unity does not seem to correlate across different analytes. Thus, it is theorized that uncertainties arise from inaccuracy in compound integration rather than from instabilities in the AutoInject system.

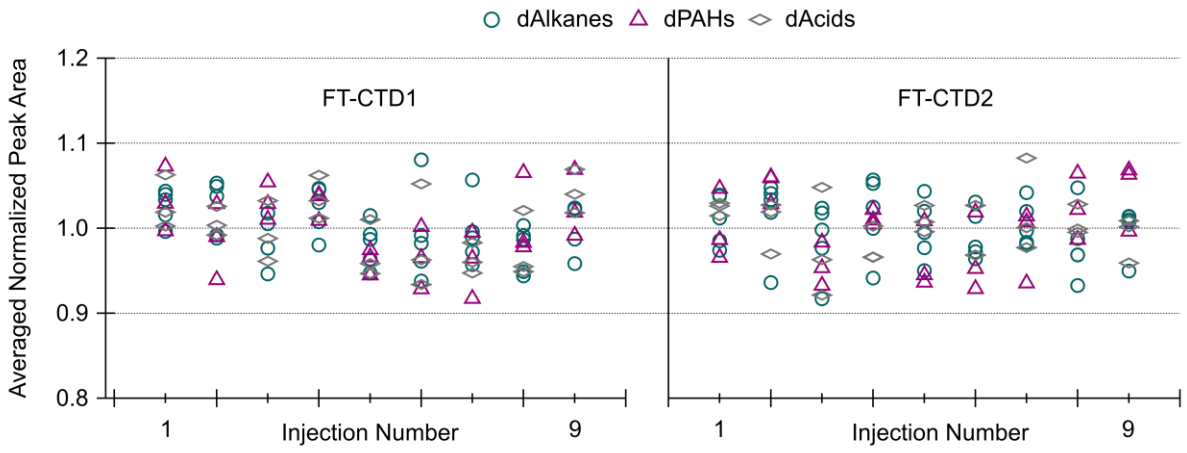

Figure 3.6. Reproducibility of the custom automatic injection system. Nine injections containing 5ng.μL^{-1} of deuterated alkanes (hexadecane-d34, eicosane-d42, tetracosane-d50, octacosane-d58, dotriacontane-d66), PAHs (pyrene-d10, chrysene-d10, perylene-d12), and organic acids (lauric-d23 acid, palmitc-d31 acid, stearic-d35 acid) are shown. Markers differentiate each chemical class. The y-axis is the response of each compound relative to its average response over the nine runs.

Analyte Thermal Desorption and Transfer

As detailed in **Section 3.2.3**, in the SV-TAG system samples are simultaneously collected, and TD-GC/MS analysis is performed in series. Therefore, in a typical duty cycle, analytes present in FT-CTD2 are analyzed immediately after collection/injection, in contrast to FT-CTD1, where

the sample's thermal desorption occurs, approximately, 27 minutes after collection/injection. To investigate the impact of thermal desorption timing on the transfer of analytes in the system, as well as to compare the transfer efficiency of each collector for various chemical species, a series of standard injections were performed alternating the thermal desorption order of the cells.

Table 3.2 summarizes the experimental approach and main objectives. Triplicate injections of 5 $ng.\mu l^{-1}$ standard solutions diluted from the EPA 625 Semivolatile Calibration Mix (Sulpeco 506559, Sigma Aldrich, St. Louis, MO) were performed, and a total of 22 analytes were integrated. They are listed in **Table 3.3** along with relevant physical properties. Compounds were chosen spanning a wide range of volatility and polarities to study the relationship between these properties and transfer efficiency. Results are investigated as the relative response of FT-CTD1 to FT-CTD2 for all three cases outlined in **Table 3.2** and shown as different colored bars in **Figure 3.7**.

TABLE 3.2. The experimental approach to investigate the impact of thermal desorption timing and analyte transfer efficiency in the SV-TAG system.

	Thermal Desorption Order		
FT-CTD1 **FT-CTD2**	Second First	First First	Second Second
Case Scenario #	0 (yellow bars)	1 (light blue bars)	2 (dark blue bars)
Objective	Thermal Desorption Timing Effect	Intercell Transfer Efficiency	Intercell Transfer Efficiency

In **Figure 3.7**, results are presented with increasing retention time on the x-axis and increasing polarity (represented as oxygen-to-carbon ratio – O:C) on the y-axis. The graph is subdivided into three Regions (A,B,C) based on the experimental observations. Region A represents compounds of lower boiling points, i.e., higher volatilities. Region B groups semi-volatile compounds, while Region C displays lower volatility species. Note that these compounds are more theoretically classified as I/SVOCs and this subclassification is therefore applicable solely to this analysis. For each compound, numbered as in **Table 3.3**, three bars represent the

results from each of the experimental conditions considered. Error bars were calculated as the 90% confidence interval of the mean of the triplicate injections. **Tables A3.3 - A3.5** (Apeendix A3 – Section A3.1) detail the integrated peak area values for all case scenarios studied.

TABLE 3.3. List of chemical compounds used to investigate the impact of thermal desorption timing and analyte transfer efficiency in the SV-TAG system.

	Compound Name	Formula	MW[a] (g.mol^{-1})	O:C	BP[a] (K)	RT (s)
2	Hexachlorocyclopentadiene	C5Cl6	272.77	0	512.15	408.72
4	2-Chloronaphthalene	C10H7Cl	162.62	0	529.15	427.94
7	Acenaphthylene	C12H8	152.20	0	543.15	455.13
8	Acenaphthene	C12H10	154.21	0	550.54	466.66
10	Fluorene	C13H10	166.22	0	570.44	500.65
12	Azobenzene	C12H10N2	182.22	0	566.15	512.18
14	Perchlorobenzene	C6Cl6	284.78	0	582.55	537.00
15	Phenanthrene	C14H10	178.23	0	610.03	563.01
16	Anthracene	C14H10	178.23	0	615.18	566.56
18	Fluoranthene	C16H10	202.25	0	655.95	640.16
19	Pyrene	C16H10	202.25	0	667.95	654.35
1	Chlorocresol	C7H7ClO	142.58	0.14	508.15	390.99
3	2,4,6-Trichlorophenol	C6H3Cl3O	197.45	0.17	519.15	416.70
5	Dimethyl phthalate	C10H10O4	194.19	0.40	556.85	450.40
6	2,6-Dinitrotoluene	C7H6N2O4	182.14	0.57	558	453.65
9	Diethyl phthalate	C12H14O4	222.24	0.33	567.15	497.10
11	4-Chlorodiphenyl ether	C12H9ClO	204.65	0.08	557.65	502.13
13	4-Bromodiphenyl ether	C12H9BrO	249.11	0.08	578.2	533.75
17	Dibutyl phthalate	C16H22O4	278.35	0.25	613.15	603.80
20	Benzyl-butyl phthalate	C19H20O4	312.36	0.21	643.15	700.46
21	Bis(2-ethylhexyl) phthalate	C24H38O4	390.56	0.17	657.15	739.18
22	Di-n-octyl phthalate	C24H38O4	390.56	0.17	657.15	779.08

Note. Chemical compounds are from the EPA 625 semi-volatile calibration mixture. The table separates non-polar (top) from polar (bottom) compounds and lists them with increasing RT.
Abbreviations: MW, molecular weight; BP, boiling point; RT, retention time.
[a]Properties retrieved from *The Yaws Handbook of Thermodynamics Properties for Hydrocarbons and Chemicals* (2018)[52]

Investigating the non-polar compounds in Region A, the yellow bars indicate that there is a significant difference in the collectors' response when desorbing at different times, with FT-CTD1 demonstrating lower efficiency compared to FT-CTD2 (fraction of signal less than unity).

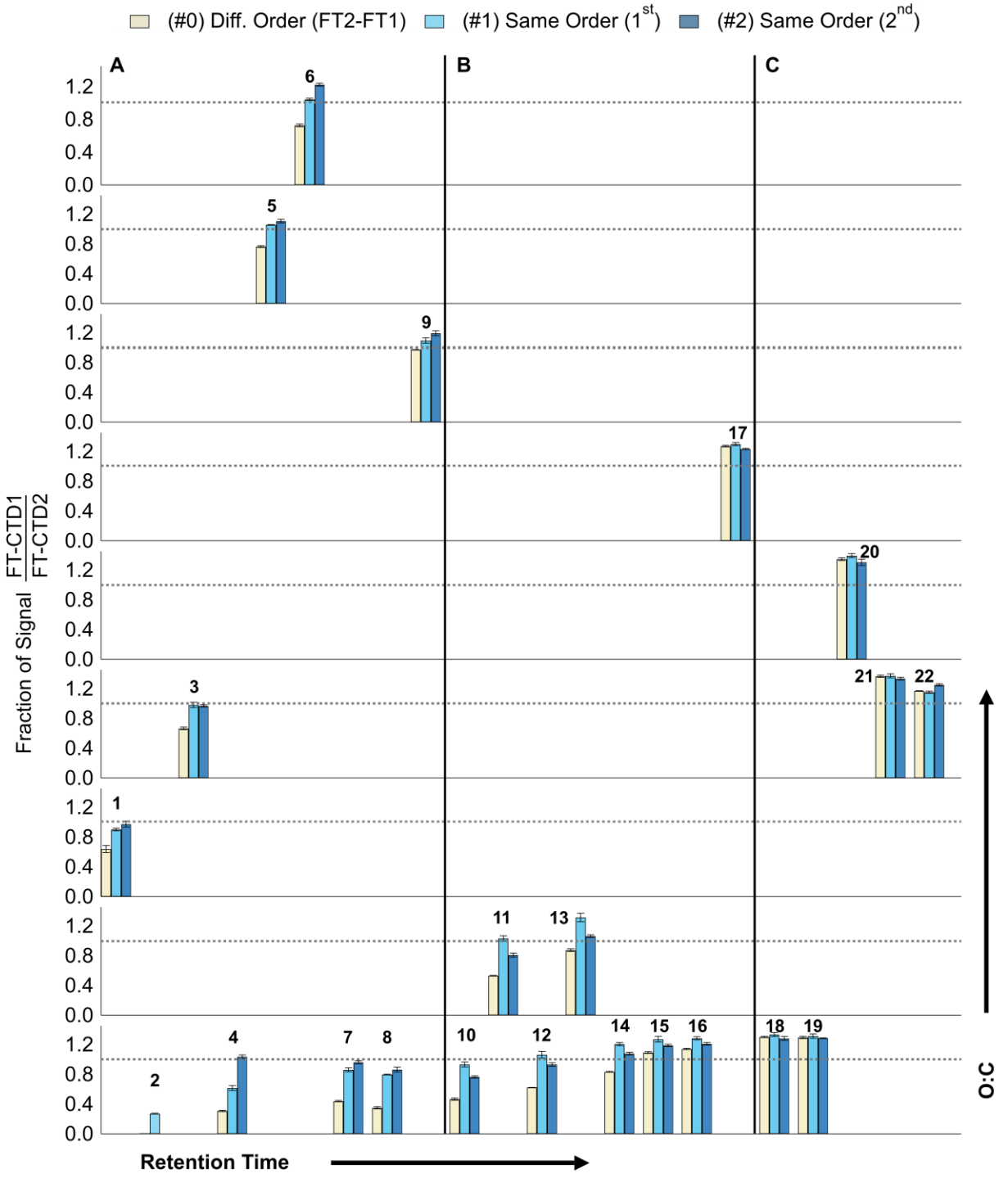

Figure 3.7. Investigation of thermal desorption timing and analyte transfer efficiency in the SV-TAG system. Three different thermal desorption scenarios were considered. The experimental results are displayed in the graph as different colored bars representing the average ratio between FT-CTD1 and FT-CTD2 signals for 5ng.μL^{-1} injections of an array of semi-volatility compounds listed in Table 3.3. Error bars denote a 90% confidence interval of the mean of the triplicate injections. Results are arranged with increasing volatility on the x-axis and increasing polarity on the y-axis.

Since, in this case (scenario #0), FT-CTD1 is the second cell to be analyzed, it is conjectured that the higher volatility analytes are experiencing evaporation in FT-CTD1 during the idle time between injection and thermal desorption. Hexachloropentadiene (compound 2), the most volatile non-polar species, is then considered to examine this hypothesis.

While this analyte is detected in both cells when thermal desorption occurs right after injection (Table A3.4 – scenario #1), no signal was observed in either collector when they idled between injection and thermal desorption (Table A3.5 – scenario #2). Since no other losses (such as changes in transfer efficiency due to high molecular weight and/or increased polarity) are expected in scenario #2 for non-polar compounds in Region A, this leads to the conclusion that low boiling point compounds collected in the second cell to be desorbed (either FT-CTD1 or FT-CTD2) will experience evaporation in the SV-TAG system. This could be a direct result of the increased idling time and/or fluctuations in the system's temperature during the first thermal desorption, both promoting an alternative thermodynamic phase equilibrium inside the instrument.

In scenario #1 (light blue bars), the response of the cells is compared when both collectors do not experience idling time between injection and thermal desorption, thus no evaporation losses are expected, and the fraction of FT-CTD1 signal relative to FT-CTD2 should be equal to one. The fact that non-polar compounds 2 to 8 demonstrate a ratio below this value, suggests that a different artifact is contributing to losses in FT-CTD1 when this cell desorbs right after injection. As described in **Section 3.2.3**, following standard injection, both collectors are purged at low flow to remove water and oxygen from the system. Therefore, is presumed that the non-polar high-volatility compounds injected into FT-CTD1 do not consistently interact with the cell's internal surfaces and instead are purged through the vent system. This incomplete analyte-collector

interaction is not observed for larger, less volatile non-polar compounds eluting at later retention times (Regions B&C), implying that molecular weight plays a role in purging-related losses.

By comparing the magnitude of the yellow and light blue bars, it is possible to estimate the extent of analyte evaporation in FT-CTD1, since, in both scenarios, FT-CTD2 response remains constant. It is noted that polar compounds in Region A experience overall less evaporation compared to non-polar compounds in the same volatility range. In addition, the near-unity values of the light blue bars demonstrate an improvement in analyte-collector interactions in FT-CTD1. This behavior can be expected because of the oxygen-bond strength between polar species and the active collection surfaces, a characteristic that enhances the retention of these analytes in the system, minimizing evaporation and purging losses. For polar compound 9, the intensity of the light blue bar is even greater than one, which indicates that FT-CTD1 demonstrates better performance in the transfer of this analyte compared to FT-CTD2. It is speculated that this difference in the transfer efficiency arises from heterogeneity in the coating material of FT-CTD2 and/or its respective transfer lines which results in strong interactions between the analyte and the collector's transfer paths, decreasing FT-CTD2 efficiency with increasing compounds' polarity (trend of light blue bars for polar compounds 9 to 22).

As previously established when investigating hexachloropentadiene's behavior, it is expected that FT-CTD2 also undergo evaporation losses. By examining the magnitude of the dark blue bars (scenario #2), insights into the degree of evaporation experienced by the analyte in each one of the collection cells can be investigated. The fraction of FT-CTD1 signal relative to FT-CTD2 should be equal to one if both cells provide similar conditions for the analyte when idling between injection and desorption in the absence of transfer efficiency-related losses. Considering non-polar compound 4, given the magnitude of the dark blue bar, one might conclude that intercell

evaporation losses are comparable. However, investigating the non-polar trend from compound 4 to 10, a decrease in the intensity of the dark blue bars with retention time is observed. This suggests that evaporation losses in FT-CTD1 are indeed greater than FT-CTD2's and tend to increase with decreasing compounds' volatility. This is counter-intuitive since high-volatility compounds should experience greater evaporation. Yet, the reason for the observed trend is that compounds eluting at earlier retention times (i.e., high-volatility compounds) are less sensitive to fluctuations in temperature since they favor the gas phase due to their elevated vapor pressures. In contrast, with increasing retention time, small temperature differences across the cells are sufficient to result in uneven intercell evaporation trends, since the vapor pressure of analytes eluting at those retention times fall into the semi-volatile range where their gas and particle phases are in dynamic equilibrium. Thus, it is concluded that FT-CTD1 evaporation losses are greater than FT-CTD2 for compounds sensitive to differences in the collector's temperature.

Non-polar compounds of lower volatility (Region C) do not experience evaporation as seen by comparing the magnitude of the yellow and light blue bars. Therefore, the intensity of the dark blue bars is associated with differences in transfer efficiency between the collectors. Indeed, these non-polar compounds (18 and 19) have high molecular weight and analyte transfer is known to be affected by this characteristic in TD-GC/MS systems.[26,49] Thus, it can be inferred from the greater than one magnitude of the dark blue bars in Region C that FT-CTD1 better performs at transferring high molecular weight analytes in the SV-TAG system.

A similar analysis can be done for compound 22. This analyte does not undergo evaporation, thus, again, the magnitude of the dark blue bars must correspond with differences in transfer efficiency between the collectors. As expected, the fraction of FT-CTD1 signal relative to FT-CTD2 is greater than one since FT-CTD2 transfer efficiency decreases with increasing

compounds' polarity and molecular weight. However, by comparing the magnitude of the yellow (scenario #0) and dark blue bars (scenario #2), it is possible to estimate the effect of increasing idle time in the transferring of the analyte in FT-CTD2, since, in both scenarios, FT-CTD1 response remains constant, and no evaporation is observed. Therefore, the increase in the magnitude of the dark blue bars compared to the yellow bars for compound 22 corresponds to a decrease in FT-CTD2 transfer efficiency due to increasing idling time. It was already recognized that FT-CTD2 transfer efficiency decreases with increasing compounds' polarity due to strong interactions between the analyte and the collector's transfer paths, now, it is acknowledged that these interactions tend to increase when the cell idles for extended periods. Therefore, it is concluded that the transfer of oxygenated compounds in FT-CTD2 tends to decrease with both increasing polarity and idling thermal desorption time.

In summary, it was observed that volatile and semi-volatile species will experience evaporation in the SV-TAG if the sample idles in the collection cells between injection and thermal desorption. For compounds sensitive to small temperature fluctuations in the system, evaporation losses will be greater in FT-CTD1 compared to FT-CTD2. Furthermore, small molecular weight low polarity compounds were found to not consistently interact with FT-CTD1's internal surfaces resulting in purging-related losses when thermal desorption took place right after injection. However, FT-CTD1 demonstrated better performance in transferring high molecular weight and oxygenated compounds, with FT-CTD2 polar efficiency decreasing with increasing O:C ratio and idling thermal desorption time. **Table A3.6** (Appendix A3 – Section A3.1) summarizes the above observations for each compound in **Figure 3.7.** This analysis, in addition to providing insights into how competently operate the SV-TAG system, elucidates the importance of frequent internal injections (achieved by the automatic feature of the calibration injection system) to closely track

fluctuations in the collectors' transfer efficiencies, a crucial aspect that affects the reliability of the SV-TAG measurements.

3.3.2 The Dual-Stage Collection Cell Performance

Collection Reproducibility

To investigate the reproducibility of the dual-stage cells independently of the performance of the AutoInject system, six chromatograms from indoor measurements during the ALPACA field campaign were selected as potential samples. Since reproducibility is difficult to accomplish in the field due to non-idealities such as temperature fluctuations, drifts in detector sensitivity, and changes in sample loading due to ambient concentration variability, the prospective samples were collected on the same day, in a 10-hour window (from 01:00 to 11:00) during the unoccupied period of the study, thus minimizing field-related interferences. In addition, solely non-denuded collections were considered to eliminate fluctuations due to gas-particle phase partitioning.

The reproducibility of indoor-related compounds (phthalates and organic esters) was initially investigated to ensure that the indoor ambient does not undergo significant changes throughout the respective sampling period. Confirming the suitability of the selected samples, the reproducibility of non-indoor related compounds was then explored. All the compounds considered for this analysis are listed in **Table A3.7** (Appendix A3 – Section A3.1). The reproducibility results are summarized in **Figure 3.8.**

Within each collector (**Figure 3.8A** and **3.8B**) both phthalates and organic esters demonstrated good reproducibility, thus validating the applicability of the indoor samples to examine the overall collection performance of the cells. Alkanes, PAHs, and carboxylic acid followed the good agreement observed with the indoor-related compounds.

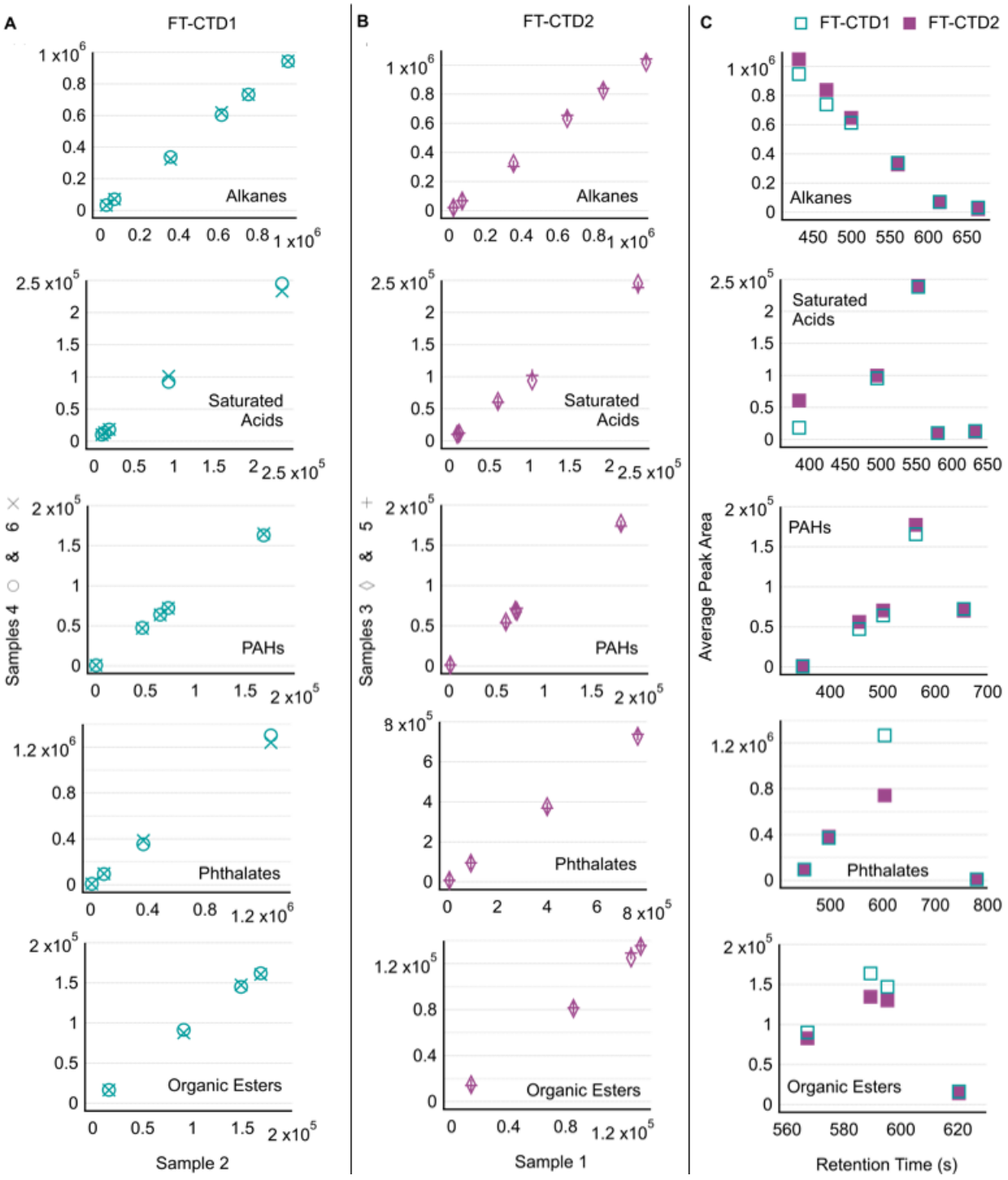

Figure 3.8. Reproducibility of the SV-TAG system. Each horizontal set of graphs corresponds to the reproducibility analysis of a different chemical class: alkanes, saturated acids, PAHs, phthalates, and organic esters. **(A)-(B)** Correlation between three ambient collection samples for FT-CTD1 and FT-CTD2, respectively. **(C)** Comparison between the individual cells responses.

Figure 3.8C compares the response across the individual cells. As expected from the extensive discussion in **Section 3.3.1**, FT-CTD2 responses are greater than FT-CTD1 at early retention time given the evaporation losses experienced by the analyte collected in the latter cell. However, this difference diminishes with increasing retention time due to the decrease in FT-CTD2 transfer efficiency for high molecular weight and high polarity compounds.

Design Artifacts

Sampling of VOCs and SVOCs using thermally desorbable solid adsorbents has proven its usefulness in many environmental applications and has become a routine technique.[28,33-35] Thus, to increase the analytical capability of the SV-TAG system, the second stage of the collection cell was designed for the trapping of low boiling point I/SVOCs through the adsorbent Tenax® TA. In general, artifact formation is common in thermal desorption from solid adsorbents. Previous studies have investigated Tenax® degradation patterns by exposure to numerous reactive species. DPQ (2,6-diphenyl-p-benzoquinone) and DPHQ (2,6-diphenyl-p-hydroquinone) are dominant degradation products from Tenax® reactions with nitrogen oxide species.[37,40,41] However, they have also been observed as artifacts when the adsorbent is exposed to ozonolysis products.[40,41] The degradation pattern of ozone has been demonstrated to be complex, including frequently reported phenyl-substituted carbonyl compounds of varying volatilities.[38,40-42] Here, the formation of DPQ and DPHQ in the SV-TAG system is investigated. Artifacts that arise from Tenax®-O3 exposure are also explored. Samples collected by the SV-TAG system during the ALPACA campaign are used to carry out this analysis and the impact of the identified artifacts in quantifying ambient I/SVOCs collected with the custom dual-stage cell is addressed.

DPQ and DPHQ Formation

The oxidative polymerization of 2,6-diphenylphenol produces poly(2,6-diphenyl-p-phenylene oxide) (PPPO), a porous polymer resin commercialized as the solid adsorbent Tenax®. DPQ and DPHQ are known degradation products that resemble the PPPO structure; however, the formation mechanism of these artifacts is still unknown. It has been suggested that DPQ is produced from chain scission or removal of a terminal group of the polymer after NO and NO2 exposure[36,41]. However, the thermal degradation of polymers also follows these decomposition pathways.[53-54]. Clausen and Wolkoff's[40] detailed investigation of DPQ and DPHQ formation followed by TD-GC/MS analysis demonstrated that the two compounds are interconverted in the analytical system by redox reaction during thermal desorption and in the hot interfaces of the MS. **Figure 3.9** illustrates the polymeric structure of Tenax® and the interconversion reactions of the two degradation products.

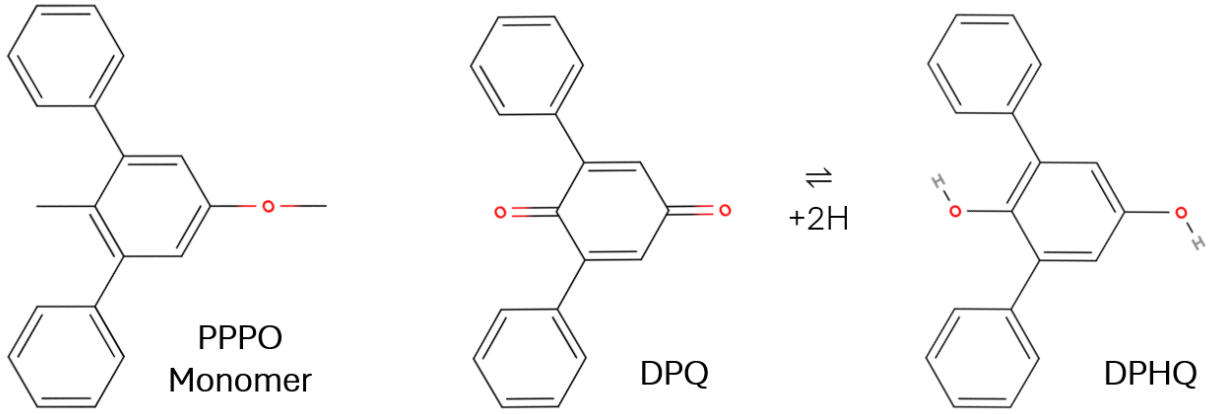

Figure 3.9. Monomer structure of poly(2,6-diphenyl-p-phenylene oxide)(PPPO/Tenax®) and two of its degradation products (DPQ: 2,6-diphenyl-p-benzoquinone, and DPHQ: 2,6-diphenyl-p-hydroquinone) with their interconversion reactions. Structures built using molview.org.

SV-TAG system blanks with conditioned Tenax® have not shown the presence of DPQ and DPHQ (or any other Tenax® artifacts) arising from the thermal decomposition of the polymer (see

Section 3.3.1). However, it is of interest to understand the extent of DPQ and DPHQ interconversion reactions in the analytical system. To achieve this, since fresh non-treated adsorbents have a higher number of readily degradable oligomers (byproducts remaining on adsorbents after manufacturing) that can produce artifacts during thermal desorption, non-conditioned Tenax® was installed in the collection cells, and sequential blank chromatograms were obtained from the default SV-TAG TD-GC/MS analysis method.

Figure 3.10A shows the chromatogram obtained from FT-CTD2 blanks. The elevated baseline and numerous large peaks presented very high and potentially excessive loadings to the GC/MS system. However, each partial conditioning (successive blanks) largely eliminated the observed decomposition products. The peaks in Figure **3.10A1** represent the SIC chromatograms of DPHQ (*m/z* 262) from each GC run. **Figure 3.10A2** the decay of this artifact in terms of the remaining signal fraction calculated from peak integrations. FT-CTD1 demonstrated a similar behavior (**Figure A3.3** – Appendix A3 – Section A3.3). While DPQ was not identified in these blanks, it is not possible to affirm that this compound was not formed by Tenax® thermal degradation in the SV-TAG system given the interconversion of DPQ and DPHQ during TD-GC/MS analysis. However, it is appropriate to speculate that quinone reduction prevails over oxidation in the SV-TAG system.

To examine the formation of DPQ and DPQH from Tenax® degradation during ambient sampling with the SV-TAG system, mass spectral deconvolution PMF analysis was performed separately in all non-denuded outdoor and indoor ALPACA chromatograms to identify DPQ and DPHQ in the samples and obtain their qualitative trends throughout the campaign. **Figure A3.4** (Appendix A3 – Section A3.3) shows the DPQ and DPHQ factors identified in the outdoor PMF samples. While **Figure A3.5** (Appendix A3 – Section A3.3) exhibits the results of the indoor

analysis. The chromatograms contained both DPQ and DPHQ, or DPHQ only, but never DPQ only, agreeing with previous observations.[40]

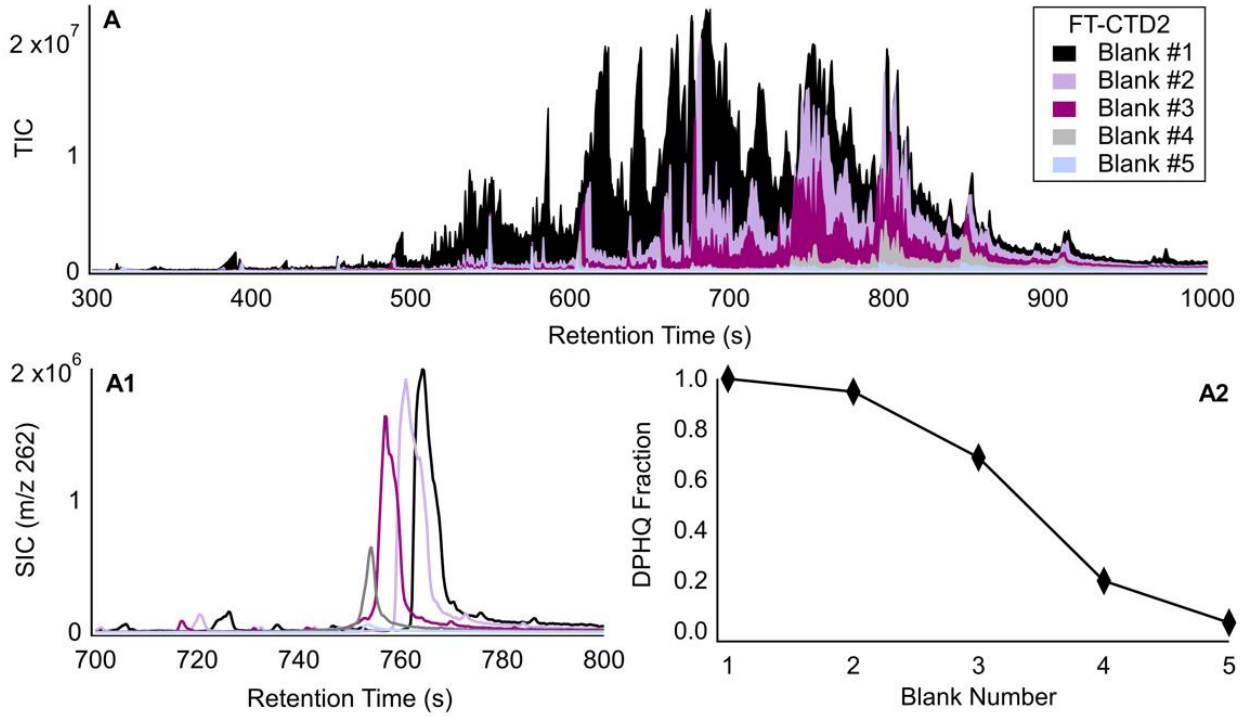

Figure 3.10. Evolution of Tenax® conditioning FT-CTD2. **(A)** Chromatogram obtained from successive blanks after installing fresh Tenax® in the collection cell. **(A1)** Display DPHQ, as *m/z* 262 peaks, from each run. **(A2)** DPHQ decay in terms of the remaining signal fraction calculated from peak integrations. DPQ was not identified in these blanks suggesting quinone reductions prevail over oxidation during TD-GC/MS analysis in the SV-TAG system.

Since DPQ and DPHQ are interconverted in the analytical system, they are considered a single compound here, thus their factor abundances were summed and Pearson correlation analysis was performed between the resulting timeseries and measured ambient concentration of NO2, NO, NOx and O3. A good correlation ($r > 0.5$) was observed between [DPQ + DPHQ] and nitrogen oxide species, while no correlation was found between ozone and these artifacts (**Figure 3.11A**). Clausen and Wolkoff[40] and Klenø et al[41] had previously reported that exposure of Tenax® to NO2 is dominated by [DPQ + DPHQ] (> 98% chromatogram abundance). Hanson et al[37] have also

observed these compounds as decomposition products from reactions between the adsorbent and NO. However, Klenø et al noted that the production of [DPQ + DPHQ] yielded 50 times less from NO exposure than for NO2, under the same experimental conditions. Nevertheless, in this analysis, both NO and NO2 appear to equivalently promote the degradation of the polymer.

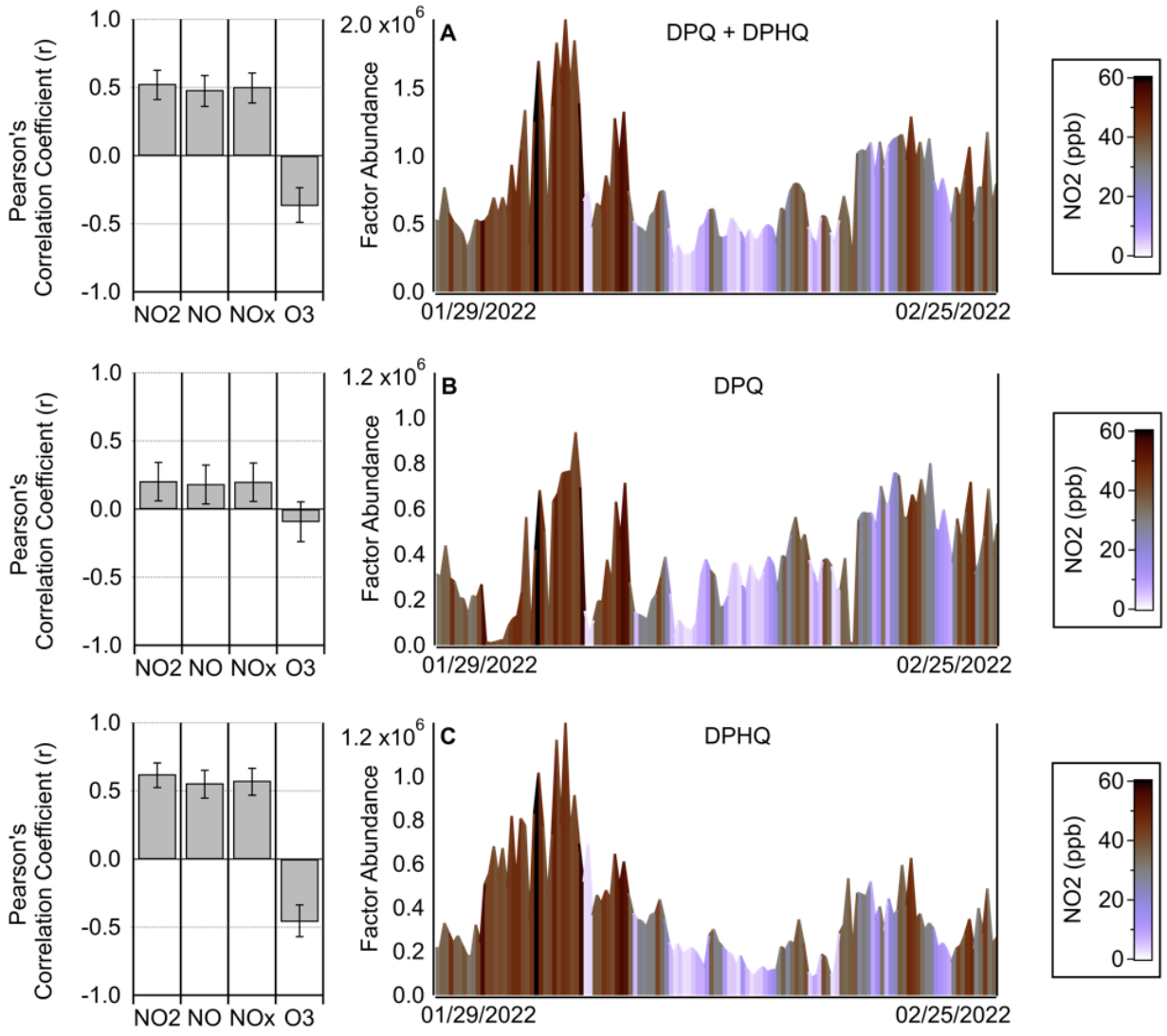

Figure 3.11. Formation of DPQ and DPQH from Tenax® degradation during outdoor ambient sampling with the SV-TAG system. Qualitative abundances obtained from mass spectral deconvolution PMF analysis **(A)** Summed DPQ and DPHQ abundances. **(B)** Deconvoluted DPQ abundances. **(C)** Deconvoluted DPHQ abundances.

Deconvoluted DPQ and DPHQ correlation analysis (**Figures 3.11B and 3.11C**) demonstrate that DPHQ is the major Tenax® degradation product from NOx exposure, diverging from previous studies that identified DPQ as the abundant peak.[40,41] This dominance of DPHQ over DPQ could be associated with the previously observed prevalence of quinone reduction over oxidation reactions in the SV-TAG system, making it reasonable to expect that some of the NOx-produced DPQ is reduced to DPHQ during the TD-GC/MS analysis.

In addition, a previous study[40] also investigated the effect of sampling flow rate in the formation of DPQ and DPHQ from Tenax®-NO2 exposure. The authors observed that increasing the sampling flow from 0.2 $L.min^{-1}$ to 1.5 $L.min^{-1}$ (650% increase) while maintaining all other parameters constant, increased DPHQ yield from 24% to 100% in tubes composed of 40 mg of Tenax® TA (35-60 mesh). In the SV-TAG (30 mg – 60-80 mesh), the high sampling flow rate of 8.3 $L.min^{-1}$ could be favoring the formation of DPHQ over DPQ in the system after NO2 exposure.

Another factor contributing to the NOx-related DPQ/DPHQ observed yields could be related to the chemical composition of the adsorbed sample. In the same study mentioned above, it was recognized that exposure to limonene after Tenax® exposure to NO2 yielded DPHQ only. The authors concluded that the reduction of DPQ by limonene best explained this observation. While the artifacts DPQ and DPHQ do not interfere with the analysis of I/SVOCS, the consumption of the adsorbed sample to produce these decomposition products can result in negative biases that should be addressed.

Although DPQ and DPHQ are mainly produced by Tenax® exposure to nitrogen oxide species, they have also been identified as degradation products from reactions between the polymer and reactive species already present in the adsorbed sample, and/or produced in the system by thermally liable compounds that decompose during thermal desorption.[40,41] To understand the

extent of these Tenax®-sample reactions in the SV-TAG system, DPQ and DPHQ formation from Tenax® exposure to collected potential ozonolysis products (samples collected at higher ozone levels) is investigated.

Figure 3.12A shows a scatter plot that represents the fraction of DPQ, calculated as the ratio DPQ/[DPQ + DPHQ], as a function of ozone and nitrogen dioxide concentrations. At high NO2 and low O3 levels (dashed box), DPQ and DPHQ are mainly formed by Tenax®-NOx reactions, and their yields will depend on three main factors: the extent of DPQ reduction in the analytical system during TD-GC/MS analysis; the extent of DPQ reduction by compounds present in the adsorbed sample; and the additional formation of DPQ and DPHQ from secondary reactions.

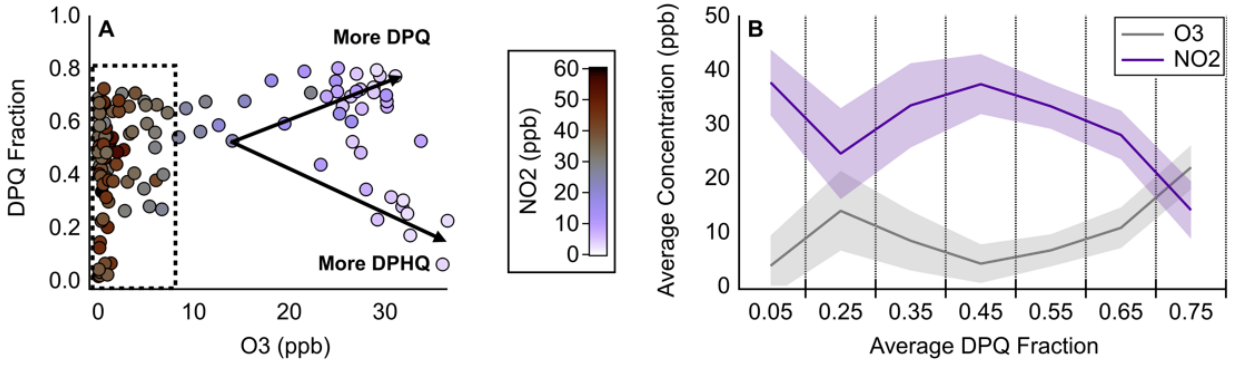

Figure 3.12. Secondary DPQ/DPHQ formation from Tenax® exposure to reactive and/or thermally liable outdoor ozonolysis products. **(A)** Fraction of DPQ, calculated as the ratio DPQ/[DPQ + DPHQ], as a function of ozone (O3) and nitrogen dioxide (NO2) concentrations. **(B)** Average O3 and NO2 concentrations observed at each DPQ average yield. Shaded regions denote a 90% confidence interval of the calculated mean.

At increasing O3 levels, NO2 concentrations tend to decrease. Thus, DPQ and DPHQ formation must be associated with other mechanisms different from Tenax®-NOx exposure. It is known from previous studies[40,41] that O3 itself does not produce DPQ or DPHQ in significant amounts. This finding coincides with the presented dataset from the observed strong negative correlation between O3 and [DPHQ+DPQ]. Therefore, it is conjectured that the presence of these

artifacts at low NO2 and higher O3 concentrations in the SV-TAG system is related to Tenax® degradation from exposure to reactive and/or thermally liable ozonolysis products.

To address the extent of DPQ and DPHQ formation from Tenax®-NOx reactions and from Tenax exposure to reactive and/or thermally liable ozonolysis products, the average O3 and NO2 concentrations were calculated at each DPQ fraction bin. In **Figure 3.12B**, it is noted that from bins 0.05 to 0.25 and 0.45 to 0.75 DPQ yields increase by Tenax® reaction with ozonolysis products, while from bins 0.25 to 0.45 the observed DPQ abundances are mainly resulting from the adsorbent reaction with nitrogen oxide species. Indeed, exposure to both NOx and ozonolysis products generates DPQ and DPHQ as artifacts, however, exposure to ozonolysis products seems to favor DPQ formation over DPHQ as seen by the former larger yields at higher O3 levels.

Indoor results are shown in **Figure 3.13** as DPHQ fraction timeseries since indoor samples are expected to be dominated by DPHQ due to the low indoor ozone concentrations, combined with more probable terpene-induced DPQ reduction reactions, and the prevalence of DPQ to DPHQ conversion during TD-GC/MS analysis. Indeed, DPHQ preponderates in the indoor samples. The 20th percentile of the calculated fraction is 0.76, signifying that in 80% of the data DPHQ yields are above 0.76.

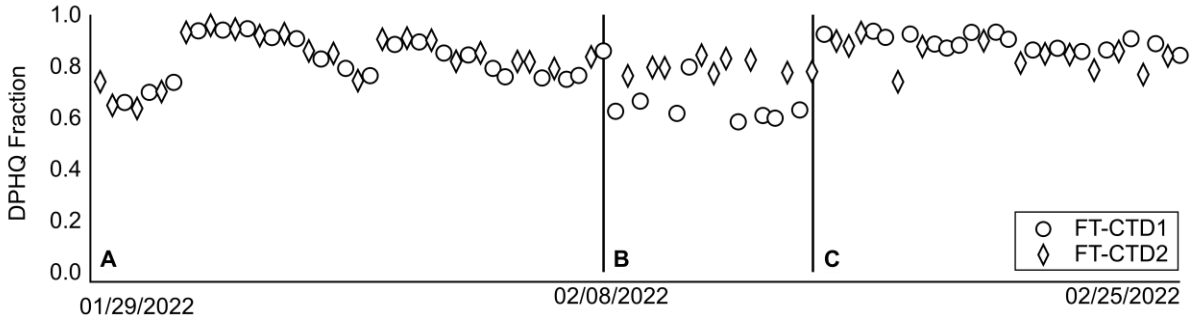

Figure 3.13. Indoor deconvoluted DPHQ fractions. DPHQ preponderates in the indoor samples, with 80% of the chromatograms showing yields of at least 0.76. Regions A and C represent similar degradation patterns across cells. DPHQ decay in FT-CTD1 results from changes in reaction yields due to the greater de-stabilization of the polymer in that collector.

Figure 3.13 also deconvolutes the DPHQ fraction from Tenax® degradation in FT-CTD1 and in FT-CTD2. In Region A, the adsorbents present in both cells demonstrate similar degradation trends, however, in Region B there is a clear decay in FT-CTD1 DPHQ yields compared to FT-CTD2. At that time, an atypical cooking experiment was performed inside the test home. The perturbation produced extremely high particulate matter concentrations that contained great amounts of fatty acids. It is believed that the elevated number of free radicals generated during this experiment promoted an uneven de-stabilization (reduction by chain elimination) of the adsorbent present in each cell, with FT-CTD1 containing more readily degradable oligomers which changed the DPQ/DPHQ reaction yields in that collector. This hypothesis is then corroborated by the trends observed in Region C. The degradation pattern resumed to previously observed comparable fractions after replacing the Tenax® bed of each cell. However, this change in DPHQ yield in Region B does not seem significant in the outdoor samples, possibly due to the already low DPHQ fraction observed during that period (**Figure A3.6** – Appendix A3 – Section A3.3).

Tenax® Degradation Products from Ozone Exposure

The degradation pattern resulting from Tenax®-O3 reactions is complex. Different studies reported highly variable yields and trends that seem to be dependent on both O3-related variables and TD-GC/MS methods/systems.[39,41,42] Lee et al[42] summarized all identified positive artifacts from the 1980s to the early 2000s. **Table 3.4** lists solely previously observed degradation products within the SV-TAG volatility range. They were then investigated as potential O3 related artifacts in the system. Outdoor samples were first examined for the identification of these compounds given the overall higher O3 levels compared to indoors. Indoor samples were explored based on the observed outdoor results.

TABLE 3.4. Previously identified positive Tenax®-O3 artifacts.

Compound Name	Formula	MW[a]	Qual. Ions	SVTAG Outdoor	SVTAG Indoor	RT (s)
Benzoic acid	C7H6O2	122.12	105; 122	✓✓	✓✓	338.68
Decanal	C10H20O	156.26	43; 41; 55	x	x	-
p-Hydroquinone	C6H6O2	110.11	110; 81	x	x	-
Phenyl glyoxylic acid	C8H6O3	150.13	105; 77; 51	x	x	-
Phthalic anhydride	C8H4O3	148.12	104; 76; 50	✓✓	x	401.33
Phenylmaleic anhydride	C10H6O3	174.15	102; 174	✓✓	x	482.62
Benzophenone	C13H10O	182.22	105; 77; 182	✓x	✓x	513.95
Phenyl Benzoate	C13H10O2	198.22	105; 77	✓	x	522.23
1,2-Diphenylethanone	C14H12O	196.24	105; 77	✓	x	545.59
Diphenylethanedione	C14H10O2	210.23	105; 77	✓	x	568.93
Benzoic anhydride	C14H10O3	226.23	105; 77	✓	x	604.99
Diphenyl propanetrione	C15H10O3	238.24	105; 77	✓	x	636.33
2,6-Diphenylphenol	C18H14O	246.30	246	✓✓	✓✓	677.41
2,4-Diphenyl-4-cyclopentene-1,3-dione	C17H12O2	248.27	248; 90; 118	✓✓	✓✓	-
Unknown aromatic ketone[b]			248; 105; 77			699.27

Note. Adapted from Lee et al. (2006)[42] considering solely compounds within the SV-TAG volatility range. The two compounds below the solid line co-elute in the system.
(✓✓) Compound identified as positive artifact; (✓**x**) Compound identified but it is not a positive ozone artifact; (✓) Compound identified but it was not investigated due to near detection limit abundances; (**x**) Compound not identified.
Abbreviations: MW, molecular weight (in $g.mol^{-1}$); Qual. Ions, qualifier ions; RT, retention time.
[a]Properties retrieved from *The Yaws Handbook of Thermodynamic Properties for Hydrocarbons and Chemicals* (2018)[52]
[b]Compound identification was achieved by comparison with reported qualifier ions.

Many compounds listed in **Table 3.4** are of significant ambient occurrence with concentrations possibly correlating with ground-level O3 trends, thus making it challenging to deconvolute Tenax® artifact formation from ambient concentrations without proper Tenax®-O3 blank calibration. However, wintertime tropospheric O3 concentrations in the Arctic are overall low compared to mid-latitude regions due to the weak *in situ* photochemical production of O3, combined with O3 titration by accumulated NO from near-ground emissions.[55] These unique

conditions lead to near-zero O3 during strong polluted periods.[56] Increases in ground-level O3 concentrations during the ALPACA campaign are associated with cleaner periods due to O3-rich air mass transport (especially stratosphere-troposphere exchange) that promotes the dispersion of accumulated tropospheric pollutants.[44] **Figure A3.7** (Appendix A3 – Section A3.3) illustrates the relationship between O3 and total organics particle concentrations during the campaign. This anti-correlation between pollution and O3 provides a particular scenario that facilitates the identification of SV-TAG Tenax®-O3 artifacts since ambient abundances are expected to decrease with increasing tropospheric O3, while artifact formation must demonstrate a positive correlation.

From the outdoor non-denuded samples, 12 of 15 previously reported compounds were identified in the SV-TAG system but only three demonstrated high abundances at high O3 levels. Their trends are highlighted in **Figure 3.14.** Timeseries were obtained from the PMF mass spectral deconvolution analysis formerly discussed in **Section 3.2.6.** O3 doses were calculated by multiplying the collected sample volume by the measured O3 concentrations at that time. Note that relatively high O3 levels are needed for significant artifact formation. These compounds are considered solely degradation products in the outdoor samples since their abundances do not seem relevant in the absence of O3. The increase in the artifact yields at lower O3 levels in Regions B and C is a result of ambient collections in less stable polymers due to exposure to high levels of free radicals and shorter adsorbent conditioning after replacement.

The remainder products were found in small amounts and some of their trends are discussed in Appendix A3 (**Section A3.2**). Benzophenone, previously classified as a unique Tenax®-O3 degradation product, did not exhibit any correlation with O3 in the SV-TAG system, therefore it was not considered an artifact. This observation supports the complexity and TD-

GC/MS specificity of Tenax®-O3 degradation pathways, which led to the investigation of SV-TAG-specific O3 artifact formation discussed below.

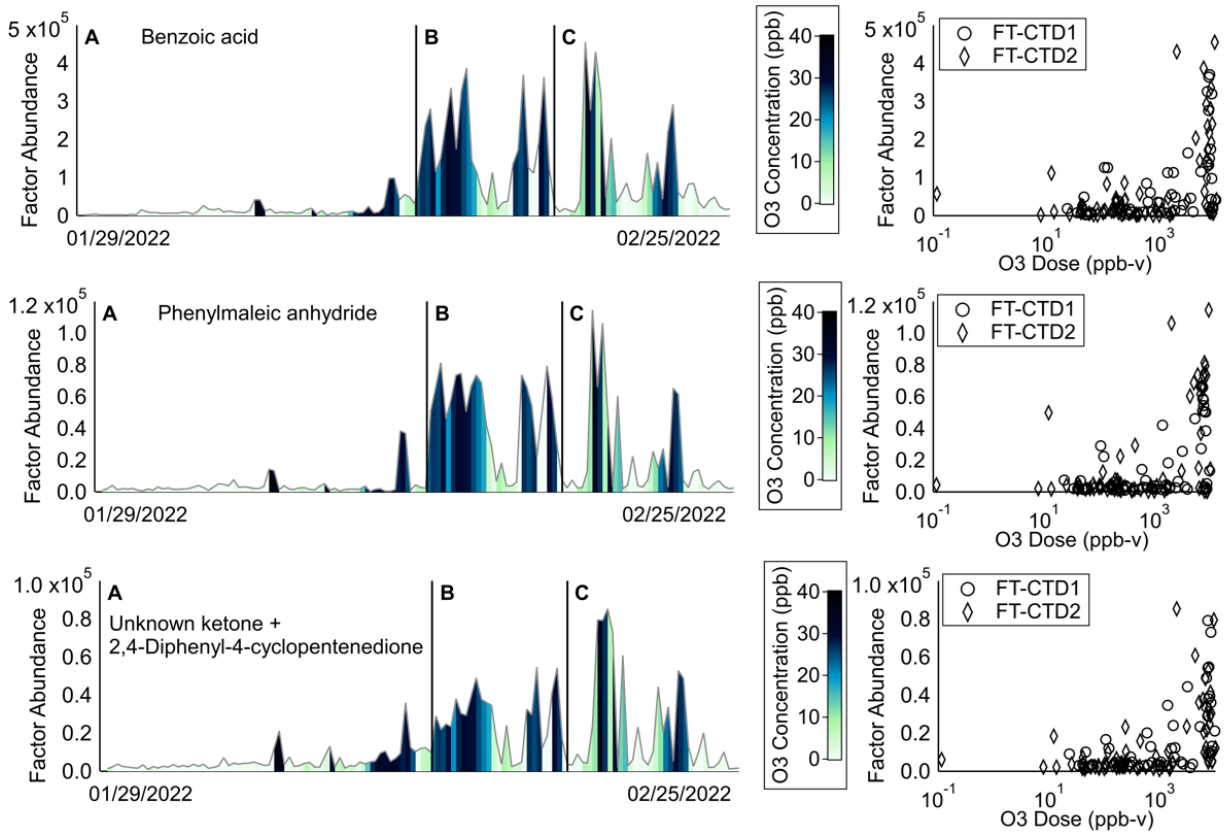

Figure 3.14. The three most abundant SV-TAG Tenax® -Ozone (O3) artifacts previously reported in the literature. Scatter plots on the right highlight the relationship between O3 dose and artifact abundances.

Low-volatility Tenax®-O3 artifacts tend to resemble the adsorbent structure, thus previously identified compounds in the non-denuded outdoor samples that could have derived from the Tenax® polymer were investigated as potential artifacts using Pearson correlation analysis. Indeed, diphenylmaleic anhydride was found to be a Tenax®-O3 degradation product not previously reported in the literature, showing the strongest O3 correlation when considering all other ozone artifacts analyzed (**Figure A3.10** – Appendix A3 – Section A3.3).

High-volatility Tenax®-O3 artifacts do not necessarily resemble the polymer structure, thus, their identification as potential artifacts are more challenging. PMF mass spectral deconvolution analysis was performed in the retention time window before 500s and the correlation between the identified factors and benzoic acid was investigated since benzoic acid is within the considered volatility range and it was found to be a specific Tenax®-O3 degradation product. **Figures A3.11 and A3.12** (Appendix A3 – Section A3.3) summarize the correlation analysis and PMF results demonstrating that no other high-volatility strong Tenax®-O3 artifact was identified. It is important to notice that this finding does not eliminate the presence of weaker high-volatility O3-related degradation products, however, if they do exist ambient measurements of these compounds should not be compromised given their low Tenax®-O3 reaction yields.

Only three SV-TAG Tenax®-O3 artifacts were identified in the indoor samples (**Table 3.4**). This low Tenax®-O3 impact indoors is predicted since O3 concentrations tend to be 75% lower indoors compared to outdoors.[57] The plots in **Figure 3.15** show the trends of the two most abundant degradation products as a function of outdoor O3 levels (measured at indoor sampling times). Outdoor concentrations were used because of the fragmentary indoor trace gas data. Similar to the outdoor observations, these compounds were found to be solely degradation products in the indoor samples given their near-zero abundances in the absence of O3.

As already discussed, during the ALPACA camping, outdoor O3 levels were even lower than average ambient concentrations given the reduced solar activity during wintertime in Arctic regions combined with strong temperature inversions. These conditions minimize even more the impact of Tenax®-O3 artifacts in indoor samples. This is a positive observation because Tenax®-O3 reactions are the only degradation pathway known to form high volatility artifacts that could interfere with the measurements of I/SVOCs indoors.

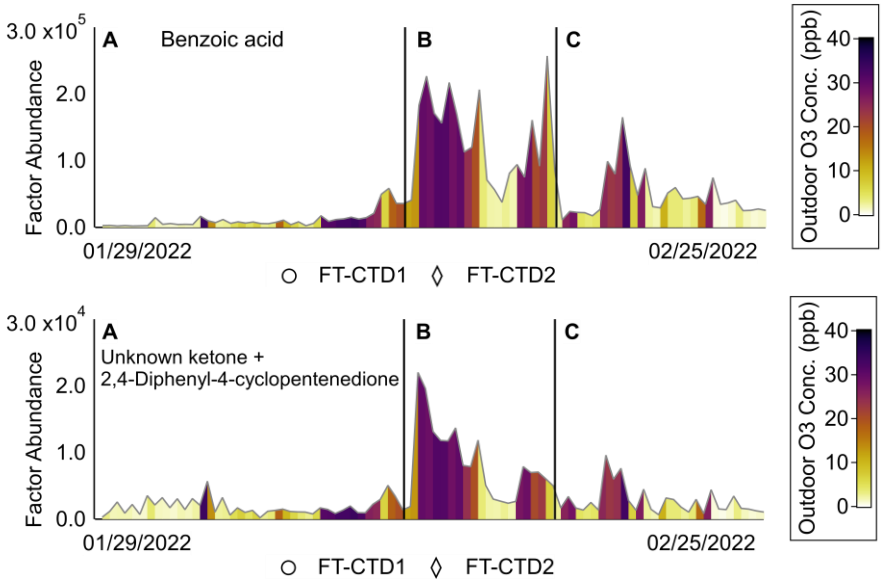

Figure 3.15. Two of three indoor SV-TAG Tenax® -O3 artifacts.

In the analysis carried out above, DPQ/DPHQ were found to be the dominant artifacts in the SV-TAG system and primarily formed from Tenax® exposure to NO2. Secondary DPQ/DPHQ formation seemed to arise from Tenax® reactions with the adsorbed sample and/or Tenax® exposure to reactive species produced in the system by thermally liable compounds that decompose during thermal desorption. Although Tenax®-sample reactions are expected to be minimal[41], the consumption of the adsorbed sample to produce DPQ/DPHQ can contribute to negative measurement biases. Thus, it is recommended to develop specific calibration procedures for Tenax®-NOx exposure to deconvolute DPQ/DPHQ formation from exposure to nitrogen oxide species and other reaction pathways.

Tenax®-O3 degradation products were less abundant in magnitude compared to artifacts from Tenax®-NO2 exposure. However, the degradation pattern of O3 demonstrated higher complexity. Although not prominent in the SV-TAG samples here investigated (given low O3 field concentrations), previous studies reported the formation of numerous compounds of high volatility from Tenax®-O3 exposure that could interfere with I/SVOC measurements. In addition, O3 is also

known to react with previously adsorbed analytes. Helmig's[58] comprehensive review discusses the substantial sample losses that may occur, especially for terpenoids. Although thoughtful O3 calibration could be an applicable approach to anticipate the identification of these potential artifacts before laboratory experiments and field campaigns, given the complexity and specificity of Tenax®-O3 degradation pathways, the use of O3 scrubbers may be a more suitable solution to address O3-related artifacts.

In summary, it was observed that Tenax® produces sampling artifacts in the SV-TAG system when the adsorbent is exposed to reactive gaseous species. However, the impact of the degradation products can be addressed with specific system blank calibrations by exposing the collection cells to expected NOx and O3 concentrations. The installation of an upstream O3 scrubber might also be a considered route to minimize artifact-measurement interferences by reducing the extent of Tenax®-O3 reactions. During his investigation, Lee et al[42] reported that most O3 artifacts significantly decreased to only trace levels after two or three exposure-conditioning cycles after a first-order (exponential) decrease. Thus, further investigation can be done to determine the optimal adsorbent age that yields the least number of artifacts without compromising adsorbent-sample retention in the SV-TAG system.

During the ALPACA campaign, most of the observed artifacts were of low volatility and easily identifiable given the similarity between their functional groups and the Tenax® structure. The field conditions minimized the formation of positive and negative O3-related artifacts. Only a few high-volatility relevant atmospheric pollutants were prone to bias because of the formation of Tenax® artifacts in the SV-TAG system (i.e. benzoic acid, phthalic anhydride, and benzophenone). Therefore, the analytical capability of the instrument in measuring I/SVOCs during the campaign was not compromised. The results here presented lead to the conclusion that

high-volatility compounds can be effectively measured, and reliable phase partitioning can be estimated by deploying the newly developed dual-stage Tenax® SV-TAG collector.

3.3.3 Collection Cells Design Comparison

Collection Capability

To evaluate the extent of the enhanced collection capability of the new dual-stage filter-Tenax® collection cell, two additional collector models were considered: a single-stage cell featuring solely the high-surface-area metal fiber filter, and a dual-stage design with the metal filter on the first stage and a quartz filter installed on the second stage. Collection capabilities were compared by performing in-series ambient sampling during the ALPACA campaign. To minimize field-related interferences in the comparison results, such as differences in the collection capabilities due to changes in sample loading arising from ambient concentration variability, non-denuded indoor samples were collected on the same day, in a 6-hour window (from 04:00 to 10:00) when the test home was unoccupied. A significant pressure drop was observed when deploying the dual-stage quartz filter cell (flow rate decreased from 8.3 to 6.6 $L.min^{-1}$), therefore all samples examined here were normalized considering the standard 10-minute collection at 8.3 $L.min^{-1}$.

Figure 3.16A overlays the chromatograms obtained by deploying the three different cell designs. The effectiveness of the dual-stage Tenax® model in collecting higher volatility compounds can be unequivocally observed. To quantify the recognized difference, all three chromatograms were binned by retention time, considering a 30s-time window, and their TIC abundances were summed. The y-axis in **Figure 3.16B** represents the contribution of each design to the total TIC abundance at each respective bin. While all three collectors demonstrate comparable efficiencies in the recovery of low-volatility analytes, the dual-stage Tenax® cell is

responsible for 60%, on average, of the total signal observed at retention times from 6 to 8 minutes, peaking at 70% between 6.5-7.5 minutes.

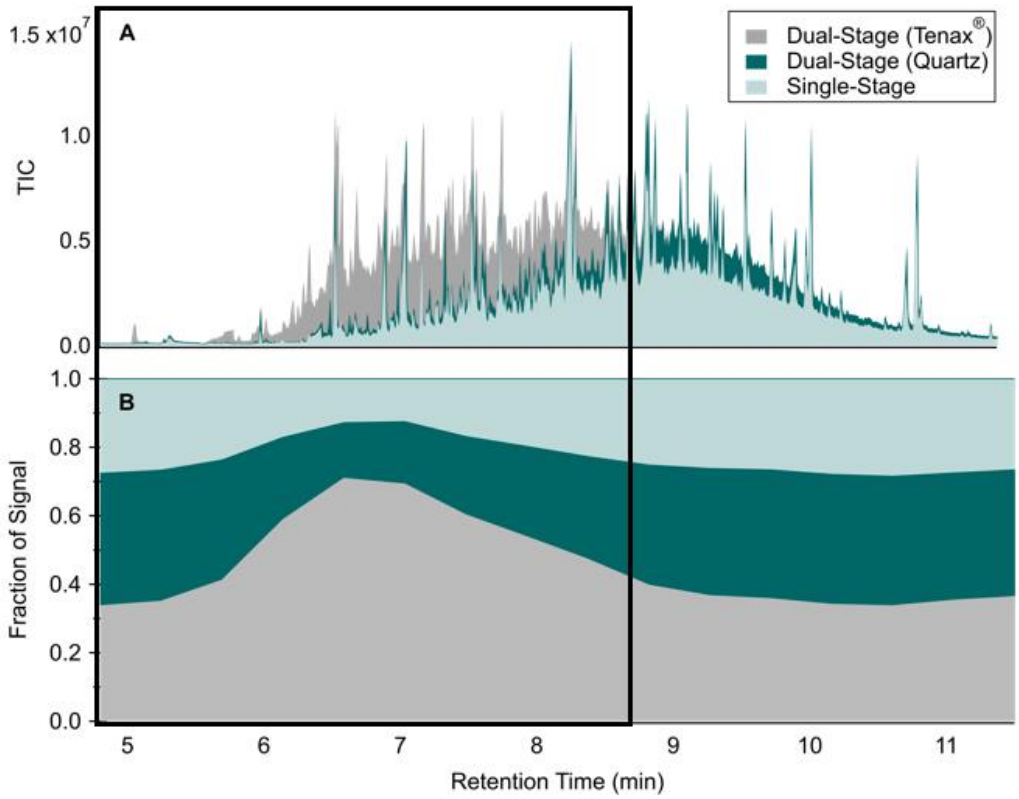

Figure 3.16. Cells design comparison. **(A)** Overlayed chromatograms obtained by 10-minute collections deploying three cell designs: single-stage, dual-stage with quartz filter, and dual-stage with Tenax®. **(B)** Fraction of the total signal (summed all three TICs) relative to each cell design as a function of retention time.

The above analysis provides a general understanding of the bulk differences in the collection capability of the three designs. A more comprehensive approach involves quantifying the observed differences including chemical information. To achieve that, the chromatograms obtained with the dual-stage Tenax® cell and the single-stage filter cell were used for the PMF mass spectral deconvolution analysis. Calculations were performed in the retention time window outlined in **Figure 3.16.** A 17-factor solution was chosen to represent the dataset since it was determined to be the best solution that maximized identifiable unique factors while minimizing

factor splitting. Plots and additional discussion regarding the considered PMF solution can be found in Appendix A3 (**Section A3.4**). It is important to mention the residual factor was not considered here but it was found to contain fraction abundances of individual compounds loaded and identified in the main solution, thus this analysis represents solely an approximation, yet it provides an insightful understanding of the capabilities of the collectors.

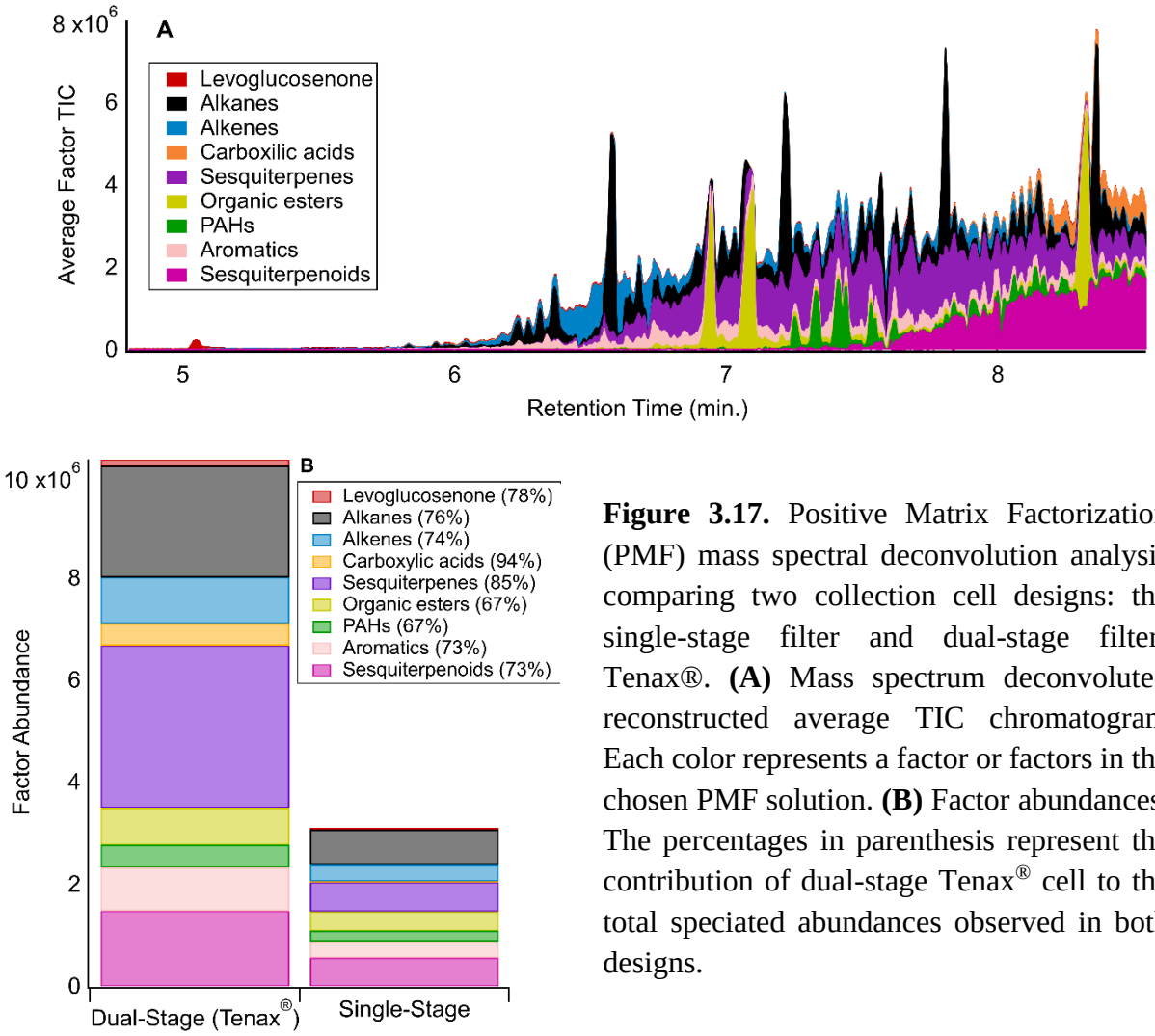

Figure 3.17. Positive Matrix Factorization (PMF) mass spectral deconvolution analysis comparing two collection cell designs: the single-stage filter and dual-stage filter-Tenax®. **(A)** Mass spectrum deconvoluted reconstructed average TIC chromatogram Each color represents a factor or factors in the chosen PMF solution. **(B)** Factor abundances. The percentages in parenthesis represent the contribution of dual-stage Tenax® cell to the total speciated abundances observed in both designs.

Figure 3.17 displays the selected factors that elucidate the differences in collection efficiencies between the designs considered. Overall, the total abundance detected by the dual-

stage cell is more than three times greater than what is seen when deploying the single-stage cell. Speciated efficiencies were estimated by summing each individual factor and calculating the fraction of the abundance relative to each cell design. The percentages in parenthesis represent the contribution of dual-stage Tenax® cell to the total speciated abundances. The evident high efficiency of the dual-stage design in collecting lower boiling point compounds of varying functionalities translates into a more versatile and more capable instrument for the study of I/SVOC emissions and transformations.

Limits of Detection of the Dual-Stage Cell

To better understand the capability of the dual-stage cells in collecting lower boiling point semi-volatile organic species, limits of detection of selected compounds eluting in the retention time window highlighted in **Figure 3.16** were calculated. Per Equation 3.1, calibration curves are required for LOD calculations and they were obtained from single injections of varying concentrations (0.2 – 1 – 2 – 3 $ng.\mu L^{-1}$) of diluted standard solutions from the EPA 625 Semivolatile Calibration Mix (Sulpeco 506559, Sigma Aldrich, St. Louis, MO). **Figure A3.14** (Appendix A3 – Section A3.4) displays the resulting calibration curves.

Detection limits are shown in **Figure 3.18** as a function of retention time and polarity for both collection cells. Limits tend to increase with increasing volatility and polarity as expected from the detailed discussion regarding analyte transfer efficiencies in **Section 3.3.1.** Overall, detection limits were around 0.01 ng. Considering a 10-minute collection at 8.3 $L.min^{-1}$, this value corresponds to 0.12 $ng.m^{-3}$, which is below measured concentrations for most compounds of interest. It is important to mention that detection limits can always be scaled by increasing collection times, but with the cost of sacrificing time resolution.

Figure 3.18. SV-TAG detection limits calculated for selected SVOCs of varying polarities and volatilities.

3.4 Conclusions

It was demonstrated that the development of the dual-stage collection and thermal desorption cell expands the analytical capability of the SV-TAG system by effectively trapping high volatility I/SVOCs through the adsorbent Tenax® TA. This enhanced collection capability combined with the hourly time resolution translates into an efficient instrument for the investigation of the dynamics of I/SVOC emissions and transformations.

Artifact formation from Tenax® exposure to reactive species was observed, yet it did not compromise the analytical capability of the instrument in the conditions studied. For future applications, it is recommended to address the impact of Tenax® degradation in conjunction with field and laboratory measurements. This can be achieved by performing system blank calibrations by exposing the collection cells to expected NOx and O3 concentrations. The installation of an upstream O3 scrubber might also be a considered route to minimize artifact-measurement interferences by reducing the extent of Tenax®-O3 reactions.

The dual-cell arrangement provides more accurate phase-partitioning quantification. However, analyte retention and transfer differ between collectors, and it is necessary to

characterize these differences for reliable measurements. Frequent injections of internal standards provide a means to closely track the fluctuations in the collectors' efficiencies and it is achieved by the incorporation of the custom automatic calibration system, also described in this work.

References

1. Donahue NM, Kroll JH, Pandis SN, Robinson AL. A two-dimensional volatility basis set – Part 2: Diagnostics of organic-aerosol evolution. *Atmos. Chem. and Phys*. 2012;12(2):615-634.

2. Robinson AL, Donahue NM, Shrivastava MK, et al. Rethinking Organic Aerosols: Semivolatile Emissions and Photochemical Aging. *Science*. 2007;315(5816):1259-1262.

3. Cross ES, Hunter JF, Carrasquillo AJ, et al. Online measurements of the emissions of intermediate-volatility and semi-volatile organic compounds from aircraft. *Atmospheric Chemistry and Physics*. 2013;13(15):7845-7858.

4. Hatch LE, Rivas-Ubach A, Jen CN, Lipton M, Goldstein AH, Barsanti KC. Measurements of I/SVOCs in biomass-burning smoke using solid-phase extraction disks and two-dimensional gas chromatography. *Atmospheric Chemistry and Physics*. 2018;18(24):17801-17817.

5. Drozd GT, Zhao Y, Saliba G, et al. Detailed Speciation of Intermediate Volatility and Semivolatile Organic Compound Emissions from Gasoline Vehicles: Effects of Cold-Starts and Implications for Secondary Organic Aerosol Formation. *Environmental Science & Technology*. 2019;53(3):1706-1714.

6. Chen T, Zhang P, Chu B, et al. Secondary organic aerosol formation from mixed volatile organic compounds: Effect of RO2 chemistry and precursor concentration. *npj Climate and Atmospheric Science*. 2022;5(1).

7. Shrivastava M, Cappa CD, Fan J, et al. Recent advances in understanding secondary organic aerosol: Implications for global climate forcing. *Reviews of Geophysics*. 2017;55(2).

8. Williams BJ, Goldstein AH, Kreisberg NM, Hering SV. In situ measurements of gas/particle-phase transitions for atmospheric semivolatile organic compounds. *Proceedings of the National Academy of Sciences of the United States of America*. 2010;107(15):6676-6681.

9. Fortenberry C, Walker M, Dang A, et al. Analysis of indoor particles and gases and their evolution with natural ventilation. *Indoor Air*. 2019;29(5):761-779.

10. Kristensen K, Lunderberg DM, Liu Y, et al. Gas–Particle Partitioning of Semivolatile Organic Compounds in a Residence: Influence of Particles from Candles, Cooking, and Outdoors. *Environmental Science & Technology*. 2023;57(8):3260-3269.

11. Liang Y, Wernis RA, Kristensen K, et al. Gas–particle partitioning of semivolatile organic compounds when wildfire smoke comes to town. *Atmospheric Chemistry and Physics*. 2023;23(19):12441-12454.

12. Liu H, Man H, Cui H, et al. An updated emission inventory of vehicular VOCs and IVOCs in China. *Atmospheric Chemistry and Physics*. 2017;17(20):12709-12724.

13. Wu L, Wang X, Lu S, Shao M, Ling Z. Emission inventory of semi-volatile and intermediate-volatility organic compounds and their effects on secondary organic aerosol over the Pearl River Delta region. *Atmospheric Chemistry and Physics*. 2019;19(12):8141-8161.

14. Chang X, Zhao B, Zheng H, et al. Full-volatility emission framework corrects missing and underestimated secondary organic aerosol sources. *One Earth*. 2022;5(4):403-412.

15. Stella, Pandis SN. Contribution of intermediate-volatility organic compounds from on-road transport to secondary organic aerosol levels in Europe. *Atmospheric Chemistry and Physics*. 2024;24(2):891-909.

16. An J, Huang C, Huang D, et al. Sources of organic aerosols in eastern China: a modeling study with high-resolution intermediate-volatility and semivolatile organic compound emissions. *Atmospheric Chemistry and Physics*. 2023;23(1):323-344.

17. Lucattini L, Poma G, Covaci A, de Boer J, Lamoree MH, Leonards PEG. A review of semi-volatile organic compounds (SVOCs) in the indoor environment: occurrence in consumer products, indoor air and dust. *Chemosphere*. 2018;201:466-482.

18. Weschler CJ, Nazaroff WW. Semivolatile organic compounds in indoor environments. *Atmospheric Environment*. 2008;42(40):9018-9040.

19. Sonne C, Xia C, Dadvand P, Targino AC, Lam SS. Indoor volatile and semi-volatile organic toxic compounds: Need for global action. *Journal of Building Engineering*. 2022;62.

20. Salthammer T, Zhang Y, Mo J, Koch HM, Weschler CJ. Assessing Human Exposure to Organic Pollutants in the Indoor Environment. *Angewandte Chemie Int. Ed.* 2018;57(38).

21. Garrido JA, Parthasarathy S, Moschet C, Young TM, McKone TE, Bennett DH. Exposure Assessment For Air-To-Skin Uptake of Semivolatile Organic Compounds (SVOCs) Indoors. *Environmental Science & Technology*. 2018;53(3):1608-1616.

22. Williams BJ, Goldstein AH, Kreisberg NM, Hering SV. An In-Situ Instrument for Speciated Organic Composition of Atmospheric Aerosols: Thermal DesorptionAerosol GC/MS-FID (TAG). *Aerosol Science and Technology*. 2006;40(8):627-638.

23. Kreisberg NM, Hering SV, Williams BJ, Worton DR, Goldstein AH. Quantification of Hourly Speciated Organic Compounds in Atmospheric Aerosols, Measured by an In-Situ Thermal Desorption Aerosol Gas Chromatograph (TAG). *Aerosol Sci. and Technology*. 2009;43(1):38-52.

24. Zhao Y, Kreisberg NM, Worton DR, Teng AP, Hering SV, Goldstein AH. Development of an *In Situ* Thermal Desorption Gas Chromatography Instrument for Quantifying Atmospheric Semi-Volatile Organic Compounds. *Aerosol Science and Technology*. 2012;47(3):258-266.

25. Zhao Y, Kreisberg NM, Worton DR, et al. Insights into Secondary Organic Aerosol Formation Mechanisms from Measured Gas/Particle Partitioning of Specific Organic Tracer Compounds. *Environmental Science & Technology*. 2013;47(8):3781-3787.

26. Isaacman-VanWertz G, Kreisberg NM, Yee LD, et al. Online derivatization for hourly measurements of gas- and particle-phase semi-volatile oxygenated organic compounds by thermal desorption aerosol gas chromatography (SV-TAG). *Atm. Meas. Techn.*. 2014;7(12):4417-4429.

27. Isaacman G, Kreisberg NM, Worton DR, Hering SV, Goldstein AH. A versatile and reproducible automatic injection system for liquid standard introduction: application to in-situ calibration. *Atmospheric Measurement Techniques*. 2011;4(9):1937-1942.

28. Vera T, Villanueva F, Lenka Wimmerova, Tolis EI. An overview of methodologies for the determination of volatile organic compounds in indoor air. *Applied Spectroscopy Reviews*. 2022;57(8):625-674.

29. Rothweiler H, Wäger PA, Schlatter C. Comparison of Tenax Ta and Carbotrap for sampling and analysis of volatile organic compounds in air. *Atmospheric Environment Part B Urban Atmosphere*. 1991;25(2):231-235.

30. Batterman S, Metts T, Kalliokoski P, Barnett E. Low-flow active and passive sampling of VOCs using thermal desorption tubes: theory and application at an offset printing facility. *Journal of Environmental Monitoring*. 2002;4(3):361-370.

31. Marcillo A, Viktorija Jakimovska, Widdig A, Birkemeyer C. Comparison of two common adsorption materials for thermal desorption gas chromatography – mass spectrometry of biogenic volatile organic compounds. *Journal of Chromatography A*. 2017;1514:16-28.

32. Jia C, Fu X, Nored A, Namuun Batbaatar, Smith L. Comparison of generic Tenax and specialized PAH tubes for monitoring polycyclic aromatic hydrocarbons in the ambient air. *Atmospheric Pollution Research*. 2023;14(6):101780-101780.

33. ISO 16017-1:2000. Indoor, ambient and workplace air – Sampling and analysis of volatile organic compounds by sorbent tube/thermal desorption/capillary gas chromatography Part 1.

34. ISO 16017-2:2003. Indoor, ambient and workplace air – Sampling and analysis of volatile organic compounds by sorbent tube/thermal desorption/capillary gas chromatography Part 2.

35. Woolfenden, E. A.; McClenny, W. A. Compedium Method TO-17: Determination of Volatile Organic Compounds in Ambient Air using active sampling onto sorbent tubes. Environmental protection agency EPA/625/R-96/010b, US EPA, January 1999.

36. Neher MB, Jones PW. In situ decomposition product isolated from Tenax GC while sampling stack gases. *Analytical Chemistry*. 1977;49(3):512-513.

37. Hanson RL, Clark CR, Carpenter RL, Hobbs CH. Evaluation of Tenax-GC and XAD-2 as polymer adsorbents for sampling fossil fuel combustion products containing nitrogen oxides. *Environmental Science & Technology*. 1981;15(6):701-705.

38. Pellizzari E, Demian B, Krost K. Sampling of organic compounds in the presence of reactive inorganic gases with Tenax GC. *Analytical Chemistry*. 1984;56(4):793-798.

39. Cao XL, Hewitt C. Study of the Degradation by Ozone of Adsorbents and of Hydrocarbons Adsorbed during the Passive Sampling of Air. *Environmental Science & Technology*. 1994;28(5):757-762.

40. Per Axel Clausen, Wolkoff P. Degradation products of Tenax TA formed during sampling and thermal desorption analysis: Indicators of reactive species indoors. *Atmospheric Environment*. 1997;31(5):715-725.

41. Klenø JG, Wolkoff P, Per Axel Clausen, Wilkins CK, Pedersen T. Degradation of the Adsorbent Tenax TA by Nitrogen Oxides, Ozone, Hydrogen Peroxide, OH Radical, and Limonene Oxidation Products. *Environmental Science & Technology*. 2002;36(19):4121-4126.

42. Lee JH, Batterman S, Jia C, Chernyak SM. Ozone Artifacts and Carbonyl Measurements Using Tenax GR, Tenax TA, Carbopack B, and Carbopack X Adsorbents. *Journal of the Air & Waste Management Association*. 2006;56(11):1503-1517.

43. Dang AJ, Kreisberg NM, Cargill TL, et al. Development of a Multichannel Organics In situ enviRonmental Analyzer (MOIRA) for mobile measurements of volatile organic compounds. EGUsphere [preprint]. Published online August 31, 2023.

44. Simpson WR, Mao J, Fochesatto GJ, et al. Overview of the Alaskan Layered Pollution And Chemical Analysis (ALPACA) Field Experiment. *ACS ES&T Air*. 2024;1(3).

45. Zhang Y, Williams BJ, Goldstein AH, Docherty K, Ulbrich IM, Jimenez JL. A Technique for Rapid Gas Chromatography Analysis Applied to Ambient Organic Aerosol Measurements from the Thermal Desorption Aerosol Gas Chromatograph (TAG). *Aerosol Science and Technology*. 2014;48(11):1166-1182.

46. Zhang Y, Williams BJ, Goldstein AH, Docherty KS, Jimenez JL. A technique for rapid source apportionment applied to ambient organic aerosol measurements from a thermal desorption aerosol gas chromatograph (TAG). *Atmospheric Measurement Techniques*. 2016;9(11):5637-5653.

47. Kelly WR, Hotes SA. Importance of Chemical Blanks and Chemical Yields in Accurate Trace Chemical Analysis. *Journal of Research of the National Bureau of Standards*. 1988;93(3):228-232.

48. *Blanks in Method Validation Supplement to Eurachem Guide the Fitness for Purpose of Analytical Methods*. First Edition, 2019.

49. Lavrich RJ, Hays MD. Validation Studies of Thermal Extraction-GC/MS Applied to Source Emissions Aerosols. 1. Semivolatile Analyte−Nonvolatile Matrix Interactions. *Analytical Chemistry*. 2007;79(10):3635-3645.

50. Magnusson B, Örnemark U, eds. *The Fitness for Purpose of Analytical Methods: A Laboratory Guide to Method Validation and Related Topics*. Second Edition, 2014.

51. GrossJH. *Mass Spectrometry : A Textbook*. Springer; 2017.

52. Satyro M, Yaws CL. *The Yaws Handbook of Thermodynamic Properties for Hydrocarbons and Chemicals*. Gulf Professional Publishing; 2018.

53. Witkowski A, Stec AA, Richard HT. Thermal decomposition of polymeric materials. In: Hurley MJ, Gottuk D, Hall JR, et al., eds. Springer New York; 2016:167-254.

54. Buch A, Imène Belmahdi, Szopa C, et al. Role of the Tenax® Adsorbent in the Interpretation of the EGA and GC-MS Analyses Performed With the Sample Analysis at Mars in Gale Crater. *Journal of Geophysical Research: Planets*. 2019;124(11):2819-2851.

55. Whaley CH, Law KS, Jens Liengaard Hjorth, et al. Arctic tropospheric ozone: assessment of current knowledge and model performance. *Atmospheric Chemistry and Physics*. 2023;23(1):637-661.

56. Cesler-Maloney M, Simpson WR, Miles T, Mao J, Law KS, Roberts TJ. Differences in Ozone and Particulate Matter Between Ground Level and 20 m Aloft are Frequent During Wintertime Surface-Based Temperature Inversions in Fairbanks, Alaska. *Journal of Geophysical Research: Atmospheres*. 2022;127(10).

57. Nazaroff WW, Weschler CJ. Indoor ozone: Concentrations and influencing factors. *Indoor Air*. Published online October 5, 2021.

58. Helmig D. Ozone removal techniques in the sampling of atmospheric volatile organic trace gases. *Atmospheric Environment*. 1997;31(21):3635-3651.

CHAPTER 4

Investigation of Gas-Particle Phase Partitioning of Speciated Organic Compounds during the Alaskan Layered Pollution And Chemical Analysis (ALPACA) Field Campaign

Abstract

This chapter discusses the dynamics of phase partitioning of atmospheric organic compounds under sustained cold and dark conditions during the Alaskan Layered Pollution And Chemical Analysis (ALPACA) field campaign that took place in Fairbanks, Alaska in the winter of 2022. According to previous studies, there is an accumulation of fine particulate matter in the Arctic during wintertime and early spring due to longer temperature inversions that trap pollutants in the lower atmosphere. However, the understanding of atmospheric transformations of these pollutants is poor and so is the extent of human exposure in this unique environment. Indoor and outdoor gas and particle concentrations were measured using the custom-developed Semi-Volatile Thermal Desorption Aerosol Gas Chromatograph (SV-TAG) and observed particle phase fractions were compared against the absorptive partitioning theory, commonly used to describe gas-particle phase transfer dynamics in atmospheric models. It was recognized that the shift in compounds' vapor pressures, due to the extremely low wintertime temperatures, effectively drove gas-to-particle partitioning. However, measurements did not satisfactorily agree with the modeled results. It was found that temperature-induced shifts in both particle volatility and viscosity influenced the evaporation and condensation behavior of atmospheric organic aerosol particles and the assumption of instantaneous reversible equilibrium used to predict phase partitioning dynamics is not suitable to describe this process under cold and dark conditions, and consequently to accurately address the impact of Arctic air pollution on both climate and human health.

4.1. Introduction

Wintertime in Arctic cities is characterized by larger air pollutant emissions since the extremely low temperatures incite intensive domestic heating and power generation, and contribute to the poor operational efficiency of mobile sources.[1] The reduced solar radiation limits atmospheric photochemical activity and promotes the persistence of surface-based temperature inversions, which trap high concentrations of particulate matter (PM) in the lower troposphere due to the increase in the atmosphere stability, and the decrease in vertical mixing.[2] Indeed, the Alaskan city of Fairbanks is one of the most polluted cities in the United States, classified by the US Environmental Protection Agency as a nonattainment area, regularly exceeding the 24h national standard for fine particulate matter concentration ($PM_{2.5}$, < 2.5 μm in diameter) of 35 $\mu g.m^{-3}$.[3]

The high levels of pollution lead to concerns about the health effects of poor air quality on the Arctic population. During wintertime, residents spend most of their time indoors,[4] therefore, human exposure to air pollution during this season reflects the extent of infiltration, indoor pollution sources, and the chemical and physical transformations associated with outdoor-indoor transport. However, the lack of chemically detailed observations of wintertime air pollution in the Arctic has limited the understanding of the fundamental process driving this problem and its impact on the local communities.[1,5]

For instance, organic compounds, which comprise a significant portion of atmospheric particulate matter[6] are found in both the gaseous and particulate forms and they can partition between these two phases driven by changes in ambient conditions such as temperature and total PM concentration.[7] However, the dynamics and reversibility of this process under cold and dark conditions are not fully understood as well as the extent of particle-to-gas partitioning upon warming during outdoor-indoor transport in high-latitude residences. Among these and other

relevant Arctic wintertime pollution-related inquiries, the Alaskan Layered Pollution And Chemical Analysis (ALPACA) field campaign was deployed in the winter of 2022 to improve understanding of pollution sources and chemical processes under these unique conditions.[8]

The reduced photochemical activity and the low ambient temperatures directly affect the dynamics of organic aerosols (OA) gas-particle partitioning due to their impact on both volatility distribution and particle viscosity. While the vapor pressures of the aerosols' constituents will determine their affinity to the gaseous or particulate phases,[7] the inverse correlation between viscosity and bulk diffusivity of organic molecules will influence the equilibration timescales of multiphase transport.[9,10] Model simulations demonstrated that for less-viscous aerosols, the gas-particle equilibration timescale is limited by the compounds' volatilities, however for partitioning involving highly viscous particles, phase transfer is also affected by bulk diffusivity.[11] This kinetically limited evaporation and growth is responsible for the formation of heterogeneously mixed particles due to the establishment of local equilibrium between the gas phase and the near-surface particle bulk,[9,11-13] which was found to further suppress evaporation ensuring efficient long-range transport in the atmosphere of molecules trapped inside the OA matrix.[14,15]

The volatility of atmospheric OA is expected to decrease with increasing oxidation levels.[16] The viscosity's dependence on the chemical compound's identity mirrors that of the vapor pressure, i.e. an increase in oxidation levels corresponds to an increase in viscosity.[17] Thus, solely considering the minimal photooxidation chemistry during wintertime in Arctic regions, atmospheric OA should demonstrate low viscosity and higher volatilities. However, a decrease in temperature shifts both particle volatility distribution and viscosity to the opposite extreme.[11] Indeed, aerosol growth and yields are more considerable at lower temperatures due to the enhanced condensation of organic species classified as semi-volatile under ambient conditions,[18] while

evaporation is hindered as a consequence of both the decrease in vapor pressure and the slowing of diffusional molecular motion in highly viscous cold particles.[19]

This work, therefore, focuses on the investigation of the multiphase transport of speciated organic compounds during the ALPACA campaign to better understand the interplay of volatility distribution and particle viscosity governing the dynamics of gas-particle partitioning under cold and dark conditions, and the extent of this process upon infiltration. The Semi-Volatile Thermal Desorption Aerosol Gas Chromatograph (SV-TAG) provided hourly measurements of outdoor and indoor OA gas and particle concentrations. Aided by supporting measurements, particle phase fraction observations were compared against the absorptive partitioning theory to address the suitability of the assumption of quasi-equilibrium evaporation and growth to predict wintertime OA fate in Arctic regions.

4.2. Materials and Methods

4.2.1. ALPACA Overview and Field Description

Study goals and design are discussed in detail in an overview manuscript.[8] In brief, the ALPACA campaign was structured to improve understanding of outdoor and indoor air pollution in cold climates during low-photochemical activity, in collaboration with the local community to assist in the sustainable development of the Arctic and promote better air quality for its residents. The field campaign took place in Fairbanks, Alaska from January 17th through February 25th, 2022, and a suite of instruments was deployed across five different sites to obtain meteorological, snow composition, particle, and gas measurements.

Indoor and outdoor sampling was conducted in a single-story house located in the residential Shannon Park neighborhood (64.850°N, 147.676°W) 1 m above and 2.6 km ENE from

the University of Alaska Fairbanks Community and Technical College (CTC) downtown site. Given the absence of primary roads in the neighborhood, a more residential pollution profile is expected in the area. The house had a footprint of 1549 ft^2 and an attached garage of 531 ft^2 where most of the instruments were kept, including the SV-TAG. **Figure A4.1** (Appendix A4 – Section A4.1) shows the geographical location of the house site and a 3-D model of the home, including key indoor sources and inlet locations. The door between the garage and the house was replaced and sealed to separate the house from the instruments.

During the campaign, the house was heated by a hot-air furnace system with continuous air recirculation to keep indoor air well mixed. The house was also tested for air tightness and thermal resistance by an energy audit from the National Renewable Energy Laboratory's Alaska Campus which determined a leakage of 2.6 air exchanges per hour at a 50 Pa pressure difference prior to the campaign, and a leakage of 2.8 under the same test conditions after all instruments were fully operational. The house was unoccupied throughout the study except when indoor experimental perturbations were performed. These experiments included pellet stove emissions, cooking activities, and incense burning. However, in this work, phase partitioning analysis is limited to measurements obtained during unoccupied periods.

4.2.2. Instrumentation and Sampling Strategy

A complete list of the instruments deployed at the house site during the 2022 ALPACA field study can be found in the overview paper.[8] Here, focus will be given to instruments that provided measurements considered for the investigation of gas-particle partitioning during the campaign, i.e. the SV-TAG system (custom-built), the High-Resolution Time-of-Flight Aerosol Mass Spectrometer (HR-ToF-AMS, Aerodyne, Inc., Billerica, MA), and the Aethalometer®

(AE33, Magee Scientific, Berkeley, CA) that were installed in the garage; and two MODULAIR-PM air quality sensors (QuantAQ, Somerville, MA), one kept indoors and the other, outdoors.

A detailed description of the SV-TAG system can be found in **Chapter 3**. Succinctly, the instrument comprises two identical dual-stage collection cells arranged in parallel for simultaneous gas and particle sampling. In series thermal desorption and subsequent gas chromatography-mass spectrometry (GC/MS) allows for the *in situ* analysis of the collected material. While one cell collects a non-denuded sample (gases plus particles), the other cell collects a denuded one (particles only). Automatic actuated two 3-way ball valves are installed upstream of the collectors permitting their roles to be swapped to avoid cell-to-cell bias. For the ALPACA campaign, two 40 cm long (30 mm OD) 500-channel activated carbon denuders (ADI-DEN2, Aerosol Dynamics Inc., Berkeley, CA) were used to remove gas phase species. These devices were designed for the effective removal of SVOCs with minimal particle losses (<5%) at ambient concentration levels.[20]

During the campaign, two separate inlet lines were used to alternate between indoor and outdoor sampling. A schematic and detailed description of the SV-TAG inlet system is found in Appendix A4 (Section A4.2 – **Figure A4.2**). In brief, extensive care was taken to maintain thermodynamic equilibrium before gas phase removal, a crucial aspect to ensure the accuracy of gas-particle partitioning measurements. The indoor denuder was insulated with foam to avoid thermal losses due to temperature gradients in the garage, while the outdoor denuder was kept in an insulated box maintained at ambient temperatures by air-circulation of outdoor air. Gas and particle losses were minimized by conditioning the sample lines in between collections with a continuous flow of air of the next sample.

The SV-TAG sampled with cyclones installed on each sample line that provided a particle cutoff (d_{p50}) of approximately 1.0 μm under typical flow rates of 16.7 $L.min^{-1}$. Each cell collected

at 8.3 L.min^{-1} which kept the total residence time of the sample in the denuder low (~ 2 seconds), minimizing negative artifacts from denuder sampling (i.e. removal of particle phase compounds from volatilization in the denuder due to the removal of the gas phase). Default collection times were 10 minutes indoors – 10 minutes outdoors which allowed hourly sampling between the two environments. However, depending on ambient conditions (i.e. cleaner outdoor periods) collection times were increased, sacrificing time resolution. Internal standards were injected in both cells immediately after each collection using the custom AutoInject system (see details in **Chapter 3**) to enable data correction due to run-to-run variability, further discussed in **Section 4.2.3.** After collection, each cell was thermally desorbed in series in a two-step process. Subsequent chromatographic analysis was performed in an Agilent 6890A GC by ramping the non-polar column (RTX-5Sil MS 20 m long, 0.18 mm ID, 0.18 μm film thickness) at a rate of 22.50^{o}C.min^{-1} from 50^{o}C to 315^{o}C (hold 3 min.); while a 70eV quadrupole mass spectrometer (Agilent G1098, 5973N MSD) provided mass spectral detection. **Figure 4.1** shows outdoor and indoor example chromatograms obtained from 10-minute collections during the campaign.

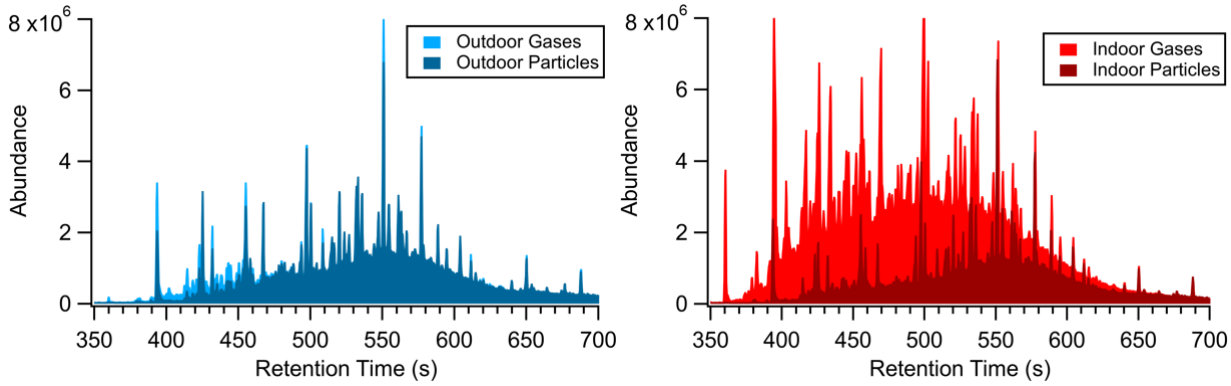

Figure 4.1. Outdoor (left) and indoor (right) 10-minute collection SV-TAG example chromatograms obtained during the ALPACA campaign. Darker colors represent denuded (particle-only) samples while lighter colors show gas phase measurements (non-denuded minus denuded). Note the magnitude of gaseous species indoors while organics outdoors are primarily found in the condensed phase.

While the SV-TAG provided speciated gas and particle OA information enabling direct phase partitioning estimation, the measurements obtained with the remainder of the instruments listed above were used as model inputs for comparison between observations and thermodynamic equilibrium predictions. The AMS operated in V-mode measuring non-refractory PM bulk composition for particles with aerodynamic diameter values between 50-1000 nm,[21] while the Aethalometer® provided real-time black carbon concentrations by measuring aerosol light absorption at seven wavelengths spanning the near ultraviolet to near-infrared spectrum (370 – 1050 nm). Both instruments used a separated fast-switching automated inlet system allowing 10-minute indoor/10-minute outdoor sampling cycles acquiring data at 1Hz. Indoor and outdoor temperature and relative humidity data were retrieved from the air quality sensors.

4.2.3. Data Processing and Speciated Gas and Particle Quantification

Focus on the SV-TAG data processing and quantification will be given since the AMS calibration procedure and quantification analysis are provided elsewhere.[21] Compound identification was achieved by searching with the National Institute for Standards and Technology (NIST) Mass Spectral Search Program (Demo Version 2.0f) and peak integration was performed on single ion using the TAG ExploreR and iNtegration (TERN) software[22] written in Igor Pro (Wavemetrics, Inc, Lake Oswego, OR). Identification quality was determined based on the following criteria: A) the compound was positively identified using standard injections; B) the compound was identified with a match quality above 75%.

After integration, raw MS signals were time-dependent-corrected for within-cell variability caused by detector drifts and fluctuations in desorption-transfer efficiency throughout the campaign as described by Kreisberg et al[23] and detailed in Appendix A4 (**Section A4.2**). Cell-

dependent polar and non-polar de-trending correction factors were also applied to external standard injection signals to generate multi-point mass calibration curves (1 - 25 ng). Corrected MS sample signals (peak areas) were then converted to mass concentration by dividing the calculated mass by the collection volume. Compounds present in the external standards were directly quantified while compounds not included in the standard mixture were quantified by MS signal retention time-dependent interpolation or by surrogate compounds. Compounds were selected to represent the major sources of pollution in the neighborhood. The full list of compounds considered in this work along with relevant quantification information is found in **Table A4.2** (Appendix A4 – Section A4.2). **Table A4.3**, in the same section, shows their average gas and particle, indoor and outdoor concentrations during the campaign.

4.2.4. Phase Partitioning Estimations

Phase partitioning observations are placed in the context of F_p values which represent the time-dependent particle phase fraction of each compound of interest throughout the campaign calculated from their quantified denuded and non-denuded SV-TAG measurements (Equation 4.1).

$$F_{p,i} = \frac{P_i(t)}{P_i(t)+G_i(t)} \quad \textbf{(4.1)}$$

Where $F_{p,i}$ is the particle phase fraction of compound i at a given time t; P_i is the concentration of compound i in the particulate phase at time t; and G_i is the concentration of compound i in the gaseous phase at the same time t. Field observations are compared against the thermodynamic equilibrium absorptive partitioning theory,[24] commonly used to describe OA gas-particle phase transfer in chemical transport models.[25] The absorptive phase partitioning constant, used to characterize the position of equilibrium, is given by Equation 4.2 and it is related to the fraction of particle-phase space using Equation 4.3.

$$K_{p,i} = \frac{f_{om} 760 RT}{MW_{om} \zeta_i p^o_{L,i} 10^6} \quad \textbf{(4.2)} \qquad F_{p,i} = \frac{K_{p,i} PM}{K_{p,i} PM + 1} \quad \textbf{(4.3)}$$

Where $K_{p,i}$ $(m^3.\mu g^{-1})$ is the speciated gas-particle partitioning constant; f_{om} is the fraction of the total aerosol mass that is organic matter; R ($8.2 \times 10^{-5}\ m^3.atm.mol^{-1}.K^{-1}$) is the ideal gas constant; T (K) is the temperature of interest; MW_{om} $(g.mol^{-1})$ is the average molecular weight that is organic matter in the aerosol; ζ_i is the activity coefficient of compound i in the organic aerosol mixture; $p^o_{L,i}$ $(Torr)$ is the liquid (or sub-cooled) vapor pressure of compound i at temperature T; 760 is a pressure conversion factor; 10^6 is a mass conversion factor; and PM $(\mu g.m^{-3})$ is the total ambient particulate matter concentration.

In this work, F_p values at PM_1 are evaluated since they reflect the aerosol composition measured by the AMS and the SV-TAG. Thus, PM values were calculated by summing all AMS species (i.e. organics, sulfate, nitrate, ammonium, and chloride) plus black carbon measured by the Aethalometer®. f_{om} is determined by dividing the AMS organics by the total PM_1 concentrations. The average OA molecular weight was determined by averaging the molecular weight of approximately 200 species identified by the SV-TAG ($MW_{om} = 236.95\ g.mol^{-1}$). The activity coefficient used to describe non-idealities between compound i and the aerosol mixture is evaluated at three different values (i.e. $\zeta_i = 0.1; 1; 10$).

Compounds' vapor pressures are traditionally estimated using thermodynamic empirical equations, such as the famous Antoine equation. For best $K_{p,i}$ accuracy, vapor pressures should be calculated at every temperature of interest. However, $p^o_{L,i}$ parametrization parameters are not widely available for temperatures below the melting (or freezing) point of a compound. The melting points of the compounds here considered for phase partitioning analysis are above the average outdoor temperature during the campaign (253.15 K), thus making it difficult to directly

estimate $p_{L,i}^{o}$ at these extremely low temperatures. Therefore, the following approach was considered. Vapor pressures were calculated at a chosen reference temperature using a parametrization equation from the Design Institute for Physical Property Research/AIChE (DIPPR®) project 801 database,[26] and extrapolated to the temperature of interest using the Clausius-Clapeyron relationship:

$$ln\frac{p_{L,i}^{o}(T)}{p_{L,i}^{o}(T_{ref})} = -\frac{\Delta H_{vap,i}(T_{ref})}{R}\left(\frac{1}{T} - \frac{1}{T_{ref}}\right) \quad \textbf{(4.4)}$$

Where $p_{L,i}^{o}(T)$ is the vapor pressure in Torr of compound i at the temperature of interest T (K); $p_{L,i}^{o}(T_{ref})$ is the calculated vapor pressure in Torr of compound i at the chosen reference temperature T_{ref} (K); R $(8.314\, J.mol^{-1}.K^{-1})$ is the ideal gas constant; and $\Delta H_{vap,i}(T_{ref})$ $(J.mol^{-1})$ is the speciated enthalpy of vaporization at the reference temperature.

Equation 4.4 assumes that the enthalpy of vaporization of compound i is independent of temperature between T and T_{ref}, this assumption only holds for values of T_{ref} close to T. In order to minimize errors associated with this pressure conversion, the choice of reference temperature was such that, if:

$$\bar{T} < T_{m,i} \;\rightarrow\; T_{ref,i} = T_{m,i} \text{ or}$$

$$\text{If } \bar{T} > T_{m,i} \;\rightarrow\; T_{ref,i} = \bar{T}$$

Where, $\bar{T}$ is the average indoor or outdoor temperature; $T_{m,i}$ is the melting point of compound i; and $T_{ref,i}$ is the reference temperature choice for compound i. The model sensitivity to the choice of reference temperature is evaluated in **Section 4.3.1.** Enthalpies of vaporization were calculated at the chosen reference temperature using a parametrization equation from the DIPPR® project 801 database.[26] Relevant thermodynamic properties, parameterization equations, and model input parameters are found in Appendix A4 (**Section A4.3**).

4.3. Results and Discussion

4.3.1. Model Sensitivity Analysis and Results

Model Sensitivity

As discussed above, the choice of the temperature of reference affects the vapor pressure estimations used for phase partitioning calculations, therefore, to investigate the impact of this parameter in the absorptive partitioning model, $F_{p,i}$ values were calculated for all the compounds considered in this work using varying values of initial temperatures for vapor pressure estimations, i.e.: $T_o = T_{ref,i}$; $T_o = T_{ref,i} + 50K$; $T_o = T_{ref,i} + 100K$; $T_o = T_{ref,i} + 150K$. Where $T_{ref,i}$ is the default reference temperature of compound i, chosen by the methodology described in **Section 4.2.4** and listed in **Tables A4.7 – A4.9** (Appendix A4 – Section A4.3). Increasing temperatures are used for this analysis because the procedure considered to determine $T_{ref,i}$ yields the minimum temperature (at which vapor pressure thermodynamic parameters are available) that decreases the difference between $T_{ref,i}$ and $\bar{T}$ ambient, ensuring the correct application of the Clausius-Clapeyron equation.

Figures 4.2A and **4.2B** show the outdoor and indoor average modeled $F_{p,i}$ values for a series of alkanes calculated using $T_{ref,i}$ and increasing reference temperatures for the ideal mixture scenario, i.e. $\zeta_i = 1$. It is observed that the particle phase fraction of each compound decreases as the choice of reference temperature increases. To understand this trend, Equation 4.4 is re-written:

$$p_{L,i}^{o}(T) = p_{L,i}^{o}(T_{ref}) \times \exp\left[\frac{\Delta H_{vap,i(T_{ref})}}{R} \times \left(\frac{1}{T_{ref}} - \frac{1}{T}\right)\right] \quad \textbf{(4.5)}$$

Note that the enthalpy of vaporization acts as a correction factor for the vapor pressure calculated at a given reference temperature. While, vapor pressure increases with increasing temperatures, enthalpies of vaporization decrease with increasing temperatures since less energy is required to

undergo the phase change from a hotter liquid to the gas phase. Therefore, when adopting a higher reference temperature, the small value of the enthalpy of vaporization will not be sufficient to correct the high vapor pressure calculated and accurately estimate this property at lower temperatures. Thus, the Clausius-Clapeyron-extrapolated $p^{o}_{L,i}(T)$ will be greater than expected at the desired ambient temperature. Higher $p^{o}_{L,i}(T)$ yields lower $F_{p,i}$ since the compounds' affinity to the gas phase increases with increasing vapor pressures, justifying the trend observed.

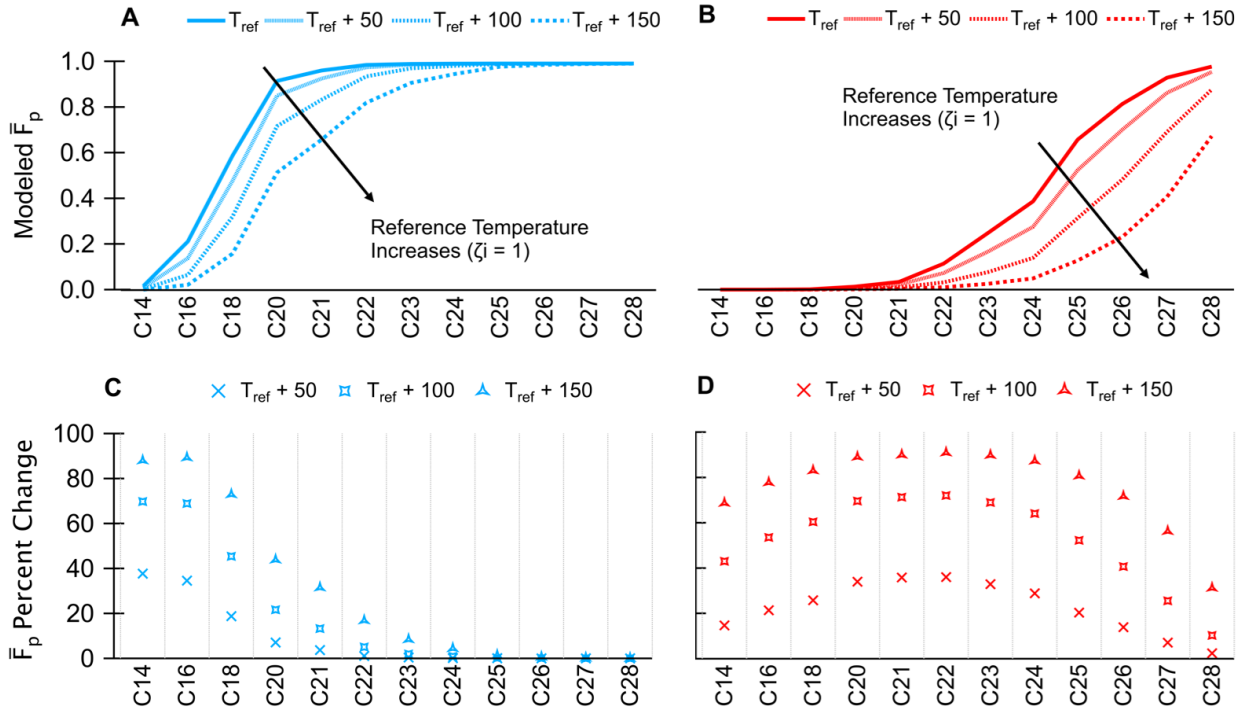

Figure 4.2. Absorptive partitioning model sensitivity analysis concerning the choice of the reference temperature (T_{ref}) used for the estimation of thermodynamic parameters (i.e. vapor pressures and enthalpies of vaporization). **(A)-(B)** Outdoor and indoor (respectively) average particle phase fractions calculated for the alkane series assuming unity-value for the activity coefficient for varying values of T_{ref}. **(C)-(D)** Outdoor and indoor (respectively) absolute percent change between speciated average particle phase fractions calculated using the default reference temperature and increasing T_{ref}.

Figures 4.2C and **4.2D** show the absolute percent change between the average $F_{p,i}$ values calculated using $T_{ref,i}$ and increasing reference temperatures for both indoor and outdoor

conditions assuming $\zeta_i = 1$. These plots represent the absolute percent error when using large ranges of $T_{ref,i}$ - $\bar{T}$ ambient. For the outdoor results, it is observed that this error tends to decrease with increasing compounds' carbon number. This is expected because, although the vapor pressure correction factor decreases with increasing $T_{ref,i}$, the intrinsic lower volatilities of larger compounds yield sufficiently low $p^o_{L,i}$, contributing to larger particle-bound estimation even at those higher reference temperatures. In other words, under outdoor conditions, the accuracy-dependency of the vapor pressure estimation on the correction factor decreases as the compounds' boiling point increases.

Indoors, the same trend is observed from docosane (C22) and beyond due to the same rationalization above. From C14 to C20, the percent error tends to increase with increasing carbon number, and it can also be justified by the accuracy-dependency of the vapor pressure estimation on the correction factor. However, in this latter case, compounds of lower carbon number have sufficiently high $p^o_{L,i}$ that vapor pressure overcorrection due to higher enthalpy values can be neglected, but it becomes more significant as the compounds' boiling point increases since lower $p^o_{L,i}$ values are expected. Similar trends were observed for polycyclic aromatic hydrocarbons (PAHs) and biomass-burning related compounds (BBOA) of similar boiling points.

Model Results

Figure 4.3 summarizes modeled particle phase fraction values for selected alkanes under outdoor and indoor conditions during the ALPACA campaign. Additional alkanes, PAHs, and BBOA-related compounds plots can be found in Appendix A4 (**Section A4.3**). In both environments, particle-bound estimations tend to increase with decreasing the activity coefficient. This behavior is predicted by investigation of Equation 4.2 since ζ_i modifies $p^o_{L,i}$.

Figure 4.3. Modeled absorptive phase partitioning behavior for selected alkanes during the ALPACA campaign considering three different values for the activity coefficient. **(A)-(C)** Calculated particle phase fraction (F_p) values as a function of temperature at outdoor and indoor conditions, respectively. **(B)-(D)** Calculated F_p values as a function of particulate matter (PM) concentration at outdoor and indoor conditions, respectively.

Physically, small values of the activity coefficient translate into stronger interactions between compound i and the condensed aerosol mixture compared to intermolecular interactions involving only compound i (assuming Lewis/Randall reference state)[27] thus, yielding greater F_p values. The power of these interactions can be seen in the tetradecane and docosane outdoor predictions. While tetradecane is expected to be solely in the gas phase when assuming greater than unity values for the activity coefficient, a relevant amount of this species is found in the particle phase at low temperatures if $\zeta_i < 1$. On the other extreme, docosane only partitions to the gas phase at greater values of the activity coefficient.

Another mutual and foreseen F_p trend observed under both outdoor and indoor conditions is the increase of this value with decreasing temperatures and increasing PM concentrations that results from the decrease in compounds' vapor pressure and the increase in surface area available for condensation. However, the intrinsic F_p values observed for the same compound outdoors and indoors vary greatly. For instance, while octadecane is expected to partition dynamically under outdoor ambient conditions, the same compound completely transitions to the gas phase when found indoors. The outdoor trend is justified by the more polluted and colder conditions compared to the indoor environment, which enhances gas-to-particle phase partitioning.

To aid the visualization of the shift in compounds' volatilities with decreasing temperatures, the outdoor and indoor temperature-dependent calculated vapor pressures were converted to saturation mass concentrations using Equation 4.6:

$$C_i^o(T) = \frac{p_{L,i}^o(T) MW_i 10^6}{760RT} \quad \textbf{(4.6)}$$

Where $C_i^o(\mu g.m^{-3})$ is the saturation mass concentration of compound i at temperature T (K); $p_{L,i}^o$ $(Torr)$ is the liquid (or sub-cooled) vapor pressure of compound i at temperature T (K);

MW_i $(g.mol^{-1})$ is the molecular weight of compound i; R $(8.2 \times 10^{-5}\ m^3.atm.mol^{-1}.K^{-1})$ is the ideal gas constant; 760 is a pressure conversion factor; 10^6 is a mass conversion factor.

Each highlighted region in **Figure 4.4** represents a volatility class.[28] From high to low volatility: intermediate volatility organic compounds (IVOC), semi-volatile organic compounds (SVOC), low volatility organic compounds (LVOC), and extremely low volatility compounds. (E)LVOCs are predominately in the particle phase under standard conditions. SVOCs dynamically partition between gas and particle, while IVOCs reside almost exclusively in the gas phase. The left plot shows saturation concentrations calculated using the field's indoor conditions, while the right plot shows the same property under outdoor ambient conditions. Each compound shows a distribution of C^o values as a function of indoor and outdoor temperatures.

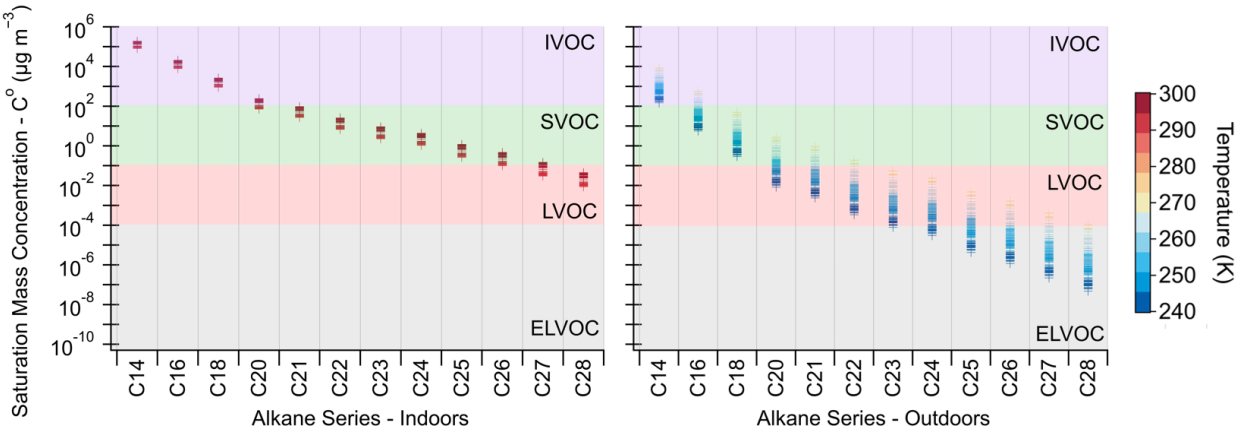

Figure 4.4. Alkanes volatility distribution under indoor (left) and outdoor (right) ambient conditions observed during the ALPACA campaign.

While the majority of these alkanes are in the I/SVOC range indoors, when exposed to low outdoor temperatures, they tend to behave as (E)LVOCs. When combining this dramatic decrease in volatility distribution, with the tropospheric-accumulated PM emissions in the Arctic, it is foreseen that these compounds are effectively driven to the particle phase outdoors. In the next sections, the extent of these two parameters in promoting gas-particle phase transfer is evaluated

using measured F_p values. The impact of these extreme wintertime conditions on the observed dynamics of gas-particle partitioning indoors, outdoors, and upon infiltration is also investigated.

4.3.2. Observed Phase Partitioning Dynamics

The timeseries of the measured outdoor particle phase fraction of the alkane series is shown as a heat map plot in **Figure 4.5.** The right axis corresponds to the temperature and PM concentrations throughout the campaign. Elevated particle-bound observations are represented by cooler colors, while the increase in the gas phase fraction can be recognized by the shift to warmer colors along the horizontal axis. The compounds are ordered from high to low volatility along the left axis, with tetradecane being the most volatile alkane considered. Similar heat map-timeseries plots highlighting the outdoor phase partitioning behavior of selected PAHs and BBOA-relevant compounds can be found in Appendix A4 (**Section A4.4**).

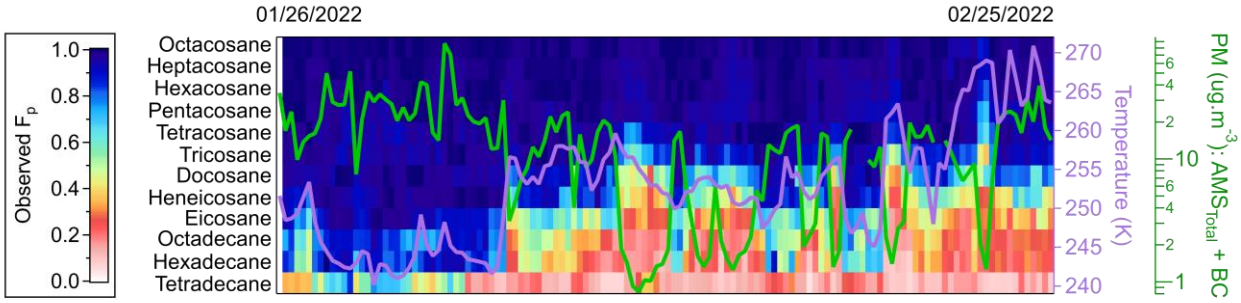

Figure 4.5. Timeseries of the observed outdoor particle phase fraction of selected alkanes throughout the ALPACA field campaign.

The impact of change in both temperature and PM concentration on the phase partitioning dynamics of the alkane series can be easily visualized in this plot. For instance, at the beginning of the campaign, when ambient temperatures were low and PM was accumulated in the lower troposphere, the bulk observed particle phase fraction was its highest, since the high volatility

compounds were effectively driven to the particle phase due to the shift in their vapor pressure by the decrease in ambient temperatures (**Figure 4.4**). The fluctuations in PM concentrations do not appear to strongly alter the particle phase fraction of these compounds, suggesting that during this cold period, temperature is the primary phase partitioning driver.

The higher and fairly constant temperatures in the middle of the campaign, demonstrate the effect of fluctuations in PM concentrations on the evaporation and condensation of these compounds. For example, the apparent particle-to-gas partitioning of heneicosane and docosane clearly correlates with abrupt decreases in PM mass during that period. The higher volatility compounds also show a decrease in particle-bound observation due to this reduction in surface area available for condensation. At the end of the campaign, when temperatures were the highest, a more dynamic behavior was perceived, driven by both temperature and PM changes.

While the above evaluation provides a qualitative understanding of how these two parameters regulate each individual compound particle and gas concentrations in the aerosol system, a quantitative analysis can be performed by investigating the linear relationship between changes in the observed F_p values and changes in both ambient temperature and PM concentration. Linear correlation analysis was performed for alkanes, PAHs, and BBOA-related compounds, with the methodology discussed in detail in Appendix A4 (**Section A4.4**). Overall, the effect of temperature was demonstrated to be stronger than PM in promoting gas-particle partitioning across all three chemical classes. The strength of the correlation decreased as retention time increased. In addition, no correlation was observed for compounds eluting at earlier retention times. This examination corroborates the dependency of vapor pressure in predicting OA phase partitioning (Equation 4.2) and indicates that distinct behaviors are expected in different volatility regions.

To investigate the latter affirmation, i.e. the dynamics of phase partitioning as a function of volatility, individual alkanes were selected based on their saturation concentration classification outdoors (see **Figure 4.4**) and their observed particle phase fraction was plotted as a function of both temperature and PM concentrations. **Figure 4.6** shows the resulting scatter plots of tetradecane (C14 – IVOC), octadecane (C18 – SVOC), and tetracosane (C24 – LVOC). Examining the distribution of F_p values of tetradecane, it is noted that, at moderate temperatures, this compound gravitates towards the gas phase since the observed particle phase fraction values are regularly low and do not change even at increasing PM concentrations (orange-highlighted region). However, when temperatures decrease enough, simultaneously decreasing the compound's vapor pressure, tetradecane actively partitions to the particle phase as seen by the varying F_p values delineated by the blue-highlighted region.

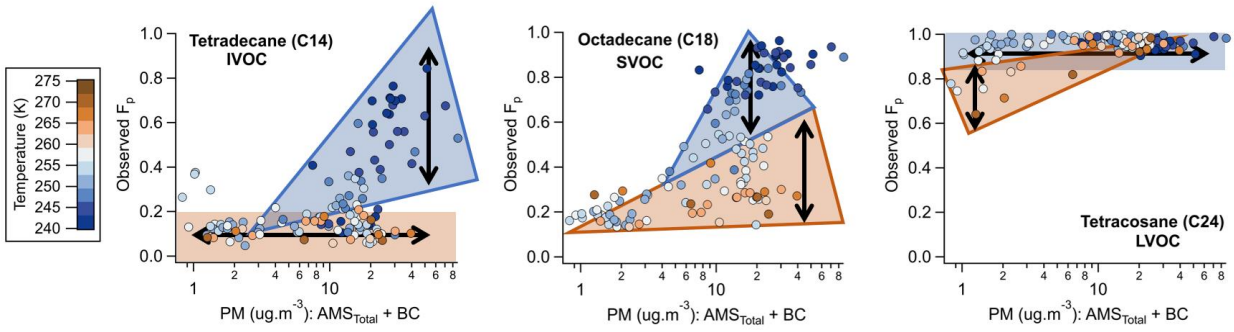

Figure 4.6. Outdoor phase partitioning dynamics of selected alkanes of varying volatilities.

On the other volatility extreme, the opposite trend is recognized. Tetracosane tends to stay in the particle phase, even at higher temperatures, if PM concentrations are elevated (blue-highlighted region). In this volatility region, partitioning to the gas phase only seems to occur when both PM mass is low, and ambient temperatures sufficiently increase to promote the increase in the compound's vapor pressure and thus its affinity to the gas phase (orange-highlighted region). Octadecane exhibits the transition behavior between the two volatility extremes. In this SVOC

region, gas-particle partitioning is observed at both low and moderate temperatures as evidenced by the varying F_p values in both the blue- and orange-highlighted regions. The impact of temperature in decreasing the compound's volatility can be seen by the shift in the phase partitioning trend to higher values of F_p at the same PM concentrations as temperature decreases.

Therefore, the observed phase partitioning dynamics can be described by three different regimes depending on the compound's vapor pressures. For compounds of high saturation concentrations, ambient temperatures need to decrease to encourage condensation, while for compounds of low saturation concentrations, temperatures ought to increase to enable evaporation. Since a high- and low-threshold temperature must be reached to promote gas-particle transfer, two different temperature-limited phase partitioning regimes are defined in these volatility extremes. Compounds of saturation concentrations within the bounds of these extremes demonstrate a temperature-dependent partitioning regime where dynamic phase transfer is observed.

It is of interest to understand how the boundaries of these regimes change with chemical composition. The relationship between particle phase faction, temperature, and PM concentrations was investigated for individual PAHs and BBOA-related compounds, and **Figure 4.7** illustrates the regime transition as a function of retention time and oxygen-to-carbon (O:C) ratios. Markers differentiate chemical classes and distinct colors represent each partitioning regime. Orange symbolizes the temperature-limited regime at high volatilities while blue indicates the temperature-limited regime at low volatilities. Black markers are associated with the temperature-dependent regime.

Examining the trend for non-polar compounds (O:C = 0), it is noticed that PAHs transition from the high saturation concentration temperature-limited to the temperature-dependent partitioning regime at a later retention time compared to alkanes. This observation can be justified

by the difference in volatilities of the compounds eluting at 500s. The average saturation mass concentration of the respective alkane (hexadecane) was calculated as 80.1 $\mu g.m^{-3}$ while the corresponding PAHs (fluorene) held a mean value equal to 807.1 $\mu g.m^{-3}$ under the same ambient conditions. Since the PAH is an order of magnitude more volatile than the alkane, the phase partitioning dynamics of the former it is expected to be best described by the high-volatility temperature-limited regime. This shift in transition due to the difference in chemical class volatilities remains true at the low end of the volatility spectrum when the alkanes switch from temperature-dependent to temperature-limited, but PAHs' phase transfer is still described by the dynamic behavior due to its higher saturation concentrations.

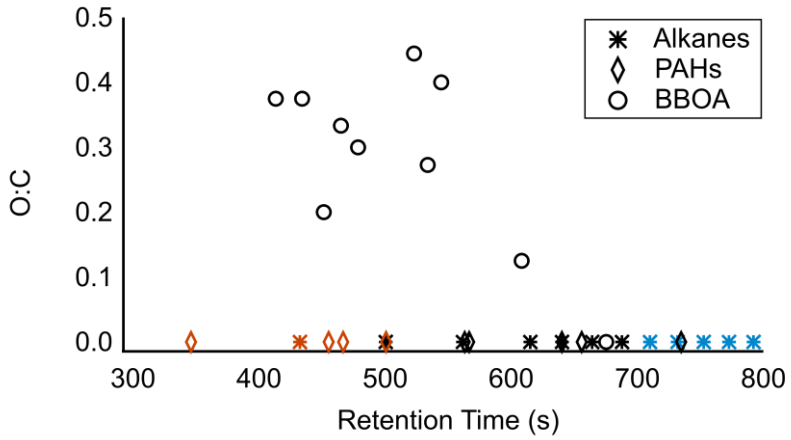

Figure 4.7. Partitioning regimes boundaries as a function of chemical composition. Orange and blue markers represent, respectively, the temperature-limited regime at high and low saturation concentrations, while black markers exhibit the temperature-dependent regime.

The effect of polarity is investigated by examining the trend of BBOA-related compounds. The increase in the level of oxygenation of a molecule is known to decrease its vapor pressure due to its stronger intermolecular attractions compared to non-polar compounds. Their low volatilities explain the absence of these species in the early retention time temperature-limited partitioning regime. Furthermore, from the estimated saturation mass concentrations of the considered polar

species, the transition from the temperature-dependent to the low-volatility temperature-limited regime for BBOA-related compounds must occur at $C^o < 1.17\ x\ 10^{-2}$ μg.m^{-3} (palmitic acid saturation mass concentration).

By establishing these three regimes, one can rationalize how F_p values must vary within each volatility region. For instance, compounds in the high saturation concentration temperature-limited regime favor the gaseous phase, thus when these species partition from particle-to-gas, it is reasonable to assume that re-condensation is negligible and F_p values are primarily a function of evaporation rates. On the other hand, since compounds in the low saturation concentration temperature-limited regime favor the particulate phase, re-evaporation is minimal when these species move from gas-to-particle and F_p values are a consequence of observed condensation rates. Finally, in the temperature-dependent regime, since these compounds dynamically transfer between the gaseous and condensed phases, F_p values will represent the extent of these two processes. **Figure A4.13** (Appendix A4 – Section A4.4) highlights each partitioning regime and shows how the alkane series average F_p values vary as a function of saturation concentration. In the following section, the ability of the thermodynamic equilibrium absorptive partitioning theory to predict this phase transport dynamic is evaluated.

4.3.3. Modeled and Measured Phase Partitioning Comparison

Outdoor Results

Figure 4.8 displays the outdoor particle phase fraction of alkanes observed during the ALPACA campaign averaged at two different ambient temperature ranges. The left plot represents mean F_p values at temperatures varying from 240-255K, while the right plot shows the average particle-bound observations calculated at 255-271K. Grey lines represent the equilibrium

absorptive partitioning predictions considering three different values for the activity coefficient. Marker's colors represent each established partitioning regime (i.e. orange and blue: temperature-limited; black: temperature-dependent). As expected, a decrease in $\overline{F_p}$ values is seen as temperature increases due the shift in compounds volatility to higher values at elevated ambient temperatures.

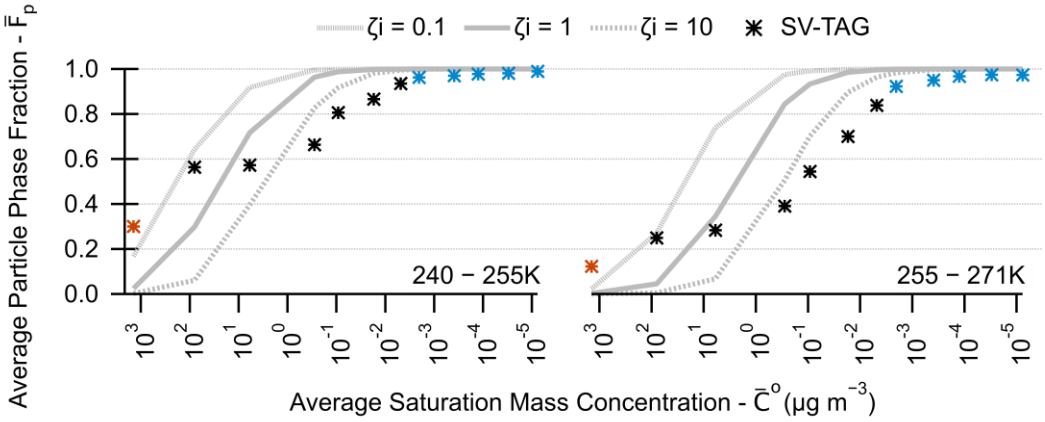

Figure 4.8. Average outdoor particle phase fraction (F_p) of alkanes observed during the ALPACA campaign. Left plot represents mean F_p values at temperatures varying from 240-255K. Right plot shows the average F_p calculated at 255-271K. Grey lines represent the equilibrium absorptive partitioning predictions considering three different values for the activity coefficient. Marker's colors represent each established partitioning regime (orange and blue: temperature-limited; black: temperature-dependent).

Previous studies have shown that the phase transition of alkanes can be well described by the absorptive partitioning model with values for the activity coefficients between 1 and 10.[7,29] Here, particle-bound observations follow $\zeta i \leq 1$ for volatile compounds in the high saturation concentration temperature-limited and temperature-dependent regimes. On the other hand, lower-volatility species in the temperature-dependent regime and temperature-limited regime at low saturation concentrations demonstrate $\zeta i > 10$. It has been suggested that large values of the activity coefficient are associated with phase separation.[16,30] Viscous aerosols tend to yield heterogeneously mixed particles[11] therefore, it is speculated that the model vs. measurement discrepancies here observed arise from temperature-induced shifts in particle viscosity, resulting

in a kinetically limited phase partitioning behavior in contrast to the instantaneous equilibrium assumed by the absorptive model.

To investigate the above hypothesis, phase state estimations at observed temperature, relative humidity, and organic mass loadings were calculated following the methodology described by Shiraiwa et al.[12] Calculations are detailed in Appendix A4 (**Section A4.4**). It was found that atmospheric OA adopted a semi-solid viscous state throughout the campaign duration and thus phase transfer is foreseen to be impacted by the slowing of diffusional motion that accompanies the increase in viscosity.

Considering the behavior observed in the high saturation concentration temperature-limited regime, where it was previously established that particle-bound observation derives from molecular evaporation rates, the underestimation of F_p values by the absorptive model is explained by the fast evaporation assumption that underlies the instantaneous equilibrium presupposition. Since an evaporating molecule experiences great resistance when diffusing from the inner bulk to the surface of highly viscous particles, evaporation rates are expected to be slow, contributing to the higher-than-predicted particle phase fraction observation. Indeed, numerous laboratory and modeling studies have reported a decrease in evaporation rates due to an increase in bulk diffusion limitations with increasing particle viscosity.[19,31-34]

The atmospheric growth of viscous aerosols yields heterogeneously mixed particles due to slow re-evaporation and relatively quick establishment of local equilibrium between the gas phase and the near-surface bulk, resulting in steep concentration gradients within the particle.[9,11-15] Particle-bound measurements of species in the low saturation concentration temperature-limited regime are directly proportional to the available near-surface layer for condensation ($F_p \propto f_{om}$). The instantaneous reversible gas-particle equilibrium considered by the absorptive partitioning

model relies on the implicit assumption that the aerosol particle is homogeneously mixed, which in turn predicts that the fraction of absorbing organic matter is the entire condensed phase, thus overestimating F_p values when condensation dominates, an observation foreseen by recent modeling results.[35] The gradual change from when particle-bound observations are controlled by slow evaporation ($\zeta i \leq 1$) to when F_p values are primarily a function of the layered condensation ($\zeta i > 10$) can be recognized in the temperature-dependent regime trend.

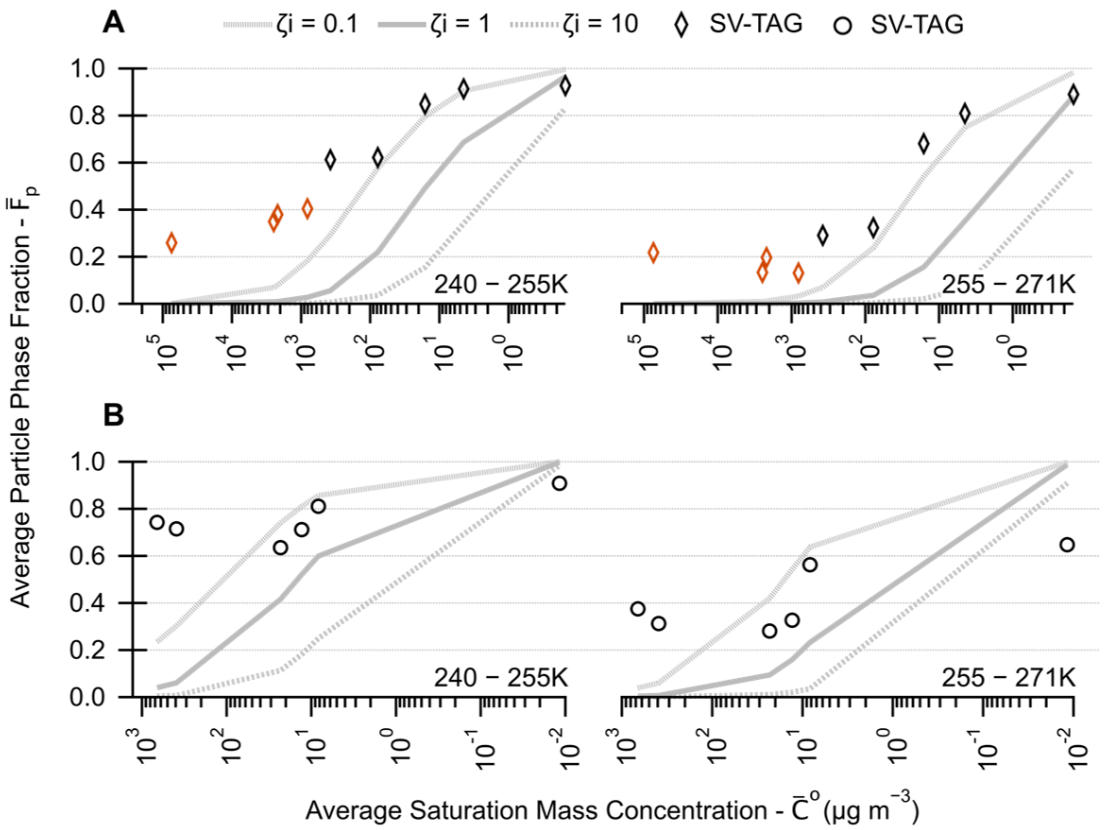

Figure 4.9. Average outdoor particle phase fraction (F_p) of polycyclic aromatic hydrocarbons **(A)** and biomass burning related compounds **(B)** observed during the ALPACA campaign. Left and right plots represent F_p values at different temperature ranges. Grey lines display the equilibrium absorptive partitioning predictions. Marker's colors represent each established partitioning regime (orange: temperature-limited; black: temperature-dependent).

Figure 4.9 above summarizes temperature-binned-averaged outdoor F_p values for selected PAHs and BBOA-related compounds. Since particle phase fraction values are described by

$\zeta i \leq 1$, kinetically limited evaporation is the driving mechanism of ambient particle-bound observations for the species here considered, except for the least volatile BBOA (palmitic acid) for which particle-bound observations seem to be better defined by layered condensation ($\zeta i > 10$). Interestingly, the measured particle phase fraction of the most volatile PAH (naphthalene) does not seem to greatly change with increasing outdoor temperatures, suggesting that this compound is effectively trapped in the inner bulk of the particle by the OA viscous layers. This examination aids in understanding previous observations of high particle phase concentrations of PAHs in remote regions,[36] since the suppressed evaporation and minimal degradation experienced by these molecules due to their low-bulk diffusivities and long mixing timescales ensure their efficient long-range transport. Indeed, recent modeling results have demonstrated that accounting for OA coatings in effectively shielding condensed PAHs brings model predictions into significantly better agreement with field measurements.[15]

Now, only compounds of which phase-transfer is described by the kinetically limited evaporation ($\zeta i \leq 1$) will be considered to investigate how evaporation trends vary as a function of chemical composition and thus how it affects this trapping mechanism. The absolute percentage of evaporation is calculated by considering the difference between $\overline{F_p}$ values observed at 255-271K and at 240-255K, and it is plotted in **Figure 4.10** against the molecular radius of gyration of each species (obtained from DIPPR® project 801 database)[26] which is inversely proportional to its diffusion coefficient, as elucidated by the Stokes-Einstein relationship:[9]

$$D = \frac{k_b T}{6\pi a \eta} \quad \textbf{(4.7)}$$

Where D is the molecular self-diffusion coefficient; k_b is the Boltzmann constant; T is the temperature; a is the effective molecular radius; and η is the dynamic viscosity of the particle.

Markers in **Figure 4.10** differentiate chemical classes and are colored as a function of the calculated average outdoor saturation concentrations of each species.

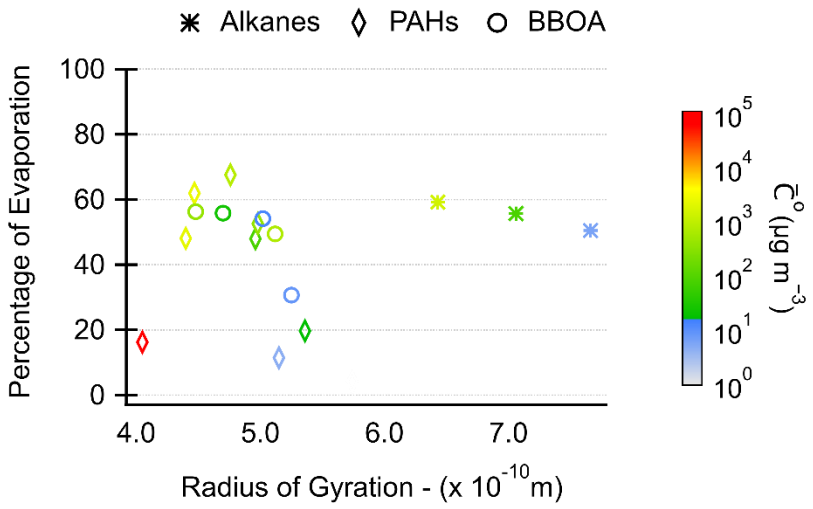

Figure 4.10. Evaporation experienced by selected alkanes, PAHs and BBOA-related compounds as a function of both molecular radius of gyration ($\propto$ diffusivity^{-1}) and average saturation mass concentration (volatility). Vertical axis values are expressed as the absolute percentage difference between $\overline{F_p}$ values observed at 255-271K and 240-255K.

An intriguing behavior is observed. Considering solely PAHs and BBOA-related compounds, less evaporation is experienced by species of both smaller and larger radii of gyration, i.e. faster and slower diffusing, respectively. A possible explanation is that the fast-moving small molecule infiltrates further into the particle at cold temperatures, embedding within the OA matrix, which suppresses its evaporation when temperature increases. In contrast, molecules of larger radius of gyration do not respond quickly enough to changes in gas-phase composition due to their limited diffusivity. Molecules found in between these extremes, do not move fast enough to get trapped into the inner bulk of the particle but their moderate diffusivity is sufficient to increase their sensitivity to changes in ambient gas-phase composition, granted the higher evaporation observed (large percentage difference).

The impact of volatility in this case (i.e. $\zeta i \leq 1$) seems to be overpowered by the kinetic limitations imposed by the higher particle viscosity since very volatile compounds show decreased evaporation compared to less volatile ones, and species of similar saturation concentration exhibit different evaporation trends that can be explained by their different radius of gyration (or diffusivities). This observation is consistent with models and laboratory experiments showing that evaporation rates of organic compounds from viscous and cold particles are controlled by bulk diffusivity rather than volatility.[11,19]

The fact that the alkanes show high evaporation, and yet detain larger radii of gyration (i.e. small diffusivities), suggests that these compounds must be condensing in the outer layers of the OA. This supposition can justify their responsiveness to changes in gas-phase composition. The higher concentration of PAHs and biomass-burning related compounds in the inner layers of the OA can be rationalized by their shorter mixing timescales due to their greater diffusivities compared to alkanes. However, if primary emissions during the campaign contained higher concentrations of PAHs and biomass-burning related compounds, compared to alkane levels, a similar OA concentration distribution can be expected, as subsequent particle growth would increase the concentration gradients between the surface and inner layers, promoting efficient trapping.

Indoor Results

It was observed that gas-particle phase partitioning of organic compounds outdoors within a volatility region is impacted by kinetic diffusion limitations due to the increase in particle viscosity as temperature decreases. The extreme temperature difference between indoor (~20^{o}C) and outdoor (~ -20^{o}C) promotes an increase in the OA volatility distribution as seen in **Figure 4.4.**

Furthermore, viscosity decreases with increasing temperature due to higher molecular kinetic energy that minimizes internal friction.[11,34] Therefore, it is of interest to examine how the dynamics of phase partitioning of organic compounds respond to these changes in both OA volatility and viscosity upon infiltration.

Figure 4.11 summarizes average indoor F_p values for selected alkanes and PAHs and compares the observed results with the predictions from the absorptive partitioning model, and the outdoor particle-bound measurements. Indeed, an increase in bulk evaporation is recognized following OA infiltration due to the increase in compounds' vapor pressures. However, indoor F_p values are still greater than expected if the instantaneous reversible gas-particle equilibrium is assumed. Since particle phase fraction values are described by $\zeta i \leq 1$ (kinetically limited evaporation), it is speculated that evaporation involving viscous particles is contributing to the particle-bound observations indoors.

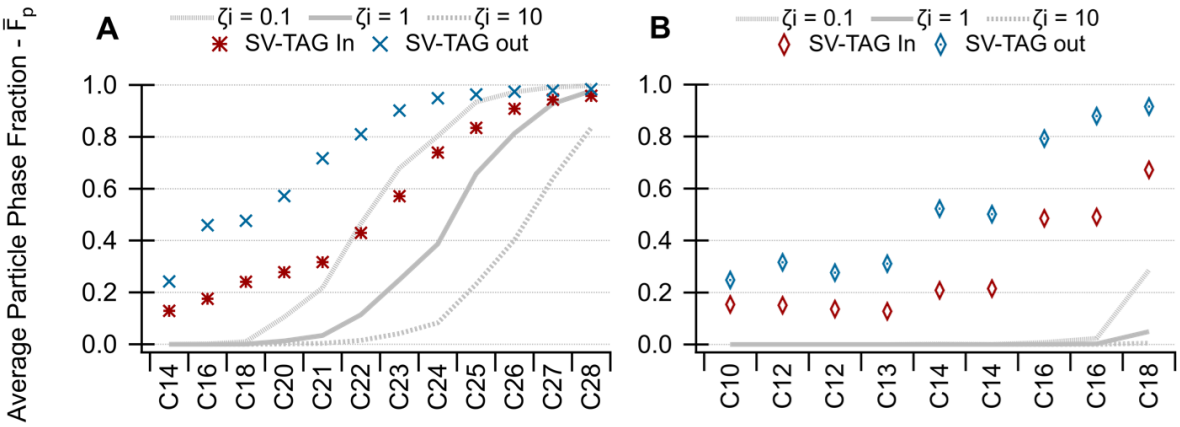

Figure 4.11. Average particle phase fraction (F_p) of alkanes **(A)** and polycyclic aromatic hydrocarbons **(B)** observed during the ALPACA campaign. Red and blue markers describe respectively, indoor, and outdoor averages. Grey lines represent the equilibrium absorptive partitioning predictions considering three different values for the activity coefficient.

Indoor OA phase state estimations followed the methodology described in Appendix A4 (**Section A4.4**) using the relevant indoor ambient parameters, and it was found that a semi-solid

viscous state prevailed even at the increased indoor temperatures. This observation is justified by the drier condition indoors, which is known to increase viscosity.[11,12,17,34] In addition, viscosity has also been found to increase as the more volatile components evaporate from the OA,[33] since the evaporation of the smaller molecules, increases the concentration of the least volatile larger species that are more viscous due to their higher glass transition temperatures.[12,17,34]

Therefore, similar to the outdoor observations, slow evaporation indoors results from diffusion limitation involving highly viscous aerosols. This dramatic increase in equilibration timescales contributes to lingering concentrations of toxic compounds in indoor particulate matter posing great risks to human health. For instance, while gas-phase inhalation exposure can directly partition into the epithelial lining fluid of the lung, inhalation of semi-volatile compounds associated with submicron particles penetrate deeper into the respiratory tract and interact with cellular layers longer, slowing releasing SVOCs as gas-phase are depleted.[37,38]

Exposure to particulate PAHs is correlated with adverse health outcomes in the respiratory, cardiovascular, and reproductive systems, in addition to its known cancerogenic effects,[39-42] and while thermodynamic equilibrium predicts that all the PAHs here considered should be solely or primarily in the gaseous phase upon infiltration, their particle-bound observations are astounding. Average gas and particle indoor and outdoor PAHs concentrations are found in **Table A4.3** (Appendix A4 - Section A4.2).

Equilibration Timescales

The kinetic multi-layer model of gas-particle interactions in aerosols and clouds (KM-GAP) model[43] was used to evaluate the timescale to achieve gas–particle equilibrium of measured compounds dominated by condensation or evaporation. The KM-GAP model comprises several

compartments and layers, which include a gas phase, a near-surface gas phase, a sorption layer, a surface layer, and multiple bulk layers. The model takes into account the temperature dependency of gas phase diffusion, adsorption and desorption, surface-bulk exchange, and bulk diffusion.[11]

Simulations were performed into preexisting non-volatile monodispersed particles in a closed system. Number concentrations were set to reproduce the average indoor and outdoor total OA mass concentrations (C_{OA}) considering a particle diameter of 200 nm. The effect of viscosity was investigated by varying the bulk diffusion coefficient (D_b) from 10^{-8} to $10^{-18}\ cm^2 s^{-1}$ and the effect of volatility was explored by varying C^o from 10^5 to $10^{-5}\ ug.m^{-3}$. The equilibration timescale (τ_{eq}) is calculated as the e-folding time, t, when the following criterion is met:

$$\tau_{eq} = \frac{|C_p(t) - C_{p,eq}|}{|C_{p,0} - C_{p,eq}|} < \frac{1}{e} \quad \textbf{(4.8)}$$

Where $C_{p,0}$ and $C_{p,eq}$ are, respectively, the initial and equilibrium mass concentrations of the partitioning compound in the particle phase. For the condensation case $C_{p,0} = 0\ ug.m^{-3}$ and, for the evaporation scenario trace amounts were assumed to be homogeneously well-mixed in the preexisting particles. Results are summarized in **Figure 4.12** which also includes a plot of the characteristic timescales of mass transport and mixing by molecular diffusion (τ_{mix}) within a particle of radius r_p, calculated as:[9]

$$\tau_{mix} = \frac{{r_p}^2}{\pi^2 D_p} \quad \textbf{(4.9)}$$

Consider the evaporation scenario under average T and C_{OA} outdoor conditions (**Figure 4.12A**). For less viscous or liquid particles, i.e., $D_b = 10^{-8}\ cm^2 s^{-1}$, the time required for the system to reach equilibrium decreases with increasing volatility (C^o). Therefore, in this regime, τ_{eq} is insensitive to bulk diffusivity but sensitive to volatility. For lower D_b values, τ_{eq} increases with increasing C^o. This behavior results from kinetic limitations arising from the increase in

particle viscosity. Note that equilibration timescales for $10^{-14} < D_b < 10^{-18}\ cm^2 s^{-1}$ vary from 4 minutes to 50 days. As previously discussed and demonstrated in Appendix A4 (**Section A4.4**), during the campaign, OA particles adopted a semi-solid/viscous state, and therefore, these longer evaporation equilibration timescales corroborate the conclusions of this work. Meaning that, for I/SVOCs, the higher SV-TAG F_p values compared to the absorptive partitioning model estimations are a consequence of the temperature-induced shift in particle viscosity, which results in τ_{eq} being controlled by bulk diffusivity, culminating in the observed slow evaporation rates. The same behavior is observed indoors (**Figure 4.12C**), with timescales also varying from minutes to days.

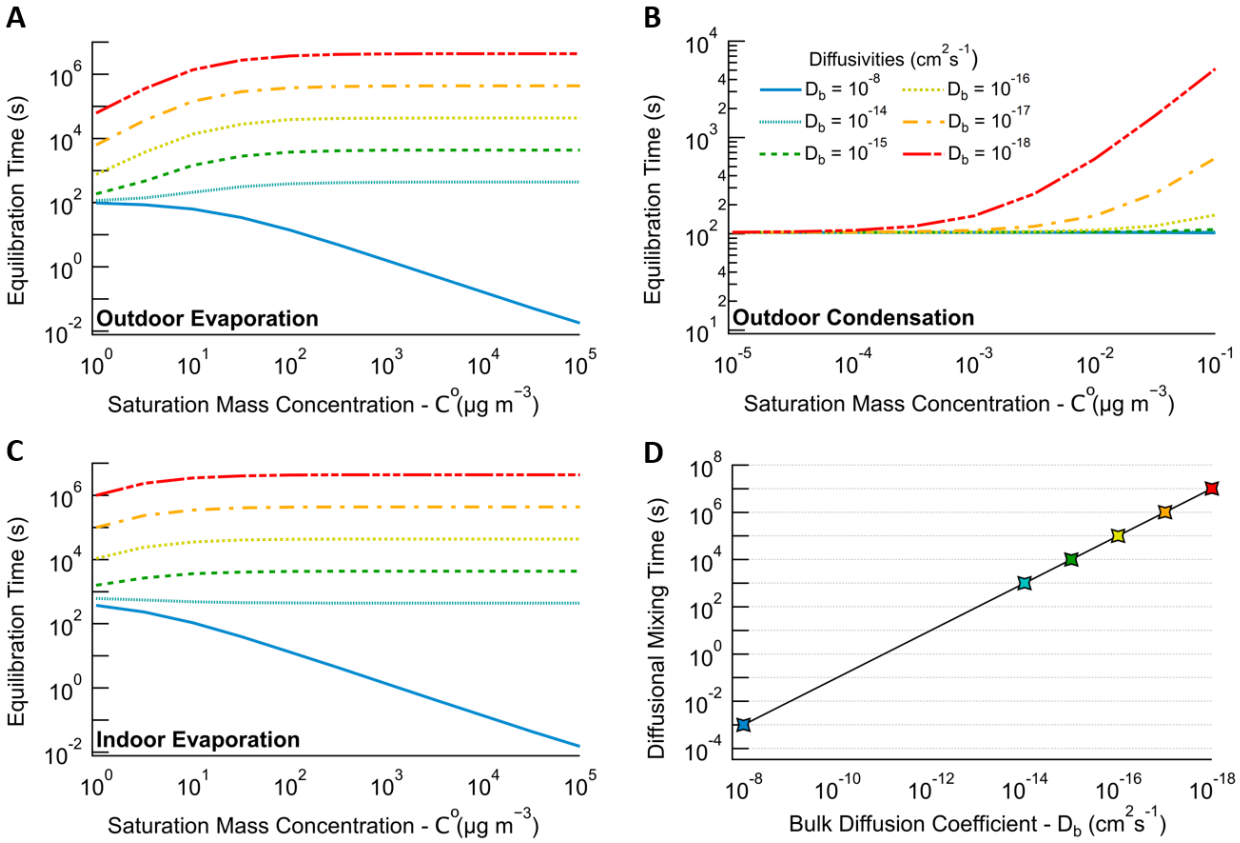

Figure 4.12. Gas-particle partitioning equilibration timescales. **(A)** Outdoor evaporation. **(B)** Outdoor condensation. **(C)** Indoor evaporation. **(D)** Characteristic time of bulk diffusion for varying values of diffusion coefficients.

The outdoor condensation scenario is shown in **Figure 4.12B.** In this case, τ_{eq} is plotted for C^o values within the (E)LVOC range since it represents the volatility window where F_p values are mainly driven by condensation (Figure 4.8). Note that for low-volatility compounds, i.e., $10^{-5} < C^o < 10^{-4}\ \mu g.m^{-3}$ equilibration timescales are fast (~ 100 s) and insensitive to bulk diffusivity. In this regime, τ_{eq} is controlled by volatility due to the very slow re-evaporation rates of (E)LVOCs (condensation sink).[44,45]

However, it is important to investigate the type of equilibrium reached for each D_b considered. Analyzing **Figure 4.12D**, it is observed that the diffusional mixing time for lower viscosity particles ($D_b = 10^{-8}\ cm^2 s^{-1}$) is much smaller than the time to reach equilibrium ($10^{-3} \ll 10^2\ s$), and thus particles are homogeneously well-mixed at τ_{eq}. In contrast, for decreasing diffusivities, $\tau_{mix} \gg \tau_{eq}$ due to strong kinetic limitations in highly viscous particles. This prevents the entire particle bulk from reaching complete equilibrium and τ_{eq} is defined as the time required for the OA system to reach local equilibrium between the gas phase and the near-surface bulk. Thus, at τ_{eq} particles are heterogeneous as a result of the steep concentration gradients between the particle surface and the inner bulk. The reduced absorbing organic matter available for condensation justifies the overestimated F_p values by the absorptive partitioning model compared to the SV-TAG measurements.

For $C^o > 10^{-4}\ \mu g.m^{-3}$ equilibration timescales increase with both volatility and viscosity (decreasing D_b). This increase results from re-evaporation being more significant for higher volatility species with the rate of this phase transfer being affected by the strong kinetic limitations of bulk diffusion. Therefore, it is concluded here that the dependence of equilibration timescales on both volatility and bulk diffusivity needs to be accounted for when predicting gas-particle phase partitioning of atmospheric aerosols during wintertime in Arctic regions.

4.4. Conclusions

This work elucidated the interplay of volatility distribution and particle viscosity governing OA gas-particle phase transfer under cold and dark conditions. Three partitioning regimes were established based on the particle-bound observations of compounds of varying volatilities under different ambient conditions. Compounds of both high- and low-saturation concentrations were found to partition solely after a threshold temperature was reached and thus, two different temperature-limited regimes were established. Compounds of saturation concentrations within the bounds of these extremes demonstrated a temperature-dependent behavior where dynamic gas-particle transfer was observed. However, this phase transfer dynamic was found to be also dependent on bulk diffusivity due to kinetic limitations arising from the increase in particle viscosity with decreasing temperatures.

After infiltration, an increase in bulk evaporation was observed due to the temperature-induced shift in the OA volatility distribution. However, particle-bound estimations indoors were still greater than predicted by the absorptive partitioning theory. Although particle viscosity is expected to decrease with increasing temperatures, the drier conditions indoors combined with a higher concentration of larger molecules in OA upon evaporation of the more volatile species, contributed to the persistence of semi-solid particles after infiltration. Therefore, low molecular diffusivity was found to be the determining factor justifying the observed slow evaporation rates.

These results demonstrate that the assumption of instantaneous reversible equilibrium used to predict phase partitioning dynamics is not suitable to describe this process under cold and dark conditions. The highly viscous heterogenous particles formed outdoors are likely to maintain its phase state when transported indoors, therefore, the dependence of equilibration timescales on both volatility and bulk diffusivity needs to be considered for predictions of gas-particle phase

concentrations in chemical transport and health exposure models to accurately address the impact of Arctic air pollution on both climate and human health.

References

1. Schmale J, Arnold SR, Law KS, et al. Local Arctic Air Pollution: A Neglected but Serious Problem. *Earth's Future*. 2018;6(10):1385-1412.

2. Cesler-Maloney M, Simpson WR, Miles T, Mao J, Law KS, Roberts TJ. Differences in Ozone and Particulate Matter Between Ground Level and 20 m Aloft are Frequent During Wintertime Surface-Based Temperature Inversions in Fairbanks, Alaska. *Journal of Geophysical Research: Atmospheres*. 2022;127(10).

3. Environmental Protection Agency (EPA). Air Plan Partial Approval and Partial Disapproval; AK, Fairbanks North Star Borough; 2006 24-Hour PM2.5 Serious Area and 189(d) Plan. *Federal Register*. 2023;88(232):84626-84676.

4. Leech JA, Nelson WC, Burnett RT, Aaron S, Raizenne ME. It's about time: A comparison of Canadian and American time–activity patterns. *Journal of Exposure Science & Environmental Epidemiology*. 2002;12(6):427-432.

5. Willis MD, Leaitch WR, Abbatt JPD. Processes Controlling the Composition and Abundance of Arctic Aerosol. *Reviews of Geophysics*. 2018;56(4):621-671.

6. Jimenez JL, Canagaratna MR, Donahue NM, et al. Evolution of organic aerosols in the atmosphere. *Science (New York, NY)*. 2009;326(5959):1525-1529.

7. Williams BJ, Goldstein AH, Kreisberg NM, Hering SV. In situ measurements of gas/particle-phase transitions for atmospheric semivolatile organic compounds. *Proceedings of the National Academy of Sciences of the United States of America*. 2010;107(15):6676-6681.

8. Simpson WR, Mao J, Fochesatto GJ, et al. Overview of the Alaskan Layered Pollution And Chemical Analysis (ALPACA) Field Experiment. *ACS ES&T Air*. 2024;1(3).

9. Shiraiwa M, Ammann M, Koop T, Poschl U. Gas uptake and chemical aging of semisolid organic aerosol particles. *Proceedings of the Nat. Academy of Sci.*. 2011;108(27):11003-11008.

10. Shiraiwa M, Seinfeld JH. Equilibration timescale of atmospheric secondary organic aerosol partitioning. *Geophysical Research Letters*. 2012;39(24).

11. Li Y, Shiraiwa M. Timescales of secondary organic aerosols to reach equilibrium at various temperatures and relative humidities. *Atm. Chemistry and Physics*. 2019;19(9):5959-5971.

12. Shiraiwa M, Li Y, Tsimpidi AP, et al. Global distribution of particle phase state in atmospheric secondary organic aerosols. *Nature Communications*. 2017;8(1).

13. Schervish M, Shiraiwa M. Impact of phase state and non-ideal mixing on equilibration timescales of secondary organic aerosol partitioning. *Atm. Chem. and Phys*. 2023;23(1):221-233.

14. Zelenyuk A, Imre D, Beránek J, Abramson E, Wilson J, Shrivastava M. Synergy between Secondary Organic Aerosols and Long-Range Transport of Polycyclic Aromatic Hydrocarbons. *Environmental Science & Technology*. 2012;46(22):12459-12466.

15. Shrivastava M, Lou S, Zelenyuk A, et al. Global long-range transport and lung cancer risk from polycyclic aromatic hydrocarbons shielded by coatings of organic aerosol. *Proceedings of the National Academy of Sciences*. 2017;114(6):1246-1251.

16. Donahue NM, Epstein SA, Pandis SN, Robinson AL. A two-dimensional volatility basis set: 1. organic-aerosol mixing thermodynamics. *Atmospheric Chemistry and Physics*. 2011;11(7):3303-3318.

17. DeRieux WSW, Li Y, Lin P, et al. Predicting the glass transition temperature and viscosity of secondary organic material using molecular composition. *Atmospheric Chemistry and Physics*. 2018;18(9):6331-6351.

18. Stolzenburg D, Fischer L, Vogel AL, et al. Rapid growth of organic aerosol nanoparticles over a wide tropospheric temperature range. *Proceedings of the National Academy of Sciences of the United States of America*. 2018;115(37):9122-9127.

19. Li Z, Tikkanen OP, Buchholz A, et al. Effect of Decreased Temperature on the Evaporation of α-Pinene Secondary Organic Aerosol Particles. *ACS Earth and Space Chemistry*. 2019;3(12):2775-2785.

20. Zhao Y, Kreisberg NM, Worton DR, Teng AP, Hering SV, Goldstein AH. Development of an *In Situ* Thermal Desorption Gas Chromatography Instrument for Quantifying Atmospheric Semi-Volatile Organic Compounds. *Aerosol Science and Technology*. 2012;47(3):258-266.

21. DeCarlo PF, Kimmel JR, Trimborn A, et al. Field-Deployable, High-Resolution, Time-of-Flight Aerosol Mass Spectrometer. *Analytical Chemistry*. 2006;78(24):8281-8289.

22. Isaacman-VanWertz G, Sueper DT, Aikin KC, et al. Automated single-ion peak fitting as an efficient approach for analyzing complex chromatographic data. *Journal of Chromatography A*. 2017;1529:81-92.

23. Kreisberg NM, Hering SV, Williams BJ, Worton DR, Goldstein AH. Quantification of Hourly Speciated Organic Compounds in Atmospheric Aerosols, Measured by an In-Situ Thermal Desorption Aerosol Gas Chromatograph (TAG). *Aerosol Sci. and Technology*. 2009;43(1):38-52.

24. Pankow JF. An absorption model of gas/particle partitioning of organic compounds in the atmosphere. *Atmospheric Environment*. 1994;28(2):185-188.

25. McFiggans GB, Alfarra MR, Allan J, et al. A review of the state-of-the-science relating to secondary particulate matter of relevance to the composition of the UK atmosphere : Full technical report to Defra, project AQ0732. eprints.whiterose.ac.uk. Published November 26, 2015.

26. American Institute of Chemical Engineers (AIChE). *DIPPR Project 801 - Full Version*. Design Institute for Physical Property Research

27. Koretsky MD. *Engineering and Chemical Thermodynamics*. Wiley; 2013.

28. Donahue NM, Kroll JH, Pandis SN, Robinson AL. A two-dimensional volatility basis set – Part 2: Diagnostics of organic-aerosol evolution. *Atmospheric Chemistry and Physics*. 2012;12(2):615-634.

29. Kristensen K, Lunderberg DM, Liu Y, et al. Gas–Particle Partitioning of Semivolatile Organic Compounds in a Residence: Influence of Particles from Candles, Cooking, and Outdoors. *Environmental Science & Technology*. 2023;57(8):3260-3269.

30. Liu X, Day DA, Krechmer JE, Ziemann PJ, Jimenez JL. Determining Activity Coefficients of SOA from Isothermal Evaporation in a Laboratory Chamber. *Environmental Science and Technology Letters*. 2020;8(3):212-217.

31. Cappa CD, Wilson KS. Evolution of organic aerosol mass spectra upon heating: implications for OA phase and partitioning behavior. *Atmospheric Chemistry and Physics*. 2011;11(5):1895-1911.

32. Wilson JM, Imre D, Beranek J, Shrivastava MB, Zelenyuk A. Evaporation Kinetics of Laboratory-Generated Secondary Organic Aerosols at Elevated Relative Humidity. *Environmental Science & Technology*. 2014;49(1):243-249.

33. Yli-Juuti T, Pajunoja A, Tikkanen O, et al. Factors controlling the evaporation of secondary organic aerosol from α-pinene ozonolysis. *Geophysical Research Letters*. 2017;44(5):2562-2570.

34. Reid JP, Bertram AK, Topping DO, et al. The viscosity of atmospherically relevant organic particles. *Nature Communications*. 2018;9(1).

35. Wilson J, Pöschl U, Shiraiwa M, Berkemeier T. Non-equilibrium interplay between gas–particle partitioning and multiphase chemical reactions of semi-volatile compounds: mechanistic insights and practical implications for atmospheric modeling of polycyclic aromatic hydrocarbons. *Atmospheric Chemistry and Physics*. 2021;21(8):6175-6198.

36. J. Keyte I, M. Harrison R, Lammel G. Chemical reactivity and long-range transport potential of polycyclic aromatic hydrocarbons – a review. *Chemical Society Reviews*. 2013;42(24):9333-9391.

37. Liu C, Zhang Y, Weschler CJ. Exposure to SVOCs from Inhaled Particles: Impact of Desorption. *Environmental Science & Technology*. 2017;51(11):6220-6228.

38. Lammel G, Kitanovski Z, Kukučka P, et al. Oxygenated and Nitrated Polycyclic Aromatic Hydrocarbons in Ambient Air—Levels, Phase Partitioning, Mass Size Distributions, and Inhalation Bioaccessibility. *Environmental Science & Technology*. 2020;54(5):2615-2625.

39. Zhang X, Yang L, Zhang H, et al. Assessing Approaches of Human Inhalation Exposure to Polycyclic Aromatic Hydrocarbons: A Review. *International Journal of Environmental Research and Public Health*. 2021;18(6):3124.

40. John Kilpatrick D. *Investigating the Relationship of COPD, Lung Cancer, and Polycyclic Aromatic Hydrocarbons from Ambient Air Pollution*. Dissertation. 2019.

41. Moorthy B, Chu C, Carlin DJ. Polycyclic Aromatic Hydrocarbons: From Metabolism to Lung Cancer. *Toxicological Sciences*. 2015;145(1):5-15.

42. Kakavandi B, Rafiemanesh H, Giannakis S, et al. Establishing the relationship between Polycyclic Aromatic Hydrocarbons (PAHs) exposure and male infertility: A systematic review. *Ecotoxicology and Environmental Safety*. 2023;250:114485.

43. Shiraiwa M, Pfrang C, Koop T, Pöschl U. Kinetic multi-layer model of gas-particle interactions in aerosols and clouds (KM-GAP): linking condensation, evaporation and chemical reactions of organics, oxidants and water. *Atmospheric Chemistry and Physics*. 2012;12(5).

44. Riipinen I, Pierce JR, Yli-Juuti T, et al. Organic condensation: a vital link connecting aerosol formation to cloud condensation nuclei (CCN) concentrations. *Atmospheric Chemistry and Physics*. 2011;11(8):3865-3878.

45. Tröstl J, Chuang WK, Gordon H, et al. The role of low-volatility organic compounds in initial particle growth in the atmosphere. *Nature*. 2016;533(7604):527-531.

CHAPTER 5

Sources and Dynamics of Wintertime Air Pollution during the Alaskan Layered Pollution And Chemical Analysis (ALPACA) Field Campaign

Abstract

Fairbanks, Alaska, consistently experiences some of the poorest wintertime air quality in the United States. Source apportionment via Positive Matrix Factorization (PMF) was performed to identify the major sources of pollution in a residential neighborhood in the region during the winter of 2022. Speciated organic aerosol measurements were obtained by deploying the custom-developed Semi-Volatile Thermal Desorption Aerosol Gas Chromatograph (SV-TAG) system during the Alaskan Layered Pollution And Chemical Analysis (ALPACA) field campaign. In conjunction with supporting data and meteorological information, five individual factors were assigned as representations of dominant emission sources and transformative processes. One factor was associated with the emission of higher volatility species that demonstrated significantly different phase-partitioning dynamics due to the temperature-induced shift in their vapor pressures. A traffic commute source was also identified. The higher late afternoon/evening emissions compared to the morning abundances suggested a dominant contribution from less efficient vehicles from return commutes, likely due to less effort to keep engines warm when not parked for very extended periods. The overall heating factor included hydrocarbons, polycyclic aromatic hydrocarbons (PAHs), and biomass burning (BB) emissions, indicating that both fuel oil and wood combustion are a source of ground-level pollution in the neighborhood. The higher contributions of propylsyringol, syringaldehyde, and acetosyringone implied the preference for hardwood over softwood combustion. Softwood emissions were associated with strong surface-based temperature inversions which was understood as an enhancement factor due to the higher-volatility species present in softwood smoke. The last factor comprised mainly PAHs with smaller contributions from hydrocarbons and BB. Meteorological conditions and diagnostic ratio analysis proposed that this factor might be related to both residential heating and power generation emissions.

5.1. Introduction

Fairbanks, the largest city in the interior of Alaska, experiences some of the worst wintertime air pollution in the United States. With measured ambient fine particulate matter pollution ($PM_{2.5}$, <2.5 μm in diameter) often exceeding the 24-hour National Ambient Air Quality Standard (NAAQS) of 35 $\mu g.m^{-3}$, the Fairbanks-North Star Borough (FNSB) is classified by the U.S. Environmental Protection Agency (EPA) as a "serious" nonattainment area.[1] Average wintertime temperatures in the region range from –22°C to –2.0°C, with extremely low temperatures reaching below –40°C,[2] a factor that promotes an increase in local emissions throughout the winter months.[3] Surrounded by hills on three sides, the topography of Fairbanks contributes to the persistence of surface-based temperature inversions.[4] The hindrance of vertical mixing traps near-ground emissions in the lower troposphere leading to high pollution episodes.[5]

Poor air quality associated with high PM levels is among the leading health risks worldwide,[6] and an important step towards implementing emission reduction strategies is to first determine the major sources contributing to air pollution. Consider the successful case of reducing carbon monoxide (CO) levels in the region. Up until the early 2000s, vehicle emissions were responsible for Fairbanks repeatedly violating the standard CO levels of 9 ppm.[7] Mitigation strategies employed throughout the city resulted in the FNSB becoming a Carbon Monoxide Maintenance Area in 2004,[8] and nowadays, with improved automotive technologies, Fairbanks' CO levels remain within regulatory standards even under severe inversion trapping conditions.[9]

Residential heating, power generation, and transportation are identified as the principal sources of particulate air pollution in the region.[10] In fact, various source apportionment studies have demonstrated that biomass burning (BB) and fuel oil combustion are the dominant contributors.[11,12] In efforts to improve air quality, wood stove changeout programs and incentives

to switch from wood to cleaner burning fuels have been implemented in the region,[13] along with air quality alerts that prohibit the operation of solid-fuel stoves when poor dispersion of pollutants is foreseen.[14] The application of these strategies might be, in part, responsible for the observed decrease in woodsmoke contribution to Fairbanks $PM_{2.5}$ pollution between 2013-2019.[15]

A 2018 review of air pollution in the Arctic enforces the need for more information on local pollution sources,[3] a more pressing knowledge in recent years given the potential for the sources to be changed perennially as a result of the continuous regulatory efforts to reduce emissions. For instance, the same study that reported a decrease in wood combustion $PM_{2.5}$ contributions found that the percentage of particulate sulfate (SO_4) had increased in the same period.[15] A recent publication from the Alaskan Layered Pollution And Chemical Analysis (ALPACA) campaign demonstrated that primary sulfate contributed 50%-74% of the total sulfate in Fairbanks. Residential heating fuel oil was found to be the main contributor to this primary sulfate pollution.[16] These results exhibit the complexity of elaborating mitigation procedures and regulations to improve air quality in Arctic regions and the necessity of continuous source apportionment studies.

In this work, Positive Matrix Factorization (PMF) was applied to selected quantified particulate organic compounds measured by the Semi-Volatile Thermal Desorption Aerosol Gas Chromatograph (SV-TAG) during the ALPACA campaign. The goal of this analysis was to identify major components contributing to submicron ($PM_{1.0}$) pollution in a residential neighborhood in Fairbanks during the winter of 2022. The temporal patterns of the different factors were examined. Aided by supporting measurements, explanations for the variability of the factors are provided. Based on activity patterns and the meteorology of the region, the dynamics of wintertime air pollution and its major sources are inferred, providing useful information to help address the seasonal poor air quality of this region.

5.2. Materials and Methods

5.2.1. ALPACA Overview and Field Description

Aimed at improving the understanding of the sources and transformations of wintertime air pollution in the FNSB region, the ALPACA field campaign was deployed in Fairbanks from January 17th through February 25th, 2022. Meteorological, snow composition, particle, and gas data were obtained from a suite of instruments installed across the five measurement/monitoring sites, with detailed study goals and design found in the overview manuscript.[17] Here, measurements from two of the sites, shown in **Figure 5.1,** are used in conjunction to investigate the major components contributing to poor air quality in a residential neighborhood.

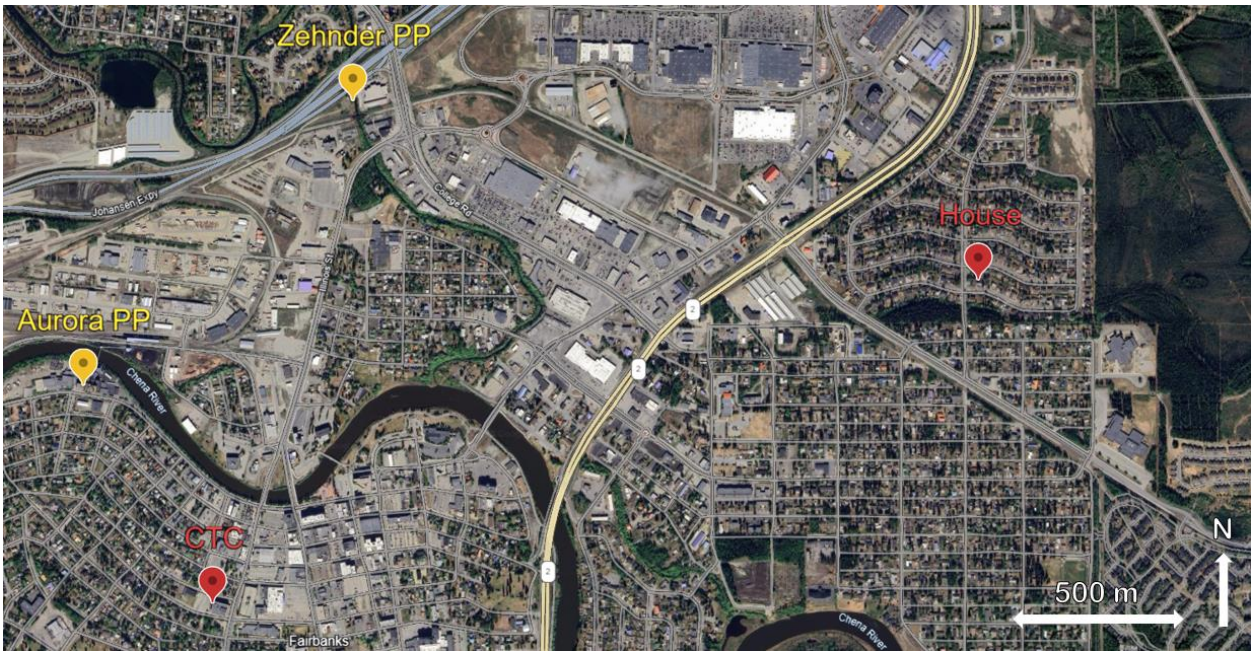

Figure 5.1. Map of Fairbanks showing the location of the downtown (CTC) and house sites in red labels. Surrounding power plants are pinned in yellow. Basemap produced by Earth.Google.com.

The house site was located in the Shannon Park neighborhood (64.850°N, 147.676°W) on the northeast side of Fairbanks. Steese Highway 2, the coal-fired Aurora power plant, and the diesel-based Zehnder power plant are situated to the west of the home. Birch Hill limits the

neighborhood on the east side, while the closest well-traveled road, W Trainer Gate Rd, is located about 300 m south of the test home. The cold winter temperatures contribute to high emissions of heating-related pollutants in the area. The primary heating source used in the test house was fuel oil. Nearby homes are expected to use a mix of fuels common in Fairbanks, likely dominated by heating oil and wood. The Alaska Fairbanks Community and Technical College (CTC) site was located in the Fairbanks downtown area, 2.6 km WSW from the home test and about 1 meter below the house site altitude (64.841°N,147.727°W). The sampling site was situated next to Barnette Street, a major downtown road, and along 7th Avenue, a less busy street but with on-road parking available. To the north and east of the site, there are mainly commercial businesses that operate during business hours. The western side of the site is predominantly residential.

5.2.2. Instrumentation

The overview paper contains a comprehensive inventory of all the apparatus deployed during the 2022 ALPACA field campaign. Here, only the instrumentation that provided relevant measurements for the source apportionment analysis is discussed.

House Site

The source apportionment-focused speciated measurements were obtained at the house site using the custom-built SV-TAG system. A detailed description of the SV-TAG can be found in **Chapter 3**. Succinctly, the system comprises two identical dual-stage collection cells arranged in parallel for simultaneous gas and particle sampling. In series thermal desorption and subsequent gas chromatography-mass spectrometry (GC/MS) allows for the *in situ* analysis of the collected material. While one cell collects a non-denuded sample (gases plus particles), the other cell collects

a denuded one (particles only). The roles of each cell are swapped after each collection to avoid cell-to-cell measurement bias.

During the campaign, two separate inlet lines were used to alternate between indoor and outdoor sampling. However, only the outdoor particle phase data is used in this source apportionment analysis. A 40 cm long (30 mm OD) 500-channel activated carbon denuders (ADI-DEN2, Aerosol Dynamics Inc., Berkeley, CA) was installed on each line to remove gas phase species. A schematic and detailed description of the SV-TAG inlet system and sampling strategy is found in **Chapter 4 Appendix** (Appendix A4 – Section A4.2 – Figure A4.2).

The SV-TAG sampled with cyclones that provided a particle cutoff (d_{p50}) of approximately 1.0 μm under typical flow rates of 16.7 $L.min^{-1}$. Each cell collected at a flow rate of 8.3 $L.min^{-1}$. Immediately after collection, internal standards were injected in both cells using the custom AutoInject system (see details in **Chapter 3**). Then, each cell was thermally desorbed in series in a two-step process. Subsequent chromatographic analysis was performed using an Agilent 6890A GC by ramping a non-polar GC column (RTX-5Sil MS 20 m long, 0.18 mm ID, 0.18 μm film thickness) at a rate of 22.50ºC.min^{-1} from 50ºC to 315ºC (hold 3 min.); while a 70eV quadrupole mass spectrometer (Agilent G1098, 5973N MSD) provided mass spectral detection. Default collection times were 10 minutes indoors – 10 minutes outdoors, but sampling times were adjusted on a few occasions when ambient conditions were cleaner.

The High-Resolution Time-of-Flight Aerosol Mass Spectrometer (HR-ToF-AMS, Aerodyne, Inc., Billerica, MA), and a gas concentration analyzer (G2401, Picarro, Santa Clara, CA) provided supporting measurements for the source apportionment analysis presented in this Chapter. The AMS operated in V-mode measuring non-refractory PM bulk composition for particles with aerodynamic diameter values between 50-1000 nm,[18] while the Picarro® instrument

granted real-time carbon monoxide (CO), carbon dioxide (CO_2) and methane (CH_4) concentrations. Both instruments used a separated fast-switching automated inlet system allowing 10-minute indoor/10-minute outdoor sampling cycles acquiring data at 1Hz.

CTC Site

Data collected at the CTC site also aided in the interpretation of the sources and dynamics of air pollution in the residential neighborhood. Four temperature probes were deployed at 3 m, 6 m, 11 m, and 23 m on a retractable tower attached to one of the CTC measurement trailers. The probes were constructed from thermistors placed inside an aspirated radiation shield built from PVC pipes utilizing a fan to provide ventilation. The temperature sensors were cross compared at the same altitude at the beginning and end of the campaign. Their relative precision was ±0.15°C over the temperature range of 20°C to −60°C. The temperature difference of 23 m minus 3 m (dT) is used here to quantify the presence and the intensity of surface-based temperature inversions.

$PM_{2.5}$ mass concentrations at 3 m and 23 m were measured by two PurpleAir® particulate matter sensors (PA-II, Draper, UT) on the CTC roof. Vertical CO_2 profiles were also obtained from infrared detectors with Fabry-Perot Interferometer sensors. However, only the measurements at 23 m are used in this work. Ground level (3 m) reactive gases measurements included mixing ratios of ozone (O_3) obtained from ultraviolet photometric detection, nitrogen oxides (NO and NO_2) from chemiluminescence-based analysis, and sulfur dioxide (SO_2) from pulsed fluorescence technology. All gas analyzers at the CTC site were calibrated on a weekly basis. Wind speed and direction were measured at 23 m with a propellor and potentiometer wind monitoring system. More information about the gases and meteorological data can be found at the National Science Foundation (NSF) Arctic Data Center (doi:10.18739/A27D2Q87W).

5.2.3. Positive Matrix Factorization (PMF) Analysis

PMF is a mathematical source apportionment technique that groups components based on their time-dependent co-variance considering their uncertainty.[19] In the atmospheric science field, it has been used to separate measured ambient chemical species (gases or particles) into co-varying factors that, taking into account supporting data and information, are generally depicted as representations of specific sources or transformative processes.[12,15,20] In this work, PMF calculations were performed on a subset of integrated and quantified SV-TAG particle-phase compounds to investigate the sources and dynamics of wintertime air pollution in an Arctic residential neighborhood. Species included in the PMF analyses were chosen to span a variety of volatilities and compound classes that represent the major sources contributing to the seasonal poor air quality in the region.

Compound identification was achieved by searching with the National Institute for Standards and Technology (NIST) Mass Spectral Search Program (Demo Version 2.0f) and peak integration was performed on single ion using the TAG ExploreR and iNtegration (TERN) software written in Igor Pro (Wavemetrics, Inc, Lake Oswego, OR). By continuous injection of polar and non-polar tracking standards after each sample collection, raw integrated MS signals could be time-dependent-corrected for within-cell variability caused by detector drifts and fluctuations in desorption-transfer efficiency throughout the sampling period. External standard injections provided the data necessary to generate multi-point mass calibration curves. The corrected MS sample signals (peak areas) were then converted to mass concentration by dividing the calculated mass by the collection volume. Compounds present in the external standards were directly quantified while species not included in the standard mixture were quantified using

surrogate compounds. More details about the SV-TAG data processing and quantification can be found in **Chapter 4 Appendix** (Appendix A4 – Section A4.2).

The PMF algorithm is fully described elsewhere.[19] Simply, an input data matrix, X, with dimensions m rows and n columns can be factorized into two matrices: $G\ (m\ x\ p)$ and $F\ (p\ x\ n)$, where p is the number of factors. A residual matrix $E\ (m\ x\ n)$ also results such that:

$$X = GF + E \quad \textbf{(5.1)}$$

Here, X is the input data matrix composed of n compounds and m chromatograms, where each element x_{ij} of the matrix represents the integrated quantified abundance of the j^{th} compound within the i^{th} chromatogram. As shown in Equation 5.1, PMF calculations separate X into G, the time series matrix, and F, the profile matrix, according to a user-specified number of factors p. The input error matrix E is calculated using known instrument precision values.

For this analysis, the error matrix was determined according to methods described in previous work[20,21] with the error matrix element, e_{ij}, corresponding to the j^{th} compound in the i^{th} chromatogram, i.e. the x_{ij} input matrix element, calculated using Equations 5.2 and 5.3.

$$e_{ij} = 2\ x\ IP \quad \textbf{(5.2)} \qquad e_{ij} = \sqrt{(z\ x\ x_{ij})^2 + (IP)^2} \quad \textbf{(5.3)}$$

Where IP is the instrument precision and z is the instrument uncertainty. If $x_{ij} \leq IP$, e_{ij} is given by Equation 5.2, otherwise, Equation 5.3 is used. The value of IP is defined here as the limit of detection, LOD, equal to 3 times the standard deviation of the baseline abundance of the integrated ion. Based on previous work, z was assumed to be 10%.[22,23]

To ensure the PMF results were not driven primarily by compounds with the highest concentrations, quantified abundances for each compound were normalized to the highest value across all chromatograms. Therefore, each column of the input data matrix contained values ranging from 0 to 1. The error matrix was then calculated following this normalization.

5.3. Results and Discussion

A 5-factor PMF solution was found to best represent the major sources contributing to the emissions and transformations of the compounds selected for this apportionment analysis. Solutions between 1 and 10 factors were considered. Solutions with fewer factors failed to separate factors with meaningful physical interpretations, whilst solutions with additional factors showed less uniqueness between factors. Factor splitting, understood as when too many factors are used to describe the dataset, was already observed when considering a 6-factor solution.

The value of Q/Q_{exp} is typically used to determine the optimal number of factors in a PMF solution.[20,24] Q, the objective function, is defined as the sum of weighted squared residuals:

$$Q = \sum_{i=1}^{m} \sum_{j=1}^{n} \left(\frac{e_{ij}}{\sigma_{ij}}\right)^2 \quad \textbf{(5.4)}$$

Where σ_{ij} is the estimated precision of the data point x_{ij}. Q_{exp} is given as:

$$Q_{exp} = m\ x\ n - p\ x\ (m + n) \quad \textbf{(5.5)}$$

If errors are underestimated, Q/Q_{exp} will exceed 1, and if overestimated, $Q/Q_{exp}$is less than 1. Ideally, a ratio close to unity is desired since it implies that the data are neither overfitted nor underfitted. However, a Q/Q_{exp} not equal to 1 does not necessarily mean that calculated results are not meaningful, as long as the overall ratio does not exceed 10.[25]

The value of Q/Q_{exp} for the 5-factor solution with fPeak = 0 was equal to 5.79 (**Figure A5.1A** – Appendix A5 – Section A5.1). The fPeak parameter allows exploration of solutions taking rotational ambiguity into account during calculations. Varying fPeak between ±1 in increments of 0.2 showed, approximately, 2% change in Q/Q_{exp} values for the considered solution. (F**igure A5.1B** – Appendix A5 – Section A5.1). This non-sensitivity of TAG measurements to variation in fPeak was also observed in previous work.[20,21]

The residual variability of the PMF analysis showed both positive and negative values, implying that at times the data variability was over-explained by the solution, and at other times, it was under-explained. The net residual term had an average value of 10% of the total variance. None of the compounds were under-explained by the chosen solution. Coniferaldehyde, retene, and propylsyringol were the most overexplained parameters by 30-35%. All the other compounds were 20% or less (**Figure A5.2** – Appendix A5 – Section A5.1). Each factor in the chosen solution is explored by combining the PMF results (profile and timeseries abundances) diurnal profiles, and correlation with meteorological parameters, trace gases, and bulk particulate matter composition.

5.3.1. Factor 1: Semi-Volatile Emissions

Figure 5.2 summarizes Factor 1 results. This PMF profile is comprised of lighter, more volatile compounds. Hexadecane to heneicosane have their highest contributions represented in this factor showing at least double the signal compared to the value observed in their second-most abundant factors. Acenaphthene, the most volatile compound considered in this source apportionment analysis, has the largest share within the compounds loaded in this factor and its signal fraction is almost 4 greater than in its second most abundant factor. These compounds demonstrate their highest abundances at the lowest temperatures, with 88% of the factor abundances above one standard deviation of the mean measured at ambient temperatures below 252K. As temperatures increased, abundances were lower but still relevant. These observations suggest that this factor represents semi-volatile species of significantly different phase partitioning dynamics when emitted at extremely low temperatures at the beginning of the campaign, compared to when they are emitted at slightly higher temperatures.

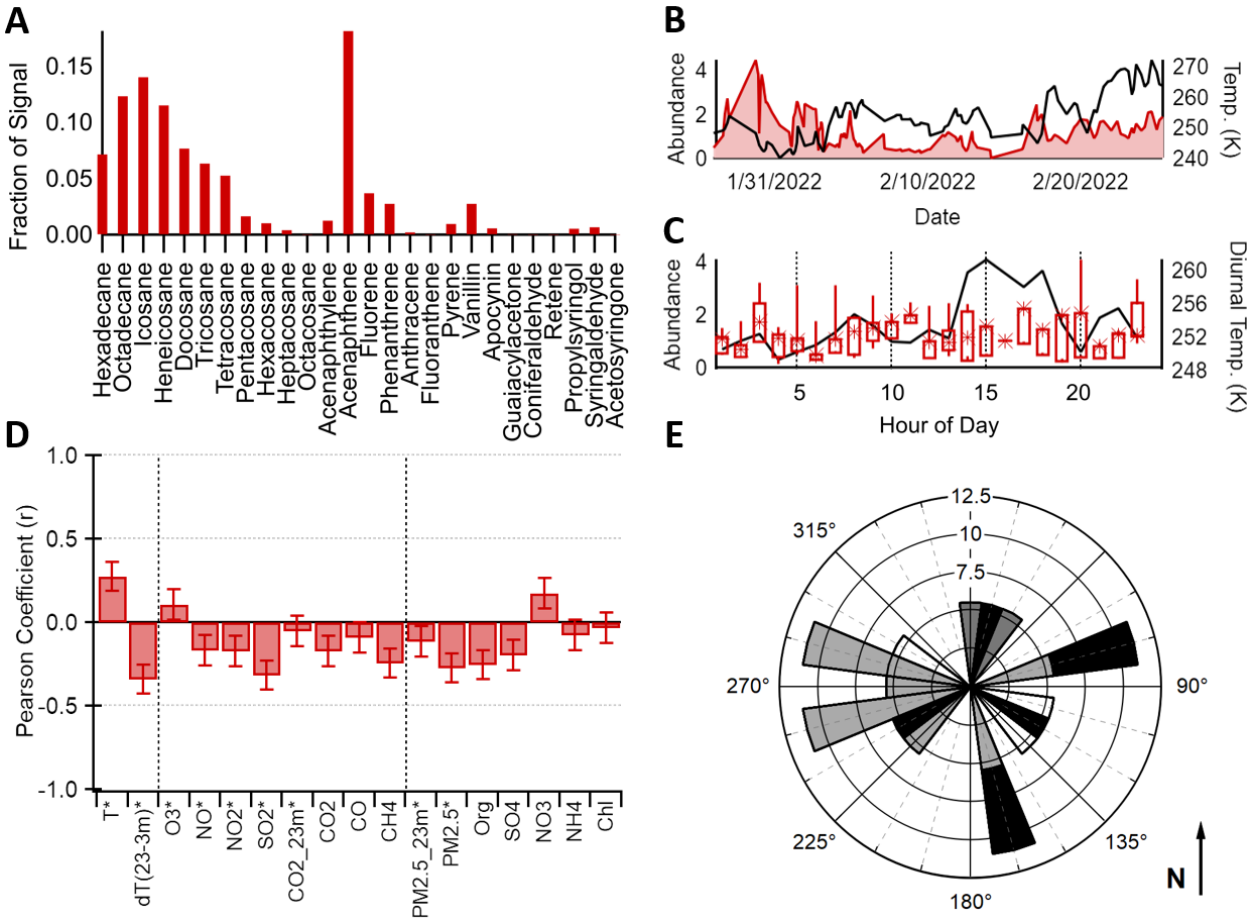

Figure 5.2. Factor 1 results. **(A)** Composition profile. **(B)** Factor timeseries (left) and outdoor temperature (right). **(C)** Diurnal variation. Markers represent the median value; bars represent the 25th and 75th percentiles; vertical lines show minimum and maximum abundances. **(D)** Pearson correlation analysis between the fraction of the factor abundance timeseries and the timeseries of meteorological conditions (first panel), trace gases (second panel), and particulate species (third panel). Asterisks denote measurements at the CTC site. **(E)** Rose plot showing the correlation of abundances and wind direction using only data points when the factor abundance was elevated (i.e. above one standard deviation of the mean factor abundance). Frequency of observations is represented by the length of each wedge. Shading corresponds to factor abundances in quartiles with darker colors indicating greater abundances.

To strengthen the above affirmation, **Table 5.1** shows the calculated vapor pressures at the minimum and maximum outdoor ambient temperatures for the alkane series considered in this analysis. Their respective particle phase fraction (F_p), estimated at these conditions by taking the ratio between their measured particle and total (gas plus particle) concentrations, is also given.

Note that for a 30K (ºC) increase in temperature, the particle-bound observations of the most volatile species (C16-C20) decrease by an average of 73%, while the least volatile compounds (C26-C28) show a negligible 1% average difference. Thus, it is reasonable to state that this factor represents species emitted with a higher particle-phase concentration at lower temperatures, but increased temperatures shift the compound's vapor pressures to higher values, decreasing their affinity to the particle phase, thus resulting in lower particle-bound emissions.

TABLE 5.1. Calculated vapor pressures and measured particle-phase fraction of selected compounds during the ALPACA campaign.

		T_{min} = 240K		T_{max} = 270K		ΔT = 30K
Compound Name	**Formula**	**P_L^o (Torr)[a]**	**F_p**	**P_L^o (Torr)[a]**	**F_p**	**ΔF_p (%)**
Hexadecane	C16H34	9.80E-07	0.7910	4.21E-05	0.1936	-75.52
Octadecane	C18H38	5.02E-08	0.7775	3.21E-06	0.2285	-70.61
Eicosane	C20H42	1.54E-09	0.8453	1.59E-07	0.2219	-73.75
Heneicosane	C21H44	4.30E-10	0.9429	5.18E-08	0.5191	-44.95
Docosane	C22H46	6.37E-11	0.9619	1.00E-08	0.7082	-26.37
Tricosane	C23H48	1.49E-11	0.9585	2.83E-09	0.9156	-4.48
Tetracosane	C24H50	5.63E-12	0.9660	1.18E-09	0.9519	-1.46
Pentacosane	C25H52	8.45E-13	0.9714	2.30E-10	0.9672	-0.44
Hexacosane	C26H54	2.34E-13	0.9773	7.45E-11	0.9714	-0.61
Heptacosane	C27H56	4.57E-14	0.9828	1.81E-11	0.9795	-0.34
Octacosane	C28H58	9.96E-15	0.9916	4.55E-12	0.9743	-1.74

Abbreviations: T_{min}, minimum outdoor temperature, T_{max}, maximum outdoor temperature, P_L^o, saturation vapor pressure, F_p, particle-phase fraction.
[a]Property retrieved from the *Design Institute for Physical Property Research/AIChE (DIPPR®) project 801 database*.[26]

The diurnal trend shows a morning abundance increase (06:00-10:00) and a peak at 17:00 that could be associated with automotive commute emissions. However, the persistence of emissions late morning and throughout the afternoon (11:00-15:00) combined with the nighttime (21:00-23:00) enhancement, suggests contributions from various sources. This affirmation is reinforced by the absence of strong correlations and a non-predominant wind direction when Factor 1 is elevated.

To understand how PMF factorizes different source compounds into one factor, a simple analysis is performed as follows. The abundance timeseries of a Factor *j* is given by Equation 5.6.

$$FA_j(t) = \sum_{i=1}^{n}[P_i(t)]_j \quad \textbf{(5.6)}$$

Where $FA_j(t)$ is Factor *j* abundance timeseries; $[P_i(t)]_j$ is the time-dependent particle phase amount of compound *i* loaded into factor *j*; and *n* is the number of compounds loaded in factor *j*.

Defining $P_i(t) = F_{p,i}(t)C_i(t)$ where $F_{p,i}(t)$ is particle phase fraction of compound *i* at a given time, and $C_i(t)$ is the total, time-dependent particle plus gas amount of compound *i*, which can be understood as its emission rate $\dot{E}_i$, Equation 5.6 can be rewritten as:

$$FA_j(t) = \sum_{i=1}^{n}[F_{p,i}(t)\dot{E}_i]_j \quad \textbf{(5.7)}$$

From Equation 5.7, one can recognize that the abundance variability of a given factor is driven by changes in both the emission rate and the temperature-dependent particle-phase composition of these emissions. The strong co-variance of particle-bound concentrations of higher volatility compounds driven by temperature-induced changes in the compounds' volatility is therefore responsible for the factorized compounds loaded in Factor 1.

5.3.2. Factor 2: Hydrocarbon Emissions

As observed in **Figure 5.3**, Factor 2 is comprised primarily of heavier hydrocarbons. Docosane to octacosane have their highest contributions represented in this factor, with tetracosane and beyond showing at least double the signal compared to the value observed in their second-most abundance factors. The non-zero abundance timeseries suggest that these compounds are continuously emitted throughout the campaign. The diurnal profile indicates two different behaviors. The nightly increase (20:00-23:00) followed by the early morning decay (01:00-05:00) is consistent with residential heating habits. The lack of BB markers proposes that oil-fired device

emissions are the sole heating source contributing to the variability of this factor since domestic heating in interior Alaska substantially comes from burning fuel oil or biomass (92%-98%).[27]

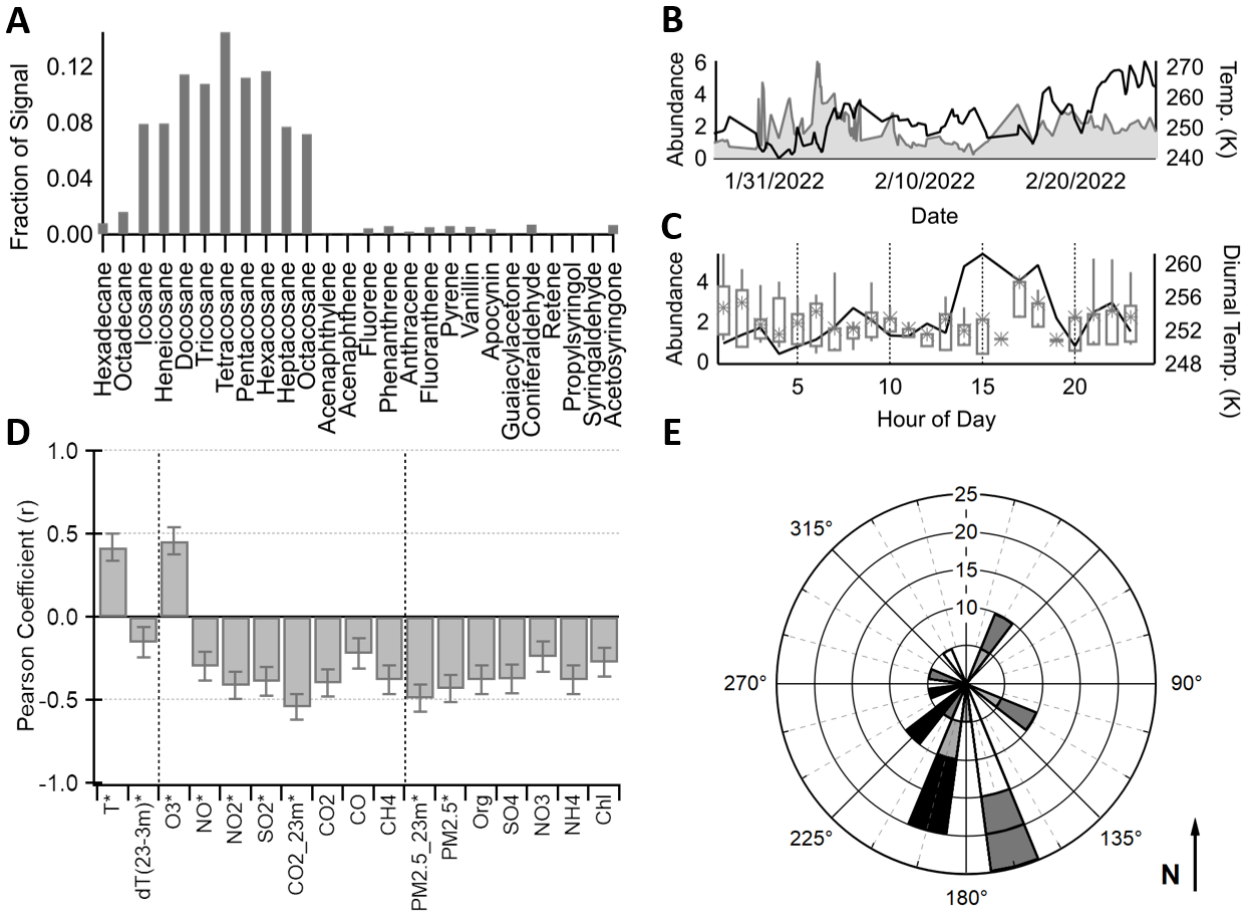

Figure 5.3. Factor 2 results. **(A)** Composition profile. **(B)** Factor timeseries (left) and outdoor temperature (right). **(C)** Diurnal variation. **(D)** Pearson correlation analysis. **(E)** Rose plot showing the correlation of abundances and wind direction. See Figure 5.2 description for further information on how to read this figure.

On the other hand, the morning enhancement (06:00-10:00) and the early-evening peak and decay (17:00-19:00) suggest automotive commute emissions. The absence of the lighter hexadecane and octadecane hydrocarbons expected from petroleum combustion[28,29] can be explained by the splitting of these more volatile emissions into Factor 1. Investigation of the correlation analysis demonstrates that the contribution of this factor tends to increase with

temperature, which is in better agreement with traffic-related than heating-related emissions. The counter-intuitive negative correlation of Factor 2 with well-known combustion trace gases and particulate matter emissions is associated with the weakening of the surface-based inversion as temperature increases throughout the day. The following paragraph describes this in more detail.

Strong nocturnal inversions, easily exceeding 0.5 $^{o}C.m^{-1}$ temperature gradient at the surface (**Figure A5.3** – Appendix A5 – Section A5.2) greatly hinder vertical mixing, leading to the accumulation of near-ground overnight emissions.[30] Contrarily, nighttime ozone concentrations tend to be their lowest due to the weak *in situ* photochemical production of O_3 in the Arctic, combined with ozone titration by accumulated NO.[31] As diurnal temperature increases, promoting stratosphere-troposphere air exchange, these trapped pollutants are dispersed while ozone concentration increases since the main source of Arctic wintertime tropospheric O_3 originates from stratospheric injection.[32] Therefore, emissions associated with diurnal temperature trends, such as commute-related traffic emissions, negatively correlate with accumulated ground-level pollutants (i.e. trace gases and particulate matter) and positively correlate with O_3, as seen in Factor 2.

The test house was located in a residential area without primary roads in the neighborhood, thus less impact from automobile emissions was foreseen. The closest well-traveled road, W Trainer Gate Rd, was located about 300 m south of the site (**Figure 5.1**). When Factor 2 abundances were elevated, winds exclusively originated from this direction and with relevant speeds (**Figure A5.4B** – Appendix A5 – Section A5.2), a highly plausible explanation for the observation of commute emissions at the house, and the apparent dominance of this source compared to heating-related emissions in Factor 2. This last statement is also corroborated by the almost double weekday average abundance compared to weekend measurements.

A recent source apportionment study in a residential area located in California showed significantly higher abundances from automobile tailpipes in the morning commute hours compared to late afternoon and evening return commute emissions.[33] This observation was understood as a result of cold engine start emissions in the early morning enhanced by cooler temperatures and generally slower wind speeds; that, in contrast to the afternoon emissions associated with warmer temperatures, increased wind speeds, and vehicle catalytic convertors already being hot, reasonably justifies the observed diurnal emission differences, since the combination of these three factors leads to the reduction and improved dispersion of pollutants.

Interestingly, during the ALPACA campaign, the opposite diurnal trend is observed. The 17:00 emissions tend to be greater than the morning peaks. The hypothesis for the exhibited diurnal profile is as follows. First, overnight hydrocarbon emissions from mobile sources are low, and the abundances observed in Factor 2 result from residential heating emissions. In Fairbanks, a study performed by Sierra Research reported that more than 98% of the residents adopt an overnight vehicle keep-warm strategy including heated garages and plug-in engine block heaters. The study also demonstrated that the common block heater plug-in during overnight soak and 5-minute warm-up idle after engine start reduced cold start $PM_{2.5}$ emissions by 74%.[34]

Therefore, the reduced early morning commute emissions from this factor analysis could be the result of more efficient overnight warmed-up engines, compared to the afternoon emissions, which show elevated abundances when pollution tends to be less accumulated thus, suggesting vehicle emissions contributions from less efficient engines. According to a test performed by Sierra Research in 2010-2011, not-plug-in vehicles emit 2 to 4 times more $PM_{2.5}$ compared to plug-in automobiles. The 15-minute test drive considered both overnight cold start emissions and emissions after parking the vehicle for 10 minutes at ambient temperatures of -25ºC and -11ºC.[34]

Therefore, the diurnal pattern observed in Factor 2 might be due to less effort to maintain engines warm when vehicles are not parked for very extended periods.

5.3.3. Factor 3: Overall Heating Emissions

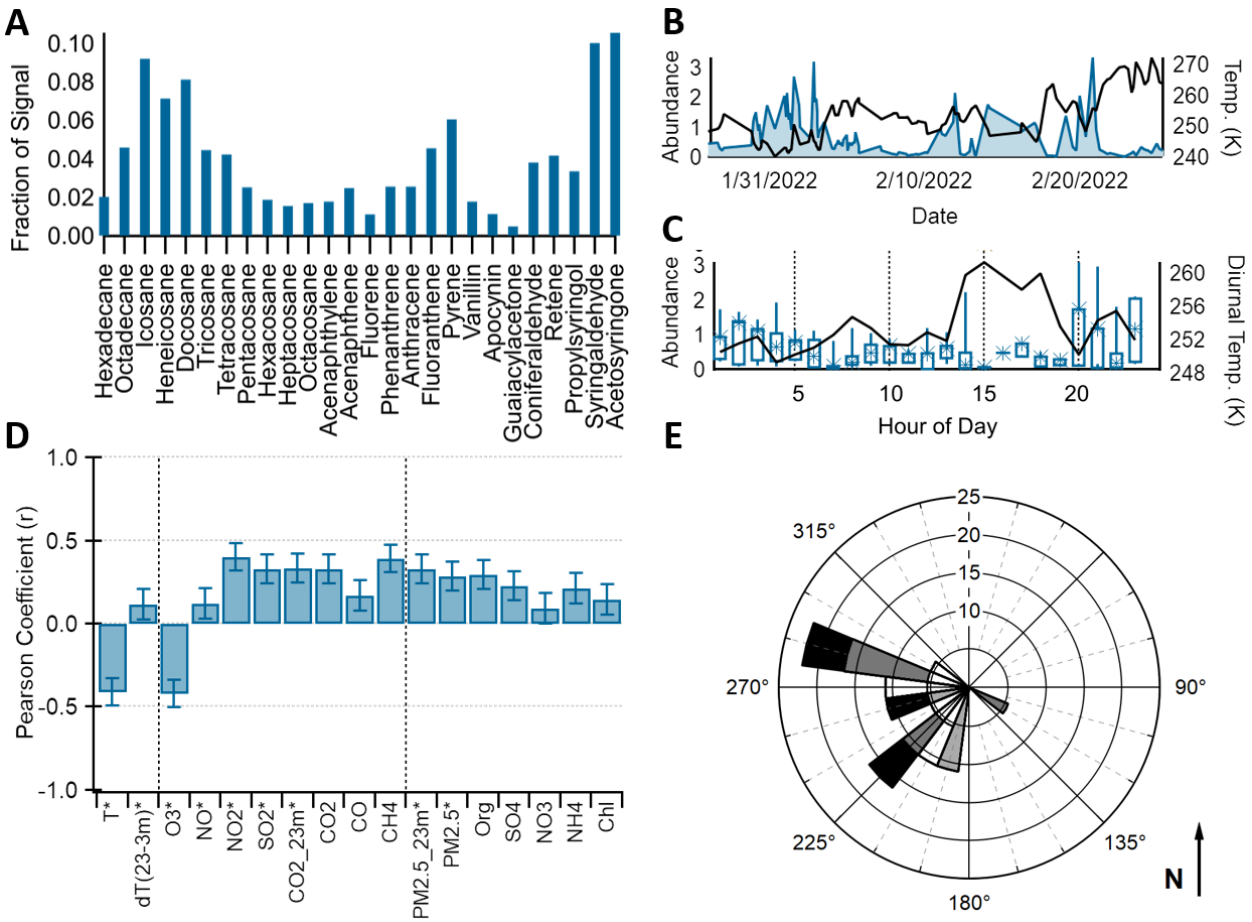

Figure 5.4. Factor 3 results. **(A)** Composition profile. **(B)** Factor timeseries (left) and outdoor temperature (right). **(C)** Diurnal variation. **(D)** Pearson correlation analysis. **(E)** Rose plot showing the correlation of abundances and wind direction. See Figure 5.2 description for further information on how to read this figure.

The chemical profile of Factor 3, shown in **Figure 5.4**, encompasses all three chemical groups considered in this analysis, i.e. hydrocarbons, polycyclic aromatic hydrocarbons (PAHs), and BB markers. The diurnal trend is consistent with residential heating habits, peaking at

nighttime with subsequent overnight decay. The continuous low emissions throughout the day confirm the dominance of heating sources depicted by this factor, with further ratification from the negative temperature correlation; meaning that Factor 3 abundances tend to increase with decreasing temperatures. The BB markers propylsyringol, syringaldehyde and acetosyringone have their highest contributions represented in this factor, corroborating the assignment of this factor to heating-related sources. Therefore, the PAHs and hydrocarbons loaded in this factor must originate from the combustion of heating-related fuels.

Western winds with moderate speeds prevailed when Factor 3 was elevated. (**Figure A5.4C** – Appendix A5 – Section A5.2). Geographically, the house site was located 350 m west to the base of Birch Hill (**Figure 5.1**), which abruptly rises at the eastern edge of Fairbanks. The absence of residences to the east of this edge and much denser population to the west validates the observed heating-related sources at the house site since eastern winds would probably contribute to the dilution of these emissions, whilst the western more polluted winds are potentially enhancing the measured concentrations.

A comprehensive study on the chemical characterization of fine particle emissions from fireplace combustion of woods grown in the northeastern United States, including, the hardwood species, maple, oak, and birch; and softwood, pine, hemlock, and fir, demonstrated that measured concentrations of syringaldehyde and acetosyringone from hardwood emissions were more than 4 times greater and emissions from softwood combustion. Birch woodsmoke was 40 times richer in propylsyringol compared to pine woodsmoke. Saturated hydrocarbons and PAHs were found only in trace amounts compared to the BB markers (**Figure A5.5** – Appendix A5 – Section A5.2).[35]

The signal fraction of alkanes and PAHs loaded in Factor 3 is comparable with the highest woodburning markers, suggesting that Factor 3 variability is influenced by both fuel oil and

domestic wood-burning emissions. Since 70-74% of the population of Fairbanks relies on fuel oil for domestic heating purposes[27] and hardwood combustion emissions co-varied with this more widely used heating fuel, it is hypothesized here that, hardwood is preferred over softwood species among residences equipped with solid fuel burning devices. This observation agrees with a recent survey[10] that reported that almost 70% of Fairbanks residents burn either Birch or Aspen logs, both species classified as hardwood.

5.3.4. Factor 4: Biomass Burning Emissions Enhancement

Factor 4 chemical profile is dominated by BB compounds with its diurnal trend in conformation with domestic heating patterns (**Figure 5.5**). However, in contrast with Factor 3, the species loaded in Factor 4 are predominantly emitted from the combustion of softwood.[35] Vanillin, apocynin, guiacylacetone, and coniferaldehyde are the major contributors to the variability of Factor 4, and as seen in **Figure A5.5** (Appendix A5 – Section A5.2), these compounds are, on average, twice more abundant in softwood than hardwood smoke. Moreover, retene, a potential marker for softwood combustion,[35,36] was found in higher amounts in Factor 4, proposing the assignment of this factor to softwood combustion sources.

A chemical mass balance source apportionment analysis using $PM_{2.5}$ data collected at different locations in Fairbanks over three winters (2009-2011), reported that woodsmoke sources accounted for 60%–80% of ground-level PM,[11] even with fuel oil being more widely used as heating fuel in the region. This is due to biomass emitting more $PM_{2.5}$ on a tons per day basis compared to other residential heating sources.[37] A PMF analysis conducted on Fairbanks particulate pollution measurements from 2005-2012, corroborated the large impact of wood combustion on poor air quality during the winter months, suggesting that 40.5% of $PM_{2.5}$ could be

attributed to this source.[12] Even though woodsmoke's contribution to ground-level pollution in Fairbanks seems to be in a downtrend,[15] it still accounts for a large portion of $PM_{2.5}$ in the region.

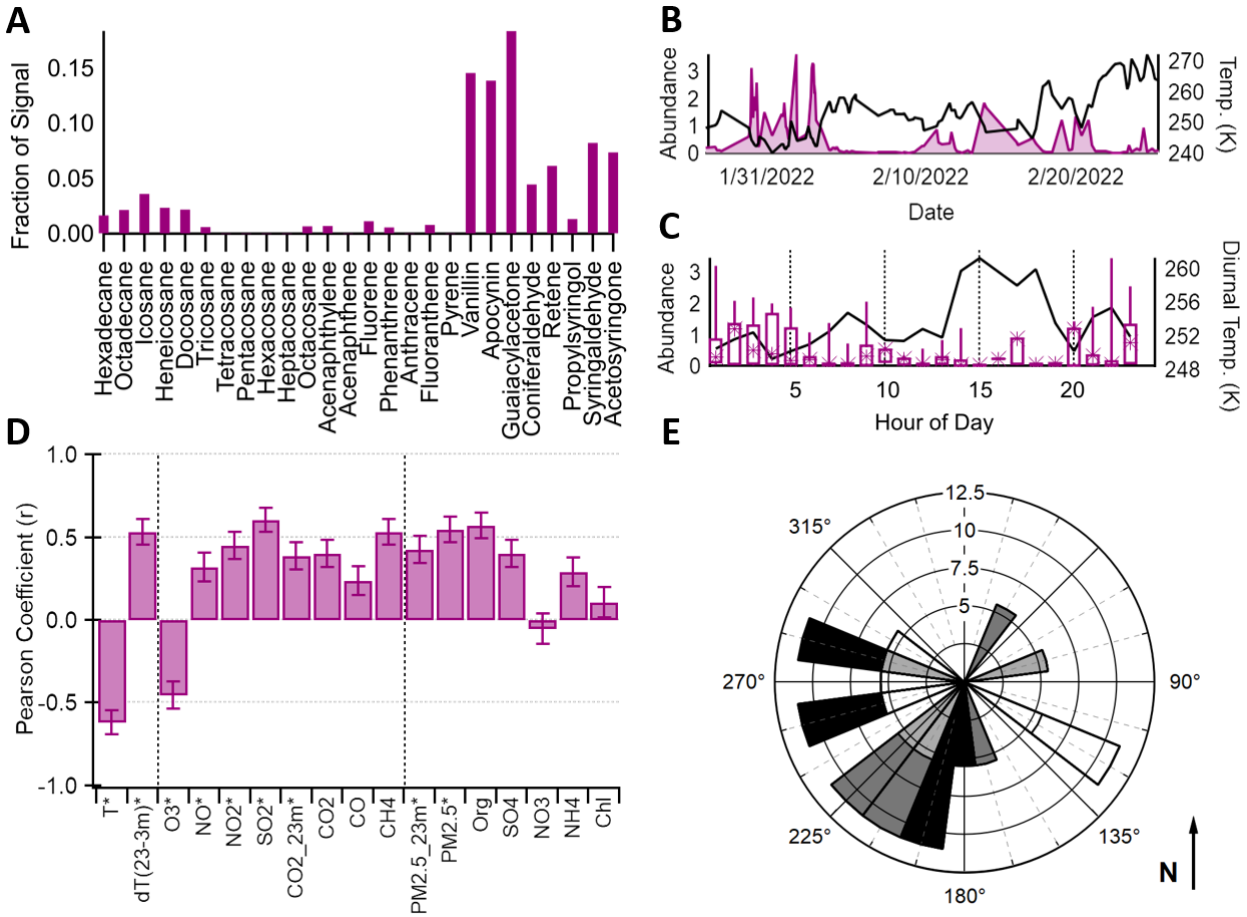

Figure 5.5. Factor 4 results. **(A)** Composition profile. **(B)** Factor timeseries (left) and outdoor temperature (right). **(C)** Diurnal variation. **(D)** Pearson correlation analysis. **(E)** Rose plot showing the correlation of abundances and wind direction. See Figure 5.2 description for further information on how to read this figure.

However, none of these studies addressed differences in woodsmoke emissions and pollution dynamics based on wood type due to the lack of speciated measurements. This PMF correlation analysis shows that Factor 4 abundances increase with the strength of the surface-based temperature inversions, indicating the enhancement of softwood combustion emissions at lower

temperatures. As previously observed in Factor 3 and corroborated by consumer attitudes in the region, hardwood species are preferred over softwood, thus the higher contribution of softwood during stronger inversions and lower temperatures is unlikely to be a representation of fuel switch under these extreme conditions. Furthermore, when $PM_{2.5}$ accumulation is foreseen, solid fuel burn bans are issued to avoid peak pollution events. Thus, the increase of Factor 4 during these periods is speculated to be related to differences in wood/woodsmoke chemical composition.

Wood is typically composed of about 25% lignin and 70% cellulosic carbohydrates.[38] Cellulose contains approximately 45% carbon, 6% hydrogen, and 49% oxygen, while lignin is about 60% carbon, 7% hydrogen, and 33% oxygen.[39] Softwood differs from hardwood in lignin content, with the former having proportionally more lignin.[40] This difference in elemental composition is reflected directly in the compounds emitted during combustion and thus, is responsible for the wood-type volatility-dependence of biomass-burning organic aerosol (BBOA).

A recent publication measured the gas and particle components of primary organic compounds emitted from soft- and hardwood log and mixed-pellet burning; and of secondary products formed from these emissions in an oxidation flow reactor.[41] The authors observed that the gas and particle spectra of aged spruce (softwood) and birch (hardwood) emissions were comparable, but the spruce primary gas-phase spectrum contained many more peaks compared to birch's spectrum, suggesting the formation of more volatile species from softwood combustion. In addition, laboratory studies using distinct fuelwood have reported size distributions with larger mode diameters from softwood combustion compared to hardwood under similar burning conditions.[42,43] This difference in particle sizes has been suggested to be the result of the higher content of more volatile organic species in softwood smoke that condenses on the soot particles due to the lower sampling temperatures compared to burning conditions.

Thus, it is hypothesized here that the condensation of higher volatility compounds from softwood combustion is enhanced during strong inversions due to the low-temperature-induced shift in the compounds' vapor pressures. Moreover, since under these conditions, particulate pollution is accumulated near ground, gas-to-particle partitioning is expected to be accentuated by the increase in available surface area for condensation. Non-predominant winds when Factor 4 is elevated combined with lower speeds (**Figure A5.4D** – Appendix A5 – Section A5.2) support the accumulation of emissions. The strong correlation of Factor 4 and total organics measured at the house and $PM_{2.5}$ at the CTC site validates the conjectured PM-influenced partitioning dynamics. These results are corroborated by a study published in 2019 that, by applying diagnostic ratios from lignin, resin acids and anhydrosugars measurements, reported softwood combustion as the dominant source of BB-related particulate pollution in Fairbanks from June 2008 to June 2009.[44]

5.3.5. Factor 5: Polycyclic Aromatic Hydrocarbon (PAH) Emissions

The last factor resulting from this source apportionment analysis is highlighted in **Figure 5.6**. Hydrocarbons, BB markers, and PAHs are present in Factor 5 however, the latter species dominate the PMF source profile. Indeed, the observed PAHs signals are two to six times higher than the values measured in their second-most abundance factors. PAHs are ubiquitous in the atmosphere. Classified as persistent organic pollutants, they originate from biogenic and anthropogenic sources. Natural processes include wildfires, volcanic eruptions, and diagenesis; whilst the combustion of coal, wood, and petroleum derivatives such as gasoline, diesel, and oil are among the major PAHs sources derived from human activities.[45,46] The nighttime enhancement succeeded by early morning decay diurnal pattern demonstrates PAHs contribution from domestic

heating sources. However, abundance spikes throughout the day suggest the additional influence of point source emissions.

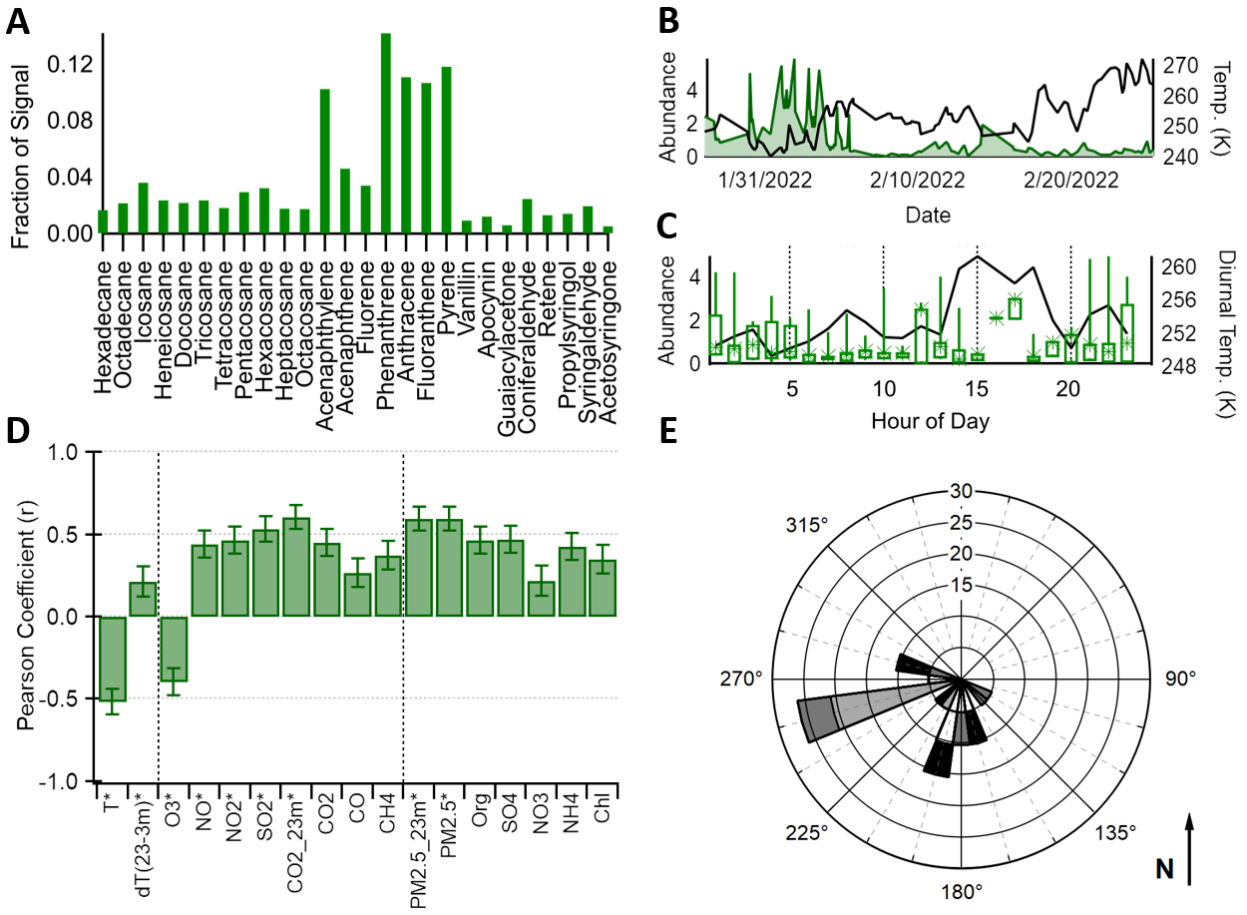

Figure 5.6. Factor 5 results. **(A)** Composition profile. **(B)** Factor timeseries (left) and outdoor temperature (right). **(C)** Diurnal variation. **(D)** Pearson correlation analysis. **(E)** Rose plot showing the correlation of abundances and wind direction. See Figure 5.2 description for further information on how to read this figure.

Higher concentrations prevailed at the beginning of the campaign when temperatures were the lowest, elucidated by the strong negative correlation between Factor 5 and ambient temperatures. Interestingly, the contribution of this factor tended to co-vary with CO_2 and $PM_{2.5}$ emissions at 23 m. This observation insinuates that Factor 5 variability is associated with more well-mixed atmospheric conditions (i.e. weak surface-based temperature inversions), a statement

confirmed in **Figure A5.6** (Appendix A5 – Section A5.2). Winds originated from the west with moderate speeds (**Figure A5.4E** – Appendix A5 – Section A5.2) when this factor was high. Also located western to the house site were two power plants: the coal-fired Aurora power plant, and the diesel-based Zehnder power plant. The less-stable atmospheric conditions when PAHs abundances were elevated, leave one questioning if power generation emissions could be impacting air quality in the Shannon Park neighborhood during the ALPACA campaign.

PAHs diagnostic ratios have been widely used to qualitatively identify and assess pollution emission sources.[47] For instance, investigation of the PAHs sources at a Koren industrial complex using both diagnostic ratios and multivariate statistic methods, led to the assessment that coal combustion was the predominant source, followed by traffic emissions, and industrial processes.[48] Outcomes of diagnostic ratios, principal component analysis, and back trajectory analysis suggested that air quality in a coastal, non-industrial site in Belgium was primarily impacted by vehicular and coal combustion emissions.[49]

However, prudence is required when using PAHs diagnostic ratios, as their values may change as a result of the environmental transformations these compounds undergo. Species examined must have similar reactivity to atmospheric oxidants and solar radiation in both gas and particle phases on the relevant timescales.[50] The ratios ANT/(ANT+PHE)* and BaA/(BaA + CHR)* are more sensitive to photodegradation than the ratios FLA/(FLA + PYR)* and IcdP/(IcdP + BghiP)*.[47] Furthermore, given the semi-volatile nature of PAHs, total concentrations (gas and particle phases) must be used to calculate diagnostic ratios since gas-particle phase partitioning has the potential to delude interpretations.[47,51-52]

* ANT/(ANT+PHE) is the ratio of the species anthracene and phenanthrene; BaA/(BaA + CHR) is benzo[a]anthracene and chrysene diagnostic ratio; FLA/(FLA + PYR) considers the fluoranthene and pyrene concentrations, and IcdP/(IcdP + BghiP) represents the indeno[1,2,3-c,d]pyrene and benzo[g,h,i]perylene species.

To determine the major emission sources of PAHs in Factor 5, the quantified non-denuded (gas plus particle) FLA/(FLA + PYR) diagnostic ratio is investigated. According to previous studies,[47-49,51,52] if the above ratio is below 0.4, the PAHs have a petrogenic source, entering the ambient air by evaporation of petroleum derivative products. If the ratio is above 0.4, the PAHs are formed by pyrogenic processes. More specifically, a FLA/(FLA + PYR) value between 0.4 - 0.5 indicate PAHs formed by the combustion of liquid fossil fuel (i.e. diesel, gasoline); while a ratio above 0.5 is associated with the combustion of organic matter such as grass, wood and coal.

Figure 5.7 highlights the diagnostic ratio source apportionment results. FLA/(FLA + PYR) values are plotted against Factor 5 abundances. The colored markers represent Factor 5 abundances above one standard deviation of the mean in order to emphasize the potential dominant source. The first observation from this analysis is that the PAHs loaded in Factor 5 seem to originate from pyrogenic emissions, not surprisingly since petrogenic evaporative contributions are expected to be minimal due to the low wintertime temperatures.

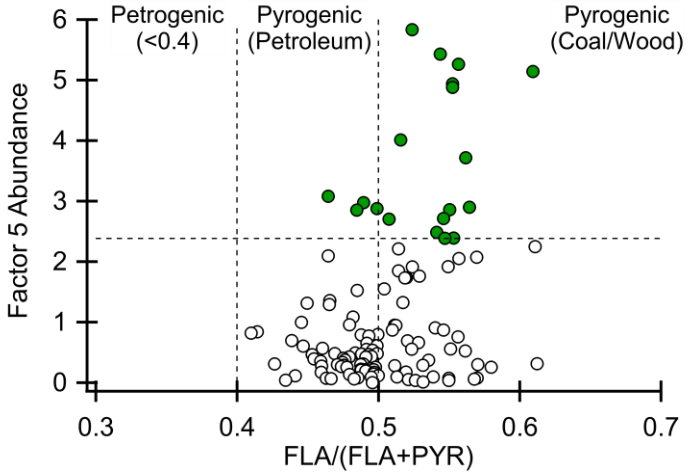

Figure 5.7. Polycyclic aromatic hydrocarbon (PAH) diagnostic ratio source apportionment analysis. The ratio considering fluoranthene (FLA) and pyrene (PYR) gas and particle concentrations is plotted against Factor 5 abundances. The colored markers represent the abundances above one standard deviation of the mean factor abundance.

Further investigation of **Figure 5.7** shows that about 79% of Factor 5 highest abundances (colored markers) are associated with FLA/(FLA + PYR) ratios greater than 0.5, indicating biomass or coal contributions. The low BB markers signals in Factor 5 chemical profile suggests minimal impact of wood combustion on these elevated concentrations, and coal emissions must be the dominant source of PAHs in Factor 5. As previously stated, the coal-fired Aurora power plant is located western to the house, and winds originated from the same direction when Factor 5 was elevated. Although having moderately high smokestack (48 m), downwash, associated with less stable conditions, could be an explanation for the potential coal observations at the house site.

For the decreased PAHs abundances (white markers), it is expected that residential heating oil ($0.4 < FLA/(FLA + PYR) < 0.5$) and BB emissions ($FLA/(FLA + PYR) > 0.5$) are the contributing sources to the variability of Factor 5, since during these times, more stable conditions prevailed, and the dominant influence of ground-level emissions is foreseen. It is important to mention that the above interpretation suggests but does not confirm the presence of coal combustion emissions at the house site given the lack of coal-burning markers in this PMF source apportionment analysis and the convoluted coal/biomass PAHs diagnostic ratios. Thus, additional work is recommended to fully assess the impact of power plant emissions to ground-level pollution during wintertime in the FNSB area.

5.4. Conclusions

In this work, PMF analysis was performed to selected quantified particulate organic compounds measured by the SV-TAG during the ALPACA campaign to identify major components contributing to submicron wintertime pollution in a residential neighborhood in Fairbanks. Five factors were found to best describe the sources and dynamics of air pollution in the area.

A factor associated with semi-volatile species demonstrated that the temperature-induced shift in compounds' vapor pressures led to significant changes in their particulate and gas phase emissions. The identification of this factor has major implications for understanding the fate of individual species after being emitted into the atmosphere, and in evaluating the contribution of different sources to particulate and gaseous air pollution.

The hydrocarbon-rich factor showed that even in the absence of major arterial roads in the neighborhood, traffic commute emissions impact air quality in this residential area. In addition, the higher return commute emissions, when pollution tends to be less accumulated during late afternoon/early evening times, suggested dominant contributions from less efficient vehicles, likely due to less effort to keep engines warm when not parked overnight. Although further investigation in the region is necessary for conclusion validation, these results could lead to more programs to incentivize engine-keep-warm behaviors.

The overall heating factor demonstrated both the impact of fuel oil and BB to air quality. The higher contribution of hardwood in this factor compared to softwood combustion species indicated the preference for the former when solid fuel is used. Increased softwood emissions were observed when surface-based temperature inversions prevailed. This factor was understood as an enhancement factor resulting from increased gas-to-particle partitioning of softwood smoke species at lower temperatures and polluted conditions. Although increasingly efforts are being made to reduce the use of wood as a heating fuel, understanding the impact of softwood and hardwood emissions to wintertime air pollution in the Arctic can help in creating mitigation strategies during the transition process to cleaner fuels.

Finally, the variability of the PAH-rich factor seemed to be influenced by both residential heating and power generation emissions, specifically coal combustion. However, due to the lack

of coal combustion markers in this analysis, these observations must be further investigated to confirm the downwash of power plant emissions and its impact on ground-level air quality.

References

1. Environmental Protection Agency (EPA). Air Plan Partial Approval and Partial Disapproval; AK, Fairbanks North Star Borough; 2006 24-Hour PM2.5 Serious Area and 189(d) Plan. *Federal Register*. 2023;88(232):84626-84676.

2. National Oceanic and Atmsopheric Administration. National Weather Service. NOAA. Accessed March 2024. https://www.weather.gov/wrh/Climate

3. Schmale J, Arnold SR, Law KS, et al. Local Arctic Air Pollution: A Neglected but Serious Problem. *Earth's Future*. 2018;6(10):1385-1412.

4. Mayfield JE, Fochesatto GJ. The Layered Structure of the Winter Atmospheric Boundary Layer in the Interior of Alaska. *Journal of Applied Meteorology and Climatology*. 2013;52(4).

5. Robinson ES, Cesler-Maloney M, Tan X, Mao J, Simpson W, DeCarlo PF. Wintertime spatial patterns of particulate matter in Fairbanks, AK during ALPACA 2022. *Environmental science*. 2023;3(3):568-580.

6. World Health Organization (WHO). Ambient (outdoor) air quality and health. Published December 19, 2022. Accessed March 2024. https://www.who.int/news-room/fact-sheets/detail/ambient-(outdoor)-air-quality-and-health

7. Transportation Research Board and National Research Council. *The Ongoing Challenge of Managing Carbon Monoxide Pollution in Fairbanks, Alaska*. National Academies Press; 2002.

8. Environmental Protection Agency (EPA). Summary of Fairbanks Carbon Monoxide (CO) Maintenance Plan. Accessed March 2024. https://www.epa.gov/air-quality-implementation-plans/summary-fairbanks-carbon-monoxide-co-maintenance-plan-and-second

9. Alaska Department of Environmental Conservation (ADEC). Fairbanks Air Quality Monitoring Data - CO. Accessed March 2024. https://dec.alaska.gov/air/air-monitoring/alaska-concerns/community-data/fairbanks-co-data/

10. Alaska Department of Environmental Convservation (ADEC). *Serious SIP Requirements, Appendix III.D.7.6 Emissions Inventory Data Amended and Adopted*.; 2019.

11. Ward T, Trost B, Conner J, Flanagan J, Jayanty RKM. Source Apportionment of PM2.5 in a Subarctic Airshed - Fairbanks, Alaska. *Aerosol and Air Quality Research*. 2012;12(4):536-543.

12. Wang Y, Hopke PK. Is Alaska Truly the Great Escape from Air Pollution? – Long Term Source Apportionment of Fine Particulate Matter in Fairbanks, Alaska. *Aerosol and Air Quality Research*. 2014;14(7):1875-1882.

13. Fairbanks North Star Borough. Change Out Programs. Accessed March 2024. https://www.fnsb.gov/386/Change-Out-Programs

14. Alaska Department of Environmental Conservation (ADEC). Air Quality Advisories/Episodes. Accessed March 2024. https://dec.alaska.gov/Applications/Air/airtoolsweb/Advisories/

15. Ye L, Wang Y. Long-Term Air Quality Study in Fairbanks, Alaska: Air Pollutant Temporal Variations, Correlations, and PM2.5 Source Apportionment. *Atmosphere*. 2020;11(11):1203.

16. Moon A, Jongebloed U, Dingilian KK, et al. Primary Sulfate Is the Dominant Source of Particulate Sulfate during Winter in Fairbanks, Alaska. *ACS ES&T Air*. 2024;1(3).

17. Simpson WR, Mao J, Fochesatto GJ, et al. Overview of the Alaskan Layered Pollution And Chemical Analysis (ALPACA) Field Experiment. *ACS ES&T Air*. 2024;1(3).

18. DeCarlo PF, Kimmel JR, Trimborn A, et al. Field-Deployable, High-Resolution, Time-of-Flight Aerosol Mass Spectrometer. *Analytical Chemistry*. 2006;78(24):8281-8289.

19. Paatero P, Tapper U. Positive matrix factorization: A non-negative factor model with optimal utilization of error estimates of data values. *Environmetrics*. 1994;5(2):111-126.

20. Williams BJ, Goldstein AH, Kreisberg NM, et al. Major components of atmospheric organic aerosol in southern California as determined by hourly measurements of source marker compounds. *Atmospheric Chemistry and Physics*. 2010;10(23):11577-11603.

21. Fortenberry C, Walker M, Dang A, et al. Analysis of indoor particles and gases and their evolution with natural ventilation. *Indoor Air*. 2019;29(5):761-779.

22. Williams BJ, Goldstein AH, Kreisberg NM, Hering SV. An In-Situ Instrument for Speciated Organic Composition of Atmospheric Aerosols:Thermal DesorptionAerosol GC/MS-FID (TAG). *Aerosol Science and Technology*. 2006;40(8):627-638.

23. Kreisberg NM, Hering SV, Williams BJ, Worton DR, Goldstein AH. Quantification of Hourly Speciated Organic Compounds in Atmospheric Aerosols, Measured by an In-Situ Thermal Desorption Aerosol Gas Chromatograph (TAG). *Aerosol Science and Technology*. 2009;43(1):3852.

24. Ulbrich IM, Canagaratna MR, Zhang Q, Worsnop DR, Jimenez JL. Interpretation of organic components from Positive Matrix Factorization of aerosol mass spectrometric data. *Atmospheric Chemistry and Physics*. 2009;9(9):2891-2918.

25. Shelly E. *EPA PMF User's Guide, 1.1*. Environmental Protection Agency; 2005.

26. American Institute of Chemical Engineers (AIChE). *DIPPR Project 801 - Full Version*. Design Institute for Physical Property Research

27. Sierra Research, Inc. *Analysis of Fairbanks 2013-2015 Home Heating Surveys*. Alaska Department of Environmental Conservation; 2015.

28. Drozd GT, Zhao Y, Saliba G, et al. Detailed Speciation of Intermediate Volatility and Semivolatile Organic Compound Emissions from Gasoline Vehicles: Effects of Cold-Starts and Implications for Secondary Organic Aerosol Formation. *Environmental Science and Technology*. 2019;53(3):1706-1714.

29. Drozd GT, Weber RJ, Goldstein AH. Highly Resolved Composition during Diesel Evaporation with Modeled Ozone and Secondary Aerosol Formation: Insights into Pollutant Formation from Evaporative Intermediate Volatility Organic Compound Sources. *Environmental Science & Technology*. 2021;55(9):5742-5751.

30. Tran HNQ, Mölders N. Investigations on meteorological conditions for elevated PM2.5 in Fairbanks, Alaska. *Atmospheric Research*. 2011;99(1):39-49.

31. Cesler-Maloney M, Simpson WR, Miles T, Mao J, Law KS, Roberts TJ. Differences in Ozone and Particulate Matter Between Ground Level and 20 m Aloft are Frequent During Wintertime Surface-Based Temperature Inversions in Fairbanks, Alaska. *Journal of Geophysical Research: Atmospheres*. 2022;127(10).

32. Whaley CH, Law KS, Jens Liengaard Hjorth, et al. Arctic tropospheric ozone: assessment of current knowledge and model performance. *Atmospheric Chemistry and Physics*. 2023;23(1):637-661.

33. Wernis RA, Kreisberg NM, Weber RJ, Drozd GT, Goldstein AH. Source apportionment of VOCs, IVOCs and SVOCs by positive matrix factorization in suburban Livermore, California. *Atmospheric Chemistry and Physics*. 2022;22(22):14987-15019.

34. Sierra Research, Inc. *Characterizing Vehicular Contributions to PM2.5 in Fairbanks, Alaska. Volume 1: Dynamometer-Based Emissions Measurements, Vehicle Keep-Warm Activities and MOVES Analysis.* Alaska Department of Environmental Conservation; 2011.

35. Fine PM, Cass GR, Simoneit BRT. Chemical Characterization of Fine Particle Emissions from Fireplace Combustion of Woods Grown in the Northeastern United States. *Environmental Science & Technology*. 2001;35(13):2665-2675.

36. Rogge WF, Hildemann LM, Mazurek MA, Cass GR, Bernd R. T. Simoneit. Sources of Fine Organic Aerosol. 9. Pine, Oak, and Synthetic Log Combustion in Residential Fireplaces. *Environmental Science & Technology*. 1998;32(1):13-22.

37. Alaska Department of Environmental Conservation (ADEC). *Amendments To: State Air Quality Control Plan. Section III.D.5.1-5.14*.; 2016.

38. Sjostrom E, Sjèostrèom E. *Wood Chemistry Fundamentals and Applications*. Elsevier Science; 2013.

39. Helfferich C. Hardwood, Softwood, Fuelwood | Geophysical Institute. www.gi.alaska.edu. Published October 1990. Accessed March 2024. https://www.gi.alaska.edu/alaska-science-forum/hardwood-softwood-fuelwood

40. Tarasov D, Leitch M, Fatehi P. Lignin–carbohydrate complexes: properties, applications, analyses, and methods of extraction: a review. *Biotechnology for Biofuels*. 2018;11(1).

41. Priestley M, Kong X, Pei X, et al. Volatility Measurements of Oxygenated Volatile Organics from Fresh and Aged Residential Wood Burning Emissions. *ACS Earth and Space Chemistry*. 2024;8(2):159-173.

42. Maruf Hossain AMM, Park S, Kim JS, Park K. Volatility and mixing states of ultrafine particles from biomass burning. *Journal of Hazardous Materials*. 2012;205-206:189-197.

43. Simões Amaral S, Andrade de Carvalho Junior J, Martins Costa MA, Soares Neto TG, Dellani R, Scavacini Leite LH. Comparative study for hardwood and softwood forest biomass: Chemical characterization, combustion phases and gas and particulate matter emissions. *Bioresource Technology*. 2014;164:55-63.

44. Haque MM, Kawamura K, Deshmukh DK, Kunwar B, Kim Y. Biomass Burning is an Important Source of Organic Aerosols in Interior Alaska. *Journal of Geophysical Research: Atmospheres*. 2021;126(12).

45. Iqbal J, Overton EB, Gisclair D. Polycyclic Aromatic Hydrocarbons in Louisiana Rivers and Coastal Environments: Source Fingerprinting and Forensic Analysis. *Environmental Forensics*. 2008;9(1):63-74.

46. Abdel-Shafy HI, Mansour MSM. A review on polycyclic aromatic hydrocarbons: Source, environmental impact, effect on human health and remediation. *Egyptian Journal of Petroleum*. 2016;25(1):107-123.

47. Tobiszewski M, Namieśnik J. PAH diagnostic ratios for the identification of pollution emission sources. *Environmental Pollution*. 2012;162:110-119.

48. Park SU, Kim JG, Jeong MJ, Song BJ. Source identification of atmospheric polycyclic aromatic hydrocarbons in industrial complex using diagnostic ratios and multivariate factor analysis. *Archives of Environmental Contamination and Toxicology*. 2011;60(4):576-589.

49. Ravindra K, Dirtu AC, Mor S, Wauters E, Van Grieken R. Source apportionment and seasonal variation in particulate PAHs levels at a coastal site in Belgium. *Environmental Science and Pollution Research*. 2020;27(13):14933-14943.

50. Galarneau E. Source specificity and atmospheric processing of airborne PAHs: Implications for source apportionment. *Atmospheric Environment*. 2008;42(35):8139-8149.

51. Ströher GL, Ré Poppi N, Raposo JL, Batista J. Determination of polycyclic aromatic hydrocarbons by gas chromatography — ion trap tandem mass spectrometry and source identifications by methods of diagnostic ratio in the ambient air of Campo Grande, Brazil. *Microchemical Journal*. 2007;86(1):112-118.

52. Zhao J, Zhang F, Chen J, Xu Y. Characterization of polycyclic aromatic hydrocarbons and gas/particle partitioning in a coastal city, Xiamen, Southeast China. *Journal of Environmental Sciences*. 2010;22(7):1014-1022.

CHAPTER 6

Conclusions

This dissertation provides scientific advances for the characterization of organic aerosol (OA) through the development of novel instrumentation and methods, and the application of these techniques to investigate the process influencing the variability of atmospheric OA volatility and chemical composition. This chapter summarizes key findings and discusses future directions expanding upon the presented work.

6.1. Major Results

6.1.1. Chapter 2: Volatility Characterization of Organic Aerosols through Thermal Evaporation and Thermal Desorption Gas Chromatography-Mass Spectrometry Techniques

In elucidating the challenges in recovering organic aerosol volatility information from the thermal evaporation of a size-selected aerosol population, it was demonstrated that the multicharged response has a larger influence on thermograms than the singly charged particles, and thus must be considered when solving the time-dependent mass transfer equation that computes the shrinkage of the particles due to evaporation. The complexity of volatility characterization using thermal evaporation measurements alone led to the combination of different techniques (i.e. thermal evaporation and thermal desorption gas-chromatography mass spectrometry – TD-GC/MS) to constrain OA volatility with chemical information, which demonstrated improvements in OA characterization. For instance, it was observed that thermally labile compounds dominate monoterpene ozonolysis secondary OA (SOA), with the least volatile species decomposing into small fragments, eluting in GC retention time windows that do not correspond to their actual

volatility. By combining both techniques, it was also possible to observe that these fragments originating from the low-volatility SOA components were also less oxidized, proposing oligomerization during SOA formation. Limonene ozonolysis SOA were more volatile and had higher oxygen-to-carbon ratios than α-pinene- and β-pinene-originating SOA. The observed differences in volatility and oxidation levels across the different aerosol systems exemplified the complexity of SOA formation and transformation pathways, providing insights into the extent and factors contributing to these processes (such as oligomerization reactions and SOA thermal stability) that are still poorly understood.[1,2]

6.2.2. Chapter 3: Development and Characterization of the Semi-Volatile Thermal Desorption Aerosol Gas Chromatograph (SV-TAG) with an Automatic Calibration Injection System

The incorporation of a newly designed Filter-Tenax® Collection and Thermal Desorption (FT-CTD) cell into the custom-developed Semi-Volatile Thermal Desorption Aerosol Gas Chromatograph (SV-TAG) system demonstrated improved sub-nanogram quantification of intermediate volatility and semi-volatile organic compounds (I/SVOCs). Compared to the single-stage metal fiber filter collector, the novel dual-stage design captured more than 3 times the total ion chromatogram signal between 4.5 and 8.5 minutes, which corresponds to the GC elution window of higher volatility species. The evident high efficiency of the dual-stage design in collecting lower boiling point compounds translates into a more versatile and more capable instrument in the study of I/SVOC emissions and transformations which was demonstrated by deploying the instrument to investigate the dynamics of air pollution during the extreme Arctic wintertime conditions (with the results discussed in Chapters 4 and 5).

6.2.3. Chapter 4: Investigation of Gas-Particle Phase Partitioning of Speciated Organic Compounds during the Alaskan Layered Pollution And Chemical Analysis (ALPACA) Field Campaign

From the SV-TAG measurements obtained during the Alaskan Layered Pollution And Chemical Analysis (ALPACA) field campaign, it was observed that temperature-induced shifts in both particle volatility and viscosity influence the evaporation and condensation behavior of atmospheric OA under cold and dark conditions. Three different partitioning regimes were identified based on the outdoor particle-bound measurements of compounds of varying volatilities under transient ambient conditions. Compounds of both high- and low-saturation concentrations were found to partition solely after a threshold temperature was reached and thus, two different temperature-limited regimes were established. Compounds of saturation concentrations within the bounds of these extremes demonstrated a temperature-dependent behavior where dynamic gas-particle transfer was observed. However, this phase transfer dynamic was found to be also dependent on bulk diffusivity due to kinetic limitations arising from the increase in particle viscosity with decreasing temperatures. The observed slow evaporation rates after infiltration were also justified by the low molecular diffusivity. These results elucidate that the assumption of instantaneous reversible equilibrium used to predict gas-particle phase partitioning is not suitable for describing this process in the extreme Arctic winter environment.

6.2.4. Chapter 5: Sources and Dynamics of Wintertime Air Pollution during the Alaskan Layered Pollution And Chemical Analysis (ALPACA) Field Campaign

Source apportionment via Positive Matrix Factorization (PMF) was performed on a subset of quantified particulate organic compounds measured by the SV-TAG during the ALPACA campaign. Five components contributing to submicron pollution in a residential neighborhood in

Fairbanks were identified. A factor associated with semi-volatile species demonstrated the relevance of understanding the dynamics of gas-particle phase partitioning under the extreme Arctic wintertime conditions in order to predict the fate of individual species after being emitted into the atmosphere, and to evaluate the contribution of different sources to gaseous and particulate air pollution. The identification of a traffic commute factor showed that even in the absence of major arterial roads in the neighborhood, automobile emissions impact air quality in the residential site. The higher return commute abundances, possibly associated with emissions from cold engines, suggest less effort to keep engines warm when vehicles are not parked overnight. Both fuel oil and wood combustion were major sources of ground-level pollution during the study. While hardwood species were found to be the preferred solid fuel, softwood emissions were enhanced during strong inversions. Polycyclic aromatic hydrocarbons measured at the house site appeared to be associated with both residential heating and power generation emissions. These findings can aid in creating mitigation strategies, such as incentivizing engine-keep-warm and fuel-switch behaviors, to improve wintertime air quality in the Fairbanks area.

6.2. Future Work

6.2.1. Chapter 2: Volatility Characterization of Organic Aerosols through Thermal Evaporation and Thermal Desorption Gas Chromatography-Mass Spectrometry Techniques

Although the observed volatility-oxidation relationship suggested oligomerization during SOA formation, the SOA thermal instability and fragmentation-induced instrumentation applied to study this aerosol system precluded the chemical investigation necessary to confirm the presence of high molecular weight species. Further elucidation of these reactions requires analytical

methods that induce less fragmentation so that molecular weight distributions and mass concentrations can be determined. Using soft ionization mass spectrometry, one could investigate the bulk thermal stability of different SOA by exposing the aerosol system to different temperatures. The results would help in understanding the uncertainties associated with studying SOA evaporation rates and, in addition, help determine the thermal desorption temperatures and rates in the GC/MS system that minimize decomposition. For highly thermally labile material, the application of two-dimensional GC/MS such as the Volatility and Polarity Separator (VAPS)[3] would considerably improve oxidation level estimations within predetermined volatility dimensions, composing a robust system for OA chemical-speciated volatility characterization.

6.2.2. Chapter 3: Development and Characterization of the Semi-Volatile Thermal Desorption Aerosol Gas Chromatograph (SV-TAG) with an Automatic Calibration Injection System

The trapping of low boiling point I/SVOCs through the adsorbent Tenax® TA installed in the newly developed FT-CTD cell improved the quantification of high volatility species, expanding the analytical capability of the SV-TAG system. However, positive and negative sampling artifacts arise from the exposure of the polymer to reactive species, requiring the development of specific calibration procedures to both characterize and minimize artifact formation that can interfere with the measurements of target analytes. The SV-TAG also features a focusing trap column that, by pre-concentrating the desorbed sample prior to injection onto the GC column, allows much higher desorption flow rates, increasing the time resolution of the instrument. During this step, any decomposition fragments are purged through the vent. However, as exemplified in Chapter 2 and demonstrated in previous studies, the thermal decomposition data holds valuable information, providing insights about aerosol classes not observable with typical gas chromatography.[4,5] The

SV-TAG system could be further improved if this decomposition data was retained without compromising the time resolution of the instrument. A consideration is the installation of a quadrupole residual gas analyzer downstream of the trap column to detect the species that are too volatile to be efficiently trapped and analyzed by the GC/MS system.

6.2.3. Chapter 4: Investigation of Gas-Particle Phase Partitioning of Speciated Organic Compounds during the Alaskan Layered Pollution And Chemical Analysis (ALPACA) Field Campaign

The results presented in Chapter 4 represent cutting-edge field observations on the interplay of volatility distribution and particle viscosity governing the dynamics of gas-particle partitioning under cold and dark conditions. The SV-TAG measurements suggested that OA low-bulk diffusivities and long mixing affect the spatiotemporal distributions of atmospheric pollutants. However, further information on advanced and detailed multiphase processes is required to describe the OA lifecycle in atmospheric models. For instance, the growth of SOA particles is critically affected by the complex interplay between partitioning and reaction in both gas and particle phases.[6] Thus, laboratory studies on OA evaporation, condensation, and chemical reactions involving relevant atmospheric pollutants under different ambient conditions are recommended for continuing progress in addressing the impact of OA on climate, air quality, and public health.

6.2.4. Chapter 5: Sources and Dynamics of Wintertime Air Pollution during the Alaskan Layered Pollution And Chemical Analysis (ALPACA) Field Campaign

Although it provides practical knowledge about the major components contributing to poor wintertime air quality in a residential neighborhood in Fairbanks, this PMF source apportionment

analysis included only a few individual compounds. However, the SV-TAG data set contains far more information than what was explored in Chapter 5. Additional details about the sources and dynamics of air pollution can be investigated by considering a higher number of chemical species.[7,8] Furthermore, performing PMF analysis on the non-denuded (gas plus particle) measurements allows for the examination of source-specific phase partitioning dynamics; while including the indoor data and relevant indoor compounds provides a means to understand the processes dictating indoor air quality upon infiltration. Unresolved complex mixtures also contain valuable chemical information that is lost with individual compound analysis, and it can be another route to be explored to improve the conclusions of this work.[9,10]

References

1. Maben HK, Ziemann PJ. Kinetics of oligomer-forming reactions involving the major functional groups present in atmospheric secondary organic aerosol particles. *Environmental Science: Processes & Impacts*. 2022;25(2):214-228.

2. Zhao Z, Yang X, Lee J, et al. Diverse Reactions in Highly Functionalized Organic Aerosols during Thermal Desorption. *ACS Earth and Space Chemistry*. 2019;4(2):283-296.

3. Martinez RE, Williams BJ, Zhang Y, et al. Development of a volatility and polarity separator (VAPS) for volatility- and polarity-resolved organic aerosol measurement. *Aerosol Science and Technology*. 2016;50(3):255-271.

4. Williams BJ, Zhang Y, Zuo X, et al. Organic and inorganic decomposition products from the thermal desorption of atmospheric particles. *Atmos. Meas. Techniques*. 2016;9(4):1569-1586.

5. Fortenberry C, Walker MJ, Zhang Y, Dhruv Mitroo, Brune WH, Williams BJ. Bulk and molecular-level characterization of laboratory-aged biomass burning organic aerosol from oak leaf and heartwood fuels. *Atmospheric Chemistry and Physics*. 2018;18(3):2199-2224.

6. Wilson J, Pöschl U, Shiraiwa M, Berkemeier T. Non-equilibrium interplay between gas–particle partitioning and multiphase chemical reactions of semi-volatile compounds: mechanistic insights and practical implications for atmospheric modeling of polycyclic aromatic hydrocarbons. *Atmospheric Chemistry and Physics*. 2021;21(8):6175-6198.

7. Williams BJ, Goldstein AH, Kreisberg NM, et al. Major components of atmospheric organic aerosol in southern California as determined by hourly measurements of source marker compounds. *Atmospheric Chemistry and Physics*. 2010;10(23):11577-11603.

8. Wernis RA, Kreisberg NM, Weber RJ, Drozd GT, Goldstein AH. Source apportionment of VOCs, IVOCs and SVOCs by positive matrix factorization in suburban Livermore, California. *Atmospheric Chemistry and Physics*. 2022;22(22):14987-15019.

9. Zhang Y, Williams BJ, Goldstein AH, Docherty K, Ulbrich IM, Jimenez JL. A Technique for Rapid Gas Chromatography Analysis Applied to Ambient Organic Aerosol Measurements from the Thermal Desorption Aerosol Gas Chromatograph (TAG). *Aerosol Science and Technology*. 2014;48(11):1166-1182.

10. Zhang Y, Williams BJ, Goldstein AH, Docherty KS, Jimenez JL. A technique for rapid source apportionment applied to ambient organic aerosol measurements from a thermal desorption aerosol gas chromatograph (TAG). *Atmos. Measurement Techniques*. 2016;9(11):5637-5653.

APPENDIX A2

Supplement of "Volatility Characterization of Organic Aerosols through Thermal Evaporation and Thermal Desorption Gas Chromatography-Mass Spectrometry Techniques"

Section A2.1. V-TDMA Model

Non-Continuous Effect – Mass Accommodation Coefficient

There are many different theories to account for non-continuous effects and imperfect surface accommodation represented by $f(Kn, \alpha)$ in Equation 2.1. This correction factor is relevant when the mean free path of the diffusing vapor molecules becomes comparable to the particle diameter. The expression for $f(Kn, \alpha)$ used in the V-TDMA model was developed by Fuchs and Sutugin and is given by Equation A2.1.[1]

$$f(Kn, \alpha) \ \frac{1+Kn}{1+0.3773Kn+1.33Kn(1+Kn)/\alpha} \qquad \textbf{(A2.1)}$$

Where Kn is the Knudsen number defined as the ratio of the suspending fluid mean free path to the aerosol particle's radius. The mass accommodation coefficient, α, is assumed to be equal to 1.

Diffusivity

Diffusion coefficients were estimated at each evaporating temperature using Equation A2.2 derived from the Chapman–Enskog kinetic theory.[2]

$$D_{AB} = \frac{0.001858T^{\frac{3}{2}}\left[\frac{1}{M_A}+\frac{1}{M_B}\right]^{\frac{1}{2}}}{P{\sigma_{AB}}^2\Omega_D} \qquad \textbf{(A2.2)}$$

Where T is the temperature, M_i is the molecular weight of azelaic acid and air, P is the pressure, σ_{AB} is the averaged Lennard Jones parameter, Ω_D is the collision integral which depends on the dimensionless temperature $T^* = kT/\varepsilon_{AB}$ calculated using Equation A2.3. The respective diffusivity parameters were obtained from Bilde et al[3] and listed in **Table A2.1**.

$$\Omega_D = \frac{1.06036}{T^{*0.1561}} + \frac{0.193}{\exp(0.47635T^*)} + \frac{1.03583}{\exp(1.52996T^*)} + \frac{1.76474}{\exp(3.89411T^*)} \qquad \textbf{(A2.3)}$$

TABLE A2.1. Diffusivity parameters for V-TDMA kinetic model calculations.

	σ (Å)[a]	**ε/k (K)[a]**
Air	3.62	97
Azelaic Acid	7.03	728.93

[a]Retrieved from Bilde et al (2003).[3]

Surface Tension

In Oxford et al[4], the authors discussed the appearance of two peaks after aerosol evaporation at higher temperatures and attributed the feature to the multicharged nature of the aerosol size distribution. The first peak is the response of the singly charged particles while the second peak results from the remainder charges. Given that these two peaks represent the same evaporating aerosol, two mass transfer equations can be solved for the same values of vapor pressure, surface tension, and mass accommodation coefficient. Since the degrees of freedom of the system decreased from two to one, if the mass accommodation is assumed to be equal to one, the surface tension and vapor pressure can be estimated by matching the measured CPC response and the one predicted by the model. A detailed description of this procedure is found in Oxford.[5] In this experiment, the two-peak feature was observed at 51.8ºC. **Figure A2.1** shows the measured and modeled response used to estimate the surface tension. The calculated value was 0.129 J.m^{-2} and assumed constant for the estimation of vapor pressures at varying temperatures.

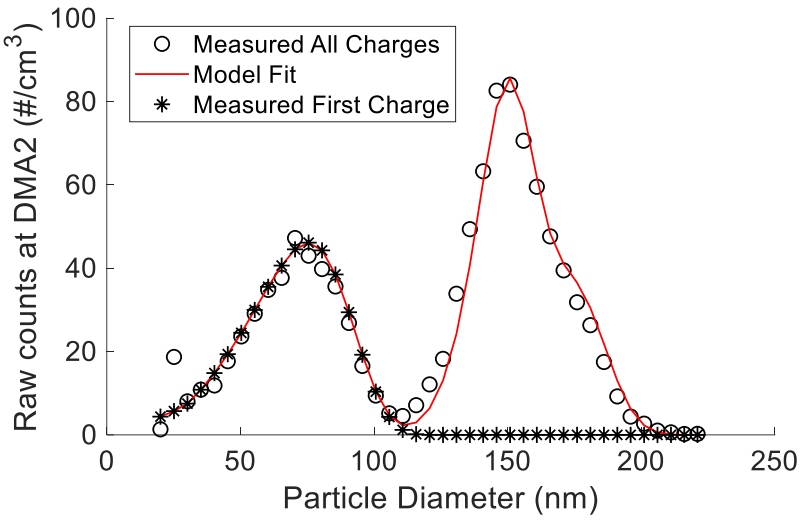

Figure A2.1. V-TDMA scan at 51.8°C used to estimate azelaic acid surface tension.

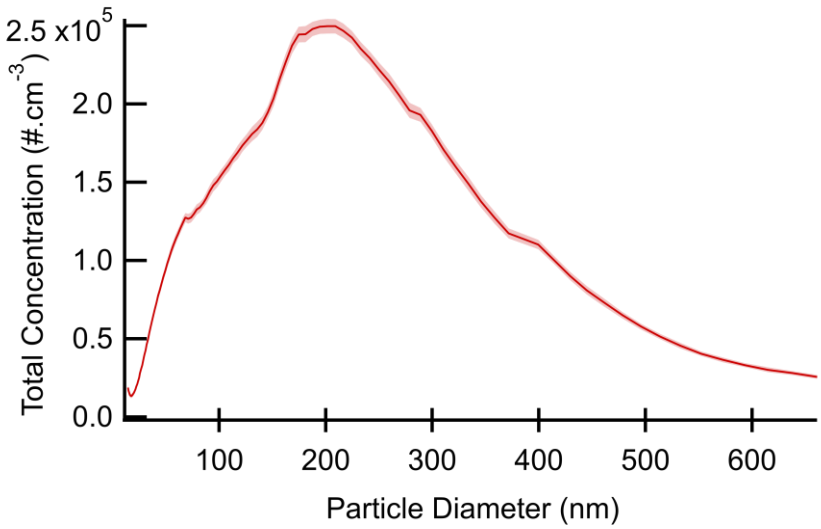

Figure A2.2. Average inlet size distribution measured by the SMPS during azelaic acid evaporation experiments. The shaded area represents one standard deviation of the mean.

Section A2.2. AMS-VTDMA Calibration

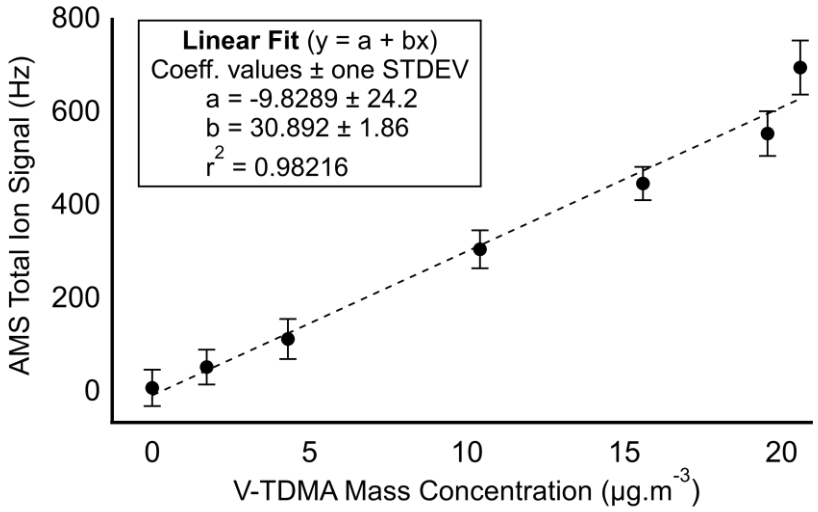

Figure A2.3. AMS calibration using the V-TDMA charge-dependent mass calculation routine for the azelaic acid evaporation experiments.

Section A2.3. SOA Evaporation Experimental Conditions

TABLE A2.2. Initial experimental conditions at each evaporating temperature for each precursor.

T (°C)	O_3 (ppm)	RH (%)	SO_4 (ug.m^{-3})
α-pinene			
21.97 ± 0.63	13.64 ± 0.03	40.95 ± 0.81	11.42 ± 0.73
58.68 ± 0.95	13.25 ± 0.08	40.40 ± 0.39	12.44 ± 0.71
88.45 ± 1.38	13.44 ± 0.06	38.85 ± 0.71	11.67 ± 0.59
Limonene			
21.46 ± 0.64	12.43 ± 0.13	39.96 ± 0.40	14.71 ± 0.65
58.64 ± 0.93	12.75 ± 0.08	39.67 ± 0.84	15.43 ± 0.78
87.53 ± 1.35	13.06 ± 0.05	38.41 ± 0.35	14.99 ± 0.62
β-pinene			
21.43 ± 0.68	12.27 ± 0.04	39.20 ± 0.34	16.36 ± 0.67
58.55 ± 0.99	12.11 ± 0.04	38.37 ± 0.35	15.90 ± 0.80
87.28 ± 1.41	12.06 ± 0.06	37.47 ± 0.33	16.52 ± 0.46

Note. The bounds given are one standard deviation of the mean.
Abbreviations: T, temperature; O_3, ozone; RH, relative humidity; SO_4, ammonium sulfate (seed particles).

Section A2.4. SOA Evaporation Experiments Methods

Volatility Regions

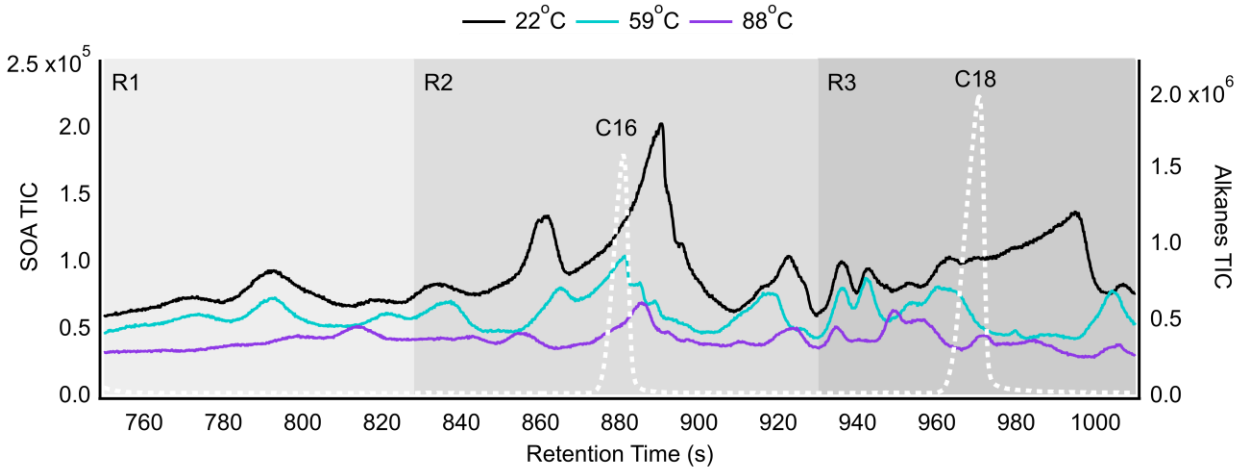

Figure A2.4. Compound window chromatograms from the evaporation of limonene ozonolysis products after retention time shift and definition of the volatility regions from the alkane standards injections. Solid lines represent SOA total ion count (TIC) chromatograms. Dotted line is the alkane series TIC. Shaded grays define the three volatility dimensions.

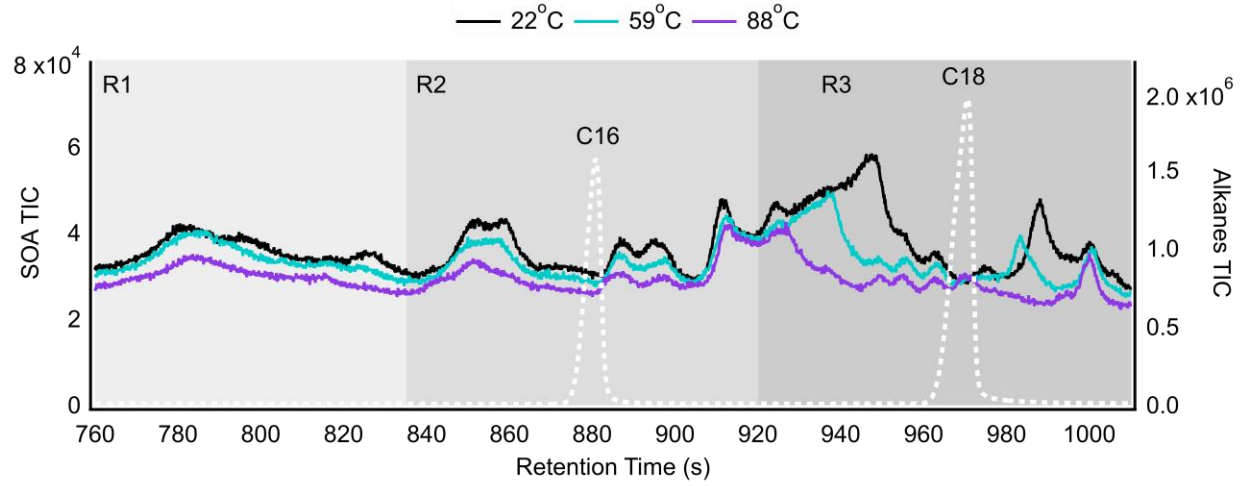

Figure A2.5. Compound window chromatograms from the evaporation of β-pinene ozonolysis products after retention time shift and definition of the volatility regions from the alkane standards injections. Solid lines represent SOA total ion count (TIC) chromatograms. Dotted line is the alkane series TIC. Shaded grays define the three volatility dimensions.

Ammonium Sulfate (seed) Concentrations vs Condensed SOA Mass

Polydisperse ammonium sulfate aerosol particles were introduced into the system to act as condensation nuclei for the VOC oxidation products. Sulfate (SO_4) concentrations were measured by the AMS. Their average values at each evaporating temperature for all three monoterpene precursors are outlined in **Table A2.2** and plotted in **Figure A2.6**.

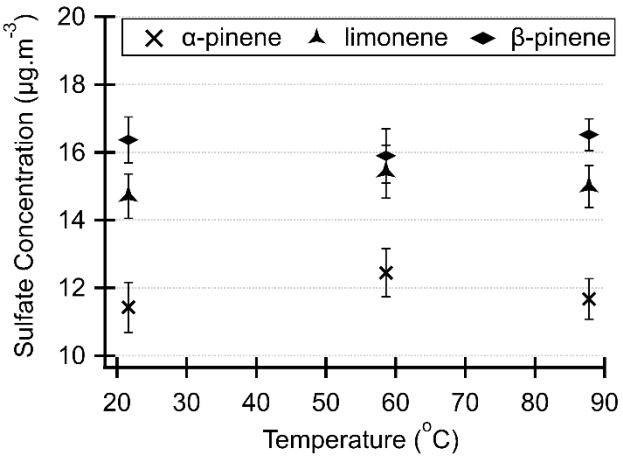

Figure A2.6. Ammonium sulfate (seed) mass concentration for the ozonolysis products of α-pinene, limonene and β-pinene (±1 stdev).

To evaluate potential change in the total condensed organic material due to fluctuations in the ammonium sulfate seed concentration throughout each precursor experiment, α-pinene oxidation products were subjected to 7 hours of evaporation at temperatures shown in **Table A2.3** while maintaining all other experimental conditions the same. **Figure A2.7** shows the ratio between the second and the first measured SOA and seed concentrations at each evaporating temperature as a function of time. For the SMPS organic mass calculations, it was first determined the ammonium sulfate mass increases dependence as a function of time. Then the seed concentrations over the 7-hour experiment were estimated based on the initial SMPS ammonium sulfate concentration measurements and the time-dependent function. The SMPS organic mass was given by subtracting the total measured SMPS mass and the calculated seed concentrations.

TABLE A2.3. Experimental conditions for the evaporation of α-pinene ozonolysis products.

Time	Temperature (ºC)	Time	Temperature (ºC)
18:00	40	22:00	100
19:00	60	23:00	60
20:00	80	00:00	80
21:00	100	01:00	40

Within a five-hour difference between measurements, SO_4 remained virtually constant while the total SOA mass varied ± 10%. Comparing measurements taken 7 hours apart, ammonium sulfate concentrations increased by approximately 4%. This increase in seed concentration corresponded to an increase of 12-18% in total condensed organic mass or, a 2-8% increase if assumed the ± 10% baseline. This range is within the GC/MS instrument accuracy and therefore, acceptable. **Figure A2.8** shows the ratio between the measured ammonium sulfate mass concentration at each experimental evaporating temperature considering the measurement at 22ºC as the reference. The horizontal red lines delimit the sulfate ratio bounds calculated during the 7-hour experiment. Although the increase in seed concentrations when evaporating α-pinene and limonene SOA at 59ºC is above the expected range, the observed difference is small. Therefore, it is foreseen that fluctuations in seed concentrations account for less than 20% of SOA mass increase during the respective experiments, not playing a significant role in the main results.

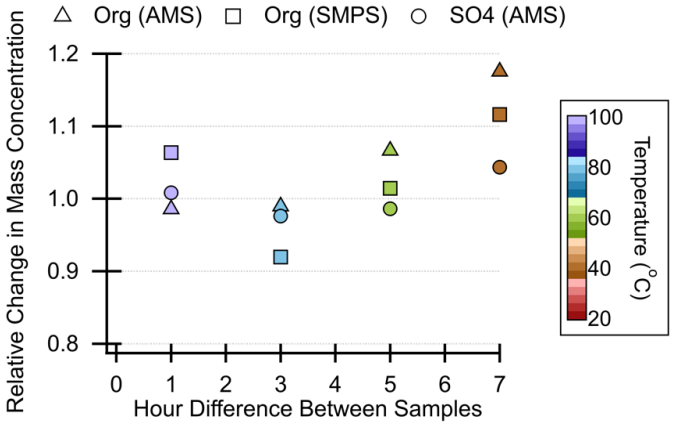

Figure A2.7. Relative change in α-pinene SOA and their respective seed concentration during a 7-hour evaporation experiment. Markers differentiate sulfate, AMS organics, and SMPS organics, while different colors represent different evaporating temperatures.

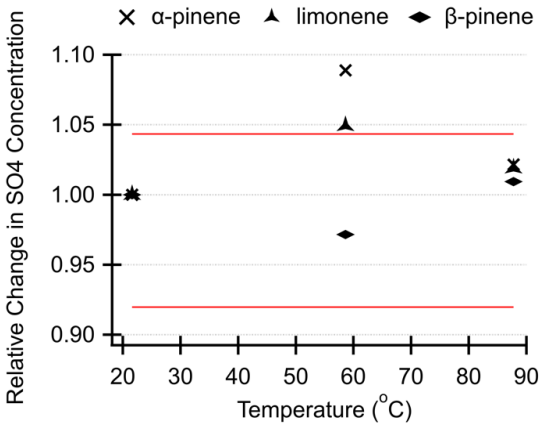

Figure A2.8. Relative change in α-pinene, limonene and β-pinene SOA seed concentration during the main evaporation experiment (22ºC, 59ºC and 88ºC). Red lines represent the fluctuations in seed concentration that corresponds to a ±10% increase in SOA mass.

PMF for Mass Spectral Deconvolution Analysis

For each SOA, all three chromatograms (22°C, 59°C and 88°C) were binned by retention time according to the method described by Zhang et al.[6] In a short description, the chromatogram binning method takes all the mass spectra in each retention time-defined bin and sums them to get one mass spectra to represent that bin. For this experiment, since each volatility region delimited by the alkanes eluting GC retention times covers a short window, only one scan per bin was considered. This choice preserves the instrument resolution, an advantage for the short-column GC/MS system since compound separation is partially sacrificed to achieve higher mass output.

To minimize the contribution of background noise in the PMF calculations, blank subtractions were performed using the resulting chromatograms from the I-CTD cell blank analysis prior to each experiment. An instrument error of 20% was chosen and all calculations were performed with fPeak = 0. This parameter allows exploration of solutions taking rotational ambiguity into account during calculations[7] but in previous work, the TAG data has not been sensitive to variation in fPeak,[8] justifying the value chosen.

The mass spectral deconvolution PMF method takes the binned chromatogram matrix as an input and factorizes it into a time series and a profile matrix that groups the chemical compounds present in the SOA sample into similar factors based on their mass spectrum similarity. In other words, each resulting factor consists of a mass spectrum that corresponds to a compound or class of compounds present in the chromatograms at each temperature. The appropriate number of PMF factors used to explain each solution was determined to maximize identifiable unique factors while minimizing factor splitting. The latter occurs when too many factors are used to explain the dataset and the information of a compound or compound class is distributed across multiple factors.

GC/MS High-Resolution Ion Mass Analysis

The high-resolution ion mass analysis is achieved by using a custom Igor Pro routine where the user selects a single scan in the chromatogram and chooses the desired unit mass fragment(s). The program automatically computes all possible ion combinations and compares them by fitting a Gaussian curve and calculating the chi-squared of each solution. The user then chooses the best result based on the ion combination and its respective accuracy.

Figure A2.9 illustrates an example case for determining the best ion combination corresponding to the mass spectrum of a known compound (pinonic acid) from the PMF solution of α-pinene ozonolysis SOA. The table shows the molecular formulas of each ion and the respective combination chi-squared value. Line 4777 was found to be the best solution. The molecular formula inferred for this factor, considering the highest value of each element in line 4777, was $C_{10}H_{14}O_3^+$. Note that this formula is different from the actual compound molecule ($C_{10}H_{16}O_3$), which demonstrates the intrinsic uncertainty in this elemental composition estimation when the parent ion is not present in the mass spectrum.

However, since compound separation was not achieved to a great extent in the SOA experiments (due to the shorter 1-meter GC column used), each PMF factor corresponds to an average mass spectrum comprised of fragments of many different compounds; thus, each PMF mass spectrum reflects an "average molecular formula". Therefore, the first approximation estimation from the high-resolution ion mass analysis still provides valuable information to help understand the degree of oxidation in each volatility region.

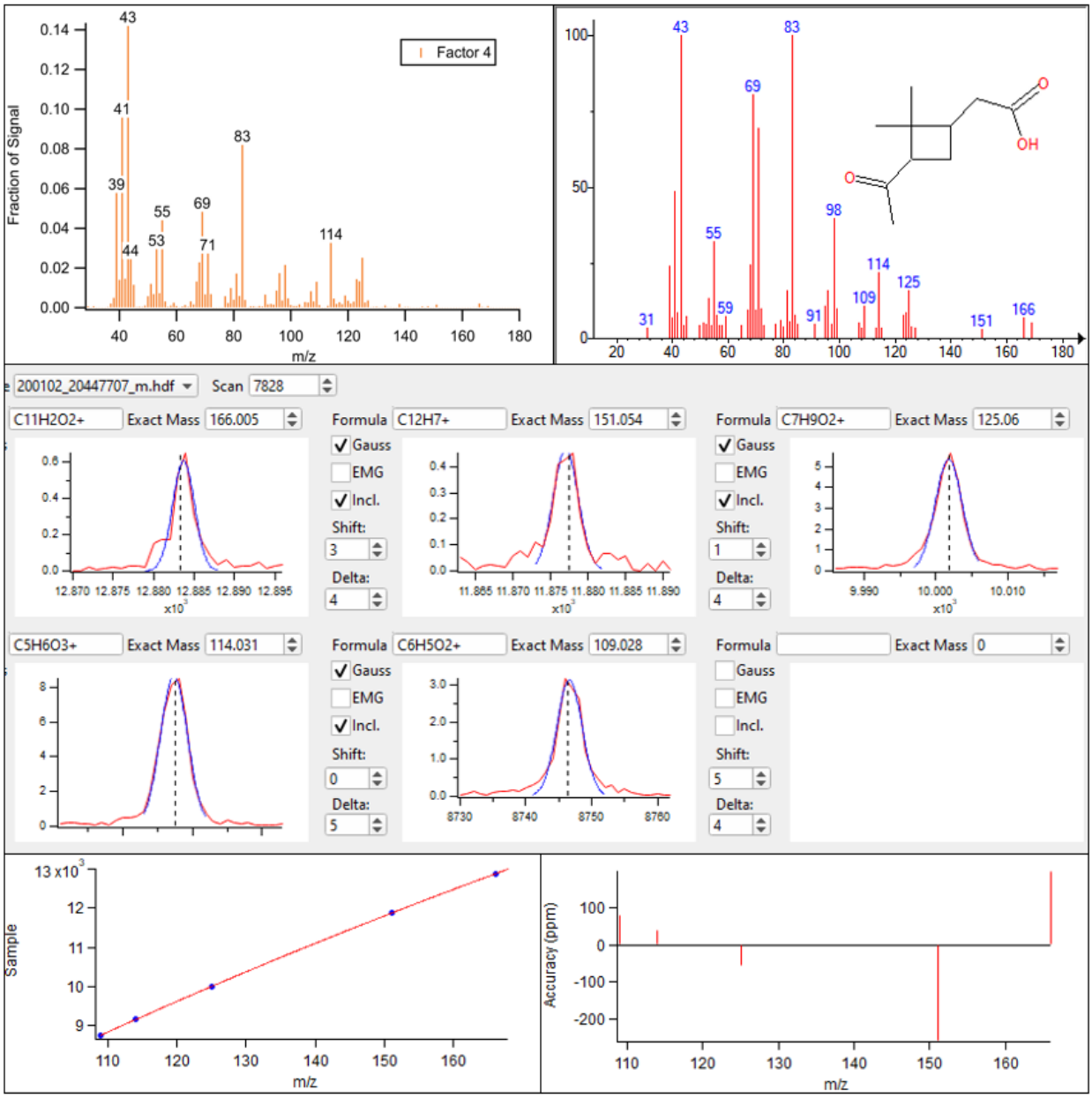

4776	C10H14O2+	C12H7+	C7H9O2+	C5H6O3+	C9H+	1.3001
4777	C10H14O2+	C12H7+	C7H9O2+	C5H6O3+	C6H5O2+	0.0021311
4778	C10H14O2+	C12H7+	C7H9O2+	C5H6O3+	C7H9O+	
4779	C10H14O2+	C12H7+	C7H9O2+	C5H6O3+	C8H13+	
4780	C10H14O2+	C12H7+	C7H9O2+	C9H6+	C5HO3+	
4781	C10H14O2+	C12H7+	C7H9O2+	C9H6+	C9H+	
4782	C10H14O2+	C12H7+	C7H9O2+	C9H6+	C6H5O2+	0.96005

Figure A2.9. Example case for determining elemental formula using high-resolution ion mass analysis.

SOA Size Distribution

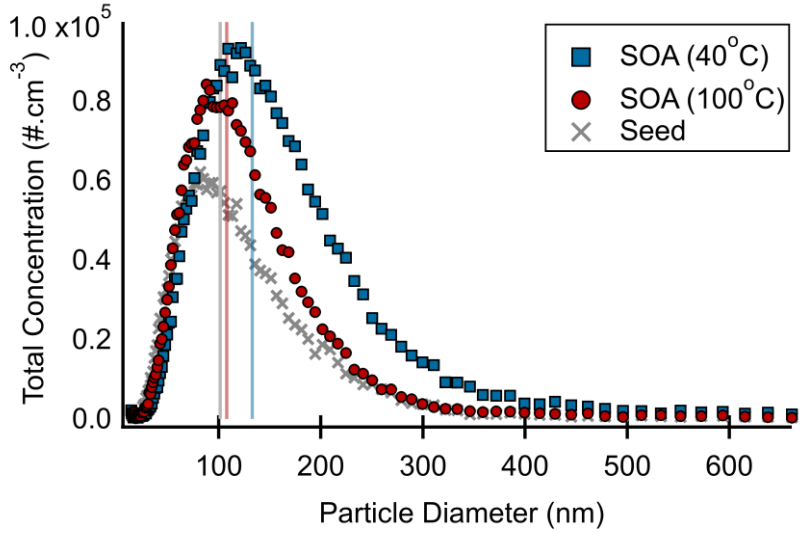

Figure A2.10. Lognormal size distribution measured by the SMPS during the α-pinene SOA 7-hour evaporation experiment. Markers and colors differentiate initial ammonium sulfate size distribution (black), the resulting distribution after SOA evaporation at 40ºC (blue), and after SOA exposure to 100ºC (red). Vertical lines represent its respective arithmetic mean diameter.

Section A2.5. SOA Evaporation Experiments Results

AMS vs PMF Thermograms

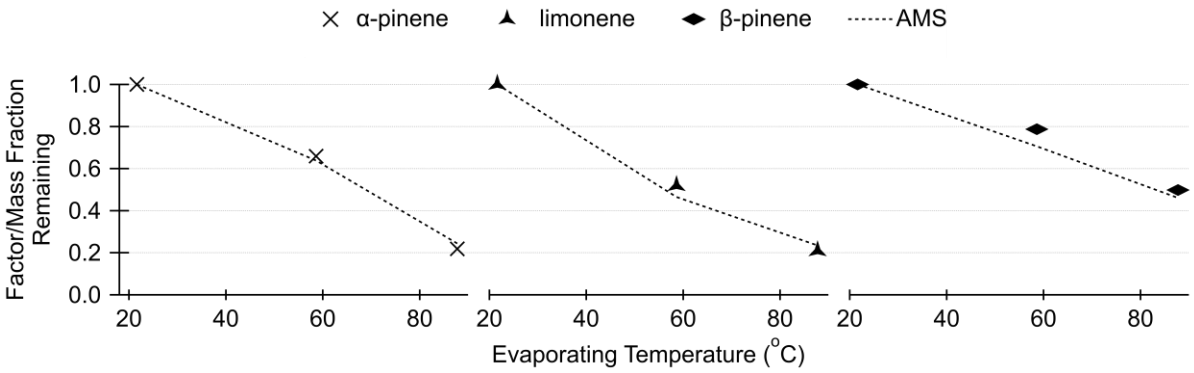

Figure A2.11. Comparison between average PMF factor fraction remaining and AMS mass fraction remaining curves for SOA obtained from different monoterpenes ozonolysis. Markers differentiate each precursor SOA, while the dotted line represents the AMS results.

Oxygenated Organic Aerosol and m/z 44 in the Thermal Decomposition Window

To investigate if the MS signal at *m/z* 44 in the thermal decomposition window corresponds to the degradation of oxygenated organic species rather than arising from remaining CO_2 gas in the desorption cell, for each monoterpene SOA, the O_2 (*m/z* 32) and CO_2 (*m/z* 44) signals were compared across the different evaporating temperatures. **Figure A2.12** display the results.

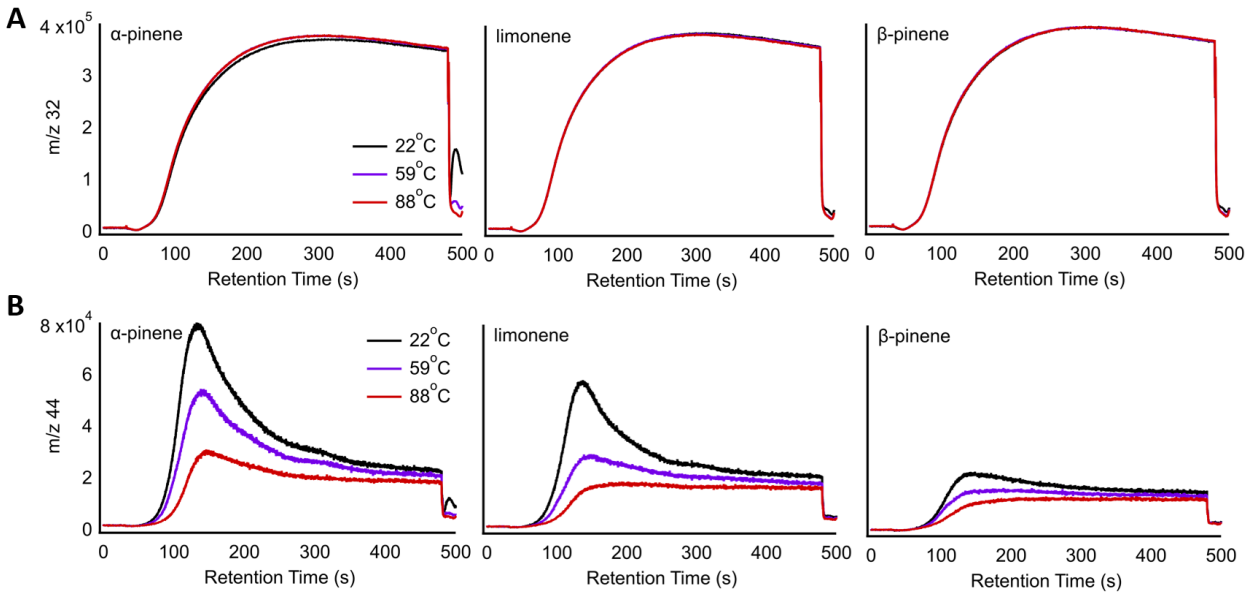

Figure A2.12. Thermal decomposition single ion count chromatograms as a function of evaporating temperature for α-pinene, limonene, and β-pinene ozonolysis SOA. **(A)** Oxygen signal (*m/z* 32). **(B)** Carbon dioxide (*m/z* 44) signal.

It is noticed that the O_2 signal is similar across all three SOA chromatograms, and it remains constant throughout each SOA evaporating experiment. If the *m/z* 44 signal was arising from CO_2 gas, it would be expected a similar pattern to the *m/z* 32 signal. However, what is observed is that the intensity of *m/z* 44 at a given evaporating temperature is different for each monoterpene SOA, and it decreases with increasing temperature. Both behaviors indicate a correlation between *m/z* 44 and the sampled SOA mass, justifying the use this ion signal in the decomposition window to investigate the level of oxidation of the different monoterpene SOA.

References

1. Seinfeld JH, Pandis SN. *Atmospheric Chemistry and Physics : From Air Pollution to Climate Change*. Wiley; 2016.

2. Welty JR, Rorrer GL, Foster DG. *Fundamentals of Momentum, Heat and Mass Transfer*. Hoboken, Nj Wiley; 2015.

3. Bilde M, Svenningsson B, Mønster JG, Rosenørn T. Even−Odd Alternation of Evaporation Rates and Vapor Pressures of C3−C9 Dicarboxylic Acid Aerosols. *Environmental Science & Technology*. 2003;37(7):1371-1378.

4. Oxford CR, Dang AJ, Rapp CM, Williams BJ. Interpretation of Volatility Tandem Differential Mobility Analyzer (V-TDMA) data for accurate vapor pressure and enthalpy measurement: Operational considerations, multiple charging, and introduction to a new analysis program (TAO). *Aerosol Science and Technology*. 2020;54(4):410-425.

5. Oxford CR. *The Role of Multi-Charged Responses: Construction and Application of a Tandem Differential Mobility Analyzer (TDMA)*. Dissertation. 2019.

6. Zhang Y, Williams BJ, Goldstein AH, Docherty K, Ulbrich IM, Jimenez JL. A Technique for Rapid Gas Chromatography Analysis Applied to Ambient Organic Aerosol Measurements from the Thermal Desorption Aerosol Gas Chromatograph (TAG). *Aerosol Science and Technology*. 2014;48(11):1166-1182.

7. Ulbrich IM, Canagaratna MR, Zhang Q, Worsnop DR, Jimenez JL. Interpretation of organic components from Positive Matrix Factorization of aerosol mass spectrometric data. *Atmospheric Chemistry and Physics*. 2009;9(9):2891-2918.

8. Williams BJ, Goldstein AH, Kreisberg NM, et al. Major components of atmospheric organic aerosol in southern California as determined by hourly measurements of source marker compounds. *Atmospheric Chemistry and Physics*. 2010;10(23):11577-11603.

APPENDIX A3

Supplement of "Development and Characterization of the Semi-Volatile Thermal Desorption Aerosol Gas Chromatograph (SV-TAG) with an Automatic Calibration Injection System"

Section A3.1. Supplemental Tables

TABLE A3.1. Section 3.2.4 – Full list of chemical compounds included in the deuterated internal calibration mixture that was used for the reproducibility analysis of the AutoInject system.

Compound Name	Formula	CAS ID	MW (g.mol^{-1})
Chrysene-d12 98 atom % D	C18D12	1719-03-5	240.36
Perylene-d12 98 atom % D	C20D12	1520-96-3	264.38
Pyrene-d10 98 atom % D	C16D10	1718-52-1	212.31
Hexadecane-d34 98 atom % D	CD3(CD2)14CD3	15716-08-2	260.65
Eicosane-d42 98 atom % D	CD3(CD2)18CD3	62369-67-9	324.81
Tetracosane-d50 98 atom % D	CD3(CD2)22CD3	16416-32-3	388.96
Octacosane-d58 98 atom % D	CD3(CD2)26CD3	16416-33-4	453.12
Dotriacontane-d66 98 atom % D	CD3(CD2)30CD3	62369-68-0	517.27
1-Hexadecan-d33-ol 98% atom % D	CD3(CD2)14CD2OH	284474-73-3	275.64
Lauric-d23 acid 98 atom % D	CD3(CD2)10CO2H	59154-43-7	223.46
Palmitic acid-d31 98 atom % D	CD3(CD2)14CO2H	39756-30-4	287.62
Stearic-d35 acid 98 atom % D	CD3(CD2)16CO2H	17660-51-4	319.69

TABLE A3.2. Section 3.2.4 – Full list of chemical compounds in the EPA 625 semi-volatile calibration mixture that was used to assess the volatility range of the SV-TAG instrument, examine intercell sensitivity, and determine limits of detection (LOD) – 2 pages

Compound Name	Formula	CAS ID	MW[a] (g.mol^{-1})	BP[a] (K)
Acenaphthene	C12H10	83-32-9	154.21	550.54
Acenaphthylene	C12H8	208-96-8	152.20	543.15
Anthracene	C14H10	120-12-7	178.23	615.18
Azobenzene	C12H10N2	17082-12-1	182.23	566.15
Benz[a]anthracene	C18H12	56-55-3	228.29	710.75
Benzo[b]fluoranthene	C20H12	205-99-2	252.32	668.65
Benzo[k]fluoranthene	C20H12	207-08-9	252.32	753.15
Benzo[ghi]perylene	C22H12	191-24-2	276.34	809.15
Benzo[a]pyrene	C20H12	50-32-8	252.32	668.65
Benzyl butyl phthalate	C19H20O4	85-68-7	312.37	643.15
Bis(2-chloroethoxy)methane	C5H10Cl2O2	111-91-1	173.04	490.9
Bis(2-chloroethyl) ether	C4H8Cl2O	111-44-4	143.01	451.65

Bis(2-ethylhexyl) phthalate	C24H38O4	117-81-7	390.56	657.15
4-Bromodiphenyl ether	C12H9BrO	101-55-3	249.11	578.15
Carbazole	C12H9N	86-74-8	167.21	627.86
4-Chlorodiphenyl ether	C12H9ClO	7005-72-3	204.66	557.65
Bis-(2-chloroisopropyl) ether	C6H12Cl2O	39638-32-9	171.07	460.45
4-Chloro-3-methylphenol	C7H7ClO	59-50-7	142.58	508.15
2-Chloronaphthalene	C10H7Cl	91-58-7	162.62	529.15
2-Chlorophenol	C6H5ClO	95-57-8	128.56	447.53
Chrysene	C18H12	218-01-9	228.29	714.15
Dibenz[a,h]anthracene	C22H14	53-70-3	278.35	792.15
Dibutyl phthalate	C16H22O4	84-74-2	278.35	613.15
1,2-Dichlorobenzene	C6H4Cl2	95-50-1	147.00	453.57
1,3-Dichlorobenzene	C6H4Cl2	541-73-1	147.00	446.23
1,4-Dichlorobenzene	C6H4Cl2	106-46-7	147.00	447.21
2,4-Dichlorophenol	C6H4Cl2O	120-83-2	163.00	483.15
Diethyl phthalate	C12H14O4	84-66-2	222.24	567.15
2,4-Dimethylphenol	C8H10O	105-67-9	122.17	484.13
Dimethyl phthalate	C10H10O4	131-11-3	194.19	556.85
2,4-Dinitrophenol	C6H4N2O5	51-28-5	184.11	591.18
2,4-Dinitrotoluene	C7H6N2O4	121-14-2	182.14	590
2,6-Dinitrotoluene	C7H6N2O4	606-20-2	182.14	590
Di-n-octyl phthalate	C24H38O4	117-84-0	390.56	657.15
Fluoranthene	C16H10	206-44-0	202.26	655.95
Fluorene	C13H10	86-73-7	166.22	570.44
Hexachlorobenzene	C6Cl6	118-74-1	284.78	582.55
Hexachloro-1,3-butadiene	C4Cl6	87-68-3	260.76	486.15
Hexachlorocyclopentadiene	C5Cl6	77-47-4	272.77	512.15
Hexachloroethane	C2Cl6	67-72-1	236.74	458
Indeno[1,2,3-cd]pyrene	C22H12	193-39-5	276.34	809.15
Isophorone	C9H14O	78-59-1	138.21	488.35
2-Methyl-4,6-dinitrophenol	C7H6N2O5	534-52-1	198.14	585.15
Naphthalene	C10H8	91-20-3	128.17	491.14
Nitrobenzene	C6H5NO2	98-95-3	123.11	483.95
2-Nitrophenol	C6H5NO3	88-75-5	139.11	489.15
4-Nitrophenol	C6H5NO3	100-02-7	139.11	489.15
N-Nitrosodimethylamine	C2H6N2O	62-75-9	74.08	425.15
N-Nitrosodi-n-propylamine	C6H14N2O	621-64-7	130.19	479.15
Pentachlorophenol	C6HCl5O	87-86-5	266.34	583.15
Phenanthrene	C14H10	85-01-8	178.23	610.03
Phenol	C6H6O	108-95-2	94.11	454.99
Pyrene	C16H10	129-00-0	202.26	667.95
1,2,4-Trichlorobenzene	C6H3Cl3	120-82-1	181.45	486.15
2,4,6-Trichlorophenol	C6H3Cl3O	88-06-2	197.45	519.15

Abbreviations: MW, molecular weight; BP, boiling point.
[a]Properties retrieved from *The Yaws Handbook of Thermodynamic Properties for Hydrocarbons and Chemicals* (2018)[1]

TABLE A3.3. Section 3.3.1 – Scenario #0: Integrated peak areas (from triplicate 5 ng.ul^{-1} injections) of the chemical compounds present in the EPA 625 semi-volatile calibration mixture that were considered to investigate the impact of thermal desorption timing and analyte transfer efficiency in the SV-TAG system **(Figure 3.7)**.The table separates non-polar (above dashed line) from polar (below dashed line) compounds and lists them with increasing retention time. The standard deviation measures how widely the integrated values are dispersed from the mean.

	Case #0: Different TD Order	**FT-CTD2**			**FT-CTD1**			**FT-CTD2**		**FT-CTD1**	
#	**Compound Name**	**Inj. #4**	**Inj. #5**	**Inj. #6**	**Inj. #4**	**Inj. #5**	**Inj. #6**	**Mean**	**σ**	**Mean**	**σ**
2	Hexachlorocyclopentadiene	88580.22	77773.63	84293.05	ND	ND	ND	83548.96	4443.037	N/A	N/A
4	2-Chloronaphthalene	1696972	1804335	1900617	542221.3	570164.1	540757.3	1800641	83178.57	551047.6	13530.66
7	Acenaphthylene	2838961	3078749	2667185	1188017	1311492	1248837	2861632	168783.3	1249448	50410.11
8	Acenaphthene	2071755	2097207	1864214	663734.4	767786.6	685749.8	2011059	104353.2	705756.9	44772.94
10	Fluorene	2075297	2225230	1992571	990989.9	977556.3	964122.7	2097699	96294.56	977556.3	10968.51
12	Azobenzene	882985.1	894000.2	905015.2	548260.8	556542	564823.3	894000.2	8993.738	556542	6761.637
14	Perchlorobenzene	809237.8	820428.9	831620.1	669274	683907.2	698540.4	820428.9	9137.515	683907.2	11947.95
15	Phenanthrene	1983349	2016199	2049048	2134326	2203430	2272534	2016199	26821.59	2203430	56423.34
16	Anthracene	1863740	1954333	2044925	2144666	2224466	2304266	1954333	73968.59	2224466	65156.43
18	Fluoranthene	2158931	2319983	2291116	2831816	2982864	2983705	2256676	70114.14	2932795	71403.83
19	Pyrene	2242809	2357922	2361460	2853807	3054951	3101432	2320730	55117.53	3003396	107464.2
1	Chlorocresol	219528.8	273413.8	292115.9	170282.6	155135.7	170707.3	261686.2	30772	165375.2	7242.493
3	2,4,6-Trichlorophenol	534290.2	601432.2	567861.2	367147.4	377421.1	387694.7	567861.2	27410.61	377421.1	8388.392
5	Dimethyl phthalate	1731146	1730044	1728942	1320440	1350532	1290349	1730044	899.9017	1320440	24569.57
6	2,6-Dinitrotoluene	326787	332765.8	338744.7	229462.6	251357.5	246413.3	332765.8	4881.719	242411.1	9375.857
9	Diethyl phthalate	1469742	1486426	1478084	1428680	1437757	1446834	1478084	6810.97	1437757	7411.38
11	4-Chlorodiphenyl ether	1085179	1072247	1059314	571195.5	570411.9	569628.3	1072247	10559.46	570411.9	639.8026
13	4-Bromodiphenyl ether	540598	575055.3	609512.6	486569.8	502932.7	519295.5	575055.3	28134.25	502932.7	13360.22
17	Dibutyl phthalate	1949625	2016926	2084227	2464432	2627579	2599067	2016926	54951.2	2563693	71146.36
20	Benzyl butylphthalate	956700.8	1032803	994751.9	1292522	1365127	1355906	994751.9	31068.59	1337852	32273.22
21	Bis(2-ethylhexyl) phthalate	1341111	1434226	1387668	1987761	1804949	1896355	1387668	38014.28	1896355	74632.93
22	Di-n-octyl phthalate	2521596	2283347	2402471	2946487	2679325	2812906	2402471	97264.75	2812906	109068.5

Abbreviations: ND, not detected; N/A, not applicable.

TABLE A3.4. Section 3.3.1 – Scenario #1: Integrated peak areas (from triplicate 5 ng.ul^{-1} injections) of the chemical compounds present in the EPA 625 semi-volatile calibration mixture that were considered to investigate the impact of thermal desorption timing and analyte transfer efficiency in the SV-TAG system **(Figure 3.7)**.The table separates non-polar (above dashed line) from polar (below dashed line) compounds and lists them with increasing retention time. The standard deviation measures how widely the integrated values are dispersed from the mean.

Case #1: Same TD Order (1st)		FT-CTD2			FT-CTD1			FT-CTD2		FT-CTD1	
#	**Compound Name**	**Inj. #4**	**Inj. #5**	**Inj. #6**	**Inj. #1**	**Inj. #2**	**Inj. #3**	**Mean**	**σ**	**Mean**	**σ**
2	Hexachlorocyclopentadiene	88580.22	77773.63	84293.05	21295.78	24350.64	22131.58	83548.96	4443.037	22592.67	1289.058
4	2-Chloronaphthalene	1696972	1804335	1900617	960697.4	1202006	1163914	1800641	83178.57	1108872	105923.4
7	Acenaphthylene	2838961	3078749	2667185	2294685	2535316	2538669	2861632	168783.3	2456223	114233
8	Acenaphthene	2071755	2097207	1864214	1472727	1664722	1670403	2011059	104353.2	1602617	91875.42
10	Fluorene	2075297	2225230	1992571	1778672	2050805	2028808	2097699	96294.56	1952761	123427.3
12	Azobenzene	882985.1	894000.2	905015.2	879363.2	984450.2	989369.3	894000.2	8993.738	951060.9	50737.68
14	Perchlorobenzene	809237.8	820428.9	831620.1	950081.5	1010025	1005952	820428.9	9137.515	988685.9	27348.02
15	Phenanthrene	1983349	2016199	2049048	2410126	2625362	2655651	2016199	26821.59	2563713	109304
16	Anthracene	1863740	1954333	2044925	2354643	2567663	2603355	1954333	73968.59	2508554	109802.4
18	Fluoranthene	2158931	2319983	2291116	2796196	3084676	3152418	2256676	70114.14	3011097	154453.8
19	Pyrene	2242809	2357922	2361460	2857907	3106586	3188489	2320730	55117.53	3050994	140568.1
1	Chlorocresol	219528.8	273413.8	292115.9	201293.3	249350.6	255177.3	261686.2	30772	235273.7	24145.23
3	2,4,6-Trichlorophenol	534290.2	601432.2	567861.2	556312.3	550128.4	562496.1	567861.2	27410.61	556312.3	5049.084
5	Dimethyl phthalate	1731146	1730044	1728942	1828866	1823678	1834055	1730044	899.9017	1828866	4236.76
6	2,6-Dinitrotoluene	326787	332765.8	338744.7	347386.3	346496.9	348275.8	332765.8	4881.719	347386.3	726.2206
9	Diethyl phthalate	1469742	1486426	1478084	1526045	1667617	1656704	1478084	6810.97	1616789	64319.83
11	4-Chlorodiphenyl ether	1085179	1072247	1059314	1037895	1127697	1157486	1072247	10559.46	1107693	50830.73
13	4-Bromodiphenyl ether	540598	575055.3	609512.6	754051.2	750998.3	757104.1	575055.3	28134.25	754051.2	2492.686
17	Dibutyl phthalate	1949625	2016926	2084227	2481493	2699306	2673848	2016926	54951.2	2618215	97234.67
20	Benzyl butylphthalate	956700.8	1032803	994751.9	1303329	1420870	1437250	994751.9	31068.59	1387150	59646.5
21	Bis(2-ethylhexyl) phthalate	1341111	1434226	1387668	1918270	1889293	1897008	1387668	38014.28	1901523	12253.3
22	Di-n-octyl phthalate	2521596	2283347	2402471	2630129	2814936	2854358	2402471	97264.75	2766474	97744.98

TABLE A3.5. Section 3.3.1 – Scenario #2: Integrated peak areas (from triplicate 5 ng.ul^{-1} injections) of the chemical compounds present in the EPA 625 semi-volatile calibration mixture that were considered to investigate the impact of thermal desorption timing and analyte transfer efficiency in the SV-TAG system **(Figure 3.7)**.The table separates non-polar (above dashed line) from polar (below dashed line) compounds and lists them with increasing retention time. The standard deviation measures how widely the integrated values are dispersed from the mean.

Case #2: Same TD Order (2nd)		FT-CTD2			FT-CTD1			FT-CTD2		FT-CTD1	
#	**Compound Name**	**Inj. #1**	**Inj. #2**	**Inj. #3**	**Inj. #4**	**Inj. #5**	**Inj. #6**	**Mean**	**σ**	**Mean**	**σ**
2	Hexachlorocyclopentadiene	ND[a]	ND[a]	ND[a]	ND[a]	ND[a]	ND[a]	N/A	N/A	N/A	N/A
4	2-Chloronaphthalene	510277.6	570101.4	520224.5	542221.3	570164.1	540757.3	533534.5	26173.63	551047.6	13530.66
7	Acenaphthylene	1279390	1330389	1296041	1188017	1311492	1248837	1301940	21233.98	1249448	50410.11
8	Acenaphthene	802900.3	845841.1	805999.7	663734.4	767786.6	685749.8	818247	19552.94	705756.9	44772.94
10	Fluorene	1255375	1333912	1258280	990989.9	977556.3	964122.7	1282522	36357.17	977556.3	10968.51
12	Azobenzene	568874.9	621758	605863.6	548260.8	556542	564823.3	598832.2	22154.53	556542	6761.637
14	Perchlorobenzene	608802.4	664541.8	633795.7	669274	683907.2	698540.4	635713.3	22795.87	683907.2	11947.95
15	Phenanthrene	1761197	1919403	1895214	2134326	2203430	2272534	1858605	69581.79	2203430	56423.34
16	Anthracene	1739827	1912290	1875902	2144666	2224466	2304266	1842673	74224.96	2224466	65156.43
18	Fluoranthene	2146555	2387741	2345803	2831816	2982864	2983705	2293366	105213.6	2932795	71403.83
19	Pyrene	2216674	2404078	2380803	2853807	3054951	3101432	2333851	83400.24	3003396	107464.2
1	Chlorocresol	169772.7	170439	170524.3	170282.6	155135.7	170707.3	170245.3	336.0012	165375.2	7242.493
3	2,4,6-Trichlorophenol	390231.4	393644.4	386818.5	367147.4	377421.1	387694.7	390231.4	2786.654	377421.1	8388.392
5	Dimethyl phthalate	1128631	1240267	1216776	1320440	1350532	1290349	1195225	48055.35	1320440	24569.57
6	2,6-Dinitrotoluene	183534.8	204828.7	206563.6	229462.6	251357.5	246413.3	198309	10470.96	242411.1	9375.857
9	Diethyl phthalate	1151279	1253327	1211565	1428680	1437757	1446834	1205390	41889.23	1437757	7411.38
11	4-Chlorodiphenyl ether	671300.4	730742.1	716765.2	571195.5	570411.9	569628.3	706269.2	25376.5	570411.9	639.8026
13	4-Bromodiphenyl ether	473887.8	479651.2	468124.4	486569.8	502932.7	519295.5	473887.8	4705.788	502932.7	13360.22
17	Dibutyl phthalate	1979355	2154765	2107582	2464432	2627579	2599067	2080567	74114.75	2563693	71146.36
20	Benzyl butylphthalate	951905.5	1089203	1039390	1292522	1365127	1355906	1026833	56750.32	1337852	32273.22
21	Bis(2-ethylhexyl) phthalate	1331384	1487623	1447075	1987761	1804949	1896355	1422027	66197.59	1896355	74632.93
22	Di-n-octyl phthalate	2117413	2339827	2291753	2946487	2679325	2812906	2249664	95552.93	2812906	109068.5

Abbreviations: ND, not detected; N/A, not applicable.

TABLE A3.6. Section 3.3.1 – Summary of the observations from investigating the impact of thermal desorption timing and analyte transfer efficiency in the SV-TAG system (**Figure 3.7**). The table separates non-polar (above dashed line) from polar (below dashed line) compounds and lists them with increasing retention time.

#	Scenario #0 (Different TD Order: FT-CTD2 → FT-CTD1)		Scenario #1 (Same TD Order: 1st)		Scenario #2 (Same TD Order: 2nd)	
	FTCTD1 / FTCTD2	Contributing Factor	FTCTD1 / FTCTD2	Contributing Factor	FTCTD1 / FTCTD2	Contributing Factor
2	N/A[a]	FT-CTD1 Evaporation	<1	FT-CTD1-Analyte Inconsistent Interaction	N/A[a,b]	FT-CTD1 and FT-CTD2 Evaporation
4	<1	FT-CTD1 Evaporation	<1	FT-CTD1-Analyte Inconsistent Interaction	=1	FT-CTD1 and FT-CTD2 Similar Evaporation
7	<1	FT-CTD1 Evaporation	<1	FT-CTD1-Analyte Inconsistent Interaction	=1	FT-CTD1 and FT-CTD2 Similar Evaporation
8	<1	FT-CTD1 Evaporation	<1	FT-CTD1-Analyte Inconsistent Interaction	<1	Greater Evaporation in FT-CTD1
10	<1	FT-CTD1 Evaporation	=1	FT-CTD1 and FT-CTD2 Similar Transfer	<1	Greater Evaporation in FT-CTD1
12	<1	FT-CTD1 Evaporation	>1	FT-CTD2 Reduced Transfer Efficiency[c]	=1	Greater Evaporation in FT-CTD1 = FT-CTD2 Reduced Transfer Efficiency[c]
14	<1	FT-CTD1 Evaporation	>1	FT-CTD2 Reduced Transfer Efficiency[c]	>1	Greater Evaporation in FT-CTD1 > FT-CTD2 Reduced Transfer Efficiency[c]
15	>1	FT-CTD2 Reduced Transfer Efficiency[c]	>1	FT-CTD2 Reduced Transfer Efficiency[c]	>1	Greater Evaporation in FT-CTD1 > FT-CTD2 Reduced Transfer Efficiency[c]
16	>1	FT-CTD2 Reduced Transfer Efficiency[c]	>1	FT-CTD2 Reduced Transfer Efficiency[c]	>1	Greater Evaporation in FT-CTD1 > FT-CTD2 Reduced Transfer Efficiency[c]
18	>1	FT-CTD2 Reduced Transfer Efficiency[c] (No Evaporation)	>1	FT-CTD2 Reduced Transfer Efficiency[c]	>1	FT-CTD2 Reduced Transfer Efficiency[c]
19	>1	FT-CTD2 Reduced Transfer Efficiency[c] (No Evaporation)	>1	FT-CTD2 Reduced Transfer Efficiency[c]	>1	FT-CTD2 Reduced Transfer Efficiency[c]

1	<1	FT-CTD1 Evaporation	<1	FT-CTD1-Analyte Inconsistent Interaction	=1	FT-CTD1 and FT-CTD2 Similar Evaporation
3	<1	FT-CTD1 Evaporation	=1	FT-CTD1 and FT-CTD2 Similar Transfer	=1	FT-CTD1 and FT-CTD2 Similar Evaporation
5	<1	FT-CTD1 Evaporation	=1	FT-CTD1 and FT-CTD2 Similar Transfer	>1	FT-CTD2 Reduced Transfer Efficiency[e]
6	<1	FT-CTD1 Evaporation	=1	FT-CTD1 and FT-CTD2 Similar Transfer	>1	FT-CTD2 Reduced Transfer Efficiency[e]
9	=1	Greater Evaporation in FT-CTD1 = FT-CTD2 Reduced Transfer Efficiency[d]	>1	FT-CTD2 Reduced Transfer Efficiency[d]	>1	FT-CTD2 Reduced Transfer Efficiency[e]
11	<1	FT-CTD1 Evaporation	=1	FT-CTD1 and FT-CTD2 Similar Transfer	<1	Greater Evaporation in FT-CTD1
13	<1	FT-CTD1 Evaporation	>1	FT-CTD2 Reduced Transfer Efficiency[c,d]	=1	Greater Evaporation in FT-CTD1 = FT-CTD2 Reduced Transfer Efficiency[c,d]
17	>1	FT-CTD2 Reduced Transfer Efficiency[c,d] (No Evaporation)	>1	FT-CTD2 Reduced Transfer Efficiency[c,d]	>1	FT-CTD2 Reduced Transfer Efficiency[c,d]
20	>1	FT-CTD2 Reduced Transfer Efficiency[c,d] (No Evaporation)	>1	FT-CTD2 Reduced Transfer Efficiency[c,d]	>1	FT-CTD2 Reduced Transfer Efficiency[c,d]
21	>1	FT-CTD2 Reduced Transfer Efficiency[c,d] (No Evaporation)	>1	FT-CTD2 Reduced Transfer Efficiency[c,d]	>1	FT-CTD2 Reduced Transfer Efficiency[c,d]
22	>1	FT-CTD2 Reduced Transfer Efficiency[c,d] (No Evaporation)	>1	FT-CTD2 Reduced Transfer Efficiency[c,d]	>1	FT-CTD2 Reduced Transfer Efficiency[c,e]

Abbreviation: N/A, not applicable.
[a] Compound not detected in FT-CTD1.
[b] Compound not detected in FT-CTD2.
[c] FT-CTD2 reduced transfer efficiency due to increasing compound molecular weight.
[d] FT-CTD2 reduced transfer efficiency due to increasing compound polarity.
[e] FT-CTD2 reduced transfer efficiency due to increasing compound polarity and idling thermal desorption time.

TABLE A3.7. Section 3.3.2. Compounds integrated to investigate the collection reproducibility of the SV-TAG system. The table separates the different chemical classes shown in **Figure 3.8.**

Compound Name	Formula	CAS	MW[a](g.mol^{-1})	O:C	BP[a](K)	RT (s)
Tetradecane	C14H30	629-59-4	198.39	0	526.73	431.48
Pentadecane	C15H32	629-62-9	212.42	0	543.83	467.25
Hexadecane	C16H34	544-76-3	226.45	0	560.01	499.47
Octadecane	C18H38	593-45-3	254.5	0	589.86	560.06
Eicosane	C20H42	112-95-8	282.55	0	616.93	614.45
Docosane	C22H46	629-97-0	310.61	0	641.75	664.40
Naphthalene	C10H8	91-20-3	128.17	0	491.14	347.54
Acenaphthylene	C12H8	208-96-8	152.19	0	543.15	455.13
Fluorene	C13H10	86-73-7	166.22	0	570.44	500.65
Phenanthrene	C14H10	85-01-8	178.23	0	610.03	563.02
Pyrene	C16H10	129-00-0	202.25	0	667.95	654.35
Nonanoic Acid	C9H18O2	112-05-0	158.24	0.222	528.75	385.09
Dodecanoic Acid	C12H24O2	143-07-7	200.32	0.167	571.85	494.74
Tetradecanoic Acid	C14H28O2	544-63-8	228.37	0.143	599.35	552.38
Pentadecanoic Acid	C15H30O2	1002-84-2	242.40	0.133	612.05	579.87
Heptadecanoic Acid	C17H36O2	506-12-7	270.46	0.118	635.75	632.48
Dimethyl Phthalate	C10H10O4	131-11-3	194.19	0.4	556.85	450.40
Diethyl Phthalate	C12H14O4	84-66-2	222.24	0.333	567.15	497.10
Dibutyl Phthalate	C16H22O4	84-74-2	278.35	0.25	613.15	603.80
Dioctyl Phthalate	C24H38O4	117-84-0	390.56	0.167	657.15	779.08
Isopropyl Myristate	C17H34O2	110-27-0	270.46	0.118	588	567.16
Homosalate	C16H22O3	118-56-9	262.34	0.187	598.15	589.33
Methyl palmitate	C17H34O2	112-39-0	270.47	0.118	690.15	595.24
Isopropyl Palmitate	C19H38O2	142-91-6	298.51	0.105	690.66	620.36

Abbreviations: MW, molecular weight; BP, boiling point; RT, retention time.
[a]Properties retrieved from *The Yaws Handbook of Thermodynamic Properties for Hydrocarbons and Chemicals* (2018)[1]

Section A3.2. Description and Operation of the SV-TAG and AutoInject System

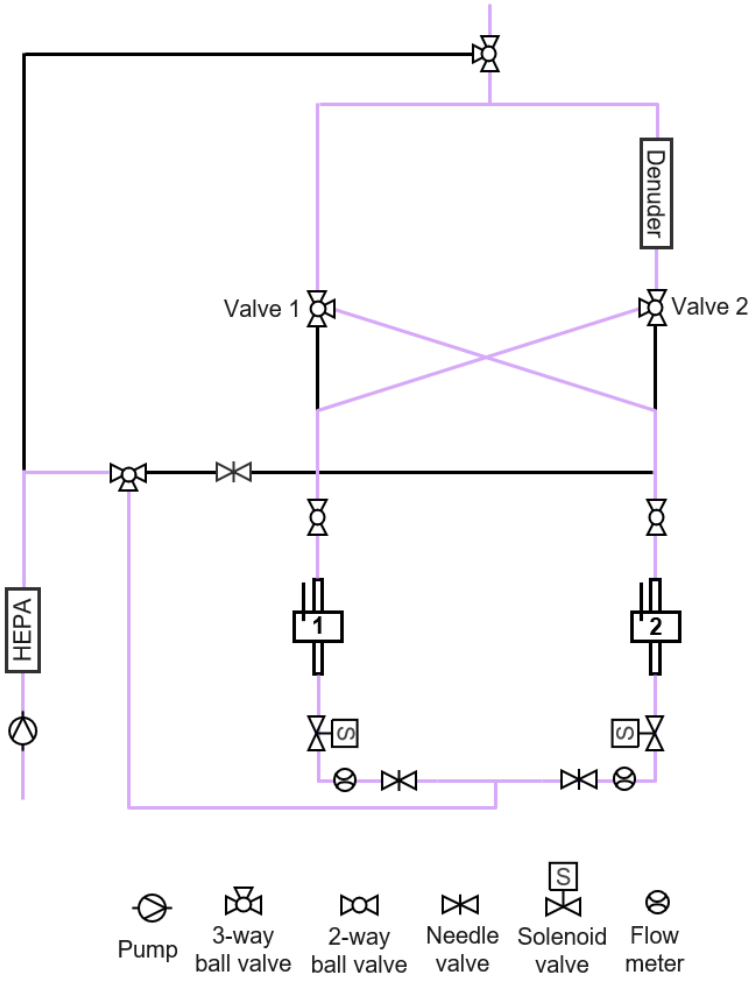

Figure A3.1. Flow diagram of the inlet system of the SV-TAG instrument. Highlighted purple paths demonstrate denuded (particle-only) collection in cell 1 and non-denuded (gas plus particle) collection in cell 2. The two in-line 3-way ball valves (valves 1 and 2) allow the cells' roles to be swapped to avoid cell-to-cell bias during continuous sampling.

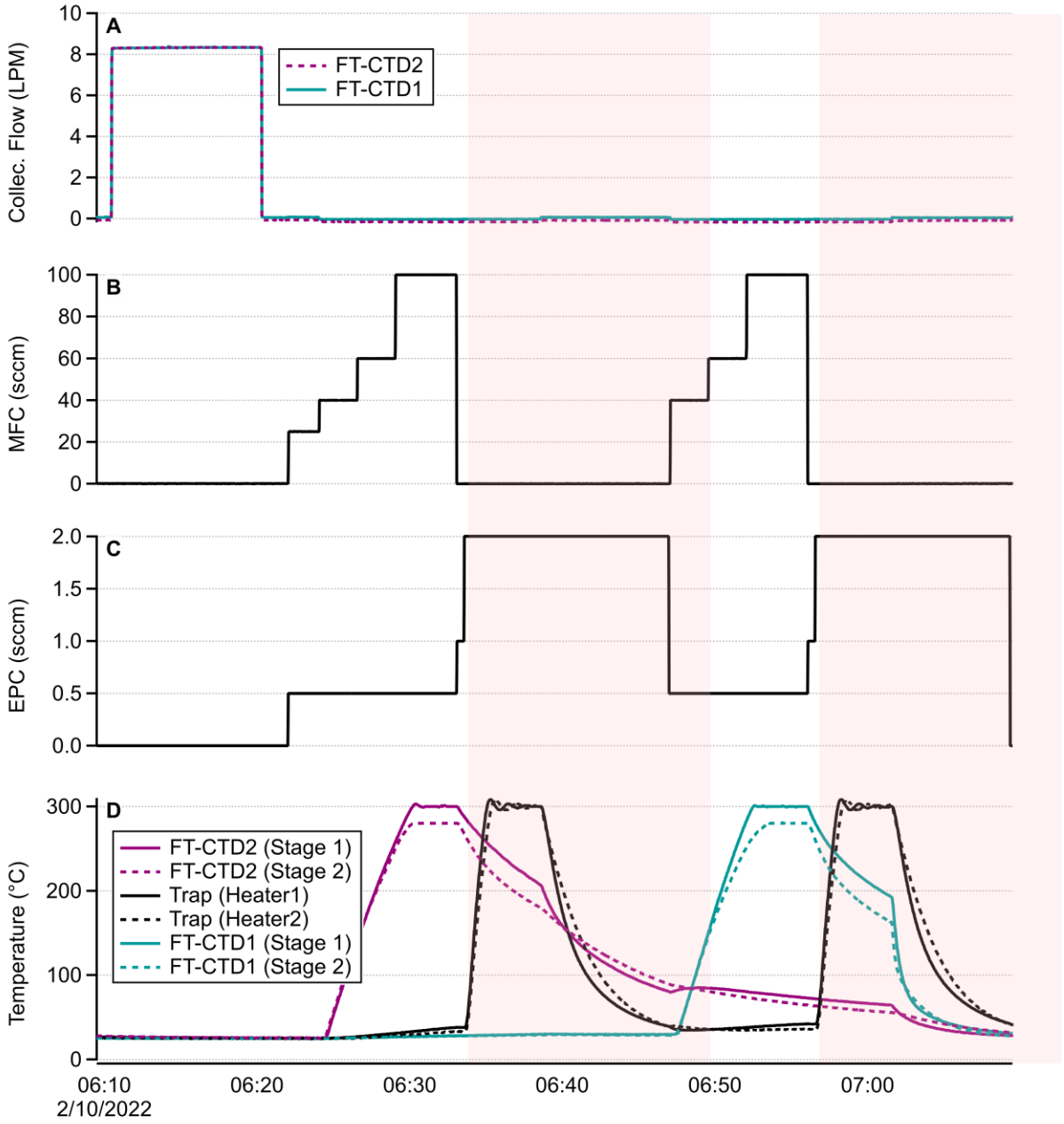

Figure A3.2. SV-TAG method run schematic. A 10-minute collection with subsequent thermal desorption (TD) is shown. The shaded areas represent each GC run. **(A)** FT-CTD cells' collection flows. **(B)** Mass flow controller (MFC) flows. Used to purge residual air from the cells as well as to transfer the collected material to the focusing trap (TD first step). **(C)** Electronic pressure controller (EPC) flows. The EPC allows precise control of the low flows used in the auxiliary lines (0.5 sccm) and, in the injection of the trapped sample (2 sccm) onto the head of the GC column (TD second step). **(D)** Temperature profiles. In the first TD step, the cells' stage 1 is heated to 300^{o}C and stage 2 is heated to 280^{o}C while the collected material is transferred to the focusing trap. In the second TD step, the trap column is heated to 300^{o}C while being backflushed into the GC/MS system. Note that subsequential collection starts while FT-CTD1 GC analysis is still in progress but the collection cells are cooled back to at least 30^{o}C.

Section A3.3. The Dual-Stage Collection Cell Performance

Design Artifacts

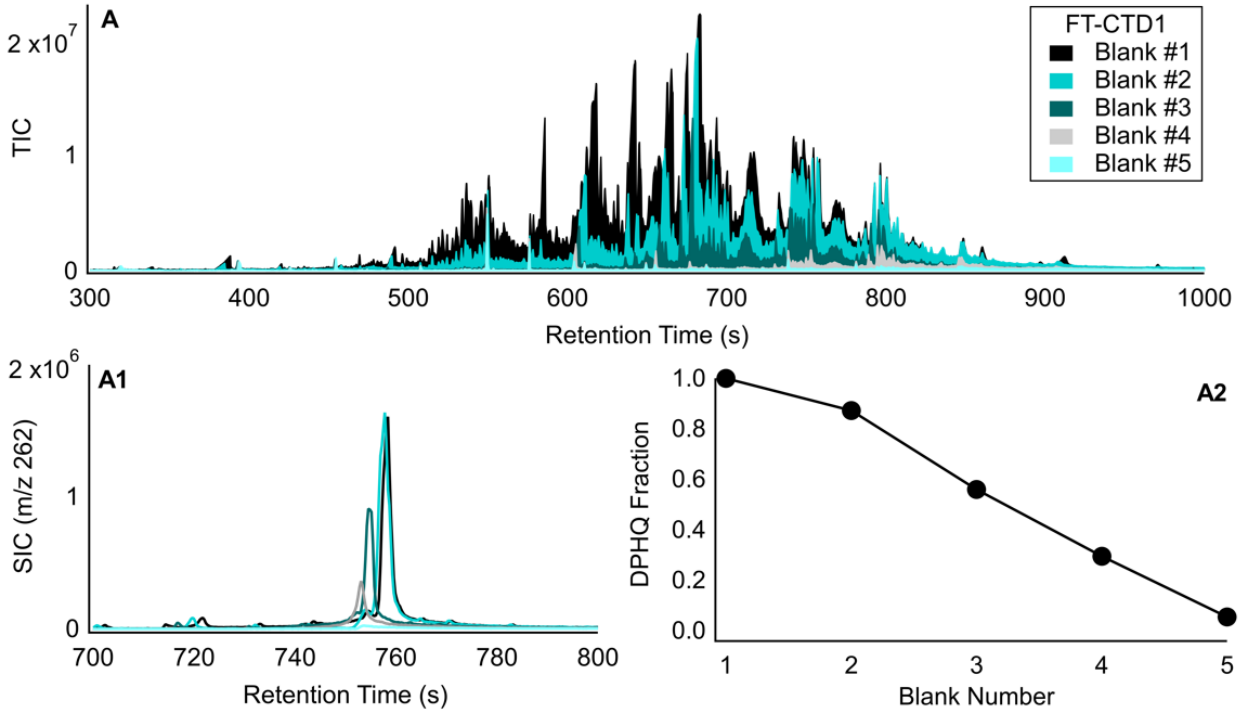

Figure A3.3. Evolution of Tenax® conditioning in FT-CTD1. **(A)** Chromatogram obtained from successive blanks after installing fresh Tenax® in the collection cell. Each partial conditioning largely eliminates the observed thermal decomposition products. **(A1)** Display DPHQ, as *m/z* 262 peaks, from each run. **(A2)** DPHQ decay in terms of the remaining signal fraction calculated from peak integrations. DPQ was not identified in these blanks suggesting quinone reductions prevail over oxidation during TD-GC/MS analysis in the SV-TAG system.

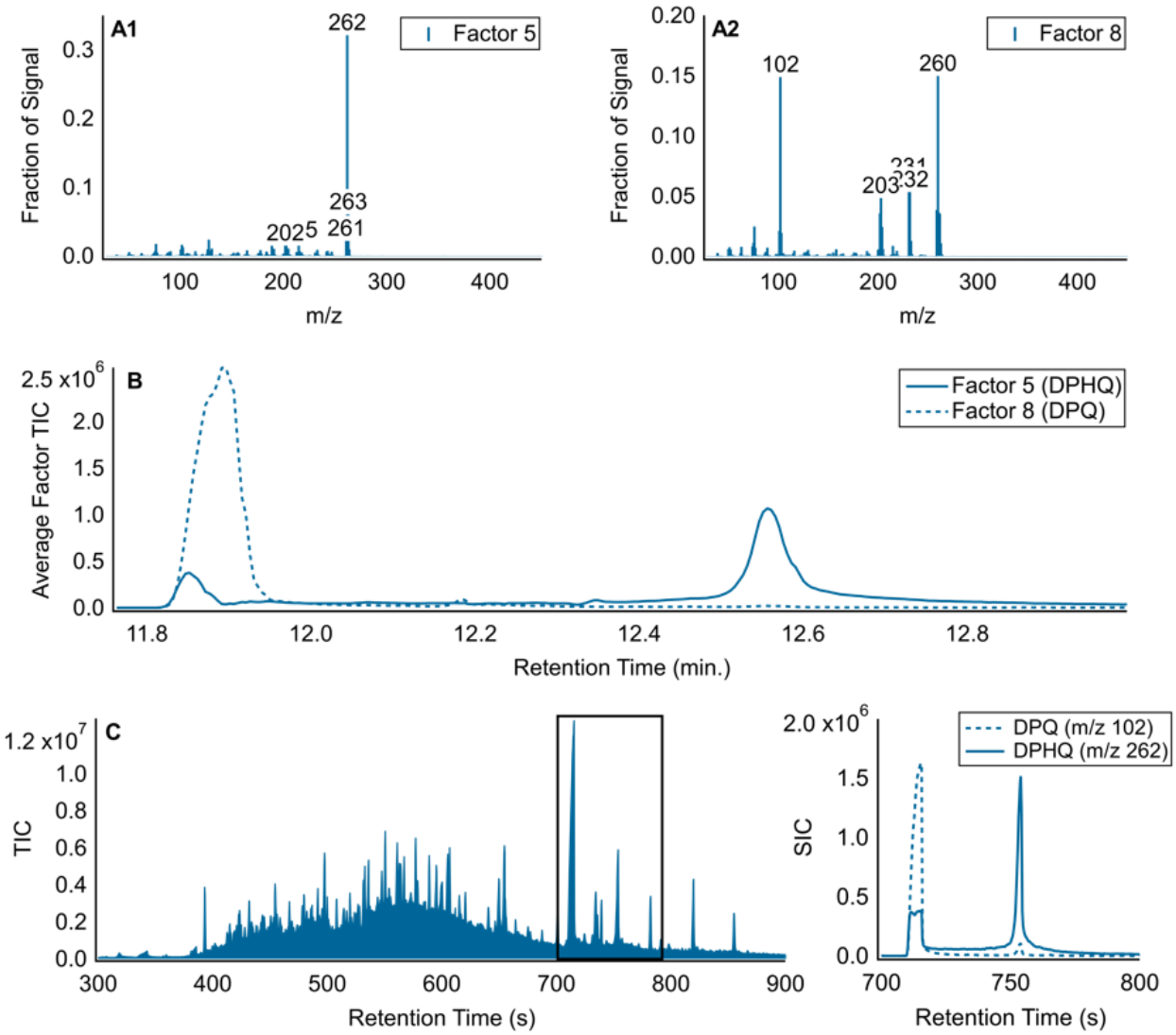

Figure A3.4. Results from the mass spectral deconvolution PMF analysis to identify DPQ and DPHQ in the outdoor non-denuded ALPACA samples. A 12-F solution was considered. **(A1)** Mass spectra of factor 5 (DPHQ). **(A2)** Mass spectra of factor 8 (DPQ). **(B)** Average binned chromatograms of the respective factors. **(C)** Example chromatogram highlighting the region in which PMF was performed (DPQ/DPHQ retention time window).

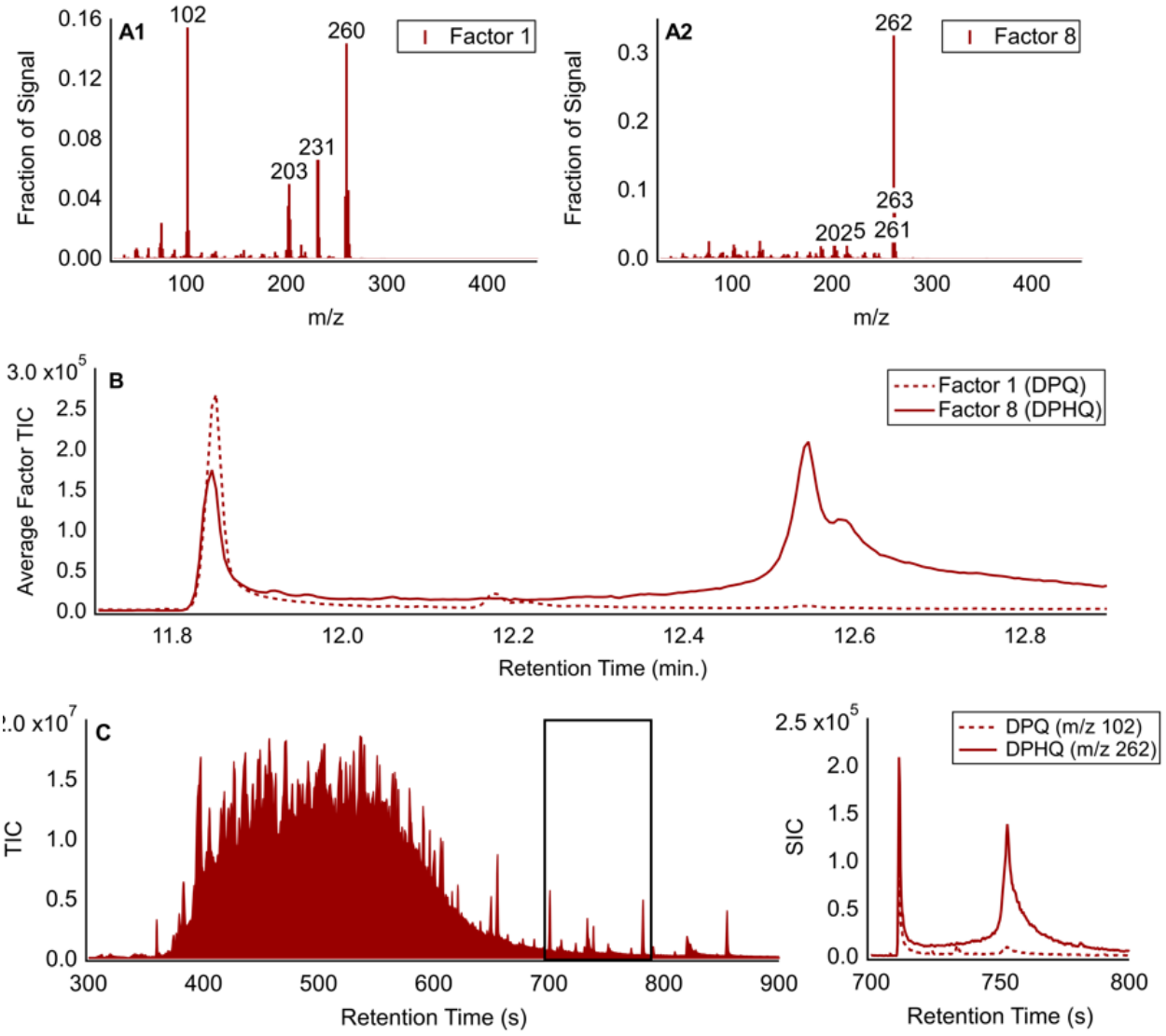

Figure A3.5. Results from the mass spectral deconvolution PMF analysis to identify DPQ and DPHQ in the indoor non-denuded ALPACA samples. A 10-F solution was considered. **(A1)** Mass spectra of factor 1 (DPQ). **(A2)** Mass spectra of factor 8 (DPHQ). **(B)** Average binned chromatograms of the respective factors. **(C)** Example chromatogram highlighting the region in which PMF was performed (DPQ/DPHQ retention time window).

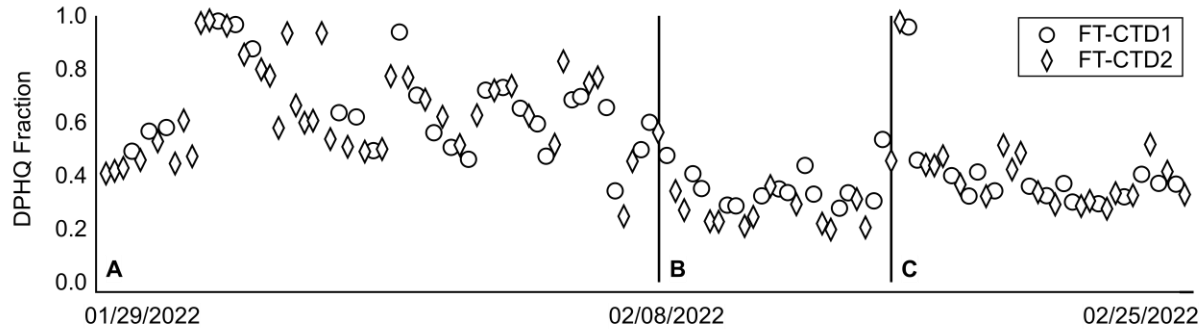

Figure A3.6. Outdoor deconvoluted DPHQ fractions. FT-CTD1 Tenax® de-stabilization in Region B has a negligible effect on outdoor samples' DPHQ fraction due to the already low reaction yields observed at that period.

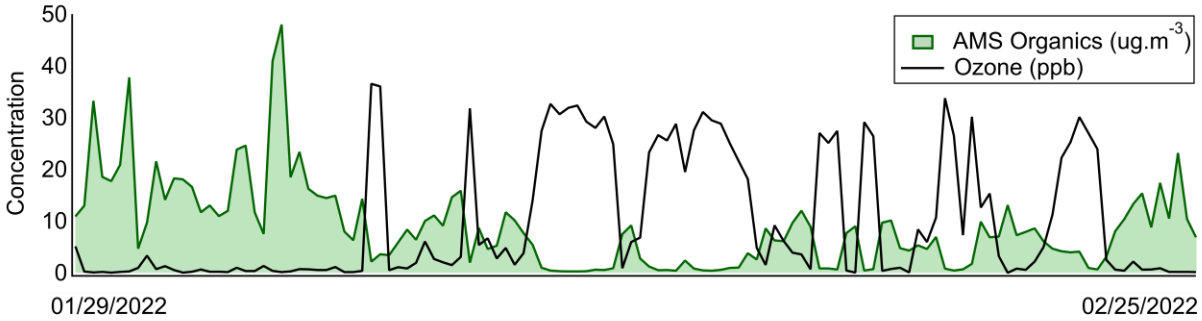

Figure A3.7. Relationship between ozone (O3) and particulate matter concentrations during the ALPACA campaign. Note that increases in O3 levels correlate with cleaner periods since, O3-rich air mass transport, which constitutes the substantial source of Arctic tropospheric O3, promotes the dispersion of accumulated ground-level emissions

Tenax® Degradation Products from Ozone Exposure

A less abundant positive O3 artifact identified in the SV-TAG was 2,6-diphenylphenol (**Figure A3.8**). Tenax® is formed from the oxidative coupling of this compound and its presence as an artifact might be associated with thermal degradation from unpolymerized material left on the adsorbent from the manufacturing process.[2,3] In addition, Klenø et al[1] also reported 2,6-diphenylphenol formation from Tenax® exposure to limonene ozonolysis products. Since O3 was absent in the mixture, they attributed Tenax® reactions with the adsorbed sample, or with thermally liable species present in the sample, as the two pathways of formation of the artifact.

In the SV-TAG system, it is observed that in Region A, 2,6-diphenylphenol is not formed in FT-CTD2 (even at high O3 levels). However, after exposure to an atypical cooking experiment, FT-CTD2- Tenax®-O3 degradation is noticed. In Region C, both cells show higher degradation at lower O3 concentrations. It is conjecture here that different thermal conditioning (aging) before field measurements resulted in a purer and more stable polymer in FT-CTD2 (absent of low molecular weight polymers from the manufacturing process) thus not degrading even at high O3 levels (long-chain polymer is more stable). The high number of free radicals generated by the atypical experiment could have destabilized (reduced by chain elimination) the adsorbent in FT-CTD2, with the more unstable smaller chains decomposing in the presence of O3. The change in degradation pattern observed in Region C (less O3 – higher artifact yields) can be associated with using new/less aged Tenax in the collectors.

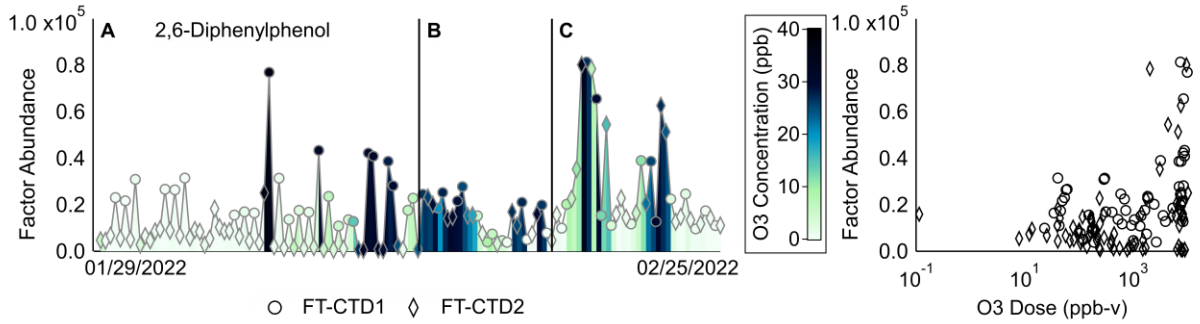

Figure A3.8. Qualitative abundances of 2,6-diphenylphenol, a Tenax®-O3 artifact previously reported in the literature and also positively identified in the SV-TAG system. Scatter plots on the right highlight the relationship between O3 dose and artifact abundances.

Benzophenone (**Figure A3.9**) has been previously identified as both an abundant[4] and a unique[2] Tenax®-O3 degradation product. Nonetheless, SV-TAG observed trends indicate that this compound is not an artifact in the TD-GC/MS system. The constant abundances in Region B and beyond suggest predictable behavior, thus non-zero abundances are not expected to be related to outdoor ambient measurements. In addition, artifact formation from the thermal decomposition of

the adsorbent is not speculated since blanks did not contain benzophenone. Therefore, it is hypothesized here that this compound could be a result of the constant Tenax® exposure to oxygen during ambient collection. In Region A, the trend change at the beginning of the campaign happened when sample lines were not being conditioned between collections, thus it is conjectured that the indoor benzophenone that was adhered to the lines was being sampled as an outdoor compound when switching from indoor to outdoor collection.

It is concluded from the analysis above that accurate quantification of benzophenone indoors requires prior estimation of benzophenone formation from potential oxygen exposure. The fact that this compound was identified as a unique artifact in previous studies and yet, it has not been found as a Tenax®-O3 artifact here, demonstrates the complexity of the Tenax® degradation pattern from O3 exposure and its TD-GC/MS specificity formation pathways.

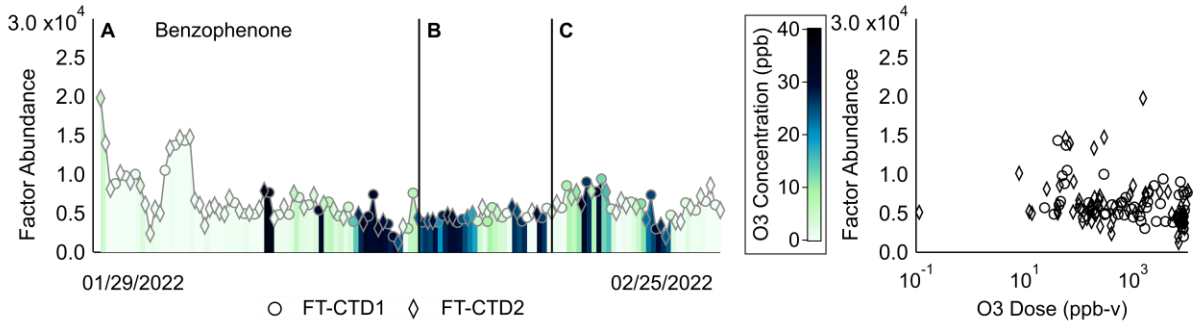

Figure A3.9. Qualitative abundances of benzophenone, a Tenax®-O3 artifact previously reported in the literature yet not positively identified in the SV-TAG system. Scatter plots on the right highlight the relationship between O3 dose and compound abundances.

SV-TAG Specific Tenax® Degradation Products from Ozone Exposure

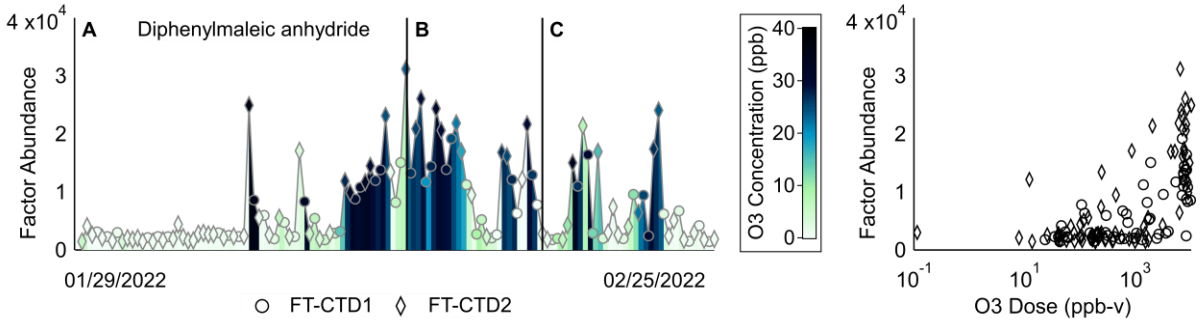

Figure A3.10. Qualitative abundances of diphenylmaleic anhydride, a Tenax®-O3 artifact not previously reported in the literature but positively identified in the SV-TAG system. Scatter plots on the right highlight the relationship between O3 dose and compound abundances.

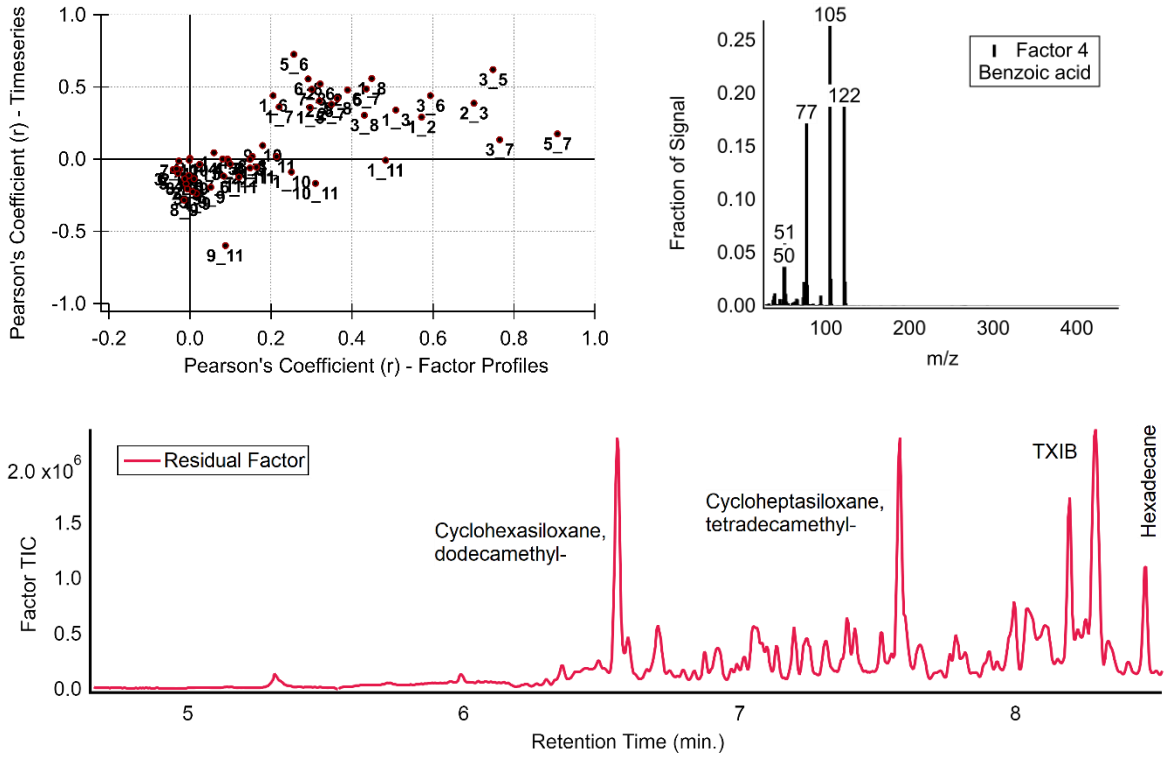

Figure A3.11. Correlation analysis from PMF mass spectral deconvolution results to investigate the formation of SV-TAG-specific high-volatility Tenax®-O3 artifacts. Similar factors have a r > 0.5. Note that none of the identified factors correlates with factor 4 (benzoic acid – unique Tenax®-O3 artifact). The residual factor (bottom plot - not included in the correlation calculations) featured individual compounds not associated with Tenax® degradation.

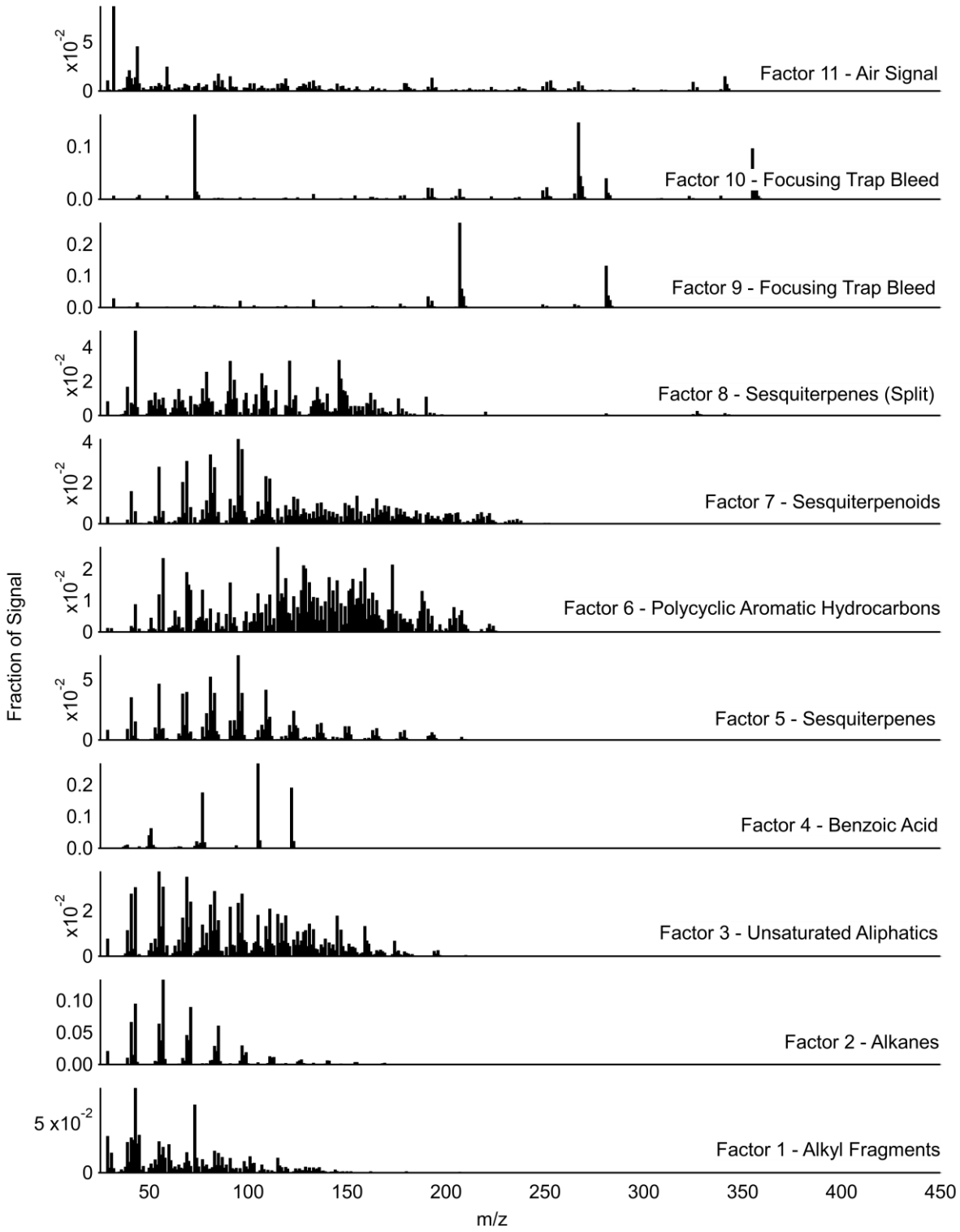

Figure A3.12. Resulting factor profiles from the PMF mass spectral deconvolution analysis to investigate the formation of SV-TAG-specific high-volatility Tenax®-O3 artifacts.

Section A3.4. Collection Cells Design Comparison

Figure A3.13 represents the resulting factor profiles from the PMF mass spectral deconvolution analysis to compare the collection capabilities of the three different cell designs. Note that factor 12 was not included in the comparison since it represents benzoic acid, which was found to be a Tenax®-O3 artifact in the SV-TAG system during the ALPACA campaign. Factors 14, 16, and 17 were also excluded since they are associated with the focusing trap column bleed. Factors 5 and 6 were found to be a split with both of them representing sesquiterpenes. Thus, their abundances were summed for the analysis discussed in the main text. Similarly, both factors 10 and 13 were added to correspond to sesquiterpenoid compounds in the sample, while factors 9 and 11 constituted aromatic species. Factor 15 are alkyl fragments that based on correlation analysis were found to be originated from alkenes identified in factor 3.

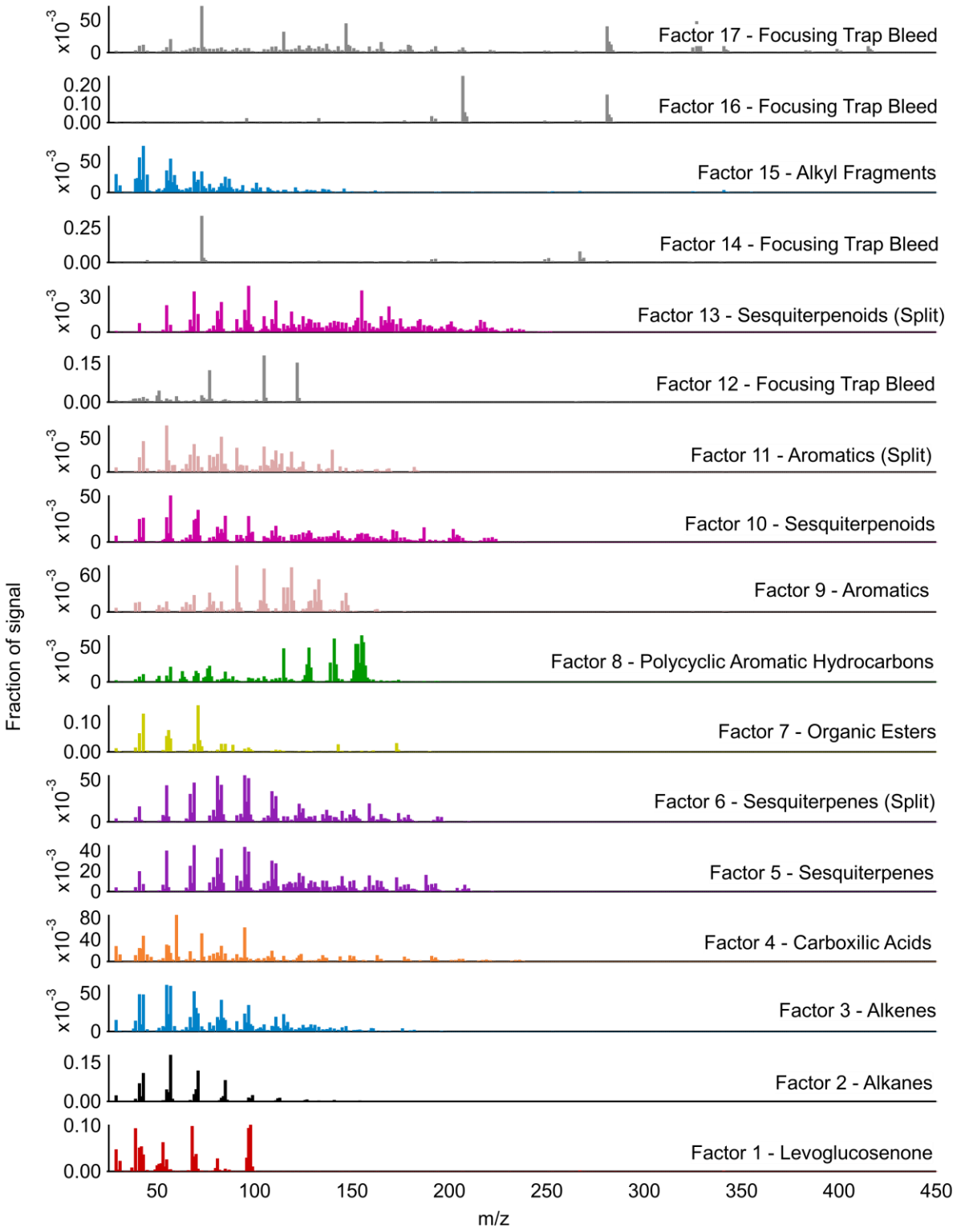

Figure A3.13. Resulting factor profiles from the PMF mass spectral deconvolution analysis to compare the collection capability of the dual-stage Tenax® cell and the single-stage filter cell.

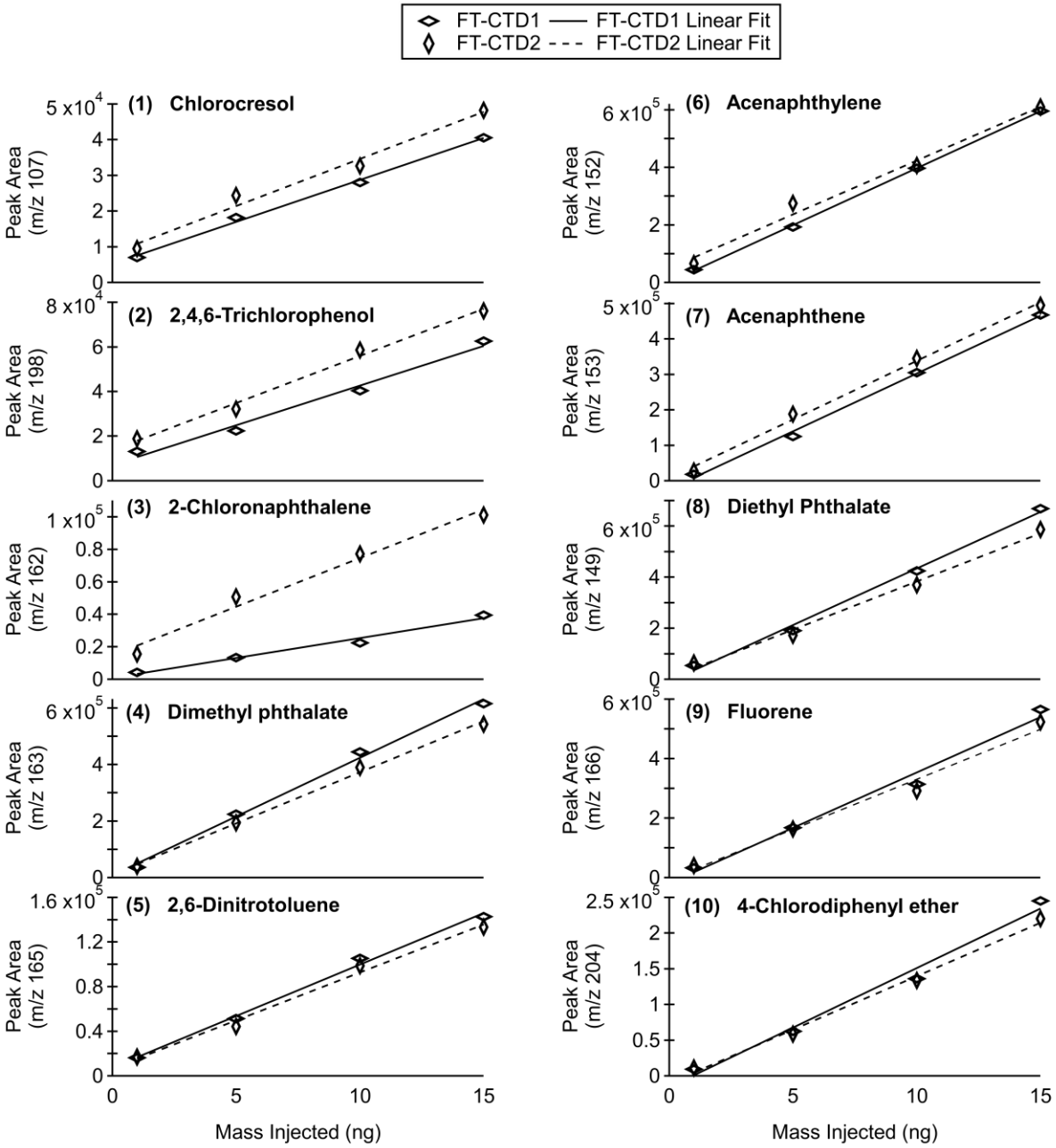

Figure A3.14. Calibration curves of selected compounds used for detection limit calculations. Compounds were present in the EPA 625 semi-volatile calibration mixture and injected masses varied from 1 to 15 ng.

References

1. Satyro M, Yaws CL. *The Yaws Handbook of Thermodynamic Properties for Hydrocarbons and Chemicals*. Gulf Professional Publishing; 2018.

2. Klenø JG, Wolkoff P, Per Axel Clausen, Wilkins CK, Pedersen T. Degradation of the Adsorbent Tenax TA by Nitrogen Oxides, Ozone, Hydrogen Peroxide, OH Radical, and Limonene Oxidation Products. *Environmental Science & Technology*. 2002;36(19):4121-4126.

3. Buch A, Imène Belmahdi, Szopa C, et al. Role of the Tenax® Adsorbent in the Interpretation of the EGA and GC-MS Analyses Performed With the Sample Analysis at Mars in Gale Crater. Journal of Geophysical Research: Planets. 2019;124(11):2819-2851.

4. Lee JH, Batterman S, Jia C, Chernyak SM. Ozone Artifacts and Carbonyl Measurements Using Tenax GR, Tenax TA, Carbopack B, and Carbopack X Adsorbents. *Journal of the Air & Waste Management Association*. 2006;56(11):1503-1517.

APPENDIX A4

Supplement of "Investigation of Gas-Particle Phase Partitioning of Speciated Organic Compounds during the Alaskan Layered Pollution And Chemical Analysis (ALPACA) Field Campaign"

Section A4.1. Field Description

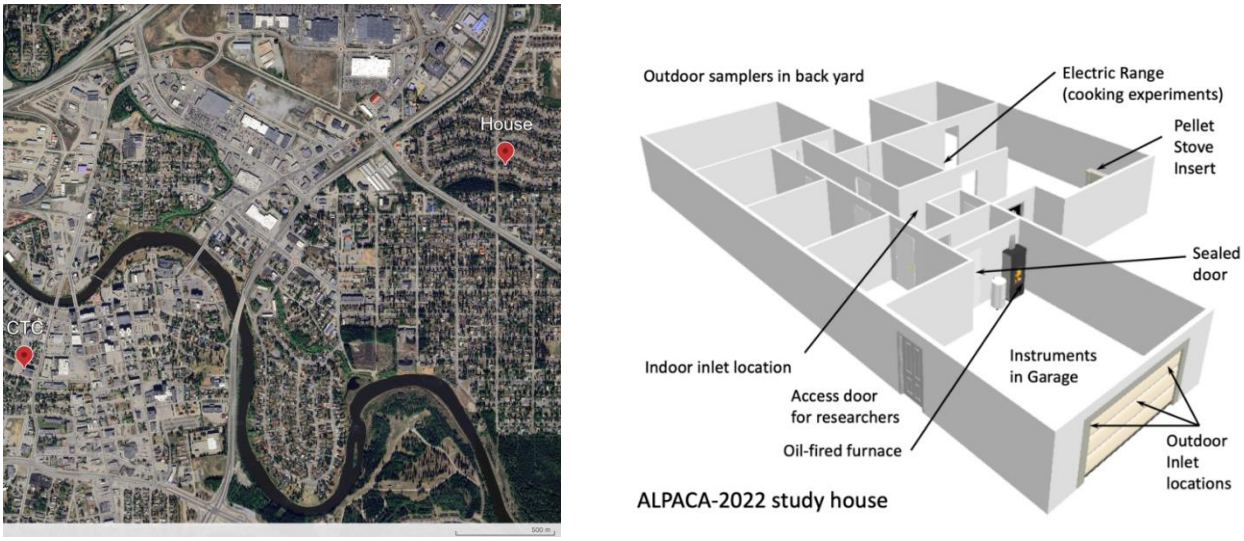

Figure A4.1. Left: Map of Fairbanks showing the location of the ALPACA house and downtown field sites. Basemap produced by Earth.Google.com; Right: The 3-D model of the home obtained from Simpson et al (2024).[1]

Section A4.2. SV-TAG Sampling and Data Processing

SV-TAG Inlets and Sampling Strategy

To ensure accurate gas and particle phase measurements, two main aspects were considered for the design of the SV-TAG inlet system. First, it was crucial to preserve the aerosols' original equilibrium state before gas-phase removal by the denuder. Therefore, denuders, and any sample lines upstream of the device, needed to be kept at the same temperature as the samples' environment. This was not a concern during indoor sampling since the SV-TAG was located inside the test-house garage, both maintained at the same temperature. Regardless, the indoor denuder and upstream sample lines were insulated with foam to avoid condensation/evaporation from garage temperature fluctuations. In contrast, outdoor sampling required a more robust setup due to the magnitude of the temperature gradient between the garage (indoors) and the sample outdoors. To prevent evaporation before gas-phase removal, the outdoor denuder was placed inside an insulated box, maintained at the same outdoor temperature by continuous circulation of outdoor air. Any sample line upstream of the denuder and not in the box was kept outside.

The second aspect that needed to be considered when designing the instrument's inlet was mitigating gas and particle wall losses during sampling. This was achieved by conditioning the sample lines in between ambient collections. A schematic of the SV-TAG inlet system highlighting sample line conditioning flows is shown in **Figure A4.2.** The schematic represents the instrument in by-pass mode after indoor sampling. While the collected material is being analyzed by thermal desorption gas-chromatography mass spectrometry, the instrument's sample lines are being conditioned for the subsequent outdoor sampling. This conditioning is achieved by the continuous flow of outdoor air through the instrument bypass (dotted blue lines), which provides thermodynamic equilibrium inside the sample lines, minimizing particle/gas losses and potential

measurement artifacts from the re-volatilization of organic species due to indoor/outdoor temperature gradient. Conditioning flow is reversed after outdoor sampling. Furthermore, all lines downstream of the denuders were insulated with foam to further minimize heat transfer between the garage and the conditioned sample lines.

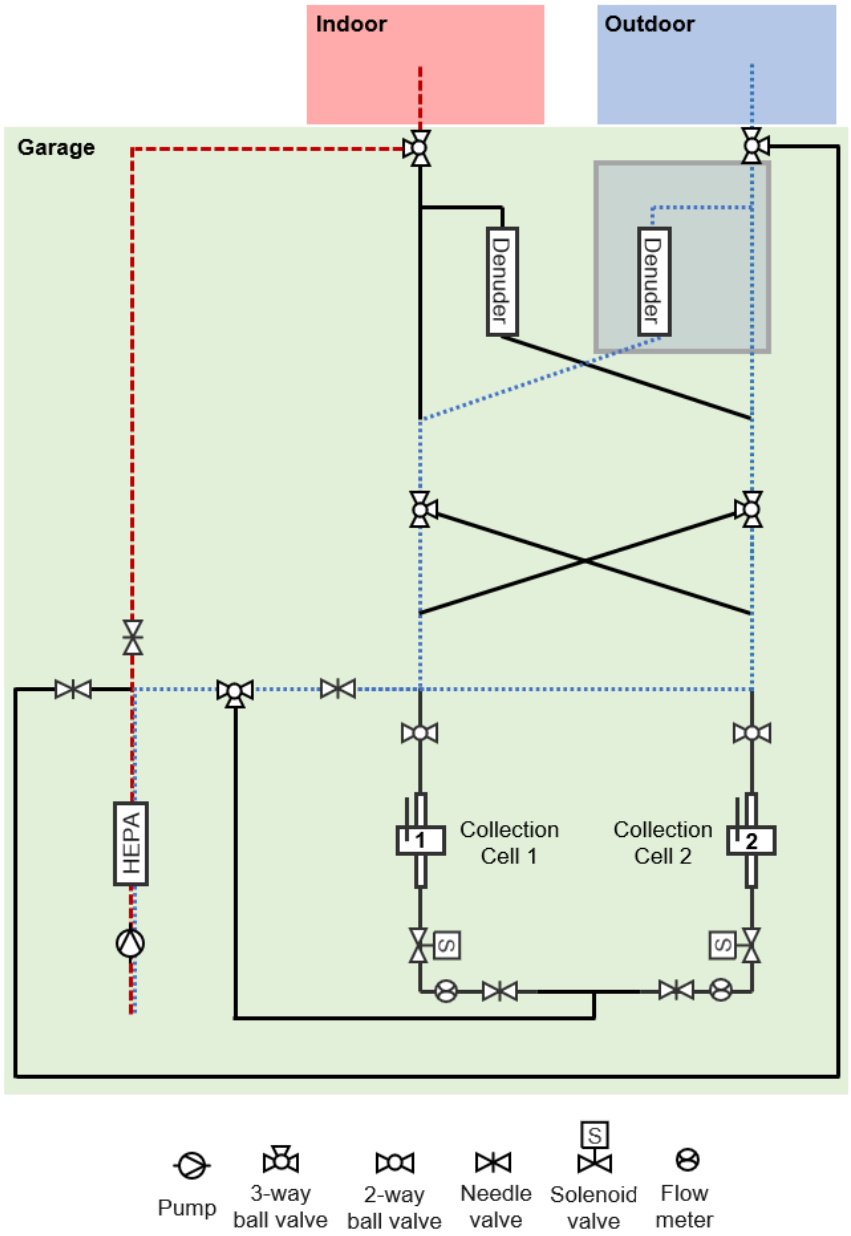

Figure A4.2. SV-TAG inlet system during the ALPACA campaign. The schematic represents the instrument in by-pass mode after indoor sampling. The collected material is being analyzed by thermal desorption gas-chromatography mass spectrometry while the instrument's sample lines are being conditioned for the subsequential outdoor sampling (dotted blue lines).

SV-TAG Data Processing and Quantification

Constant concentration (5 ng.μL^{-1}) of internal standard mixture containing deuterated polar and non-polar compounds (**Table A4.1**) were continuously injected into the SV-TAG system after almost every indoor and outdoor ambient collection, providing a means to correct for drifts in the detector and fluctuations in transfer efficiency on both the sample and external standard raw MS signals throughout the campaign duration (6-weeks). Polar and non-polar cell-dependent corrections were achieved by using the following equations:[2]

$$y_{i,j}(t) = \frac{y'_{i,j}(t)}{G_{j,k}(t)} \; with \; G_{j,k}(t) = \frac{\sum_{k=1}^{k=n} \frac{d_{k,j}(t)}{\overline{d_{k,j}(t)}}}{n} \qquad \textbf{(A4.1)}$$

Where $y_{i,j}(t)$ is the corrected MS signal (peak area) of compound i collected or injected (for calibration purposes) in cell j; $y'_{i,j}(t)$ is the raw MS signal (peak area) of compound i collected or injected (for calibration purposes) in cell j; and $G_{j,k}(t)$ is the cell-dependent polar or non-polar de-trending correction factor. In this case, $d_{k,j}(t)$ represent the peak area of deuterated compound k injected in cell j; $\overline{d_{k,j}}(t)$ is the average peak area of deuterated compound k throughout the time period considered; n is the number of polar or non-polar compounds.

TABLE A4.1. Full list of non-polar (top) and polar (bottom) deuterated chemical species included internal calibration mixture that was used for the time-dependent SV-TAG de-trending corrections.

Compound Name	Formula	CAS ID	MW (g.mol^{-1})
Chrysene-d12 98 atom % D	C18D12	1719-03-5	240.36
Perylene-d12 98 atom % D	C20D12	1520-96-3	264.38
Pyrene-d10 98 atom % D	C16D10	1718-52-1	212.31
Hexadecane-d34 98 atom % D	CD3(CD2)14CD3	15716-08-2	260.65
Eicosane-d42 98 atom % D	CD3(CD2)18CD3	62369-67-9	324.81
Tetracosane-d50 98 atom % D	CD3(CD2)22CD3	16416-32-3	388.96
Octacosane-d58 98 atom % D	CD3(CD2)26CD3	16416-33-4	453.12
Dotriacontane-d66 98 atom % D	CD3(CD2)30CD3	62369-68-0	517.27
1-Hexadecan-d33-ol 98% atom % D	CD3(CD2)14CD2OH	284474-73-3	275.64
Lauric-d23 acid 98 atom % D	CD3(CD2)10CO2H	59154-43-7	223.46
Palmitic acid-d31 98 atom % D	CD3(CD2)14CO2H	39756-30-4	287.62
Stearic-d35 acid 98 atom % D	CD3(CD2)16CO2H	17660-51-4	319.69

Figure A4.3 shows the polar and non-polar $G_{j,k}(t)$ values of each cell. Here, alkanes and polycyclic aromatic hydrocarbons (PAHs) were corrected using the non-polar de-trending factor, while biomass burning-related compounds were corrected using the polar factor. When internal standard signals were not available, corrections were performed using $G_{j,k}(t)$ linear regression values. Note that the data is divided into two different periods separating de-trending correction factors before and after MS-retuning due to a power outage. Varying concentrations ($0.1 – 5$ ng.μL^{-1}) of external standards were injected in both collectors to generate cell-dependent calibration curves using corrected MS signals. **Figure A4.4** illustrates the de-trended MS responses for a series of alkane injections. Compounds C21, C23, C25 and C27 are RT interpolated points.

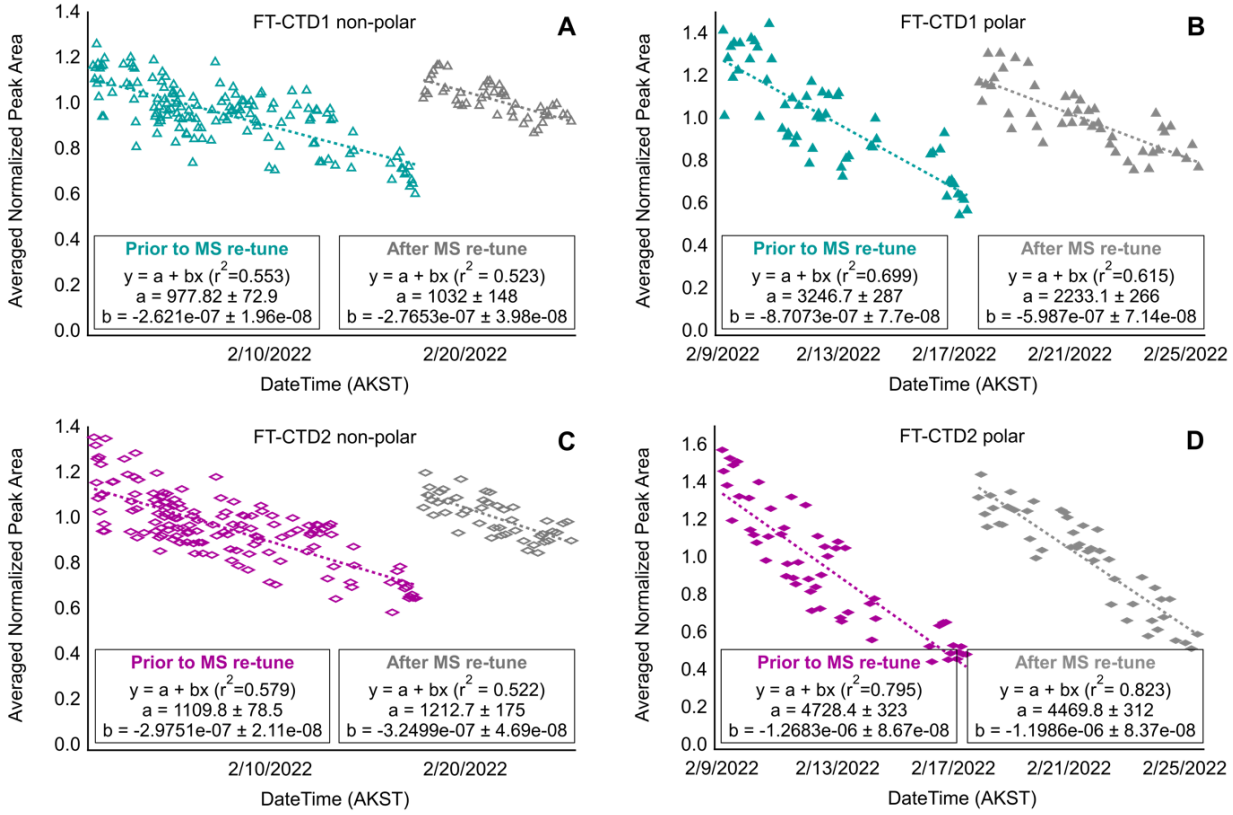

Figure A4.3. Cell-dependent de-trending functions. Vertical axis represents the average of each non-polar or polar deuterated compound response relative to its average response over the time period considered. **(A)** FT-CTD1 non-polar. **(B)** FT-CTD1 polar. **(C)** FT-CTD2 non-polar. **(D)** FT-CTD2 polar.

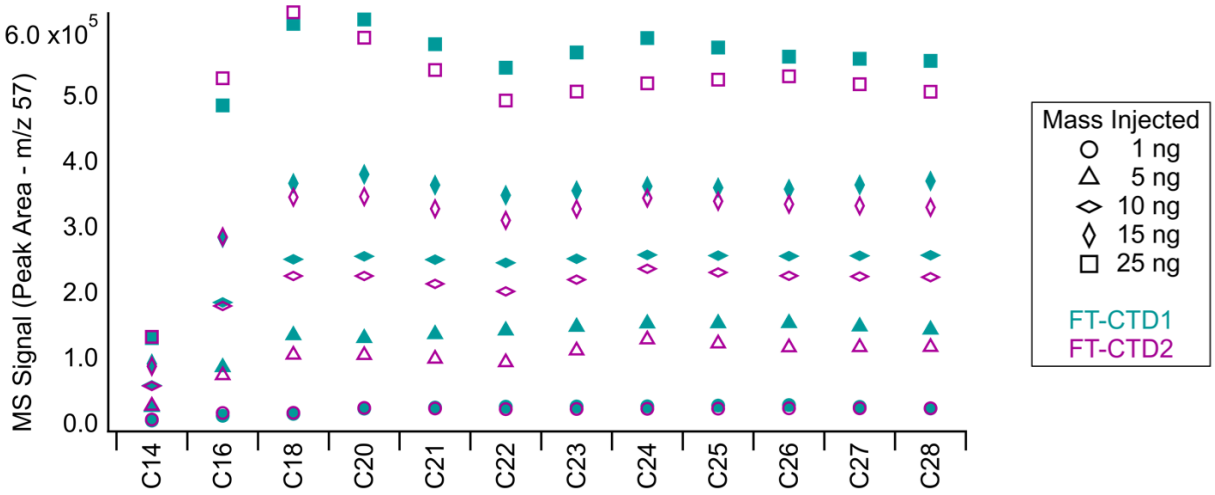

Figure A4.4. Example of corrected MS signal (integrated peak areas) used to generate alkanes calibration curves.

TABLE A4.2. List of compounds quantified for phase partitioning analysis.

Name	Formula	CAS	RT (s)	ID Conf.	Quant. Ion	G(t)	Quant. Method
Tetradecane	C14H30	629-59-4	432.38	A	57	non-polar	External Standard
Hexadecane	C16H34	544-76-3	500.36	A	57	non-polar	External Standard
Octadecane	C18H38	593-45-3	561.54	A	57	non-polar	External Standard
Eicosane	C20H42	112-95-8	615.04	A	57	non-polar	External Standard
Heneicosane	C21H44	629-94-7	640.18	B	57	non-polar	RT Interpolation
Docosane	C22H46	629-97-0	664.11	A	57	non-polar	External Standard
Tricosane	C23H48	638-67-5	687.76	B	57	non-polar	RT Interpolation
Tetracosane	C24H50	646-31-1	709.92	A	57	non-polar	External Standard
Pentacosane	C25H52	629-99-2	731.79	B	57	non-polar	RT Interpolation
Hexacosane	C26H54	630-01-3	752.48	A	57	non-polar	External Standard
Heptacosane	C27H56	593-49-7	772.59	B	57	non-polar	RT Interpolation
Octacosane	C28H58	630-02-4	792.09	A	57	non-polar	External Standard
Naphthalene	C10H8	91-20-3	346.06	A	128	non-polar	External Standard
Acenaphthylene	C12H8	208-96-8	455.13	A	152	non-polar	External Standard
Acenaphthene	C12H10	83-32-9	466.66	A	153	non-polar	External Standard
Fluorene	C13H10	86-73-7	500.65	A	166	non-polar	External Standard
Phenanthrene	C14H10	85-01-8	563.02	A	178	non-polar	External Standard
Anthracene	C14H10	120-12-7	566.56	A	178	non-polar	External Standard
Fluoranthene	C16H10	206-44-0	640.16	A	202	non-polar	External Standard
Pyrene	C16H10	129-00-0	655.82	A	202	non-polar	External Standard
Chrysene	C18H12	218-01-9	734.74	A	228	non-polar	External Standard
Syringol	C8H10O3	91-10-1	413.17	A	154	polar	External Standard
Vanillin	C8H8O3	121-33-5	434.16	A	151	polar	External Standard
Isoeugenol	C10H12O2	97-54-1	451.30	B	164	polar	Surrogate - Vanillin
Apocynin	C9H10O3	498-02-2	464.90	B	151	polar	Surrogate - Vanillin
Guaiacylacetone	C10H12O3	2503-46-0	478.50	B	137	polar	Surrogate - Vanillin
Syringaldehyde	C9H10O4	134-96-3	522.81	B	182	polar	Surrogate - Syringol
Methoxyeugenol	C11H14O3	6627-88-9	533.75	B	194	polar	Surrogate - Syringol
Acetosyringone	C10H12O4	2478-38-8	544.39	B	181	polar	Surrogate - Syringol
Palmitic acid	C16H32O2	57-10-3	608.25	A	73	polar	External Standard
Retene	C18H18	483-65-8	675.34	B	219	non-polar	RT Interpolation

Note. The table separates compounds by chemical class. Top to bottom: alkanes, polycyclic aromatic hydrocarbons, biomass-burning related.

Abbreviations: RT, retention time; ID Conf., identification confidence; Quant. Ion., quantifier ion; G(t), de-trending correction factor; Quant. Method, method of quantification.

TABLE A4.3. Average outdoor and indoor particle and gas concentrations for alkanes, polycyclic aromatic hydrocarbons, and biomass burning-related compounds.

	Outdoor		Indoor	
	Particle (ng.m^{-3})	**Gas (ng.m^{-3})**	**Particle (ng.m^{-3})**	**Gas (ng.m^{-3})**
Tetradecane	59.1129	201.9408	85.0699	583.9062
Hexadecane	36.3387	43.3593	44.8540	213.2943
Octadecane	34.7525	42.5956	55.9439	180.5893
Eicosane	11.5474	9.3479	14.3076	40.0144
Heneicosane	8.4173	3.2009	8.3741	18.5487
Docosane	9.1534	1.9816	8.6375	12.5582
Tricosane	8.1468	0.8547	8.3229	6.6561
Tetracosane	8.1796	0.4484	9.7291	3.7820
Pentacosane	7.8450	0.3071	9.3681	1.9592
Hexacosane	7.4042	0.2031	10.1615	1.0285
Heptacosane	7.6138	0.1764	9.5317	0.6488
Octacosane	7.8408	0.1286	12.1338	0.5378
Naphthalene	15.4801	46.8723	38.8998	211.5486
Acenaphthylene	4.2823	9.2541	4.0747	24.0909
Acenaphthene	2.1361	5.5965	6.3168	44.1561
Fluorene	1.6945	3.7522	4.3549	30.9114
Phenanthrene	13.7037	12.5341	9.0960	37.6847
Anthracene	3.3265	3.3110	10.2986	41.2421
Fluoranthene	7.8426	2.0588	2.3591	2.2922
Pyrene	8.3542	1.1519	2.5456	2.5919
Chrysene	28.9253	2.6839	23.3071	10.8768
Syringol	9.7062	5.6365	N/A	N/A
Vanillin	25.0439	21.9611	N/A	N/A
Isoeugenol	8.9750	3.9802	N/A	N/A
Apocynin	18.8070	11.4042	N/A	N/A
Guaiacylacetone	36.3281	20.3288	N/A	N/A
Syringaldehyde	25.5455	8.9298	N/A	N/A
Methoxyeugenol	21.7106	4.7990	N/A	N/A
Acetosyringone	23.9965	4.5026	N/A	N/A
Palmitic Acid	78.1064	16.5255	N/A	N/A
Retene	3.1123	0.6542	N/A	N/A

Note. Biomass burning-related compounds were not quantified indoors.
Abbreviations: N/A, not applicable.

Section A4.3. Absorptive Partitioning Model

Liquid vapor pressures ($p^o_{L,i}$) and enthalpies of vaporization ($\Delta H_{vap,i}$) were estimated at the chosen reference temperature ($T_{ref,i}$) using the following parametrization equations:[3]

$$p^o_{L,i}(Pa) = exp\left[A + \frac{B}{T_{ref,i}} + C\ln\left(T_{ref,i}\right) + DT^E_{ref,i}\right] \quad \textbf{(A4.2)}$$

$$\Delta H_{vap,i}(J.kmol^{-1}) = \left[A\left(1 - \frac{T_{ref,i}}{T_{c,i}}\right)\right] \times exp\left[B + C\left(\frac{T_{ref,i}}{T_{c,i}}\right) + D\left(\frac{T_{ref,i}}{T_c}\right)^2 + E\left(\frac{T_{ref,i}}{T_{c,i}}\right)^3\right] \quad \textbf{(A4.3)}$$

Where $T_{c,i}$ is the critical temperature of compound i. **Tables A4.4** to **A4.6** lists the parametrization coefficients for all the compounds considered in this work. **Tables A4.7** to **A4.9** shows the calculated outdoor and indoor model input parameters.

TABLE A4.4. Vapor pressure and enthalpy of vaporization parametrization parameters for alkanes

Name	T_c[a] (K)	Vapor Pressure Parameters					Enthalpy of Vaporization Parameters				
		A	B	C	D	E	A	B	C	D	E
Tetradecane	693	140.47	-13231	-16.859	6.5877E-06	2	120070000	1.445	-1.3846	0.42836	0
Pentadecane	708	135.57	-13478	-16.022	5.6136E-06	2	100520000	0.37778	0.50709	-0.466	0
Hexadecane	722	162.644	-15734	-19.62	6.43366E-09	3	125460000	0.81391	0.14155	-0.5337	0
Octadecane	747.8	176.668	-17476	-21.442	6.20961E-09	3	148650000	1.0254	-0.0681	-0.5139	0
Eicosane	770.6	200.329	-19958	-24.584	6.28867E-09	3	165060000	0.90122	0.29776	-0.7471	0
Heneicosane	781	204.663	-20628	-25.125	6.16043E-09	3	171710000	0.92791	0.26636	-0.7421	0
Docosane	790.9	218.966	-22078	-27.028	6.26944E-09	3	180330000	0.84251	0.49769	-0.8829	0
Tricosane	800.3	226.356	-22986	-27.986	6.22612E-09	3	187550000	0.83578	0.54269	-0.9189	0
Tetracosane	809.3	227.257	-23366	-28.061	6.05214E-09	3	192640000	0.87912	0.4622	-0.8836	0
Pentacosane	817.8	240.888	-24783	-29.866	6.15627E-09	3	201200000	0.80854	0.65387	-1	0
Hexacosane	825.25	246.362	-25530	-30.563	6.09679E-09	3	207730000	0.81591	0.66134	-1.0137	0
Heptacosane	833.7	256.369	-26657	-31.874	6.13098E-09	3	215250000	0.77911	0.76969	-1.0826	0
Octacosane	841.1	229.618	-25953	-27.79	3.85333E-12	4	193230000	0.31222	1.3451	-1.2152	0

Abbreviations: T_c, critical temperature.
[a]Property retrieved from the *Design Institute for Physical Property Research/AIChE (DIPPR®) project 801 database*.[3]

TABLE A4.5. Vapor pressure and enthalpy of vaporization parametrization parameters for PAHs.

Name	T_c[a] (K)	Vapor Pressure Parameters					Enthalpy of Vaporization Parameters				
		A	B	C	D	E	A	B	C	D	E
Naphthalene	748.4	62.964	-8137.5	-5.6317	2.2675E-18	6	50930000	-0.4458	1.0348	-0.1953	0
Acenaphthylene	792	74.677	-10061	-7.0929	1.4023E-18	6	68288000	-0.186	0.91146	-0.3648	0
Acenaphthene	803.15	71.247	-9584	-6.775	0.000001472	2	132430000	2.7425	-4.0505	1.833	0
Fluorene	826	96.008	-11340	-10.331	2.9608E-06	2	92705000	0.93138	-0.922	0.42122	0
Phenanthrene	893	94.249	-12064	-9.8971	2.11E-09	3	104110000	1.0186	-0.7696	0.13015	0
Anthracene	873	65.069	-10251	-5.7509	1.1238E-18	6	75843000	0.04948	0.52951	-0.3175	0
Fluoranthene	905	167.64	-14930	-22.241	0.016621	1	170140000	3.196	-4.9146	2.2856	0
Pyrene	974	87.97	-12914	-8.8087	9.2078E-13	4	96583000	0.2715	0.47923	-0.3938	0
Chrysene	979	91.899	-14944	-9.058	4.8938E-19	6	102630000	-0.0385	0.71173	-0.33	0

Abbreviations: T_c, critical temperature.
[a]Property retrieved from the *Design Institute for Physical Property Research/AIChE (DIPPR®) project 801 database*.[3]

TABLE A4.6. Vapor pressure and enthalpy of vaporization parametrization parameters for BBOA.

Name	T_c[a] (K)	Vapor Pressure Parameters					Enthalpy of Vaporization Parameters				
		A	B	C	D	E	A	B	C	D	E
Syringol	752.2	88.7637	-11572	-8.8571	2.35918E-18	6	94718000	0.60908	-0.3542	0.1269	0
Vanillin	777	105.83	-13646	-11.057	2.4173E-18	6	116640000	0.83247	-0.5876	0.17482	0
Isoeugenol	751.9	113.728	-12330	-12.719	4.28615E-09	3	115670000	1.4206	-1.3321	0.31996	0
Apocynin	786	107.7	-14109	-11.27	2.1295E-18	6	121520000	0.89064	-0.7331	0.27387	0
Syringaldehyde	809	83.381	-12700	-7.9096	1.55544E-18	6	122910000	1.2602	-1.6114	0.724	0
Palmitic acid	785	185.203	-20925	-21.813	4.56822E-18	6	141400000	-0.2113	2.0707	-1.4835	0

Abbreviations: T_c, critical temperature.
[a]Property retrieved from the *Design Institute for Physical Property Research/AIChE (DIPPR®) project 801 database*.[3]

TABLE A4.7. Outdoor and indoor absorptive partitioning model input parameters for alkanes.

		Outdoor Average T_{out} (K): 253.14			Indoor Average T_{in} (K): 296.01		
	T_m[a] (K)	T_{ref} (K)	P_L^o (torr) at T_{ref}	ΔH_{vap} (J.mol^{-1}) at T_{ref}	T_{ref} (K)	P_L^o (torr) at T_{ref}	ΔH_{vap} (J.mol^{-1}) at T_{ref}
Tetradecane	279.01	279.01	0.00189529	73335.91942	296.01	0.011360328	71449.2863
Pentadecane	283.072	283.072	0.000966618	77634.69192	296.01	0.003947988	76334.1462
Hexadecane	291.308	291.308	0.000590473	83669.69455	296.01	0.001025203	83035.92751
Octadecane	301.31	301.31	0.000213556	92754.42716	301.31	0.000213556	92754.42716
Eicosane	309.58	309.58	5.32913E-05	103940.4467	309.58	5.32913E-05	103940.4467
Heneicosane	313.35	313.35	3.46606E-05	107380.4256	313.35	3.46606E-05	107380.4256
Docosane	317.15	317.15	1.66252E-05	113690.9737	317.15	1.66252E-05	113690.9737
Tricosane	320.65	320.65	1.00843E-05	117964.5611	320.65	1.00843E-05	117964.5611
Tetracosane	323.75	323.75	7.55582E-06	120237.3304	323.75	7.55582E-06	120237.3304
Pentacosane	326.65	326.65	3.54537E-06	126498.6746	326.65	3.54537E-06	126498.6746
Hexacosane	329.25	329.25	2.21296E-06	130147.5163	329.25	2.21296E-06	130147.5163
Heptacosane	332.15	332.15	1.24054E-06	135283.504	332.15	1.24054E-06	135283.504
Octacosane	334.35	334.35	5.73252E-07	138663.6523	334.35	5.73252E-07	138663.6523

Note. Methodology for the choice of reference temperature is described in the main document section 4.2.4.
Abbreviations: T_{out}, outdoor temperature; T_{in}, indoor temperature; T_m, melting temperature; T_{ref}, reference temperature; P_L^o, saturation vapor pressure; ΔH_{vap}, enthalpy of vaporization
[a]Property retrieved from the *Design Institute for Physical Property Research/AIChE (DIPPR®) project 801 database*.[3]

TABLE A4.8. Outdoor and indoor absorptive partitioning model input parameters for PAHs.

		Outdoor Average T_{out} (K): 253.14			Indoor Average T_{in} (K): 296.01		
	T_m[a] (K)	T_{ref} (K)	P_L^o (torr) at T_{ref}	ΔH_{vap} (J.mol^{-1}) at T_{ref}	T_{ref} (K)	P_L^o (torr) at T_{ref}	ΔH_{vap} (J.mol^{-1}) at T_{ref}
Naphthalene	353.434	353.434	7.436803948	50952.94314	353.434	7.436803948	50952.94314
Acenaphthylene	362.65	362.65	1.274876396	62108.88071	362.65	1.274876396	62108.88071
Acenaphthene	366.56	366.56	1.500097606	60854.10076	366.56	1.500097606	60854.10076
Fluorene	387.94	387.94	2.112664432	63714.72026	387.94	2.112664432	63714.72026
Phenanthrene	372.38	372.38	0.218314326	70583.29899	372.38	0.218314326	70583.29899
Anthracene	488.93	488.93	37.13487303	61947.57836	488.93	37.13487303	61947.57836
Fluoranthene	383.33	383.33	0.117771607	73466.99724	383.33	0.117771607	73466.99724
Pyrene	423	423	0.500409332	76668.02456	423	0.500409332	76668.02456
Chrysene	531.15	531.15	7.711306156	84367.68493	531.15	7.711306156	84367.68493

Note. Methodology for the choice of reference temperature is described in the main document section 4.2.4.
Abbreviations: T_{out}, outdoor temperature; T_{in}, indoor temperature; T_m, melting temperature; T_{ref}, reference temperature; P_L^o, saturation vapor pressure; ΔH_{vap}, enthalpy of vaporization
[a]Property retrieved from the *Design Institute for Physical Property Research/AIChE (DIPPR®) project 801 database*.[3]

TABLE A4.9. Outdoor and indoor absorptive partitioning model input parameters for BBOA.

		Outdoor Average T_{out} (K): 253.14			**Indoor** Average T_{in} (K): 296.01		
	T_m[a] (K)	T_{ref} (K)	P_L^o (torr) at T_{ref}	ΔH_{vap} (J.mol^{-1}) at T_{ref}	T_{ref} (K)	P_L^o (torr) at T_{ref}	ΔH_{vap} (J.mol^{-1}) at T_{ref}
Syringol	328.65	328.65	0.069753444	71956.8435	328.65	0.069753444	71956.8435
Vanillin	355	355	0.088444977	80843.40767	355	0.088444977	80843.40767
Isoeugenol	294.68	294.68	0.005424431	72192.08904	296.0107	0.006191578	72061.88943
Apocynin	387.65	387.65	0.471358285	81063.42395	387.65	0.471358285	81063.42395
Syringaldehyde	386.15	386.15	0.221840714	80306.5564	386.15	0.221840714	80306.5564
Palmitic acid	335.66	335.66	0.000137485	112933.241	335.66	0.000137485	112933.241

Note. Methodology for the choice of reference temperature is described in the main document section 4.2.4.
Abbreviations: T_{out}, outdoor temperature; T_{in}, indoor temperature; T_m, melting temperature; T_{ref}, reference temperature; P_L^o, saturation vapor pressure; ΔH_{vap}, enthalpy of vaporization
[a]Property retrieved from the *Design Institute for Physical Property Research/AIChE (DIPPR®) project 801 database*.[3]

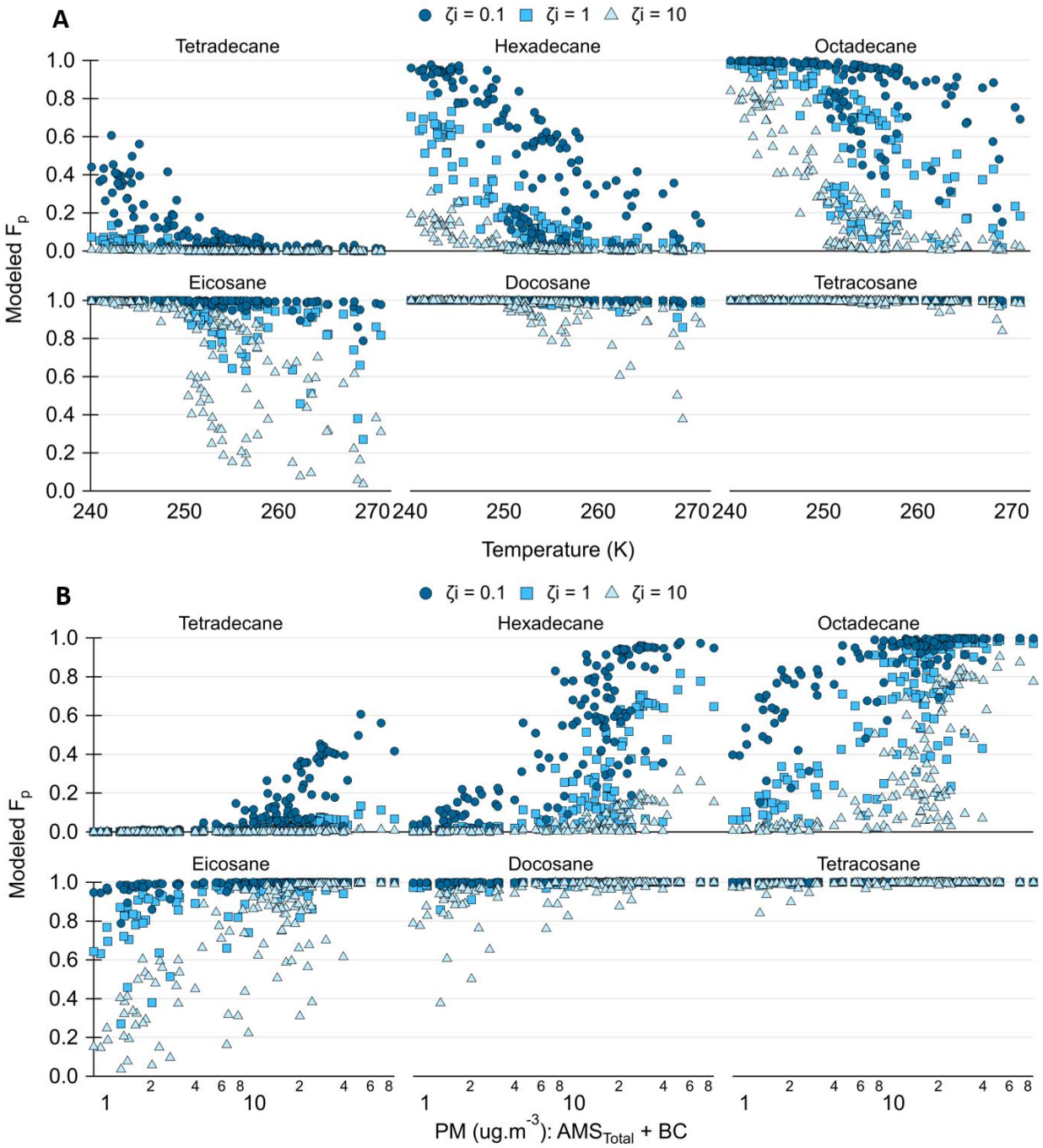

Figure A4.5. Modeled outdoor absorptive phase partitioning behavior for selected aliphatic saturated hydrocarbons (alkanes) during the ALPACA campaign considering three different values for the activity coefficient. **(A)** Calculated particle phase fraction (F_p) values as a function of temperature. **(B)** Calculated F_p values as a function of particulate matter (PM) concentration.

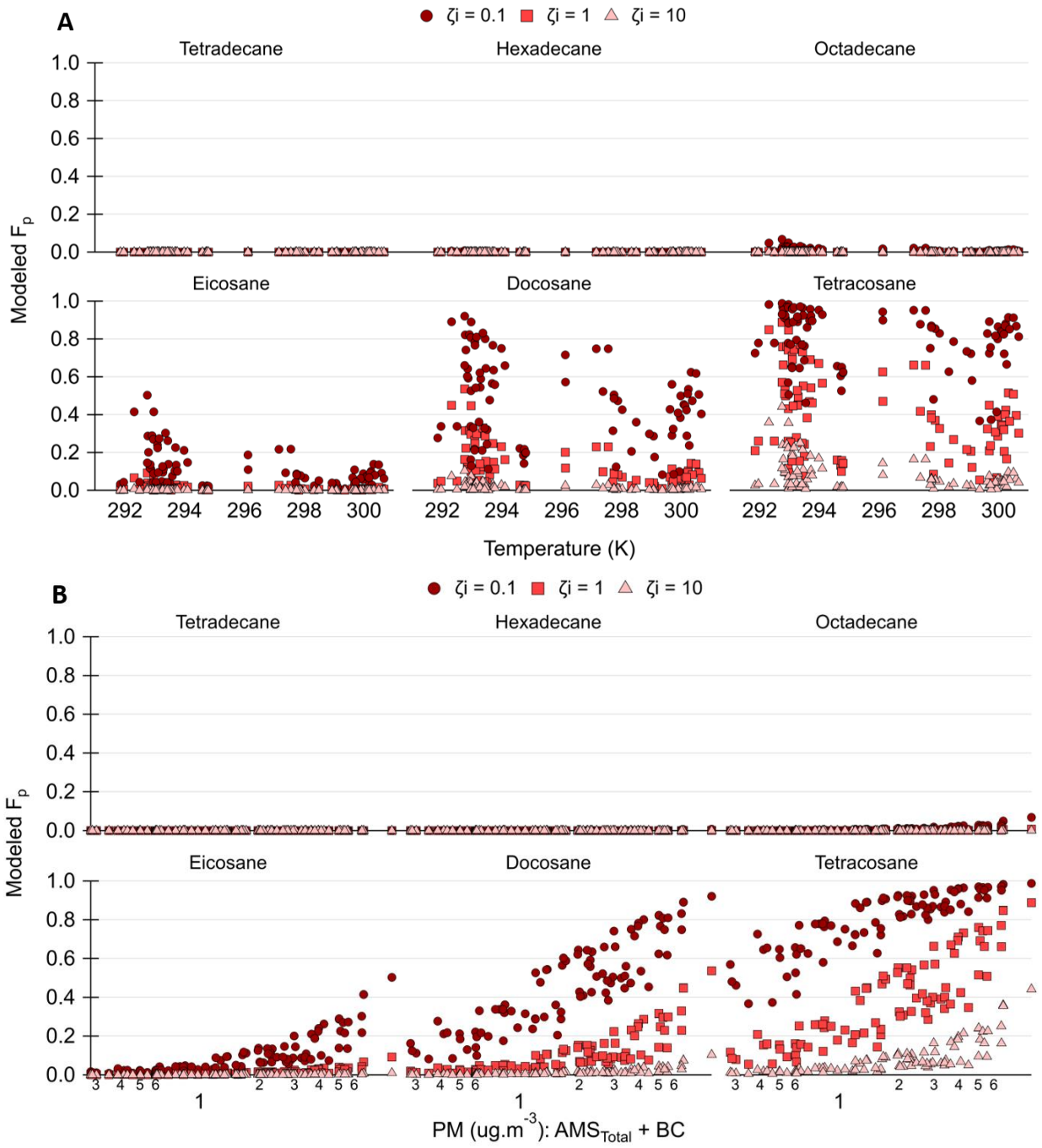

Figure A4.6. Modeled indoor absorptive phase partitioning behavior for selected aliphatic saturated hydrocarbons (alkanes) during the ALPACA campaign considering three different values for the activity coefficient. **(A)** Calculated particle phase fraction (F_p) values as a function of temperature. **(B)** Calculated F_p values as a function of particulate matter (PM) concentration.

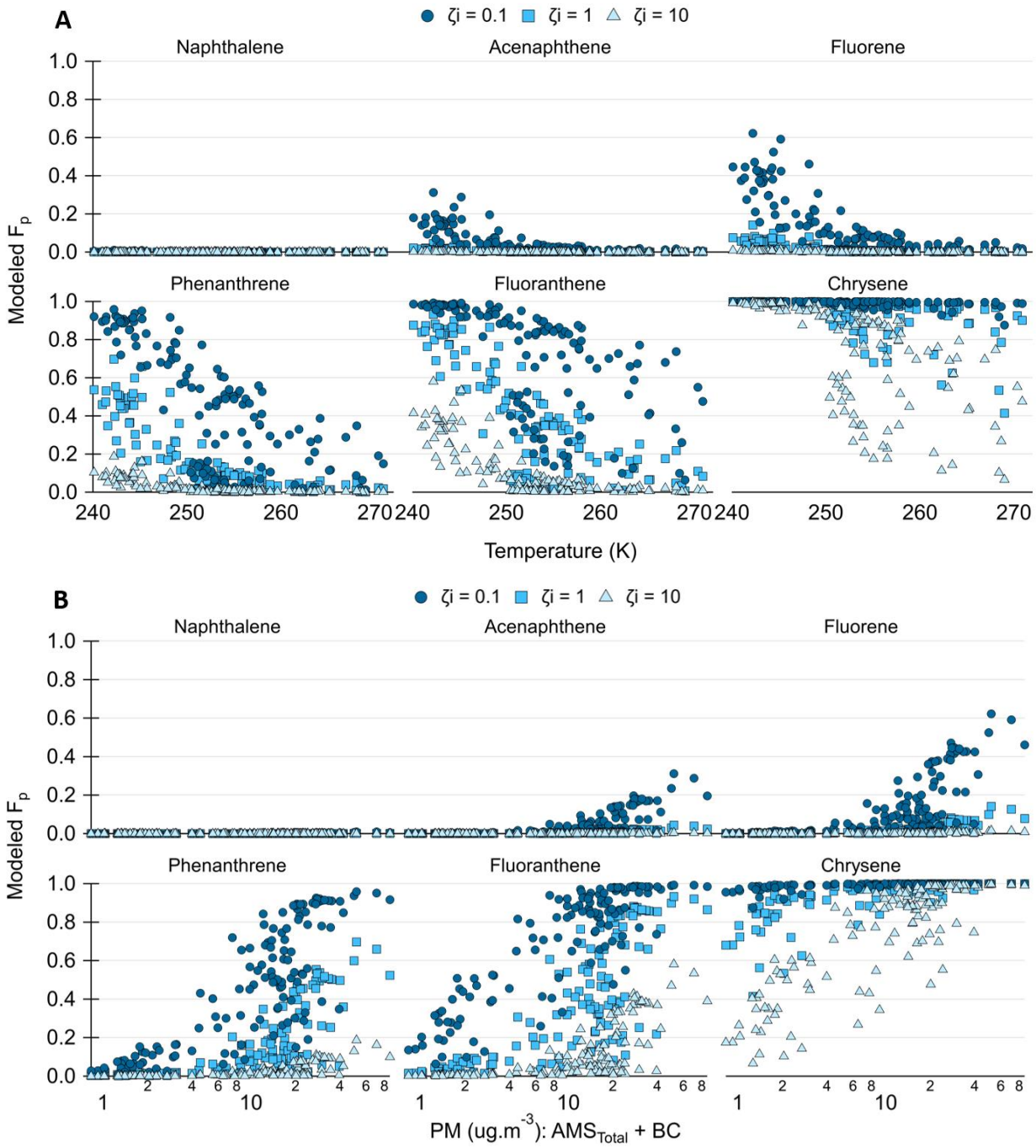

Figure A4.7. Modeled outdoor absorptive phase partitioning behavior for selected polycyclic aromatic hydrocarbons (PAHs) during the ALPACA campaign considering three different values for the activity coefficient. **(A)** Calculated particle phase fraction (F_p) values as a function of temperature. **(B)** Calculated F_p values as a function of particulate matter (PM) concentration.

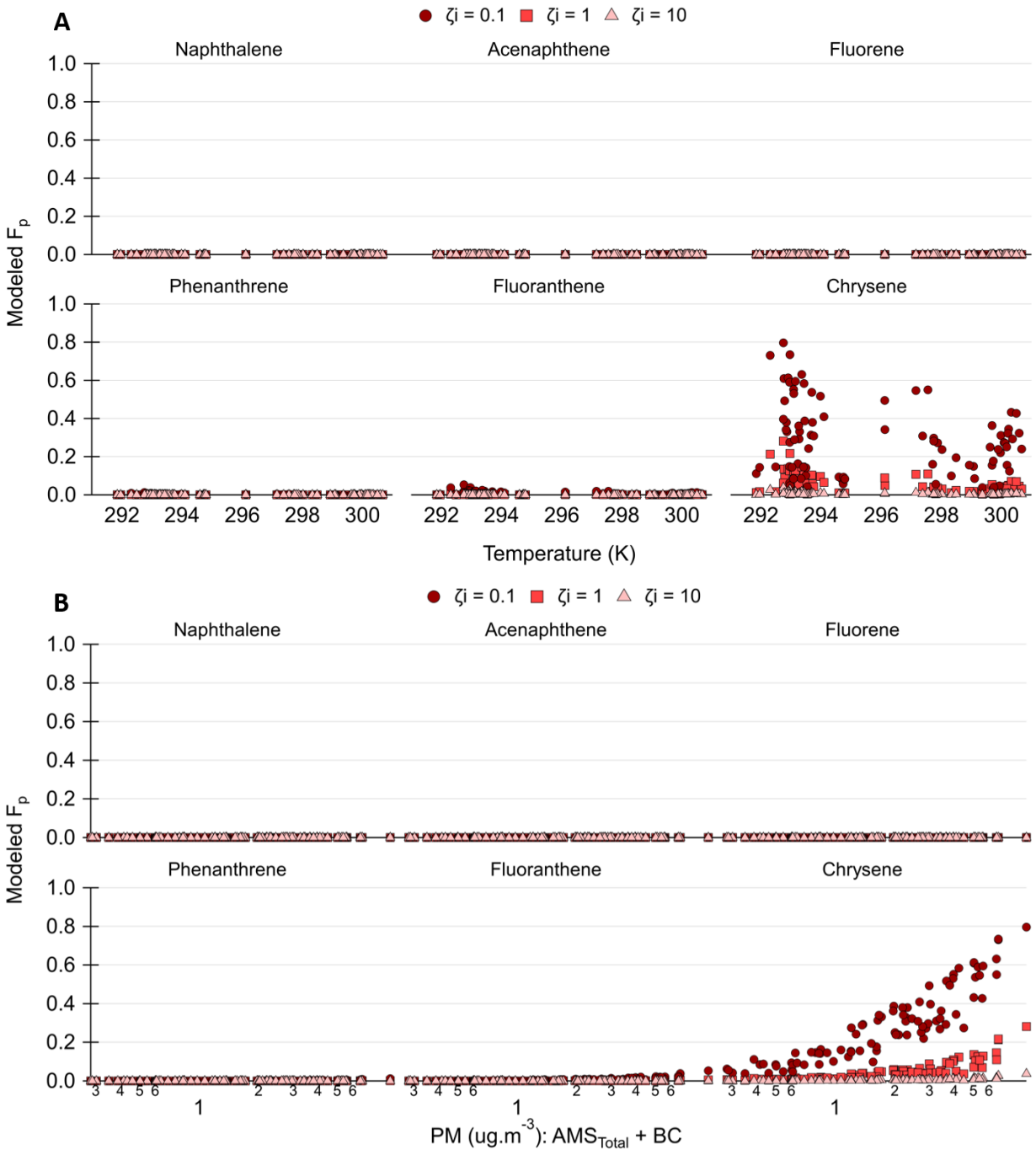

Figure A4.8. Modeled indoor absorptive phase partitioning behavior for selected polycyclic aromatic hydrocarbons (PAHs) during the ALPACA campaign considering three different values for the activity coefficient. **(A)** Calculated particle phase fraction (F_p) values as a function of temperature. **(B)** Calculated F_p values as a function of particulate matter (PM) concentration.

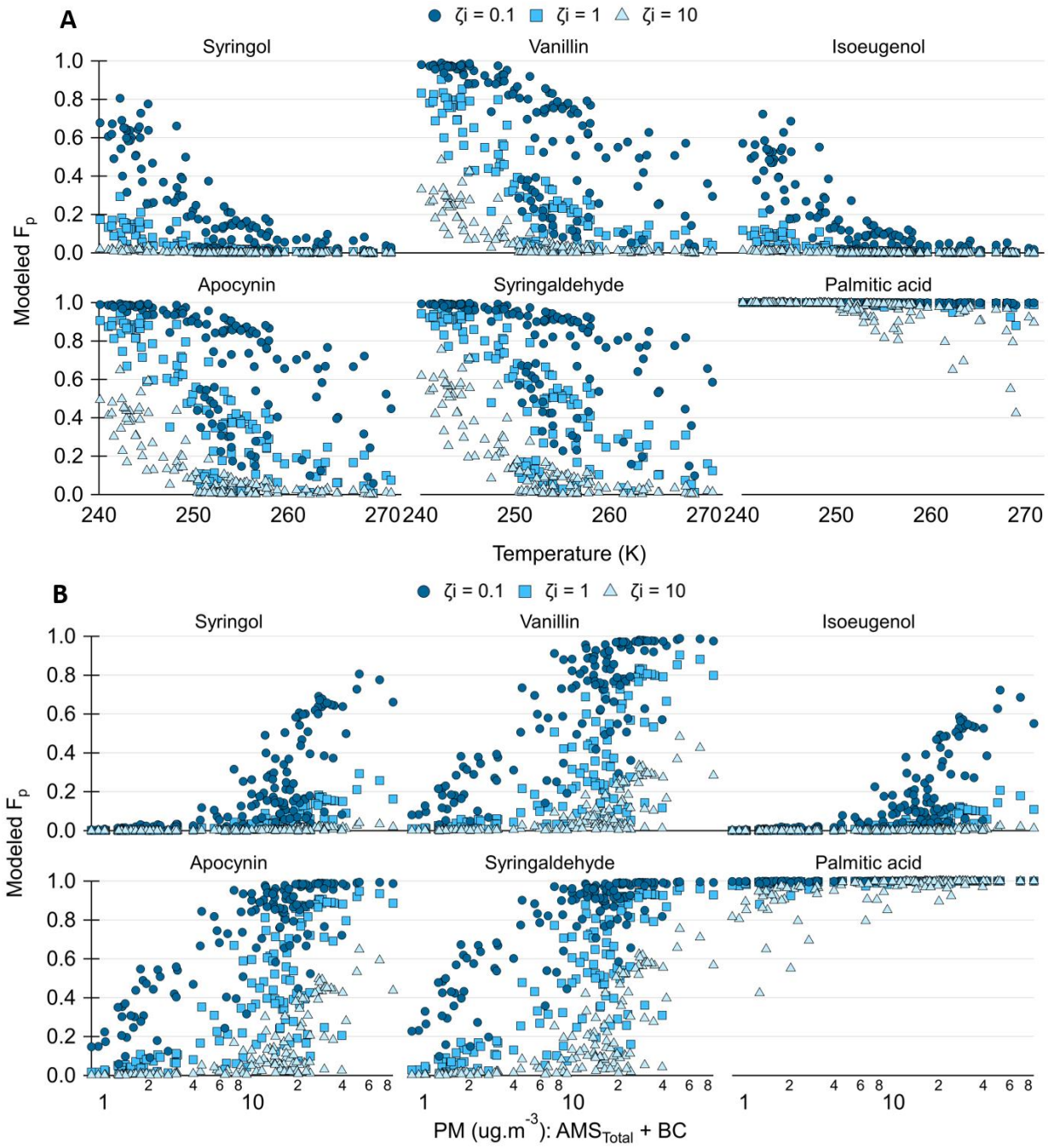

Figure A4.9. Modeled outdoor absorptive phase partitioning behavior for selected biomass-burning related compounds (BBOA) during the ALPACA campaign considering three different values for the activity coefficient. **(A)** Calculated particle phase fraction (F_p) values as a function of temperature. **(B)** Calculated F_p values as a function of particulate matter (PM) concentration.

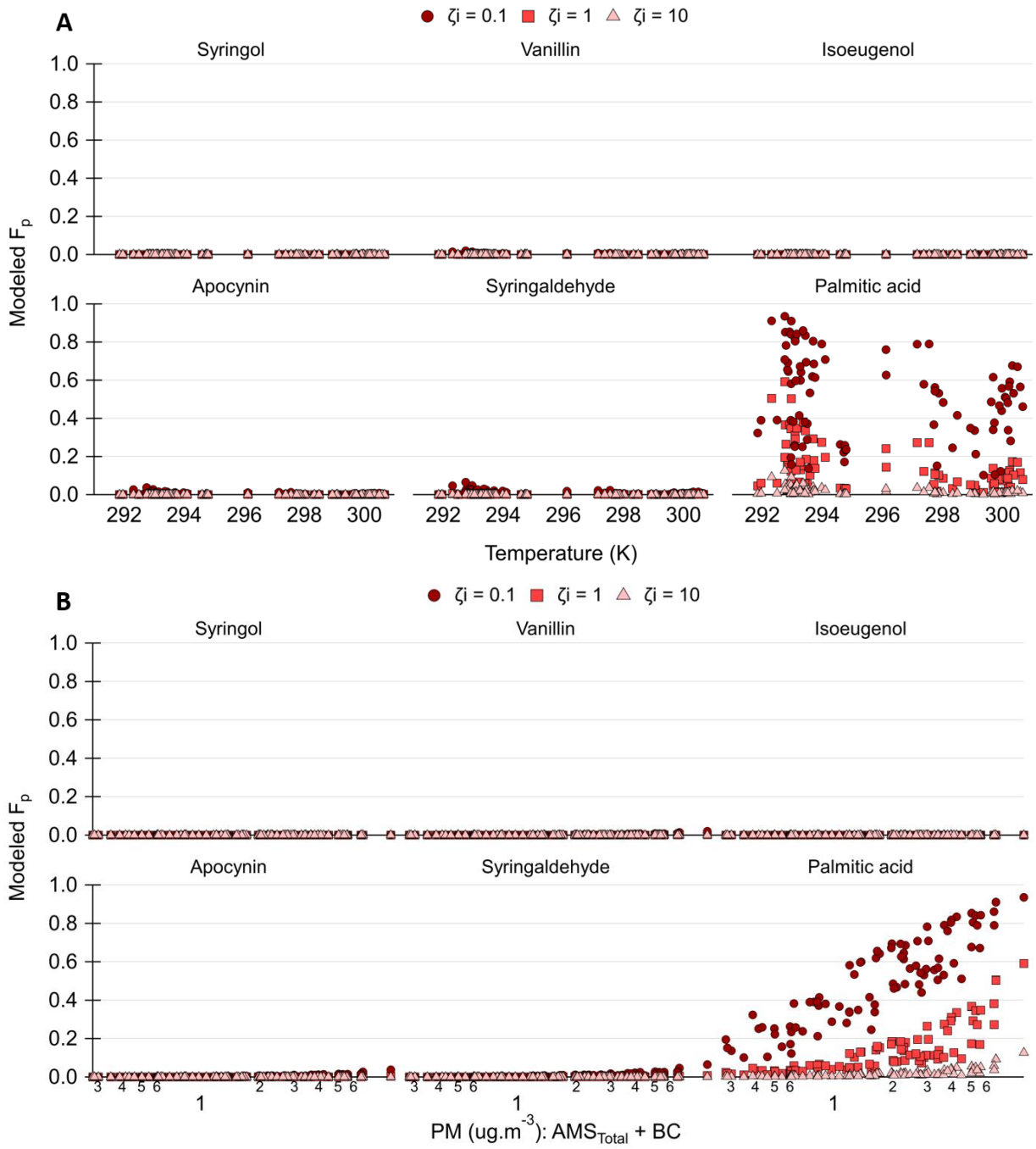

Figure A4.10. Modeled indoor absorptive phase partitioning behavior for selected biomass-burning related compounds (BBOA) during the ALPACA campaign considering three different values for the activity coefficient. **(A)** Calculated particle phase fraction (F_p) values as a function of temperature. **(B)** Calculated F_p values as a function of particulate matter (PM) concentration.

Section A4.4. Observed Phase Partitioning Dynamics

Outdoor Phase Partitioning Timeseries

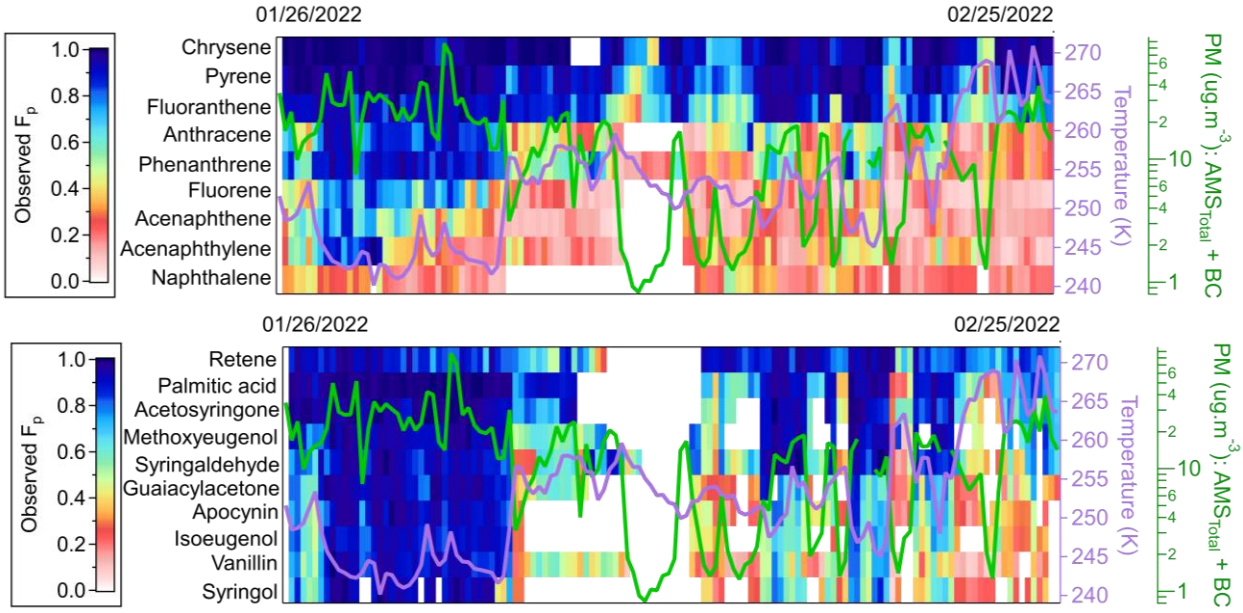

Figure A4.11. Timeseries of the observed outdoor particle phase fraction of selected polycyclic aromatic hydrocarbons (top) and biomass-burning related compounds (bottom) throughout the ALPACA field campaign. Measurements below detection limit are shown as blank spaces.

Effect of Temperature and PM Concentration on Phase Partitioning Dynamics

Linear correlation analysis was performed to compare the impact of fluctuations in temperature and PM mass on promoting changes in the observed speciated particle phase fractions. Here, this correlation is discussed in terms of the Pearson correlation coefficient (r), calculated by Equation A4.4. which yields a number between –1 and 1 that measures the strength and direction of the relationship between the two considered variables.[4]

$$r = \frac{\sum(x_i - \bar{x})(y_i - \bar{y})}{\sqrt{\sum(x_i - \bar{x})^2}\sqrt{\sum(y_i - \bar{y})^2}} \quad \textbf{(A4.4)}$$

Where x_i and y_i are the values of the respective x- and y-variable in a sample; and $\bar{x}$ and $\bar{y}$ represent their mean values. A strong correlation between PM and F_p values should demonstrate an

r value close to 1 (positive correlation) since an increase in PM promotes gas-to-particle partitioning, therefore increasing F_p. In contrast, a strong correlation between temperature and F_p values should exhibit an r value close to -1 (negative correlation) given that an increase in temperature promotes particle-to-gas partitioning, thus decreasing F_p.

Figure A4.12. summarizes the results of the correlation analysis for alkanes, PAHs, and BBOA-related compounds plotted as a function of retention time on the x-axis. Markers differentiate each chemical class and color represents either PM-F_p correlation results (green) or the temperature-F_p relationship (purple). The magnitude of the effect of temperature and PM concentrations on phase partitioning does not seem to be influenced by chemical composition, since compounds eluting at similar retention times display similar r values. However, in the same volatility region, changes in temperature more strongly drive gas-particle partitioning compared to changes in PM mass. Phase partitioning dynamics of compounds eluting before 400s or after ~650s does not seem to be actively impacted by either parameter ($|r| < 0.5$). The implication of this observation is discussed in the chapter main text (**Section 4.3.2**).

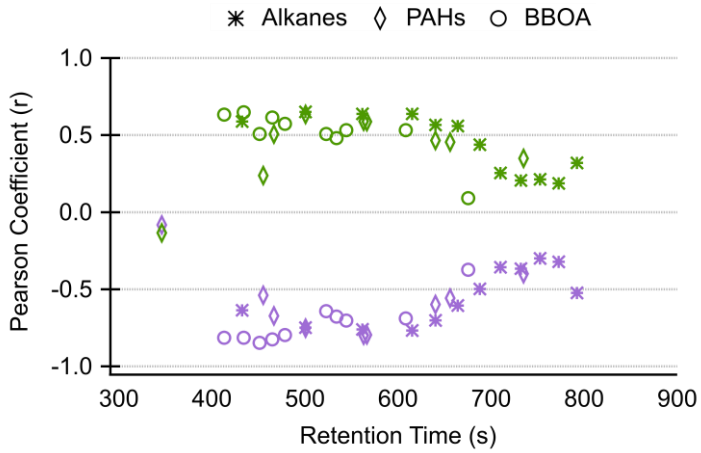

Figure A4.12. Linear correlation analysis between observed particle phase fraction (F_p) values and temperature (purple); and F_p values and particulate matter concentration (green). Markers differentiate each chemical class considered in this study, plotted against each compound respective retention time.

Particle Phase Fraction vs Partitioning Regime

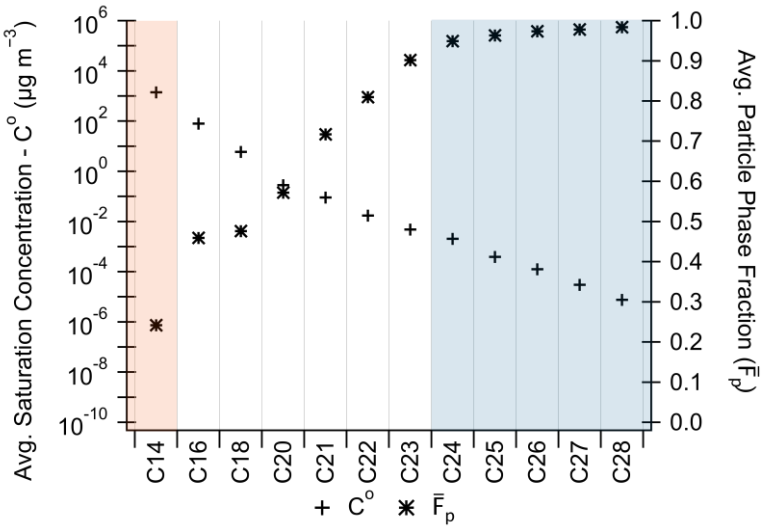

Figure A4.13. Alkanes average outdoor particle phase fraction observations at each established partitioning regime: highlighted orange region symbolizes the temperature-limited regime at high volatilities while blue indicates the temperature-limited regime at low volatilities. Non-highlighted region represents the temperature-dependent regime.

Phase State Estimation

The OA phase state can be inferred using the inverse ambient temperature (T^{-1}) scaled by the glass transition temperature of the OA ($T_g.T^{-1}$). When the ambient temperature is below T_g, meaning $T_g.T^{-1} \geq 1$, the aerosol is found in a solid/glassy state; for $T_g.T^{-1} \leq 1$, the aerosol can exist in a liquid or semi-solid state. The threshold for liquid to semi-solid transition is assumed to be at $T_g.T^{-1} \approx 0.8$, corresponding to a dynamic viscosity equal to 10^2 Pa s.[5,6]

Phase state evaluations were performed following the methodology described by Shiraiwa et al.[5] The aerosol glass transition temperature under dry conditions was calculated using a parametrization equation (Equation A4.5) based on the elemental composition of the organic compounds comprising the aerosol population, i.e. molecular weight, and oxidation level. For this study, these two parameters were estimated using the information provided by the approximately

200 compounds identified with SV-TAG. The calculated average molecular weight and oxidation levels were, respectively, 236.95 g.mol^{-1} and 0.1.

$$T_{g,0} = A + B(MW) + C(MW)^2 + D(O{:}C) + E(MW)(O{:}C) \quad \textbf{(A4.5)}$$

Where, $T_{g,0}\,(K)$ is the OA glass transition temperature under dry conditions (RH = 0); $MW(g.mol^{-1})$ is the average molecular weight; and $O{:}C$ is the average oxidation level (oxygen to carbon ratio). The parametrization parameters are:[5] $A\,(K) = -21.57$; $B\,(K.mol.g^{-1}) = 1.51$; $C\,(K.mol^2.g^{-2}) = -1.7 \times 10^{-3}$; $D\,(K) = 131.4$; $E\,(K.mol.g^{-1}) = -0.25$.

Under dry conditions T_g was estimated as 247.43 K. Note that T_g increases with increasing molecular weight, but the SV-TAG was designed to collected more volatile species, thus species of lower molecular mass. Therefore, this phase state estimation must represent the best case scenario if a liquid aerosol is desired.

Under humid conditions, OA particles take up water by hygroscopic growth in response to RH, lowering T_g and the particle viscosity. Therefore, T_g of organic–water mixtures were estimated using the Gordon–Taylor equation:

$$T_g = \frac{(1-w_{org})T_{g,w} + \frac{1}{k_{GT}} w_{org} T_{g,0}}{(1-w_{org}) + \frac{1}{k_{GT}} w_{org}} \quad \textbf{(A4.6)}$$

$$w_{org} = \frac{C_{OA}}{C_{OA}+C_w} \quad \textbf{(A4.7)} \qquad C_w = \frac{k\rho_w C_{OA}}{\rho_{OA}\left(\frac{1}{a_w}-1\right)} \quad \textbf{(A4.8)} \qquad a_w = \frac{RH}{100} \quad \textbf{(A4.9)}$$

Where T_g (K) is the average glass transition temperature under humid conditions; w_{org} is the mass fraction of organics; $T_{g,w}\,(136\,K)$ is the water glass transition temperature; k_{GT} is the Gordon-Taylor constant, assumed to be equal to 2.5;[5,6] $C_{OA}\,(\mu g.m^{-3})$ is the total organic mass concentration obtained from AMS measurements; $C_w\,(\mu g.m^{-3})$ is the water mass concentration; k is the effective hygroscopicity parameter, assumed to be equal to 0.12;[7] $\rho_w\,(1.0\,g.cm^{-3})$ is the

density of water; ρ_{OA} $(1.4\ g.cm^{-3})$ is the OA density[7]; a_w is the water activity; $RH(\%)$ is the ambient relative humidity obtained from the air quality sensors.

Figure A4.14 show the calculated $T_g.T^{-1}$ values for the observed outdoor and indoor conditions. In both environments, the OA was found in a semi-solid, viscous state.

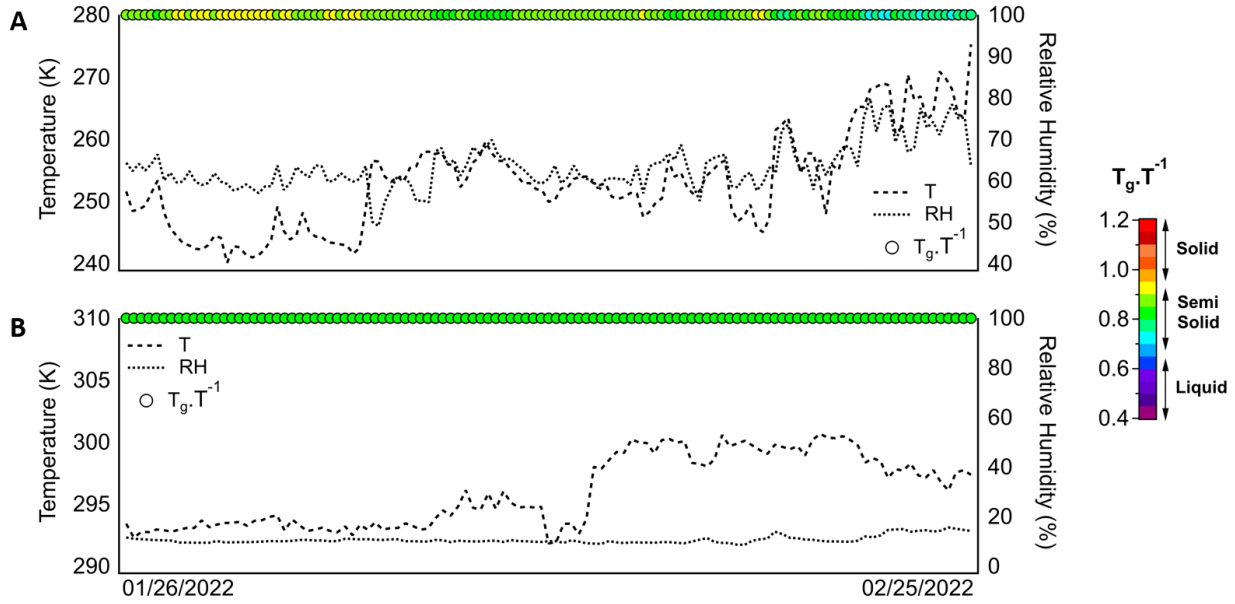

Figure A4.14. Outdoor (**A**) and indoor (**B**) phase state estimations.

References

1. Simpson WR, Mao J, Fochesatto GJ, et al. Overview of the Alaskan Layered Pollution And Chemical Analysis (ALPACA) Field Experiment. *ACS ES&T Air*. 2024;1(3).

2. Kreisberg NM, Hering SV, Williams BJ, Worton DR, Goldstein AH. Quantification of Hourly Speciated Organic Compounds in Atmospheric Aerosols, Measured by an In-Situ Thermal Desorption Aerosol Gas Chromatograph (TAG). *Aerosol Sci. and Tech.*. 2009;43(1):38-52.

3. American Institute of Chemical Engineers (AIChE). *DIPPR Project 801 - Full Version*. Design Institute for Physical Property Research

4. Berman JJ. *Data Simplification Making Complex Data Usable*. San Francisco Elsevier Science & Technology Ann Arbor, Michigan Proquest; 2016:135-187.

5. Shiraiwa M, Li Y, Tsimpidi AP, et al. Global distribution of particle phase state in atmospheric secondary organic aerosols. *Nature Communications*. 2017;8(1).

6. DeRieux WSW, Li Y, Lin P, et al. Predicting the glass transition temperature and viscosity of secondary organic material using molecular composition. *Atmospheric Chemistry and Physics*. 2018;18(9):6331-6351.

7. Pöhlker ML, Pöhlker C, Quaas J, et al. Global organic and inorganic aerosol hygroscopicity and its effect on radiative forcing. *Nature Communications*. 2023;14(1).

APPENDIX A5

Supplement of "Sources and Dynamics of Wintertime Air Pollution during the Alaskan Layered Pollution And Chemical Analysis (ALPACA) Field Campaign"

Section A5.1. PMF Solution

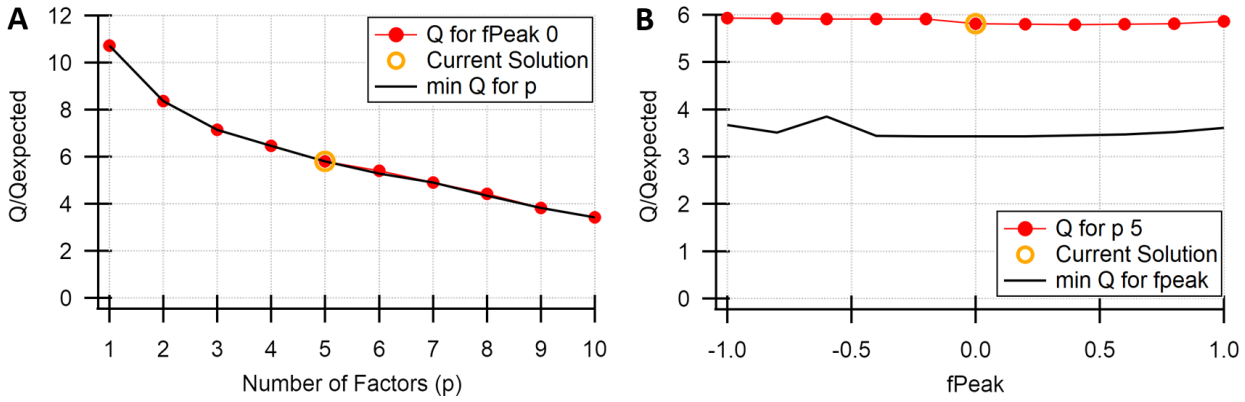

Figure A5.1. Evaluation of Q/Q_{exp}. **(A)** Q/Q_{exp} as a function of p (number of factors). **(B)** Q/Q_{exp} as a function of fPeak (rotational ambiguity).

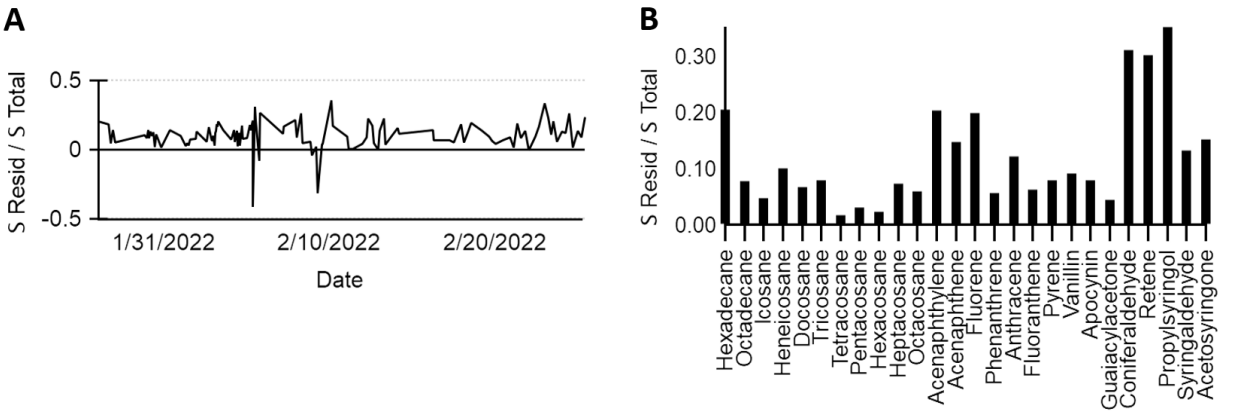

Figure A5.2. PMF residuals as a fraction of the total, which represents the fraction of the summed signal from SV-TAG compounds that were left under-explained (positive values) or over-explained (negative values). **(A)** Residual timeseries. **(B)** Residual profiles.

Section A5.2. PMF Interpretation

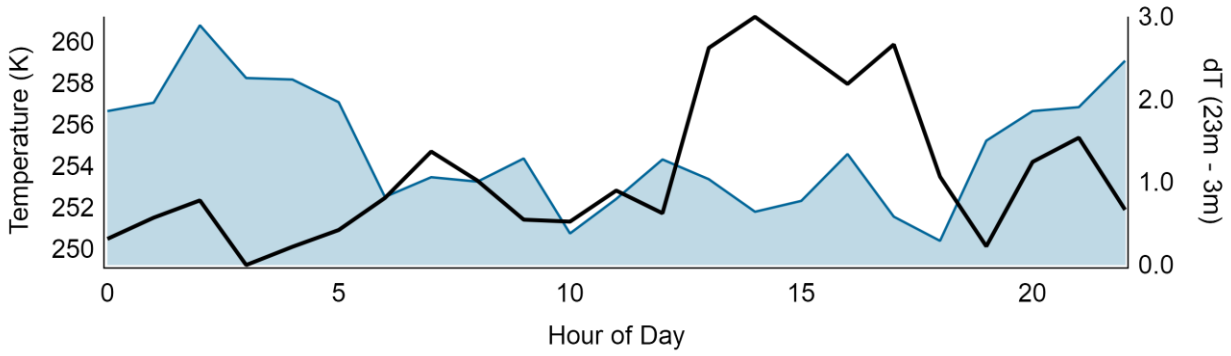

Figure A5.3. Meteorological diurnal profiles. Temperature is shown as the solid line (left). Surface-based inversion strength is delineated by the shaded blue (right).

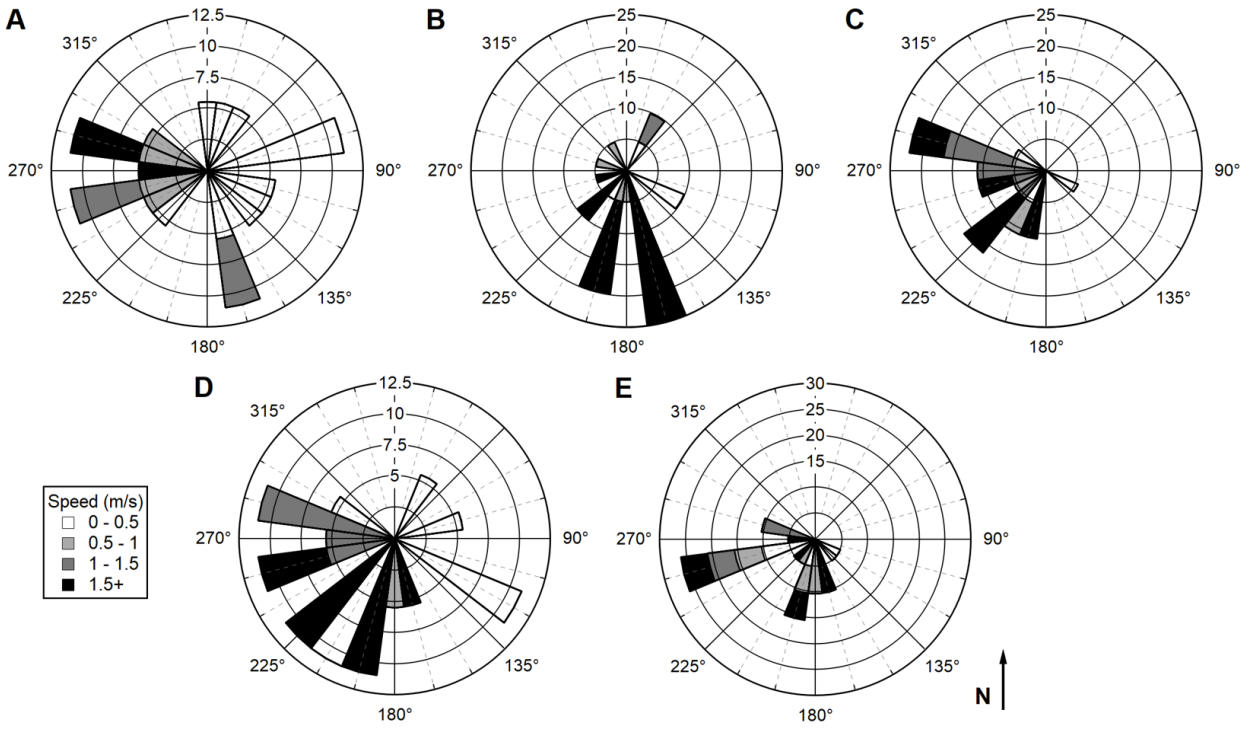

Figure A5.4. Rose plots showing the wind speed and direction when each factor abundances were elevated (>1 standard deviation above the mean factor abundance). **(A)** Factor 1. **(B)** Factor 2. **(C)** Factor 3. **(D)** Factor 4. **(E)** Factor 5.

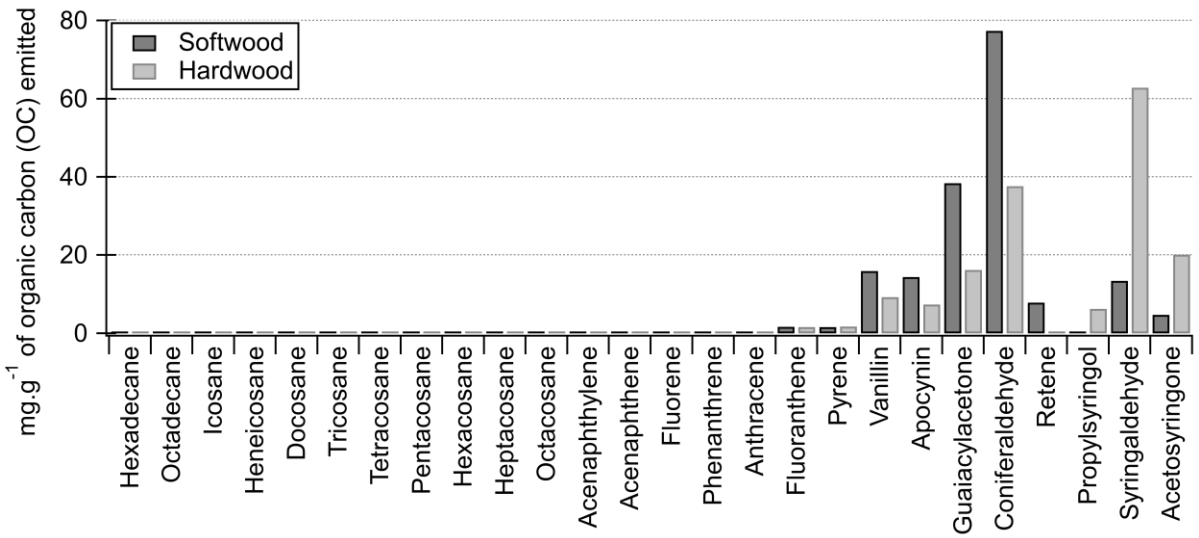

Figure A5.5. Speciation of fine particle organic compounds emitted from northeastern U.S. wood species. Adapted from Fine et al (2001).[1]

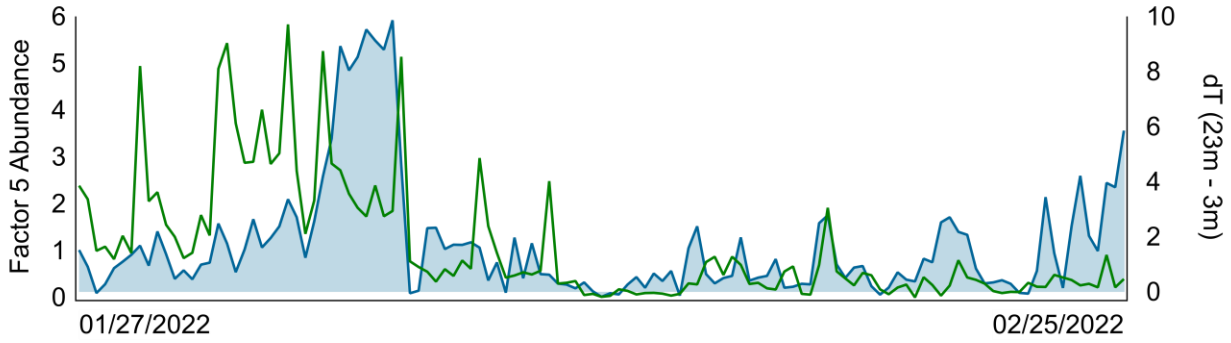

Figure A5.6. Factor 5 abundances and surface-based inversion strength. The PMF factor is shown in green (left). The 23 - 3 m temperature difference is represented by the shaded blue region (right).

References

1. Fine PM, Cass GR, Simoneit BRT. Chemical Characterization of Fine Particle Emissions from Fireplace Combustion of Woods Grown in the Northeastern United States. *Environmental Science & Technology*. 2001;35(13):2665-2675.